APPLIED COMPUTATIONAL ELECTROMAGNETICS SOCIETY JOURNAL

May 2024
Vol. 39 No. 5
ISSN 1054-4887

The ACES Journal is abstracted in INSPEC, in Engineering Index, DTIC, Science Citation Index Expanded, the Research Alert, and to Current Contents/Engineering, Computing & Technology.

The illustrations on the front cover have been obtained from the ARC research group at the Department of Electrical Engineering, Colorado School of Mines

Published, sold and distributed by: River Publishers, Alsbjergvej 10, 9260 Gistrup, Denmark

MAY 2024 REVIEWERS

Giovanni Angiulli
Behrokh Beiranvand
Jie Chen
Yogesh Kumar Coukiker
Dileepan Dhanasekaran
Liwei Guo
Guan-Long Huang
Shian Hwu
Nikolaos V. Kantartzis
Brian LaRocca
Matteo Bruno Lodi
Antonino Musolino
Andrew Peterson
Kannadhasan S.
Natarajamani S.
Masoud Sarabi
Giovanni Maria Sardi
Sivaprakash S. C.
Lei Xu
Shihyuan Yeh
Tao Yuan
Yi Zhu
Theodoros Zygiridis

THE APPLIED COMPUTATIONAL ELECTROMAGNETICS SOCIETY JOURNAL

Vol. 39 No. 5 May 2024

TABLE OF CONTENTS

Near Field Scatter from a Body of Revolution

Edward C. Michaelchuck Jr.[1], Samuel G. Lambrakos[2], and William O. Coburn[3]

[1]Signature Technology Office

[2]Space Systems Development Division
U.S. Naval Research Laboratory, Washington, D.C. 20375, USA
edward.c.michaelchuck.civ@us.navy.mil, samuel.g.lambrakos.civ@us.navy.mil

[3]Retired Electronics Engineer
Army Research Laboratory, Adelphi, MD 20378, USA
keefecoburn@comcast.net

Abstract – Better understanding of electromagnetic wave propagation through vegetation and forest environments can be achieved with the aid of modeling and simulation. Specifically, modeling the coherent summation of electromagnetic waves due to both single scatter and multi-scatter effects. To accurately perform simulations in lower frequency bands, S-band and below, the Body of Revolution (BOR) Method of Moments (MoM) must be extended to calculate the scattered electric and magnetic near-fields from BOR in the presence of a plane wave. The near field interactions specifically occur during the various higher order scattering harmonics, i.e. 2nd order and greater harmonics. Additionally, the method must accurately capture scattered fields in the presence of a non-plane wave incident upon BOR. The focus of this study is modeling lossy dielectric BOR that are characteristic of vegetation and forest environments, e.g., cylinders representing tree branches. Although the formal electric and magnetic field scattering definitions are known, this report presents analytical formulations of near field scattering from BOR for this implementation of BOR-MoM. The scattered-field extensions are validated using the commercial software FEKO©, which simulates electromagnetic-wave scattering in 3D using MoM formulation of scattered fields.

Index Terms – Body of Revolution, Method of Moments, near fields, remote sensing, scattering.

I. INTRODUCTION

Accurate modeling and simulation of electromagnetic wave scattering from vegetation within forest environments is essential for various remote sensing and communications applications including Synthetic Aperture RADAR imaging and cellular connectivity. These models should consider the coherent single and multi-path effects of electromagnetic waves propagating through environments consisting of vegetation and forests. These effects can be described using Multiple Scattering Theory (MST) [1]. Previously, multi-scatter has been characterized through shooting bounce ray methodologies where the physical optics approximations apply, $\lambda \ll \mathrm{d}$, where d is the maximum size of the scattering object [1–3]. These methodologies, however, are not suitable when the physical optics approximation no longer applies, i.e., objects in the scene are not sufficiently electrically large.

Other methods that have been studied include iterative radiative transfer methods and Fresnel double scattering using Discrete Dipole Approximation [4, 5]. Full wave solutions have also been used to examine multiple scattering effects in trees. The software FEKO©, which is for simulation of electromagnetic-wave scattering in 3D using the Method of Moments (MoM) formulation of scattered fields, was used to examine scattering from electrically small vegetation above a dielectric ground plane [6]. Additionally, a two-step hybrid method was employed, combining (1) 3D MoM (via FEKO©) to fill in the T-Matrix coefficients for the individual scatterers and (2) MST [7]. These modeling efforts [6, 7] showed exceptional results, but were not suited for the study of large stochastic forest environments due to computational requirements. Accordingly, these efforts have motivated the need for faster simulation of wave propagation through vegetation and forest environments, using MoM formulation of Maxwell's Equations.

Traditionally, trees and vegetation are characterized by axi-symmetric objects, e.g., cylinders, which allows for the use of the Body of Revolution (BOR) MoM [1–8]. The classical BOR-MoM provides a full wave solution to scattering phenomenon for incident plane waves

Submitted On: January 19, 2024
Accepted On: June 21, 2024

https://doi.org/10.13052/2024.ACES.J.390501

[9–23]. Since the method only discretizes over an analytically singular generating arc for a set of harmonics, the computational burden is an order of magnitude less than that of the traditional 3D MoM. In turn, BOR-MoM provides a fast, accurate solution for BOR. Additionally, it allows for the calculation of both near fields and far fields from the induced electric and fictitious magnetic surface currents. Previous applications of BOR-MoM analyzed singular scatterers with respect to an incident field [9–22]. These analyses included: far field electric and magnetic field expansions [9–23], RADAR Cross Section (RCS) analysis using the scattering amplitude [13, 17, 20], expansion of the integral formulation to consider a dielectric medium surrounding BOR in a layered system [15], and evaluation of the resonances of a BOR in a lossy dispersive half-space [11–12, 15]. Typically, these methodologies considered only a single scatterer or integral expansions to BOR derivation to handle multi-reflection/scatter effects that can occur in a scene.

Due to the stochastic nature of trees and foliage however, expansion of the integral operators to account for the connections between the branches is not well posed computationally, in terms of discrete numerical representation. Additionally, BOR-MoM is primarily used for single objects, and not multiple discrete scatterers, within a scene. Thus, various scatterers must interact via multi-scatter techniques rather than via integral operator additions in the impedance matrix. In turn, the nature of foliage is that of Multiple BOR (MBOR) scattering which has been extensively researched and applied to foliage [24–31]. These techniques include various methods such as cylindrical and spherical wave expansions, T-matrix approximations, and thin cylinder approximations [25–31]. To flush out the subtleties of tree scattering using MBOR approaches, however, these methods are not ideal for physically and accurately understanding the mechanisms by which the waves propagate through foliage mediums and interact when minimal assumptions are present.

To analyze these multi-scatter effects, both near field and far field scattered electromagnetic waves must be analyzed for both plane wave and non-plane wave incidence. The non-plane wave case occurs when a branch scatters onto another branch that is within the near field; the resultant incident wave upon the second branch has a specific wave front, assumed non-plane wave, across the branch [5–7].

In what follows, the focus of this paper is near field scattering from a BOR. Although the formal electric and magnetic field scattering definitions are known, this paper provides a detailed derivation of the formal scattering for this particular implementation of BOR-MoM. Note that the near field derivation is valid for all of space; however, it is not computationally advantageous to use it when in the far field for a scatterer. First, presented is a derivation for BOR-MoM. Secondly, the generalized scattered fields for all of space - including the near fields - are derived for this implementation of BOR-MoM. Then the near field calculation method is validated for both perfect electric conductors (PEC) and lossy dielectric cylinders against the 3D MoM in FEKO©.

II. BODY OF REVOLUTION METHOD OF MOMENTS

BOR is the rotation of a generating curve, planar arc *C*, about an axis, see Fig. 1. In this study, the axis of rotation will be the *z*-axis of a Cartesian coordinate system, and the generating curve will only exist in the right half plane where by definition the curve is rotated 360° around the *z*-axis. In turn, the surface, *S*, formed by BOR will be the interface separating free space and the scatterer with material properties $\varepsilon=\varepsilon_r\varepsilon_0$ and $\mu=\mu_r\mu_0$.

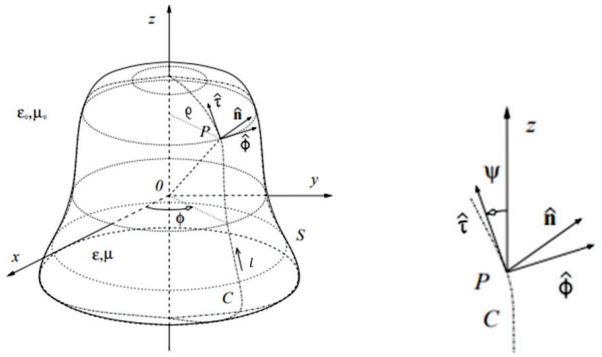

Fig. 1. A Body of Revolution where (a) is the three-dimensional model with the relevant coordinate system definitions and (b) is the coordinate definitions along the surface of BOR. Note that the BOR figure representation is from and with permission of Matthaeis and Lang [10, 11].

The coordinate unit vectors are defined in Fig. 1 by:

$$\hat{\boldsymbol{\tau}} = \sin\psi\cos\varphi\ \hat{\mathbf{x}} + \sin\psi\sin\varphi\ \hat{\mathbf{y}} + \cos\psi\ \hat{\mathbf{z}}, \quad (1)$$

$$\hat{\mathbf{n}} = \cos\psi\cos\varphi\ \hat{\mathbf{x}} + \cos\psi\sin\varphi\ \hat{\mathbf{y}} - \sin\psi\ \hat{\mathbf{z}}, \quad (2)$$

$$\hat{\boldsymbol{\varphi}} = -\sin\varphi\ \hat{\mathbf{x}} + \cos\varphi\ \hat{\mathbf{y}}. \quad (3)$$

The Electric Field Integral Equations (EFIE) used to evaluate the surface currents along the surface, *S*, are defined by:

$$\frac{\mathbf{E}_t(\mathbf{r})}{2} = \mathbf{E}_t^i(\mathbf{r}) + \\ -j\omega\mu_0(\underline{\mathbf{I}} - \hat{\mathbf{n}}\hat{\mathbf{n}})\cdot \mathrm{PV}\int_{s^+} \underline{\mathbf{G}}(\mathbf{r},\mathbf{r}')\cdot\mathbf{J}_s(\mathbf{r}')\,dS' + \\ -(\underline{\mathbf{I}} - \hat{\mathbf{n}}\hat{\mathbf{n}})\cdot \mathrm{PV}\int_{s^+} \underline{\mathbf{K}}(\mathbf{r},\mathbf{r}')\times\mathbf{M}_s(\mathbf{r}')\,dSS', \quad (4)$$

$$\frac{\mathbf{E}_t(\mathbf{r})}{2} = j\omega\mu(\underline{\mathbf{I}} - \widehat{\mathbf{n}}\widehat{\mathbf{n}}) \cdot \mathrm{PV} \int_{S^-} \underline{\mathbf{G}}(\mathbf{r},\mathbf{r}') \cdot \mathbf{J_s}(\mathbf{r}')\, dS' +$$

$$-(\underline{\mathbf{I}} - \widehat{\mathbf{n}}\widehat{\mathbf{n}}) \cdot \mathrm{PV} \int_{S^-} \underline{\mathbf{K}}(\mathbf{r},\mathbf{r}') \times \mathbf{M}_s(\mathbf{r}')\, dSS', \quad (5)$$

where $\mathbf{E}_t(\mathbf{r})$ is the tangential field on the surface, ω is the angular frequency, $\underline{\mathbf{I}}$ is the unit dyadic, PV denotes a principal value integral, $S^+$is the outer surface of S, S^- is the inner surface of $S, \underline{\mathbf{G}}(\mathbf{r},\mathbf{r}')$ is the electric dyadic Green's function, $\underline{\mathbf{K}}(\mathbf{r},\mathbf{r}')$ is the magnetic dyadic Green's function, $\mathbf{J}_s(\mathbf{r}')$ are the induced electric surface currents, and $\mathbf{M}_s(\mathbf{r}')$ are the induced, fictitious magnetic surface currents.

The incident fields and induced sources within EFIE can then be split into τ and $\boldsymbol{\varphi}$ vector components:

$$\mathbf{E}_t^i(\mathbf{r}) = E_\tau^i(l,\varphi)\hat{\boldsymbol{\tau}} + E_\varphi^i(l,\varphi)\widehat{\boldsymbol{\varphi}}, \quad (6)$$

$$\mathbf{J}_s(\mathbf{r}) = J_\tau(l,\varphi)\hat{\boldsymbol{\tau}} + J_\varphi(l,\varphi)\widehat{\boldsymbol{\varphi}}, \quad (7)$$

$$\mathbf{M}_s(\mathbf{r}) = M_\tau(l,\varphi)\hat{\boldsymbol{\tau}} + M_\varphi(l,\varphi)\widehat{\boldsymbol{\varphi}}, \quad (8)$$

where l denotes the location on generating arc, *C*.

A. Fourier series expansion

To evaluate the induced surface currents on the generating arc, EFIE are expanded in Fourier series around the *z*-axis such that MoM is only evaluated over the generating arc for a series of harmonics. The resulting induced sources are:

$$E_p{}^i(\mathbf{r}) = \sum_{n=-\infty}^{\infty} E_{p,n}{}^i e^{jn\varphi}, \quad (9)$$

$$J_p(\mathbf{r}) = \sum_{n=-\infty}^{\infty} J_{p,n} e^{jn\varphi}, \quad (10)$$

$$M_p(\mathbf{r}) = \sum_{n=-\infty}^{\infty} M_{p,n} e^{jn\varphi}, \quad (11)$$

where $p, q = \tau, \varphi$ and the Fourier Series Coefficients are defined as:

$$C_n = \frac{1}{2\pi} \int_{-\pi}^{\pi} f(\varphi) e^{-jn\varphi'} d\varphi', \quad (12)$$

for $f(\varphi) = E,\ J,\ M$, etc.

B. Method of Moments expansion

Now the electric and magnetic surface currents can be discretized for MoM such that:

$$J_{\tau,n}(l) = \sum_{m=1}^{N} J_{\tau,m,n} = \sum_{m=1}^{N} \frac{\Lambda_m^{\tau,n} P_m(l)}{\rho_m}, \quad (13)$$

$$J_{\varphi,n}(l) = \sum_{m=1}^{N} J_{\varphi,m,n} = \sum_{m=1}^{N+1} \Lambda_m^{\varphi,n} P_m(l), \quad (14)$$

$$M_{\tau,n}(l) = \sum_{m=1}^{N} M_{\tau,m,n} = \sum_{m=1}^{N} \Omega_m^{\tau,n} P_m(l), \quad (15)$$

$$M_{\varphi,n}(l) = \sum_{m=1}^{N} M_{\tau,m,n} = \sum_{m=1}^{N+1} \Omega_m^{\varphi,n} P_m(l), \quad (16)$$

where $J_{\tau,m,n}, J_{\varphi,m,n}, M_{\tau,m,n}$, and $M_{\tau,m,n}$ are the surface currents per harmonic for their respective polarization vector on each discretized segment of the generating arc, m is the segment number, N is the total number of segments, $P_m(1)$ is the chosen basis function expansion, ρ_m is the distance from the z-axis, and $\Lambda_m^{\tau,n}, \Lambda_m^{\varphi,n}, \Omega_m^{\tau,n}$, and $\Omega_m^{\varphi,n}$ are the basis function coefficients.

Testing functions are now applied using the symmetric product:

$$\langle \chi(l), \alpha(l) \rangle = \int_{-\infty}^{\infty} \chi(l) \cdot \alpha(l)\, dl. \quad (17)$$

Now the interaction matrix and incident field matrix can be evaluated for a signal harmonic on BOR generating arc. The equivalent sources are solved by inverting the interaction matrix:

$$[J_n] = [Z_n]^{-1} [E_n]. \quad (18)$$

III. SCATTERED FIELD EQUATIONS FOR A BODY OF REVOLUTION

The scattered field definition using equivalent sources is:

$$\mathbf{E}^s(\mathbf{r}) = -j\omega\mu_0 \oint \underline{\mathbf{G}}^0(\mathbf{r},\mathbf{r}') \cdot \mathbf{J}_s(r')\, dS' +$$

$$- \oint \underline{\mathbf{K}}^0(\mathbf{r},\mathbf{r}') \cdot \mathbf{M}_s(\mathbf{r}')\, dS', \quad (19)$$

$$\mathbf{H}^s(\mathbf{r}) = \oint \underline{\mathbf{K}}^0(\mathbf{r},\mathbf{r}') \cdot J_s(\mathbf{r}')\, dS' +$$

$$- j\omega\varepsilon_0 \oint \underline{\mathbf{G}}^0(\mathbf{r},\mathbf{r}') \cdot \mathbf{M}_s(\mathbf{r}')\, dS', \quad (20)$$

where $\mathbf{E}^s(\mathbf{r})$ is the scattered electric field, $\mathbf{H}^s(\mathbf{r})$ is the scattered magnetic field, r is the scattered field location, and $\mathbf{r}'$ is the surface current source location. Note that equations (19) and (20) are derived from the general formulation, $\mathbf{E}^s(\mathbf{r}) = \mathbf{E}^{\text{total}}(\mathbf{r}) - \mathbf{E}^{\text{inc}}(\mathbf{r})$. The dyadic Green's functions are defined as:

$$\underline{\mathbf{G}}^0(\mathbf{r},\mathbf{r}') = \left(\underline{\mathbf{I}} + \frac{\nabla\nabla}{k^2}\right) g^0(\mathbf{r},\mathbf{r}'), \quad (21)$$

$$\underline{\mathbf{K}}^0(\mathbf{r},\mathbf{r}') = \nabla g^0(\mathbf{r},\mathbf{r}') \times \underline{\mathbf{I}}, \quad (22)$$

where:

$$g^0(\mathbf{r},\mathbf{r}') = \frac{e^{-jk_0|\mathbf{r}-\mathbf{r}'|}}{4\pi|\mathbf{r}-\mathbf{r}'|}. \quad (23)$$

Next, the scattered electric field equations, equation (19), are separated, i.e.:

$$\mathbf{E}^s(\mathbf{r}) = -j\omega\mu_0 \mathbf{E}_1^s(\mathbf{r}) - \mathbf{E}_2^s(\mathbf{r}), \quad (24)$$

$$\mathbf{E}_1^s(\mathbf{r}) = \oint \underline{\mathbf{G}}^0(\mathbf{r},\mathbf{r}') \cdot \mathbf{J}_s(\mathbf{r}')\, dS', \quad (25)$$

$$\mathbf{E}_2^s(\mathbf{r}) = \oint \underline{\mathbf{K}}^0(\mathbf{r},\mathbf{r}') \cdot \mathbf{M}_s(\mathbf{r}')\, dS'. \quad (26)$$

A. $\mathbf{E}_1^s(\mathbf{r})$ integral expansion

The electric field integral operator for the electric surface currents, equation (25), can be combined with equations (7), (10), and (21) to yield:

$$\mathbf{E}_1^s(\mathbf{r}) = \sum_{n=-\infty}^{\infty} \mathbf{E}_{1,n}^s \{\mathbf{J}_{s,n}(\mathbf{l}')\} e^{j\varphi_s}, \quad (27)$$

where φ_s is the azimuthal scattering angle. The Fourier series coefficients are:

$$\mathbf{E}^{S}_{1,n} = \int_{S} \underline{\mathbf{G}}^{0}(\mathbf{r},\mathbf{r}) \cdot \left(\mathbf{J}_{\tau,n}\hat{\boldsymbol{\tau}}' + \mathbf{J}_{\varphi,n}\hat{\boldsymbol{\varphi}}'\right) e^{jn\varphi'} dS'. \quad (28)$$

Next, performing the dot products of the dyadic Green's function in spherical coordinates with the local BOR coordinate system, and separating the scattered field components into separate spherical components, $\widehat{\mathbf{r}}$, $\widehat{\boldsymbol{\varphi}}$, and $\widehat{\boldsymbol{\theta}}$, yields:

$$\mathbf{E}^{s}_{1,n,r} = \int_{S} g^{0}\left(\mathbf{r},\mathbf{r}'\right) F_{r}\left(\mathbf{J}_{s,n}\right) e^{jn\varphi'} dS'\hat{\mathbf{r}}, \quad (29)$$

$$\mathbf{E}^{s}_{1,n,\varphi} = \int_{S} g^{0}\left(\mathbf{r},\mathbf{r}'\right) F_{\varphi}\left(\mathbf{J}_{s,n}\right) e^{jn\varphi'} dS'\widehat{\boldsymbol{\varphi}}, \quad (30)$$

$$\mathbf{E}^{s}_{1,n,\theta} = \int_{S} g^{0}\left(\mathbf{r},\mathbf{r}'\right) F_{\theta}\left(\mathbf{J}_{s,n}\right) e^{jn\varphi'} dS'\widehat{\boldsymbol{\theta}}. \quad (31)$$

The definitions of F_r, F_φ, and F_θ are given in Appendix I. Given derivation of the proper terms accounting for the angular dependencies of the two coordinate systems, equations (29-31) can be expanded further using MoM definitions, equations (13) and (14):

$$\mathbf{E}^{S}_{1,n,r} = \sum_{m=1}^{N} \int_{S} g^{0}\left(\mathbf{r},\mathbf{r}'\right) F_{r}\left(J_{n,m}\right) e^{jn\varphi'} e^{-jn\varphi} dS'\hat{\mathbf{r}}, \quad (32)$$

$$\mathbf{E}^{s}_{1,n,\varphi} = \sum_{m=1}^{N} \int_{S} g^{0}\left(\mathbf{r},\mathbf{r}'\right) F_{\varphi}\left(J_{n,m}\right) e^{jn\varphi'} e^{-jn\varphi} dS'\widehat{\boldsymbol{\varphi}}, \quad (33)$$

$$\mathbf{E}^{s}_{1,n,\theta} = \sum_{m=1}^{N} \int_{S} g^{0}\left(\mathbf{r},\mathbf{r}'\right) F_{\theta}\left(J_{n,m}\right) e^{jn\varphi'} e^{-jn\varphi} dS'\widehat{\boldsymbol{\theta}}. \quad (34)$$

Recognizing that the basis-function sets chosen are rectangular and triangular, and that the discretization is appropriately fine, the integration over a segment can be approximated by:

$$\int_{t_A}^{t_B} f\left(l'\right) dl' = \left(t_B - t_A\right) f\left(\frac{t_B - t_A}{2}\right). \quad (35)$$

Application of this approximation, with triangular basis functions, minimizes error if either side of the basis functions (left and right of the triangle) are evaluated independently. Using equation (35) and equations (32-34), the integration along the generating arc, l, over a single segment becomes:

$$\mathbf{E}^{s}_{1,n,r,m} = \Delta l_{m,k}\rho_{m} \int_{0}^{2\pi} g^{0}\left(\mathbf{r},\mathbf{r}_{m}\right) F_{r,n,m}\left(J_{n,m}\right) e^{jn\varphi'} d\varphi'\hat{\mathbf{r}}, \quad (36)$$

$$\mathbf{E}^{s}_{1,n,\varphi,m} = \Delta l_{m,k}\rho_{m} \int_{0}^{2\pi} g^{0}\left(\mathbf{r},\mathbf{r}_{m}\right) F_{\varphi,n,m}\left(J_{n,m}\right) e^{jn\varphi'} d\varphi'\widehat{\boldsymbol{\varphi}}, \quad (37)$$

$$\mathbf{E}^{s}_{1,n,\theta,m} = \Delta l_{m,k}\rho_{m} \int_{0}^{2\pi} g^{0}\left(\mathbf{r},\mathbf{r}_{m}\right) F_{\theta,n,m}\left(J_{n,m}\right) e^{jn\varphi'} d\varphi'\widehat{\boldsymbol{\theta}}. \quad (38)$$

Consistently, this reformulation has reduced the multivariable integration to that of a single integration around the φ-axis.

B. $\mathbf{E}^{s}_{2}(\mathbf{r})$ integral expansion

As for equation (27), $\mathbf{E}^{s}_{2}$ can be expanded into Fourier series as:

$$\mathbf{E}^{s}_{2}(\mathbf{r}) = \sum_{n=-\infty}^{\infty} \mathbf{E}^{s}_{2,n}\left\{\mathbf{M}_{s,n}\left(\mathbf{l}'\right)\right\} e^{j\varphi}, \quad (39)$$

where:

$$\mathbf{E}^{s}_{2,n} = \int_{S} \underline{\mathbf{K}}^{0}(\mathbf{r},\mathbf{r}) \cdot \left(\mathbf{M}_{\tau,n}\hat{\mathbf{i}}' + \mathbf{M}_{\varphi,n}\widehat{\boldsymbol{\varphi}}'\right) e^{jn\varphi'} dS'. \quad (40)$$

Next, applying analysis similar to that for $E^{s}_{1}(r)$ yields:

$$\mathbf{E}^{s}_{2,r,n,m} = \Delta l_{m,k}\rho_{m} \int_{0}^{2\pi} D_{r,n,m}\left(M_{n,m}\right) e^{jn\varphi'} d\varphi'\hat{\mathbf{r}}, \quad (41)$$

$$\mathbf{E}^{s}_{2,\theta,n,m} = \Delta l_{m,k}\rho_{m} \int_{0}^{2\pi} D_{\theta,n,m}\left(M_{n,m}\right) e^{jn\varphi'} d\varphi'\widehat{\boldsymbol{\theta}}, \quad (42)$$

$$\mathbf{E}^{s}_{2,\varphi,n,m} = \Delta l_{m,k}\rho_{m} \int_{0}^{2\pi} D_{\varphi,n,m}\left(M_{n,m}\right) e^{jn\varphi'} d\varphi'\widehat{\boldsymbol{\varphi}}. \quad (43)$$

Note that $D_{\varphi,m}$, $D_{\theta,m}$, and $D_{r,m}$ are listed in Appendix I. Additionally, note that both $D_{o,m}$ and $F_{o,m}$ - where ô is the unit vector direction of interest - can be expanded in other coordinate systems. The Cartesian coordinate expansions of these quantities are given in Appendix II.

C. $\mathbf{H}^{s}_{1}(\mathbf{r})$ and $\mathbf{H}^{s}_{2}(\mathbf{r})$ integral expansion

Observing the forms of equations (19-20) and equations (24-26), it is apparent that $\mathbf{H}^{s}_{1}(\mathbf{r})$ and $\mathbf{H}^{s}_{2}(\mathbf{r})$ are of similar form to $\mathbf{E}^{s}_{1}(\mathbf{r})$ and $\mathbf{E}^{s}_{2}(\mathbf{r})$ except with the surface currents substituted as - $\mathbf{J_s}(\mathbf{r}') \rightarrow \mathbf{M_s}(\mathbf{r}')$ and $\mathbf{M_s}(\mathbf{r}') \rightarrow -\mathbf{J_s}(\mathbf{r}')$. Thus, based on this formal similarity and electromagnetic duality, the expansions for $\mathbf{H}^{s}_{1}(\mathbf{r})$ and $\mathbf{H}^{s}_{2}(\mathbf{r})$ are:

$$\mathbf{H}^{s}_{1,r,n,m} = \Delta l_{m,k}\rho_{m} \int_{0}^{2\pi} D_{r,n,m}\left(J_{n,m}\right) e^{jn\varphi'} d\varphi'\hat{\mathbf{r}}, \quad (44)$$

$$\mathbf{H}^{s}_{1,\theta,n,m} = \Delta l_{m,k}\rho_{m} \int_{0}^{2\pi} D_{\theta,n,m}\left(J_{n,m}\right) e^{jn\varphi'} d\varphi'\widehat{\boldsymbol{\theta}}, \quad (45)$$

$$\mathbf{H}^{s}_{1,\varphi,n,m} = \Delta l_{m,k}\rho_{m} \int_{0}^{2\pi} D_{\varphi,n,m}\left(J_{n,m}\right) e^{jn\varphi'} d\varphi'\widehat{\boldsymbol{\varphi}}, \quad (46)$$

$$\mathbf{H}^{s}_{2,n,r,m} = \Delta l_{m,k}\rho_{m} \int_{0}^{2\pi} g^{0}\left(\mathbf{r},\mathbf{r_m}\right) F_{r,n,m}\left(M_{n,m}\right) e^{jn\varphi'} d\varphi'\hat{\mathbf{r}}, \quad (47)$$

$$\mathbf{H}^{s}_{2,n,\varphi,m} = \Delta l_{m,k}\rho_m \int_0^{2\pi} g^0(\mathbf{r},\mathbf{r_m})\, F_{\varphi,n,m}(M_{n,m})\, e^{jn\varphi'} d\varphi' \widehat{\boldsymbol{\varphi}}, \tag{48}$$

$$\mathbf{H}^{s}_{2,n,\theta,m} = \Delta l_{m,k}\rho_m \int_0^{2\pi} g^0(\mathbf{r},\mathbf{r_m})\, F_{\theta}(M_{n,m})\, e^{jn\varphi'} d\varphi' \widehat{\boldsymbol{\theta}}. \tag{49}$$

IV. SCATTERED FIELD VALIDATION

The near field scattering calculations were initially examined in the far field by comparing the far field solution (scattering amplitude) of BOR-MoM - previously validated by Matthaeis and Lang [10] - with the generalized scattering equations evaluated in the far field. Additionally, the FEKO© 3D MoM solution was used to compute the near fields around cylinders, and those results were compared to BOR generalized scattering calculations within the near field of cylinders. The general scattered field equations reduce to the far field results, as expected.

The complexity of near field scattering presents a vast dataset to validate against. For brevity, only the magnitude of the scattered fields is compared for both the scattered electric and magnetic fields in the principal component directions, *r*, θ, φ, *x, y,* and *z*. The cross polarized terms are neglected, and only bistatic scattering is considered. The results presented examine only scattering from both PEC and lossy dielectric cylinders, although the methodology can and has been evaluated for other shapes and material properties, e.g., spheres. For this analysis, the incident electric field will be 377 V/m, at a frequency of 3 GHz. Figures 2 and 3 shows the scene and scattering angles.

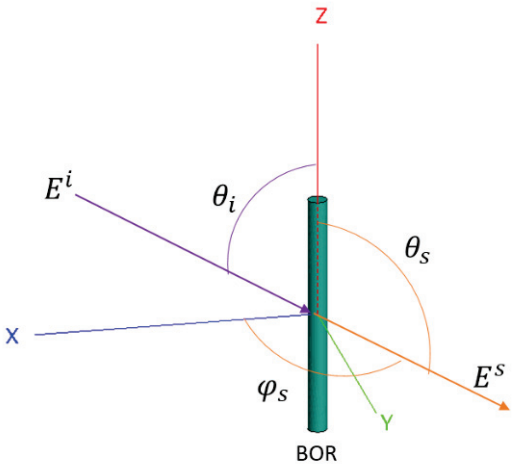

Fig. 2. Cylinder scattering scene for spherical coordinates where E^i is the incident electric field at $\varphi_i = 0°$ and an arbitrary polar angle θ_i. The variables E^S, φ_s, and θ_s are the scattered electric field vector, radial scattering angle, and polar scattering angle, respectively.

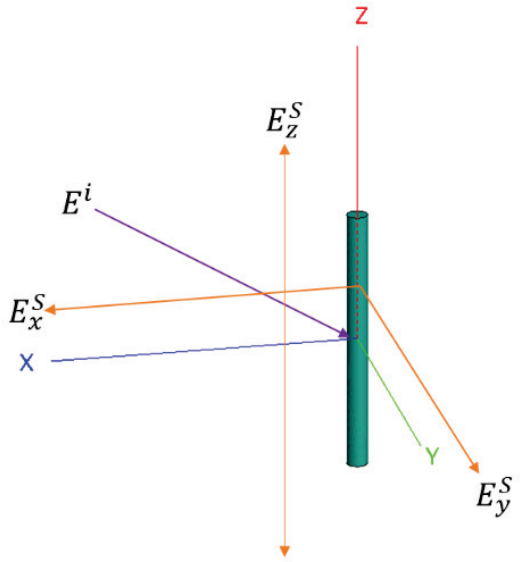

Fig. 3. Cylinder scattering scene for Cartesian coordinates where E^i is an incident electric field at $\varphi_i = 0°$ and an arbitrary polar angle θ_i. The variables E^S_x, E^S_y, and E^S_z are the cardinal direction vectors in which the scattered fields shall be examined.

A. Far field evaluation

Presented in this section is validation of the scattered electric field calculation for the far field ($r > 2D^2/\lambda$) using the generalized scattering definition for PEC BORs. Inherently, PEC BORs are of little value to vegetation scattering, but their evaluation is relevant in the total examination for the near field derivation. Table 1 lists the relevant statistics for the evaluation and validation. The first set of plots, Figs. 4–11, describe a far field comparison between BOR near field calculator and BOR scattering amplitude calculator at 100 m from BOR.

Table 1: PEC cylinder test cases for the validation of MoM with BOR, specifically cylinders

Cylinder Length	$1\lambda, 3\lambda, 5\lambda, 10\lambda$
Cylinder Radius	0.04λ
$\boldsymbol{\theta_i}$ [°]	20°
$\boldsymbol{\varepsilon_r}$	PEC
Harmonics	10
Mesh Size	$\lambda_m/10$
Range	100 m
$\boldsymbol{E_i}$	377 V/m

B. Near field electric and magnetic field validation

Presented in this section is validation of the scattered electric and magnetic field calculation for the near field

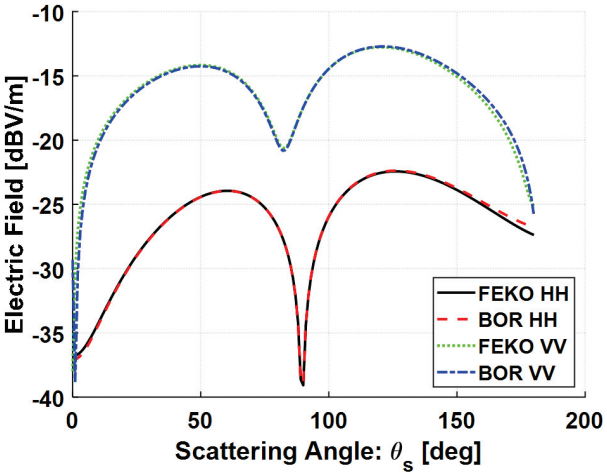

Fig. 4. Magnitude of the bistatic electric field vs. θ_s on a PEC cylinder with a radius of 0.04λ, L = 1λ, at $\theta_i = 20°$.

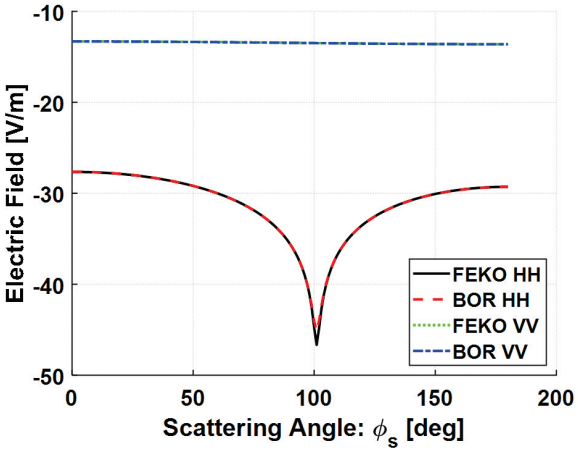

Fig. 7. Magnitude of the bistatic electric field vs. φ_s on a PEC cylinder with a radius of 0.04λ, L = 3λ, at $\theta_i = 20°$.

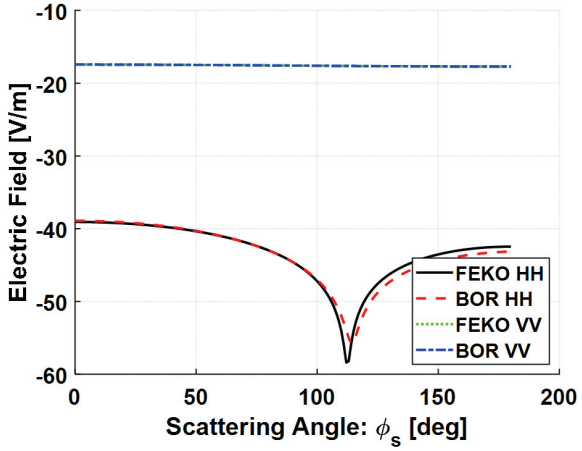

Fig. 5. Magnitude of the bistatic electric field vs. φ_s on a PEC cylinder with a radius of 0.04λ, L = 1λ, at $\theta_i = 20°$.

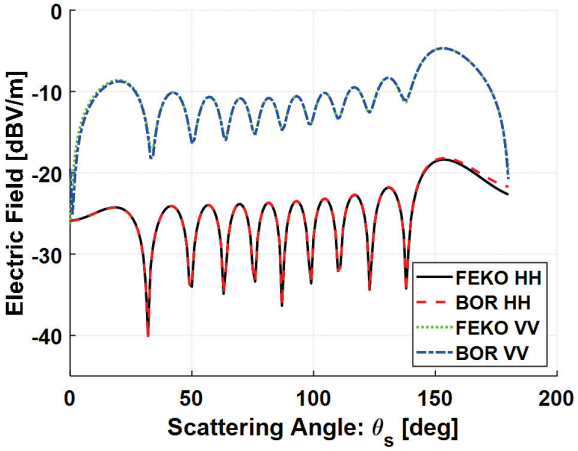

Fig. 8. Magnitude of the bistatic electric field vs. θ_s on a PEC cylinder with a radius of 0.04λ, L = 5λ, at $\theta_i = 20°$.

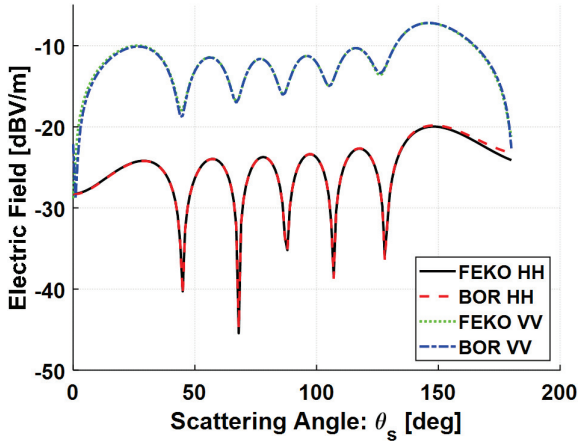

Fig. 6. Magnitude of the bistatic electric field vs. θ_s on a PEC cylinder with a radius of 0.04λ, L = 3λ, at $\theta_i = 20°$.

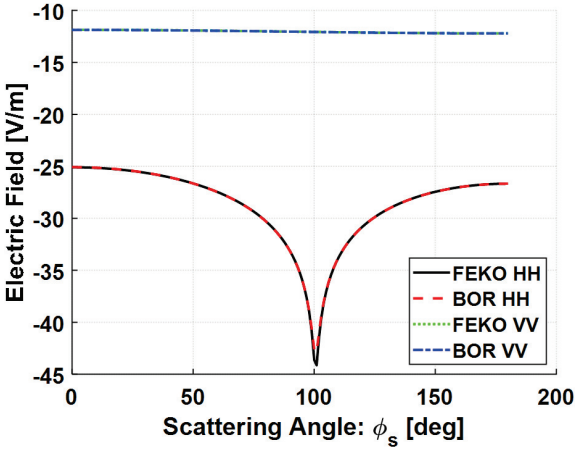

Fig. 9. Magnitude of the bistatic electric field vs. φ_s on a PEC cylinder with a radius of 0.04λ, L = 5λ, at $\theta_i = 20°$.

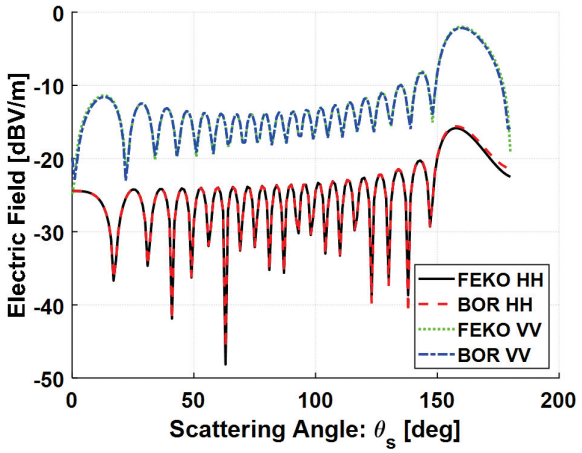

Fig. 10. Magnitude of the bistatic electric field vs. θ_s on a PEC cylinder with a radius of 0.04λ, L = 10λ, at $\theta_i = 20°$.

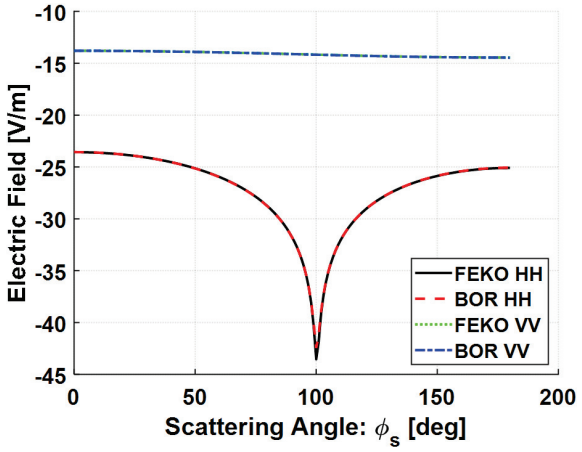

Fig. 11. Magnitude of the bistatic electric field vs. φ_s on a PEC cylinder with a radius of 0.04λ, L = 10λ, at $\theta_i = 20°$.

($r < 2D^2/\lambda$ and $kr \gg 1$) where λ is the free space wavelength and λ_m is the material adjusted wavelength, using the generalized scattering definition. Table 2 lists the relevant statistics for the evaluation and validation. The plots shown in Figs. 12–22 compare BOR near field simulation and the FEKO© 3D MoM simulation. Note that because there exists a significant number of validation cases, the plots presented tend to capture an "entourage" of validation cases.

The first set of plots, Figs. 12–15, consider near field scattering from PEC cylinders with respect to r_s, θ_s, and φ_s for both the electric and magnetic scattered fields. The second set of plots consider near field electric and magnetic field scattering from lossy dielectrics in Cartesian coordinates, i.e., scattering with respect to x_s, y_s, and z_s.

Table 2: Dielectric cylinder test cases for the validation of MoM with BOR, specifically cylinders

Cylinder Length	1λ, 5λ, 10λ
Cylinder Radius	0.04λ
Far Field Criterion	2λ, 50λ, 200λ
$\boldsymbol{\theta_i}$ [°]	45°, 90°
$\boldsymbol{\varepsilon_r}$	18-j6
Harmonics	10
Mesh Size	$\lambda_m/10$
Range	Varies
$\boldsymbol{E_i}$	377 V/m

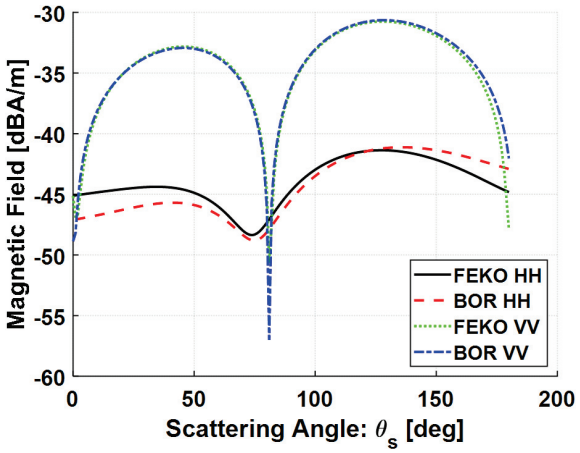

Fig. 12. Magnitude of the bistatic magnetic field vs. θ_s on a PEC cylinder with a radius of 0.04λ, L = 1λ, at $\theta_i = 45°$ at $r_s = 0.1$ m.

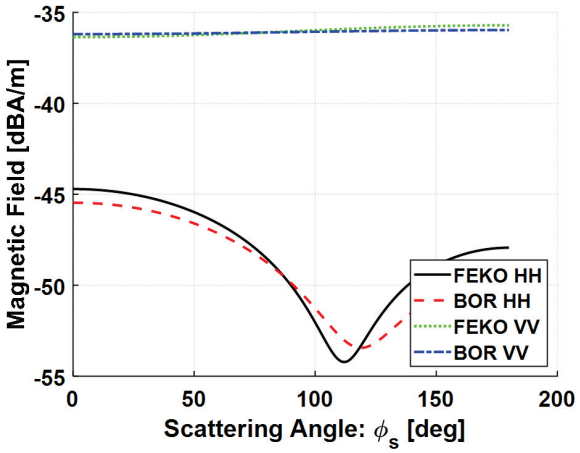

Fig. 13. Magnitude of the bistatic magnetic field vs. φ_s for a PEC cylinder with a radius of 0.04λ, L = 1λ, at $\theta_i = 45°$ at $r_s = 0.1$ m.

The following plots will switch notation from *XX*, e.g., *HH* and *VV*, where *XX* represents an *X*-polarized scatter from an *X*-polarized incident field, to XR, Xθ,

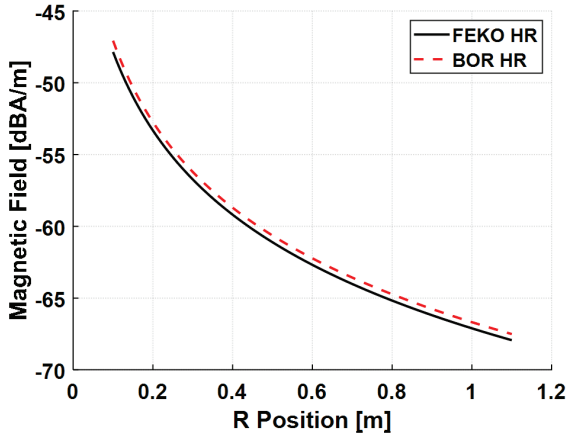

Fig. 14. Magnitude of the bistatic magnetic field vs. r_s with r polarized scattering for a PEC cylinder with a radius of 0.04λ, L = 1λ, at $\theta_i = 45^\circ$ at $r_s = 0.1$ m.

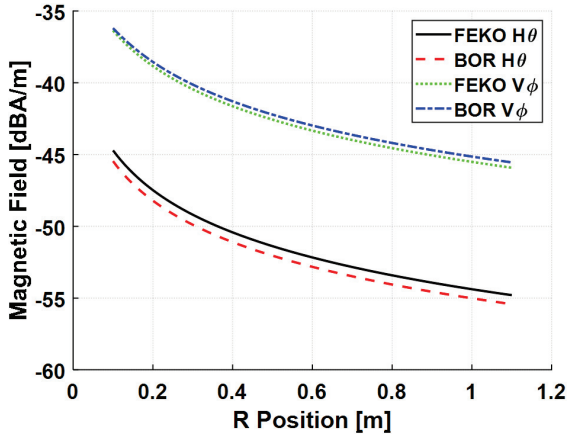

Fig. 15. Magnitude of the bistatic magnetic field vs. r_s with θ and φ polarized scattering for a PEC cylinder with a radius of 0.04λ, L = 1λ, at $\theta_i = 45^\circ$ at $r_s = 0.1$ m.

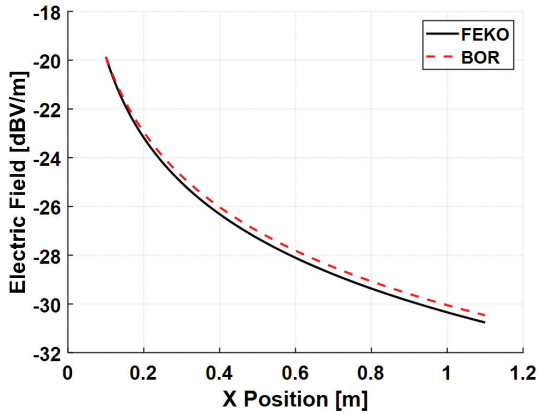

Fig. 16. Magnitude of the bistatic electric field vs. x_s for an H-polarized wave with y polarized scattering on a dielectric cylinder with $\varepsilon_r = 18 - j6$, radius of 0.04λ, L = 1λ, at $\theta_i = 90^\circ$, $y_s = 0$ and $z_s = 0$.

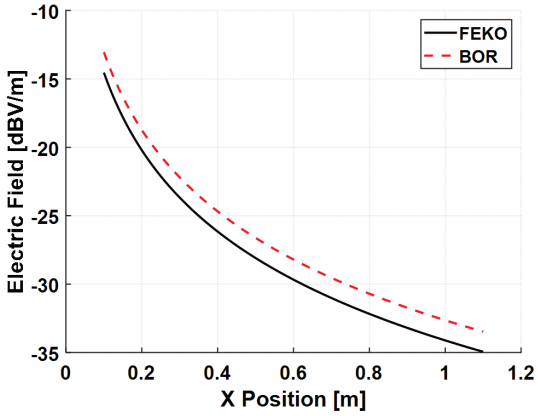

Fig. 17. Magnitude of the bistatic electric field vs. x_s for a V-polarized wave with x polarized scattering on a dielectric cylinder with $\varepsilon_r = 18 - j6$, radius of 0.04λ, L = 1λ, at $\theta_i = 90^\circ$, $y_s = 0$, and $z_s = 0$.

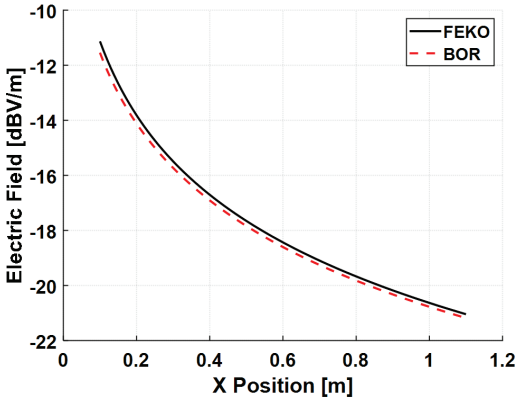

Fig. 18. Magnitude of the bistatic electric field vs. x_s for a V-polarized wave with z polarized scattering on a dielectric cylinder with $\varepsilon_r = 18 - j6$, radius of 0.04λ, L = 1λ, at $\theta_i = 90^\circ$, $y_s = 0$, and $z_s = 0$.

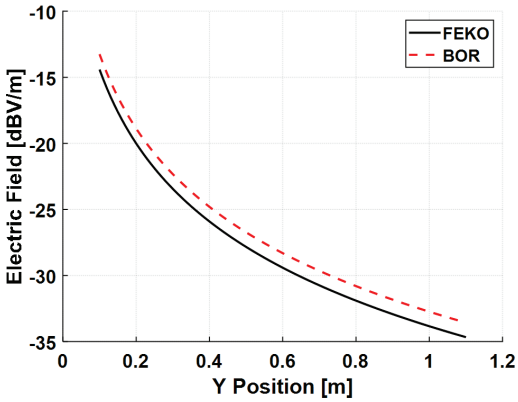

Fig. 19. Magnitude of the bistatic electric field vs. y_s for a V-polarized wave with y polarized scattering on a dielectric cylinder with $\varepsilon_r = 18 - j6$, radius of 0.04λ, L = 1λ, at $\theta_i = 90^\circ$, $x_s = 0$, and $z_s = 0$.

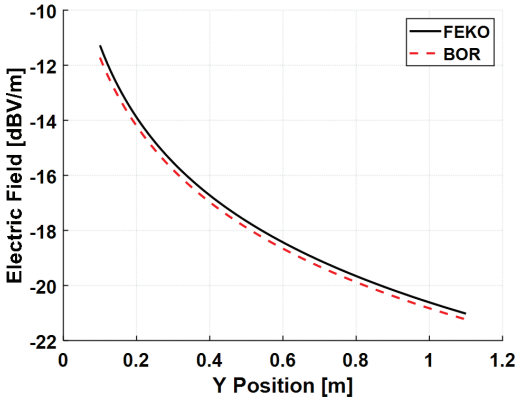

Fig. 20. Magnitude of the bistatic electric field vs. y_s for a V-polarized wave with z polarized scattering on a dielectric cylinder with $\varepsilon_r = 18 - j6$, radius of 0.04λ, L = 1λ, at $\theta_i = 90^\circ$, $x_s = 0$, and $z_s = 0$.

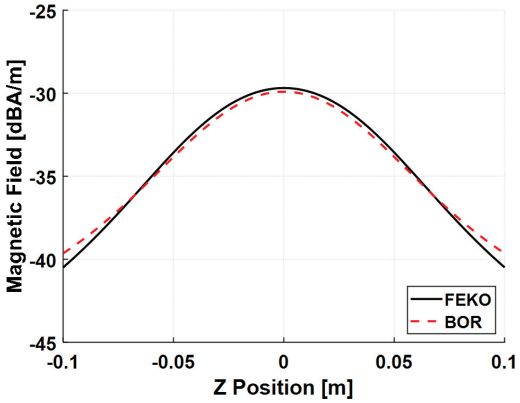

Fig. 21. Magnitude of the bistatic magnetic field vs. z_s for a V-polarized wave with *y* polarized scattering on a dielectric cylinder with $\varepsilon_r = 18 - j6$, radius of 0.04λ, L = 1λ, at $\theta_i = 90^\circ$, $x_s = 0$, and $y_s = 0$.

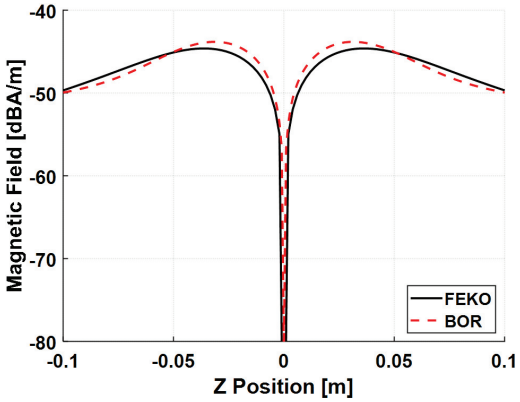

Fig. 22. Magnitude of the bistatic magnetic field vs. z_s for a H-polarized wave with *x* polarized scattering on a dielectric cylinder with $\varepsilon_r = 18 - j6$, radius of 0.04λ, L = 1λ, at $\theta_i = 90^\circ$, $x_s = 0$, and $y_s = 0$.

and Xφ, where R, θ, and φ are the scattered field polarizations and *X* is the incident field polarization, either *H* or *V*. The change creates a more understandable representation of the three (3) orthogonal scattering polarizations for near field scattering.

Throughout part B, the validations between the 3D MoM and BOR-MoM show a greater degree of error than that of the far field comparison from part A. This error can be attributed to two factors. First, this implementation of BOR-MoM uses lower order basis functions resulting in lower order accuracy, especially in the near field where the fields are highly oscillatory and volatile, i.e., Gibb's Phenomenon. Additionally, the error can be attributed to an inherent weakness of BOR-MoM, poor cross-polarization characterization of scatterers, e.g., HV and VH. This is a known phenomenon that occurs in BOR-MoM since the basis functions span only two principle directions whereas the 3D MoM basis functions span the three principle planes. Thus, the coherent summation of any cross polarized terms are neglected within this model resulting in a higher order of error. This does not affect the far field results as the cross-polarized terms are of significantly lower magnitude in the far field. Overall, this additional error can be considered inconsequential with regards to our applications; a discussion better served for a future work.

V. VECTORIZATION OF BOR

BOR-MoM was selected as the method for evaluating axisymmetric objects due to its reduction of MoM from a 3D simulation to a 2-D simulation. This reduced the memory and computing requirements from N_{3D}^2 elements to approximately $n \cdot N_{1D}^2$ elements ($n \cdot N_{1D}^2 << N_{3D}^2$), where *n* is the number of harmonics and N is the number of segments due to the discretization. Based on previous simulation results, a maximum of 10 harmonics are required; thus, any object discretized into more than 10 segments will benefit in terms of speed and memory usage from BOR methodology.

A comparison of the FEKO© MoM solution and BOR-MoM solution with respect to computation time, number of elements, and peak memory usage is presented in Tables 3, 4 and 5. Additionally, Table 4 specifically compares the effects of vectorization on BOR-MoM implementation in MATLAB©. The comparisons use a dielectric cylinder with a dielectric constant of $\varepsilon = 4$ and a radius of λ at $\theta_i = 45^\circ$ and $\varphi_i = 0^\circ$.

The test cases were run on a computer with an Intel i9-10900k CPU overclocked to 4.9 GHz all core, 64 GB of 3600 MHz DDR4 RAM, and a Samsung 970 Evo Plus NVMe SSD. Note that the computer had enough RAM such that a full in core solution was able to be run in FEKO©. If enough RAM is not available, an out of core

Table 3: BOR-MoM solution with respect to peak memory usage and computation time. Note that *N* represents the number of triangular elements and number of segments for the FEKO© and BOR meshes, respectively

	BOR-MoM Non-Vectorized		
Length	***N***	**Memory [GB]**	**Solver Time [s]**
λ	122	8.7	207
3λ	202	10.6	481
6λ	322	10.6	1111
10λ	482	10.6	2399

Table 4: Vectorized BOR-MoM solution in MATLAB© with respect to peak memory usage and computation time. Note that *N* represents the number of triangular elements and number of segments for the FEKO© and BOR meshes, respectively

	BOR-MoM Vectorized		
Length	***N***	**Memory [GB]**	**Solver Time [s]**
λ	123	22.1	29
3λ	203	22.7	78
6λ	323	24.1	196
10λ	483	26.4	469

Table 5: FEKO© 3D MoM solution with respect to peak memory usage and computation time. Note that *N* represents the number of triangular elements and number of segments for the FEKO© and BOR meshes, respectively

	FEKO© MoM		
Length	***N***	**Memory [GB]**	**Solver Time [s]**
λ	4264	1.2	61
3λ	8328	4.7	238
6λ	14664	14.5	680
10λ	23320	35.9	2005

solution must run - FEKO© writes data to and from the hard drive - which more than doubles computation time.

Overall, vectorization of BOR provided approximately a 10x speed but required additional memory usage. With regards to the 3D MoM, BOR provided an approximate 4x speed up. This implementation of BOR-MoM can be improved with regards to speed and memory usage through careful algorithm implementation in a coding language other than MATLAB©.

VI. CONCLUSION

Although scattering from BOR using MoM has been studied extensively, this paper provides derivation and application of an optimal and formally elegant mathematical formulation for near field scattering, for a particular implementation of BOR-MoM using a well-conditioned and numerically-stable basis function set. This elegant formulation should provide analysts with a direct computational encoding that minimizes required integrations. Although direct computational encodings have been derived previously for far field scattering, those derivations were not for the near fields.

The results of this study are a derivation of the generalized scattered field equations for BOR-MoM. Fields were derived for both the scattered electric and magnetic fields for all of space while accounting for the various coordinate transformations, Fourier series expansions, and basis function definitions.

The results were validated by comparison to the FEKO© 3D MoM solution near field calculations. The results showed great agreement between the different MoM implementations. The primary sources of error occurred in the reactive near field region of BOR. This error is likely due to the low order basis functions, triangular and rectangular, used within this implementation of BOR-MoM. This can be partially attributed to the occurrence of Gibb's phenomenon within the Fourier series expansions and discretization along the generating arc. The sacrifice in accuracy due to low order basis functions, however, provides a benefit in computational speed for larger MoM problem sets. Overall, the error between the FEKO© MoM and BOR-MoM is an acceptable trade-off for the $>$4x speed increase that BOR-MoM provides, providing more tractable predictive simulations in practice.

With regards to this works impact on tree scattering analysis, examining the connections between branches and the interaction between multiple discrete scatterers is important for continued model verification, validation, and performance characterization. Further examination of these aspects, and associated discussion, however, defines separate and continuing studies in themselves, and thus not within the scope of this paper. Appropriately, such discussion is within the context of future studies.

ACKNOWLEDGMENT

This work is supported by the U.S. Military and funded through the U.S. Naval Research Laboratory Edison Memorial Graduate Training Program.

REFERENCES

[1] M. Kvicera, F. Pérez Fontán, J. Israel, and P. Pechac, "A new model for scattering from tree canopies based on physical optics and Multiple Scattering Theory," *IEEE Transactions on Antennas and Propagation*, vol. 65, no. 4, pp. 1925-1933, Apr. 2017.

[2] A. Gendelman and A. Boag, "Fast multilevel physical optics algorithm for far- and near-field scattering analysis of very large targets," in *2011 IEEE International Conference on Microwaves,*

Communications, Antennas and Electronic Systems (COMCAS 2011), Tel Aviv, Israel, pp. 1-2, 2011.

[3] M. Kvicera, F. Pérez-Fontán, J. Israel, and P. Pechac, "Modeling scattering from tree canopies for UAV scenarios," in *2016 10th European Conference on Antennas and Propagation (EuCAP),* Davos, Switzerland, pp. 1-3, 2016.

[4] M. Salim, S. Tan, R. D. De Roo, A. Colliander, and K. Sarabandi, "Passive and active multiple scattering of forests using radiative transfer theory with an iterative approach and cyclical corrections," *IEEE Transactions on Geoscience and Remote Sensing*, vol. 60, pp. 1-16, 2022.

[5] Q. Zhao and R. H. Lang, "Scattering from tree branches using the Fresnel Double Scattering approximation," in *2011 IEEE International Geoscience and Remote Sensing Symposium*, Vancouver, BC, Canada, pp. 1040-1043, 2011.

[6] Y. Oh, Y. M. Jang, and K. Sarabandi, "Full-wave analysis of microwave scattering from short vegetation: An investigation on the effect of multiple scattering," *IEEE Trans. Geosci. Remote Sens.*, vol. 40, no. 11, pp. 2522-2526, Nov. 2002.

[7] W. Gu, L. Tsang, A. Colliander, and S. Yueh, "Hybrid method for full-wave simulations of forests at L-band," *IEEE Access*, vol. 10, pp. 105898-105909, 2022.

[8] M. A. Karam, "A versatile scattering model for deciduous leaves," in *IGARSS '98. Sensing and Managing the Environment. 1998 IEEE International Geoscience and Remote Sensing. Symposium Proceedings. (Cat. No.98CH36174),* Seattle, WA, USA, pp. 2387-2389, 1998.

[9] A. W. Glisson and D. R. Wilton, "Simple and efficient numerical techniques for treating Bodies of Revolution," Available https://apps.dtic.mil/sti/citations/ADA067361.

[10] S. Vitebskiy, K. Sturgess, and L. Carin, "Short-pulse plane-wave scattering from buried perfectly conducting Bodies of Revolution," *IEEE Transactions on Antennas and Propagation*, vol. 44, no. 2, pp. 143-151, Feb. 1996.

[11] S. Vitebskiy and L. Carin, "Resonances of perfectly conducting wires and Bodies of Revolution buried in a lossy dispersive half-space," *IEEE Transactions on Antennas and Propagation*, vol. 44, no. 12, pp. 1575-1583, Dec. 1996.

[12] N. Geng and L. Carin, "Wide-band electromagnetic scattering from a dielectric BOR buried in a layered lossy dispersive medium," *IEEE Transactions on Antennas and Propagation*, vol. 47, no. 4, pp. 610-619, Apr. 1999.

[13] M. Andreasen, "Scattering from Bodies of Revolution," *IEEE Transactions on Antennas and Propagation*, vol. 13, no. 2, pp. 303-310, Mar. 1965.

[14] L. Carin, N. Geng, M. McClure, J. Sichina, and Lam Nguyen, "Ultra-wide-band synthetic-aperture radar for mine-field detection," *IEEE Antennas and Propagation Magazine*, vol. 41, no. 1, pp. 18-33, Feb. 1999.

[15] N. Geng, D. R. Jackson, and L. Carin, "On the resonances of a dielectric BOR buried in a dispersive layered medium," *IEEE Transactions on Antennas and Propagation*, vol. 47, no. 8, pp. 1305-1313, Aug. 1999.

[16] J. He, T. Yu, N. Geng, and L. Carin, "Method of moments analysis of electromagnetic scattering from a general three-dimensional dielectric target embedded in a multilayered medium," *Radio Science*, vol. 35, no. 2, pp. 305-313, Mar.-Apr. 2000.

[17] J. R. Mautz and R. F. Harrington, "Radiation and scattering from Bodies of Revolution," *Applied Scientific Research*, vol. 20, pp. 405-435, 1969.

[18] T.-K. Wu and L. L. Tsai, "Scattering from arbitrarily-shaped lossy dielectric Bodies of Revolution," *Radio Science*, vol. 12, pp. 709-718, 1977.

[19] G. Pisharody and D. S. Weile, "Electromagnetic scattering from a homogeneous material body using time domain integral equations and bandlimited extrapolation," in *IEEE Antennas and Propagation Society International Symposium. Digest. Held in conjunction with: USNC/CNC/URSI North American Radio Sci. Meeting (Cat. No.03CH37450),* Columbus, OH, USA, vol. 3, pp. 567-570, 2003.

[20] J. R. Mautz and R. F. Harrington, "Electromagnetic scattering from a homogeneous Body of Revolution," Technical Report, Defense Technical Information Center, Nov. 1977.

[21] P. de Matthaeis and R. H. Lang, "Comparison of surface and volume currents models for electromagnetic scattering from finite dielectric cylinders," *IEEE Transactions on Antennas and Propagation*, vol. 57, no. 7, pp. 2216-2220, July 2009.

[22] P. de Matthaeis and R. H. Lang, "Numerical calculations of microwave scattering from dielectric structures used in vegetation models," Ph.D. thesis, ECE Department, The George Washington University, Washington, DC, 2006.

[23] A. Glisson and C. Butler, "Analysis of a wire antenna in the presence of a Body of Revolution," *IEEE Transactions on Antennas and Propagation*, vol. 28, no. 5, pp. 604-609, Sep. 1980.

[24] S. H. Yueh, J. A. Kong, J. K. Jao, R. T. Shin, and T. Le Toan, "Branching model for vegetation," *IEEE Transactions on Geoscience and Remote Sensing*, vol. 30, no. 2, pp. 390-402, Mar. 1992.

[25] T. Su, L. Du, and R. Chen, "Electromagnetic scattering for multiple PEC Bodies of Revolution using equivalence principle algorithm," *IEEE Transactions on Antennas and Propagation*, vol. 62, no. 5, pp. 2736-2744, May 2014.

[26] M. Jiang, Y. Li, Z. Rong, L. Lei, Y. Chen, and J. Hu, "Fast solving scattering from multiple Bodies of Revolution with arbitrarily metallic-dielectric combinations," *IEEE Transactions on Antennas and Propagation*, vol. 67, no. 7, pp. 4748-4755, July 2019.

[27] H. Huang, L. Tsang, A. Colliander, and S. Yueh, "Full wave simulations of vegetation/trees using 3D vector cylindrical wave expansions in Foldy-Lax multiple scattering equations," in *2019 IEEE International Conference on Computational Electromagnetics (ICCEM), Shanghai, China,* pp. 1-3, 2019.

[28] H. Huang, L. Tsang, E. G. Njoku, A. Colliander, K.-H. Ding, and T.-H. Liao, "Hybrid method combining generalized T matrix of single objects and Foldy-Lax equations in NMM3D microwave scattering in vegetation," in *2017 Progress in Electromagnetics Research Symposium - Fall (PIERS - FALL), Singapore,* pp. 3016-3023, 2017.

[29] H. Huang, L. Tsang, A. Colliander, R. Shah, X. Xu, and S. Yueh, "Multiple scattering of waves by complex objects using hybrid method of T-Matrix and Foldy-Lax equations using vector spherical waves and vector spheroidal waves," *Progress in Electromagnetics Research*, vol. 168, pp. 87-111, 2020.

[30] H. Huang, L. Tsang, E. G. Njoku, A. Colliander, T.-H. Liao and K.-H. Ding, "Propagation and scattering by a layer of randomly distributed dielectric cylinders using Monte Carlo simulations of 3D Maxwell equations with applications in microwave interactions with vegetation," *IEEE Access*, vol. 5, pp. 11985-12003, 2017.

[31] M. Kvicera, F. Pérez Fontán, J. Israel, and P. Pechac, "A new model for scattering from tree canopies based on physical optics and Multiple Scattering Theory," *IEEE Transactions on Antennas and Propagation*, vol. 65, no. 4, pp. 1925-1933, Apr. 2017.

Edward C. Michaelchuck Jr. is currently pursuing a Ph.D. in electrical engineering with a focus in applied electromagnetics at The George Washington University, Washington D.C., USA. He received a M.S. degree in electrical engineering with a concentration in applied electromagnetics from George Washington University, Washington D.C., USA, in January 2021. He received a B.S. in mechanical engineering from Rowan University, Glassboro, NJ, USA, in May 2017.

With regards to his career, he acted as a research assistant for Dr. Parth Bhavsar at Rowan University from 2015 to 2017 studying traffic monitoring systems. He interned at PSE&G Salem Nuclear Power plant in 2016. Currently, he is at the Signature Technology Office, Code 5009, at the U.S. Naval Research Laboratory, Washington, D.C., USA, since August 2017. His expertise includes multispectral signature characterization, computational electromagnetics, RF material measurements, and machine design.

Samuel G. Lambrakos received the Ph.D. degree in Physics from the Polytechnic Institute of New York University in 1983.

He is currently a Research Physicist at the U.S. Naval Research Laboratory, Code 8113, Washington, D.C., where he has been for over 35 years. His expertise is computational physics in general and has many publications, patents and awards. His recent studies concern computational materials physics and inverse spectral analysis.

William O. Coburn received his B.S. in Physics from Virginia Polytechnic Institute in 1984. He received an MSEE in Electro Physics in 1991 and Doctor of Science in Electromagnetic Engineering from The George Washington University (GWU) in 2005. His dissertation research was in traveling wave antenna design.

He has 38 years' experience as an Electronics Engineer at the Army Research Laboratory (formerly the Harry Diamond Laboratories) primarily in the area of CEM for EMP coupling/hardening, HPM, target signatures and antennas. He retired in 2019 from the RF Electronics Division of the Sensors and Electron Devices Directorate applying CEM tools for antenna design and EM analysis.

He is a Fellow of the Applied Computational EM Society (ACES) and served on the ACES Board of Directors. He is a Member of the USNC-URSI, Commission A and B (2010), Sigma Xi and an Adjunct Professor at the Catholic University of America and GWU. Coburn has authored or coauthored over 100 publications and four patents.

APPENDIX I: SPHERICAL COORDINATES

The scattering definition using equivalent sources is:

$$\mathbf{E}^{\mathrm{s}}(\mathbf{r}) = -\mathrm{j}\omega\mu_0 \oint \underline{\mathbf{G}}^0\left(\mathbf{r},\mathbf{r}'\right)\cdot\mathbf{J}_{\mathrm{s}}\left(\mathbf{r}'\right)\mathrm{d}S' + \\ -\oint \underline{\mathbf{K}}^0\left(\mathbf{r},\mathbf{r}'\right)\cdot\mathbf{M}_{\mathrm{s}}\left(\mathbf{r}'\right)\mathrm{d}S', \tag{50}$$

$$\mathbf{H}^{\mathrm{s}}(\mathbf{r}) = \oint \underline{\mathbf{K}}^0\left(\mathbf{r},\mathbf{r}'\right)\cdot\mathrm{J}_{\mathrm{s}}\left(\mathbf{r}'\right)\mathrm{d}S' + \\ -\mathrm{j}\omega\varepsilon_0 \oint \underline{\mathbf{G}}^0\left(\mathbf{r},\mathbf{r}'\right)\cdot\mathbf{M}_{\mathrm{s}}\left(\mathbf{r}'\right)\mathrm{d}S'. \tag{51}$$

Following the analysis from section III, the integration along the generating arc, l, over a single segment for a single harmonic becomes:

$$\mathbf{E}^{\mathrm{s}}_{1,\mathrm{n,r,m}} = \Delta\mathrm{l}_{\mathrm{m,k}}\rho_{\mathrm{m}}\int_0^{2\pi}\mathrm{g}^0\left(\mathbf{r},\mathbf{r_m}\right)\mathrm{F}_{\mathrm{r,n,m}}\left(\mathrm{J}_{\mathrm{n,m}}\right)\mathrm{e}^{\mathrm{jn}\varphi'}\mathrm{d}\varphi'\hat{\mathbf{r}}, \tag{52}$$

$$\mathbf{E}^{\mathrm{s}}_{1,\mathrm{n},\varphi,\mathrm{m}} = \Delta\mathrm{l}_{\mathrm{m,k}}\rho_{\mathrm{m}}\int_0^{2\pi}\mathrm{g}^0\left(\mathbf{r},\mathbf{r_m}\right)\mathrm{F}_{\varphi,\mathrm{n,m}}\left(\mathrm{J}_{\mathrm{n,m}}\right)\mathrm{e}^{\mathrm{jn}\varphi'}\mathrm{d}\varphi'\widehat{\boldsymbol{\varphi}}, \tag{53}$$

$$\mathbf{E}^{\mathrm{s}}_{1,\mathrm{n},\theta,\mathrm{m}} = \Delta\mathrm{l}_{\mathrm{m,k}}\rho_{\mathrm{m}}\int^{2\pi}\mathrm{g}^0\left(\mathbf{r},\mathbf{r_m}\right)\mathrm{F}_{\theta,\mathrm{n,m}}\left(\mathrm{J}_{\mathrm{n,m}}\right)\mathrm{e}^{\mathrm{jn}\varphi'}\mathrm{d}\varphi'\widehat{\boldsymbol{\theta}}, \tag{54}$$

$$\mathbf{E}^{\mathrm{s}}_{2,\mathrm{r,n,m}} = \Delta\mathrm{l}_{\mathrm{m,k}}\rho_{\mathrm{m}}\int_0^{2\pi}\mathrm{D}_{\mathrm{r,n,m}}\left(\mathrm{M}_{\mathrm{n,m}}\right)\mathrm{e}^{\mathrm{jn}\varphi'}\mathrm{d}\varphi'\hat{\mathbf{r}}, \tag{55}$$

$$\mathbf{E}^{\mathrm{s}}_{2,\theta,\mathrm{n,m}} = \Delta\mathrm{l}_{\mathrm{m,k}}\rho_{\mathrm{m}}\int_0^{2\pi}\mathrm{D}_{\theta,\mathrm{n,m}}\left(\mathrm{M}_{\mathrm{n,m}}\right)\mathrm{e}^{\mathrm{jn}\varphi'}\mathrm{d}\varphi'\widehat{\boldsymbol{\theta}}, \tag{56}$$

$$\mathbf{E}^{\mathrm{s}}_{2,\varphi,\mathrm{n,m}} = \Delta\mathrm{l}_{\mathrm{m,k}}\rho_{\mathrm{m}}\int_{\varphi,\mathrm{n,m}}^{2\pi}\left(\mathrm{M}_{\mathrm{n,m}}\right)\mathrm{e}^{\mathrm{jn}\varphi'}\mathrm{d}\varphi'\widehat{\boldsymbol{\varphi}}. \tag{57}$$

These equations require the expansion of $\mathrm{F}_{\mathrm{r,n,m}}$, $\mathrm{F}_{\varphi,\mathrm{n,m}}$, $\mathrm{F}_{\theta,\mathrm{n,m}}$, $\mathrm{D}_{\mathrm{r,n,m}}$, $\mathrm{D}_{\theta,\mathrm{n,m}}$, and $\mathrm{D}_{\varphi,\mathrm{n,m}}$ terms. Due to the length of the derivation for these terms, only the final results will be listed below. The F terms are:

$$\mathrm{F}_{\mathrm{r}}\left(\mathbf{J}_{\mathrm{s,n}}\right) = \begin{pmatrix} \mathrm{A}_1\mathrm{J}_{\tau,\mathrm{n}}\mathrm{C}_1 + \mathrm{A}_1\mathrm{J}_{\varphi,\mathrm{n}}\mathrm{C}_2 + \\ +\mathrm{A}_2\mathrm{J}_{\tau,\mathrm{n}}\sin\theta\sin\psi'\cos\left(\varphi-\varphi'\right) + \\ +\mathrm{A}_2\mathrm{J}_{\tau,\mathrm{n}}\cos\theta\cos\psi' + \\ +\mathrm{A}_2\mathrm{J}_{\varphi,\mathrm{n}}\sin\theta\sin\left(\varphi-\varphi'\right) \end{pmatrix}, \tag{58}$$

$$\mathrm{F}_{\varphi}\left(\mathbf{J}_{\mathrm{s,n}}\right) = \mathrm{A}_2\mathrm{J}_{\tau,\mathrm{n}}\sin\psi'\sin\left(\varphi'-\varphi\right) + \\ +\mathrm{A}_2\mathrm{J}_{\varphi,\mathrm{n}}\cos\left(\varphi-\varphi'\right), \tag{59}$$

$$\mathrm{F}_{\theta}\left(\mathrm{J}_{\mathrm{s,n}}\right) = \mathrm{A}_2\mathrm{J}_{\tau,\mathrm{n}}\cos\theta\sin\psi'\cos\left(\varphi-\varphi'\right) + \\ -\mathrm{A}_2\mathrm{J}_{\tau,\mathrm{n}}\sin\theta\cos\psi' + \\ +\mathrm{A}_2\mathrm{J}_{\varphi,\mathrm{n}}\cos\theta\sin\left(\varphi-\varphi'\right), \tag{60}$$

where the *A* terms and *C* terms are:

$$\mathrm{A}_1 = \frac{3}{\mathrm{k}_0^2\mathrm{R}^2} + \frac{3\mathrm{j}}{\mathrm{k}_0\mathrm{R}} - 1, \tag{61}$$

$$\mathrm{A}_2 = 1 - \frac{\mathrm{j}}{\mathrm{k}_0\mathrm{R}} - \frac{1}{\mathrm{k}_0^2\mathrm{R}^2}, \tag{62}$$

$$\mathrm{C}_1 = \sin\theta\sin\psi'\cos\left(\varphi-\varphi'\right) + \cos\theta\cos\psi', \tag{63}$$

$$\mathrm{C}_2 = \sin\theta\sin\left(\varphi-\varphi'\right), \tag{64}$$

and *R* in spherical coordinates is:

$$\mathrm{R} = \sqrt{\begin{matrix} \mathrm{r}^2+\mathrm{r}'^2+ \\ -2\mathrm{r}\mathrm{r}'\sin\theta\,\sin\theta'\cos\left(\varphi-\varphi'\right)+ \\ -2\mathrm{r}\mathrm{r}'\cos\theta\,\cos\theta' \end{matrix}}. \tag{65}$$

The D terms are derived as:

$$\mathrm{D}_{\mathrm{r}}\left(\mathbf{M}_{\mathrm{n}}\right) = \begin{matrix} \mathbf{M}_{\tau,\mathrm{n}}\left(\mathbf{l}'\right)\frac{1}{\mathrm{r}}\frac{\mathrm{dg}}{\mathrm{d}\theta}\sin\psi'\,\sin\left(\varphi'-\varphi\right) + \\ -\frac{\mathbf{M}_{\tau,\mathrm{n}}\left(\mathbf{l}'\right)}{\mathrm{r}\sin\theta}\frac{\mathrm{dg}}{\mathrm{d}\varphi}\cos\theta\,\sin\psi'\cos\left(\varphi-\varphi'\right) + \\ +\frac{\mathbf{M}_{\tau,\mathrm{n}}\left(\mathbf{l}'\right)}{\mathrm{r}\sin\theta}\frac{\mathrm{dg}}{\mathrm{d}\varphi}\sin\theta\,\cos\psi' + \\ +\mathbf{M}_{\varphi,\mathrm{n}}\left(\mathbf{l}'\right)\frac{1}{\mathrm{r}}\frac{\mathrm{dg}}{\mathrm{d}\theta}\cos\left(\varphi-\varphi'\right) + \\ -\mathbf{M}_{\varphi,\mathrm{n}}\left(\mathbf{l}'\right)\frac{1}{\mathrm{r}\sin\theta}\frac{\mathrm{dg}}{\mathrm{d}\varphi}\cos\theta\,\sin\left(\varphi-\varphi'\right) \end{matrix}, \tag{66}$$

$$\mathrm{D}_{\theta}\left(\mathbf{M}_{\mathrm{n}}\right) = \begin{matrix} -\mathbf{M}_{\tau,\mathrm{n}}\left(\mathbf{l}'\right)\frac{\mathrm{dg}}{\mathrm{dr}}\sin\psi'\,\sin\left(\varphi'-\varphi\right) + \\ +\mathbf{M}_{\tau,\mathrm{n}}\left(\mathbf{l}'\right)\frac{1}{\mathrm{r}\sin\theta}\frac{\mathrm{dg}}{\mathrm{d}\varphi}\sin\theta\,\sin\psi'\cos\left(\varphi-\varphi'\right) + \\ +\mathbf{M}_{\tau,\mathrm{n}}\left(\mathbf{l}'\right)\frac{1}{\mathrm{r}\sin\theta}\frac{\mathrm{dg}}{\mathrm{d}\varphi}\cos\theta\,\cos\psi' + \\ -\mathbf{M}_{\varphi,\mathrm{n}}\left(\mathbf{l}'\right)\frac{\mathrm{dg}}{\mathrm{dr}}\cos\left(\varphi-\varphi'\right) + \\ +\mathbf{M}_{\varphi,\mathrm{n}}\left(\mathbf{l}'\right)\frac{1}{\mathrm{r}\sin\theta}\frac{\mathrm{dg}}{\mathrm{d}\varphi}\sin\theta\,\sin\left(\varphi-\varphi'\right) \end{matrix}, \tag{67}$$

$$\mathrm{D}_{\varphi}\left(\mathbf{M}_{\mathrm{n}}\right) = \begin{matrix} \mathbf{M}_{\tau,\mathrm{n}}\left(\mathbf{l}'\right)\frac{\mathrm{dg}}{\mathrm{dr}}\cos\theta\,\sin\psi'\cos\left(\varphi-\varphi'\right) + \\ -\mathbf{M}_{\tau,\mathrm{n}}\left(\mathbf{l}'\right)\frac{\mathrm{dg}}{\mathrm{dr}}\sin\theta\,\cos\psi' + \\ -\mathbf{M}_{\tau,\mathrm{n}}\left(\mathbf{l}'\right)\frac{1}{\mathrm{r}}\frac{\mathrm{dg}}{\mathrm{d}\theta}\sin\theta\,\sin\psi'\cos\left(\varphi-\varphi'\right) + \\ -\mathbf{M}_{\tau,\mathrm{n}}\left(\mathbf{l}'\right)\frac{1}{\mathrm{r}}\frac{\mathrm{dg}}{\mathrm{d}\theta}\cos\theta\,\cos\psi' + \\ \mathbf{M}_{\varphi,\mathrm{n}}\left(\mathbf{l}'\right)\frac{\mathrm{dg}}{\mathrm{dr}}\cos\theta\,\sin\left(\varphi-\varphi'\right) + \\ -\mathbf{M}_{\varphi,\mathrm{n}}\left(\mathbf{l}'\right)\frac{1}{\mathrm{r}}\frac{\mathrm{dg}}{\mathrm{d}\theta}\sin\theta\,\sin\left(\varphi-\varphi'\right) \end{matrix}, \tag{68}$$

where:

$$\frac{\mathrm{dg}}{\mathrm{dr}} = \begin{pmatrix} \mathrm{r}-\mathrm{r}'\sin\theta\sin\theta'\cos\left(\varphi-\varphi'\right)+ \\ -\mathrm{r}'\cos\theta\cos\theta' \end{pmatrix}\frac{\mathrm{e}^{-\mathrm{jk}_0\mathrm{R}}}{4\pi\mathrm{R}}\left(\frac{-\mathrm{jk}}{\mathrm{R}} - \frac{1}{\sqrt{\mathrm{R}}}\right), \tag{69}$$

$$\frac{\mathrm{dg}}{\mathrm{d}\theta} = \begin{pmatrix} \mathrm{r}\mathrm{r}'\cos\theta'\sin\theta+ \\ -\mathrm{r}\mathrm{r}'\sin\theta'\cos\left(\varphi-\varphi'\right)\cos\theta \end{pmatrix}\frac{\mathrm{e}^{-\mathrm{jk}_0\mathrm{R}}}{4\pi\mathrm{R}}\left(\frac{-\mathrm{jk}}{\mathrm{R}} - \frac{1}{\sqrt{\mathrm{R}}}\right), \tag{70}$$

$$\frac{\mathrm{dg}}{\mathrm{d}\varphi} = \mathrm{r}\mathrm{r}'\sin\theta\sin\theta'\sin\left(\varphi-\varphi'\right)\frac{\mathrm{e}^{-\mathrm{jk}_0\mathrm{R}}}{4\pi\mathrm{R}}\left(\frac{-\mathrm{jk}}{\mathrm{R}} - \frac{1}{\sqrt{\mathrm{R}}}\right). \tag{71}$$

APPENDIX II: CARTESIAN COORDINATES

Similar to Appendix I, the scattered electric and magnetic fields can be expanded in the Cartesian coordinate system. The electric field ($\mathbf{E}^{\mathrm{s}}_{1,\mathrm{n,m,x}}$) as a function of the electric surface currents for a single harmonic over

a single segment is:

$$\mathbf{E}^{s}_{1,n,m,x} = \Delta l_{m,k}\rho_m \int g^0\left(\mathbf{r},\mathbf{r_m}\right) F_{x,J}\left(J_{n,m}\right) e^{jn\varphi'} d\varphi' \widehat{\mathbf{x}}, \tag{72}$$

$$\mathbf{E}^{s}_{1,n,m,y} = \Delta l_{m,k}\rho_m \int g^0\left(\mathbf{r},\mathbf{r_m}\right) F_{y,J}\left(J_{n,m}\right) e^{jn\varphi'} d\varphi' \widehat{\mathbf{y}}, \tag{73}$$

$$\mathbf{E}^{s}_{1,n,m,z} = \Delta l_{m,k}\rho_m \int g^0\left(\mathbf{r},\mathbf{r_m}\right) F_{z,J}\left(J_{n,m}\right) e^{jn\varphi'} d\varphi' \hat{\mathbf{z}}, \tag{74}$$

where:

$$\begin{aligned} F_x\left(J_{n,m}\right) = {} & A_1 C_1 R_x J_{\tau,n} + A_1 C_2 R_x J_{\varphi,n} + \\ & + A_2 \sin\psi' \cos\varphi' J_{\tau,n} - A_2 \sin\varphi' J_{\varphi,n}, \end{aligned} \tag{75}$$

$$\begin{aligned} F_y\left(J_{n,m}\right) = {} & A_1 C_1 R_y J_{\tau,n} + A_1 C_2 R_y J_{\varphi,n} + \\ & + A_2 \sin\psi' \sin\varphi' J_{\tau,n} + A_2 \cos\varphi' J_{\varphi,n}, \end{aligned} \tag{76}$$

$$\begin{aligned} F_z\left(J_{n,m}\right) = {} & A_1 C_1 R_z J_{\tau,n} + A_1 C_2 R_z J_{\varphi,n} + \\ & + A_2 \cos\psi' J_{\tau,n}. \end{aligned} \tag{77}$$

The electric field ($\mathbf{E}^{s}_{2,n,m,x}$) as a function of the fictitious magnetic surface currents for a single harmonic over a single segment is:

$$\mathbf{E}^{s}_{2,x,n,m} = \int_S D_x\left(M_{n,m}\right) e^{jn\varphi'} dS' \widehat{\mathbf{x}}, \tag{78}$$

$$\mathbf{E}^{s}_{2,y,n,m} = \int_S D_y\left(M_{n,m}\right) e^{jn\varphi'} dS' \widehat{\mathbf{y}}, \tag{79}$$

$$\mathbf{E}^{s}_{2,z,n,m} = \int_S D_z\left(M_{n,m}\right) e^{jn\varphi'} dS' \hat{\mathbf{z}}, \tag{80}$$

where:

$$\begin{aligned} D_x = {} & \mathbf{M}_{\tau,n}\left(\mathbf{l}'\right) \frac{dg}{dy} \cos\psi' + \\ & - \mathbf{M}_{\tau,n}\left(\mathbf{l}'\right) \frac{dg}{dz} \sin\psi' \sin\varphi' + \\ & - \mathbf{M}_{\varphi,n}\left(\mathbf{l}'\right) \frac{dg}{dz} \cos\varphi', \end{aligned} \tag{81}$$

$$\begin{aligned} D_y = {} & -\mathbf{M}_{\tau,n}\left(\mathbf{l}'\right) \frac{dg}{dx} \cos\psi' + \\ & - \mathbf{M}_{\tau,n}\left(\mathbf{l}'\right) \frac{dg}{dz} \sin\varphi' + \\ & - \mathbf{M}_{\varphi,n}\left(\mathbf{l}'\right) \frac{dg}{dz} \sin\varphi', \end{aligned} \tag{82}$$

$$\begin{aligned} D_z = {} & \mathbf{M}_{\tau,n}\left(\mathbf{l}'\right) \frac{dg}{dx} \sin\psi' \sin\varphi' + \\ & + \mathbf{M}_{\tau,n}\left(\mathbf{l}'\right) \frac{dg}{dy} \sin\varphi' + \\ & + \mathbf{M}_{\varphi,n}\left(\mathbf{l}'\right) \frac{dg}{dx} \cos\varphi' + \\ & + \mathbf{M}_{\varphi,n}\left(\mathbf{l}'\right) \frac{dg}{dy} \sin\varphi', \end{aligned} \tag{83}$$

and the Green's functions derivatives are:

$$\frac{dg}{dx} = \frac{\left(x - x'\right) e^{-jk_0 R}}{4\pi R} \left(\frac{-jk}{R} - \frac{1}{\sqrt{R}}\right), \tag{84}$$

$$\frac{dg}{dy} = \frac{\left(y - y'\right) e^{-jk_0 R}}{4\pi R} \left(\frac{-jk}{R} - \frac{1}{\sqrt{R}}\right), \tag{85}$$

$$\frac{dg}{dz} = \frac{\left(z - z'\right) e^{-jk_0 R}}{4\pi R} \left(\frac{-jk}{R} - \frac{1}{\sqrt{R}}\right). \tag{86}$$

A Novel Proximal Policy Optimization Approach for Filter Design

Dongdong Fan[1], Shuai Ding[1,2], Haotian Zhang[2], Weihao Zhang[4], Qingsong Jia[2], Xu Han[2], Hao Tang[2], Zhaojun Zhu[2], and Yuliang Zhou[3]

[1]Shenzhen Institute for Advanced Study, University of Electronic Science and Technology of China
Shenzhen 518110, China
dond_fan@std.uestc.edu.cn

[2]Institute of Applied Physics, University of Electronic Science and Technology of China
Chengdu 610054, China
uestcding@uestc.edu.cn

[3]School of Aeronautics and Astronautics, University of Electronic Science and Technology of China
Chengdu 610054, China

[4]School of Materials and Energy, University of Electronic Science and Technology of China
Chengdu 610054, P.R. China

Abstract – This paper proposes a proximal policy optimization (PPO) algorithm for coupling matrix synthesis of microwave filters. With the improvement of filter design requirement, the limitations of traditional methods such as limited applicability are becoming more and more obvious. In order to improve the filter synthesis efficiency, this paper constructs a reinforcement learning algorithm based on Actor-Critic network architecture, and designs a unique filter coupling matrix synthesis reward function and action function, which can solve combinatorial optimization problems stably.

Index Terms – bandpass filters (BPF), coupling matrix synthesis, Proximal Policy Optimization (PPO).

I. INTRODUCTION

With the development of wireless communication technologies such as 5G or post-5G, the requirements for the integration and design efficiency of passive microwave devices are increasing, among which filters are the most important ones since they can select specific frequencies. Filter design involves multiple steps and several factors, such as insertion loss, bandwidth, working frequency, out-of-band suppression, physical size, power capacity and stability [1].

Automation of filter design has long been pursued to enhance design efficiency [2]. In recent years, a rising number of artificial intelligent methods have been incorporated in the filter design process. Among them, optimization is a common method in the design process based on electromagnetic simulation. Optimization aims to transform the design specification into a suitable objective function, and then obtain the parameters that meet the final design requirements through an optimization algorithm. For example, rapid simulation and optimization of microwave component models based on functional substitution modeling technology can enable advanced circuit design or computer-aided tuning of microwave components [3], The coupling matrix algorithm based on neural network can realize filter synthesis and fine tuning [4–7], and the adaptive synthesis of resonant-coupled filters can be realized based on particle swarm optimization [8, 9] and spatial mapping technology [10, 11].

In this paper, we propose to solve the filter synthesis problem by applying a proximal policy optimization (PPO) algorithm based on deep reinforcement learning. We construct a neural network model based on the Actor-Critic architecture and design specific reward function and action function to synthesize the filter coupling matrix. The novelty and main contributions of this paper are as follows: (1) to the best of our knowledge, this is the first work to present a complete PPO framework and apply it to the synthesis of filter coupling matrix; and (2) based on extensive experiments, we design a model structure that can solve this problem and achieve satisfactory results.

II. METHODOLOGY: PPO ALGORITHM

A. Framework

A PPO algorithm is a reinforcement learning algorithm proposed by OpenAI in 2017 [12]. It is considered a state-of-the-art method in the field of reinforcement learning and is one of the most widely applicable

Submitted On: December 19, 2023
Accepted On: June 21, 2024

https://doi.org/10.13052/2024.ACES.J.390502

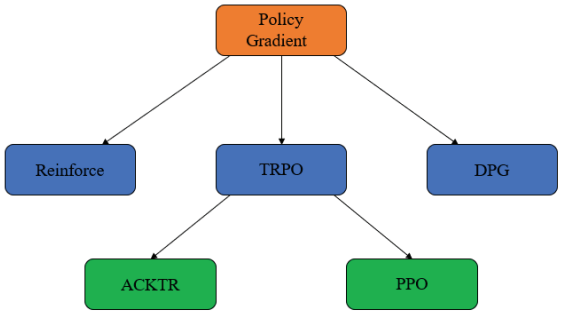

Fig. 1. PPO evolution process.

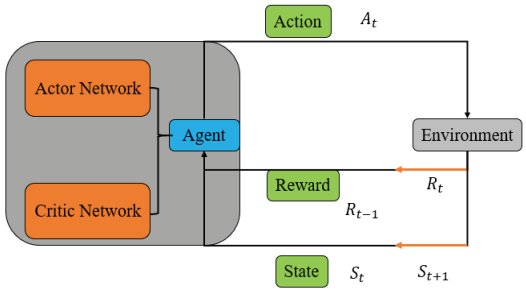

Fig. 2. Actor-Critic architecture.

algorithms in the field. Because it is simple to implement and exhibits stable performance, a PPO algorithm can handle both discrete or continuous action spaces and conduct large-scale training. It has received widespread attention in recent years due to these advantages, and its evolution is shown in Fig. 1.

The core idea of a PPO algorithm is to use PPO to train the agent. PPO is a kind of policy gradient reinforcement learning algorithm that optimizes the policy by maximizing the expected return.The core of a PPO algorithm is the use of the following policy loss function:

$$L_{CLIP}(\theta) = \hat{E}_t[min(r_t(\theta)\hat{A}_t, clip(r_t(\theta), 1-\varepsilon, 1+\varepsilon)\hat{A}_t)]. \quad (1)$$

Where we have the following definitions.

$r_t(\theta) = (\pi_\theta\ (a|s))/(\pi_{\theta old}\ (a|s))$ is the policy update ratio. The larger the $r_t(\theta)$, the higher the probability of taking action a under state s by the current policy, and the larger the update ratio relative to the old policy.

$\hat{A}_t = Q_{\pi_\theta old}\ (s,a) - V_{\pi\theta old}(s)$ is the advantage function, which represents the difference between the value of the current state and action and the average value, which is used to calculate the clipping range in the proximal ratio clipping loss. The larger the value of the advantage function, the better the current state and action, and they should obtain a larger reward.

ε is a hyper-parameter that controls the clipping range.

$clip(x,a,b)$ is a clipping function, which means that x is restricted to the interval [a,b].

$\hat{E}_t$ represents the expected experience over time steps.

To summarize: the proximal ratio clipping loss consists of two parts, and we chose the smaller one. This can ensure that the policy update does not deviate too much from the original policy, thus achieving stable and efficient training results.

The Actor-Critic network, and their basic architecture are shown in Fig. 2. The Actor network is responsible for outputting policies, i.e., the probability distribution of action selection at each state; the Critic network is responsible for estimating the state value function, i.e., the expected cumulative reward at each state. The core idea of the PPO algorithm is to limit the magnitude of policy updates to ensure that the policy does not deviate too far, thereby improving the stability and efficiency of learning.

B. Coupling matrix synthesis based on PPO

By modeling the comprehensive process of the coupling matrix as a deep reinforcement learning problem, a deep neural network model is trained by taking the performance index of the filter (such as bandwidth and return loss) as the state, the adjustment of the coupling coefficient in the coupling matrix by the agent as the action, and the change of the performance index when the coupling coefficient is adjusted as the reward. The method consists of the following modules.

State and action space: The state space refers to the set S of possible states in the coupling matrix synthesis problem, expressed as follows $S = \{s_1, s_2, , s_n\}$. The action space refers to the set A of all of the possible actions that the agent can take, expressed as follows $A = \{a_1, a_2, , a_m\}$. In this method, the agent uses discrete actions to add or subtract the elements of the coupling matrix with a fixed step length within a certain range to achieve the change of the state.

State transition: In reinforcement learning, a state transition is the agent learning by interacting with the environment, observing the current state, and then acting on its own strategy and receiving a reward or punishment from the environment. It then moves to a new state, and this process is called a state transition. The state transition function is usually expressed as:

$$s' = f(s,a), \quad (2)$$

where s is the current state, a is the action taken by the agent, and $s\prime$ is the new state transferred to by the agent.

Reward function: The reward function is used to evaluate the value of each state and action and is denoted as $R(s_t, a_t, s_{(t+1)})$. In this paper, a special reward function is proposed for coupling matrix synthesis that consists of two parts: target difference reward $R_{S_{11max}}$ and distance reduction reward $R_{S_{reduce}}$. The target difference

reward refers to the absolute difference between the maximum return loss and target return loss, and the absolute difference between the minimum out-of-band return loss and target return loss in the coupling matrix synthesis process. The target difference reward can be written in the following form:

$$R_{S_{11max}} \propto \frac{1}{S_{11max} - S_{11goal}}. \tag{3}$$

$R_{S_{reduce}}$ sets the reward by measuring the difference between the current S-parameter state and next S parameter state by means of the mean square error. We define Dist so as to construct a set consisting of the values of the S parameters of each frequency of the target state, and the mean-square error of the frequency point values between the two sets is calculated using the following formula. After the action is executed, when the Dist of the next state is greater than that of the current state, it means that the agent is moving away from the target, and the reward is 0. Otherwise, the reward is 1, thereby encouraging the agent to execute actions in the direction in which Dist becomes smaller. The award may be written as follows:

$$Dist = \frac{1}{n}\sum_{i=1}^{n}(S_{11real}(i) - S_{11goal}(i))^2, \tag{4}$$

$$R_{S_{reduce}} = \begin{cases} 1, & if newDist > lastDist \\ 0, & if newDist \leq lastDist. \end{cases} \tag{5}$$

Network architecture and training process: The basic structure of the Actor and the Critic network adopts a fully connected neural network and is shown in Fig. 3. The neural network structure in the PPO algorithm consists of an input layer, a hidden layer and an output layer.

Neural network training can be described as an optimization problem, and this optimization algorithm usually needs to calculate the gradient. In the neural network with sigmoid function, the gradient becomes smaller and smaller in the process of backpropagation and gradually approaches zero as the number of layers increases. Gradients approaching zero prevent weights from being updated during training. Such a problem is called the vanishing gradient problem. In fact, when using sigmoid activation functions, the gradient will usually vanish,especially at the beginning of learning [13, 14]. ReLU allows deep neural networks to have no gradient vanishing problem during training[15, 16]. Deep neural networks with ReLU have been proven to be effective for speech recognition[17].

In order to overcome the problem of gradient disappearance during deep neural network training, we use ReLU as the activation function.The ReLU function is expressed as:

$$f(\gamma) = \max(\gamma, 0) = \begin{cases} \gamma, & \text{if } \gamma > 0 \\ 0, & \text{otherwise.} \end{cases} \tag{6}$$

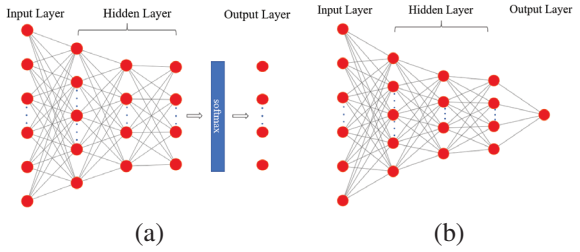

(a) (b)

Fig. 3. Actor (a) and Critic (b) network structure.

The gradient of ReLU is:

$$f'(\gamma) = \begin{cases} 1, & \text{if } \gamma > 0 \\ 0, & \text{otherwise} \end{cases}. \tag{7}$$

In the case of a negative input, it will output 0, then the neuron will not be activated. This means that only some neurons are activated at the same time, making the network sparse and thus very efficient for computation.

Step 1: The Actor and Critic networks are constructed by initializing the parameters θ_0 and ω_0.

Step 2: Collect data and store them in experience pool D_0:$D_t = (s_t, a_t, r_t, s_{(t+1)})$, where s_t represents the state at time t, a_t represents the action at time step t, r_t represents the reward at time t, and $s_{(t+1)}$ represents the state at time $t+1$.

Step 3: For each training cycle, we repeat the following steps:

a: Update the experience pool data.
b: The PPO method optimizes the policy function $\theta_k = argmax_\theta L^{CLIP}(\theta_{(k-1)}, \theta)$, where $L^{CLIP}(\theta_{(k-1)}, \theta)$ represents the loss function of the Actor network.
c: We repeat steps a and b until the specified number of training rounds is reached or the convergence condition is reached.

Step 4: Output the optimal policy function and use it to generate the agent's actions $\pi^*(a|s) = arg\max_\theta L^{CLIP}(\pi)$. The optimization process must be limited to ensure that the step size of each update is not too large to avoid excessive updating. The optimal policy function $\pi^*(a|s)$ can be obtained through the Actor network and is used to generate the actions of the agents.

III. DESIGN EXAMPLES

A. Design specification

The sixth-order dielectric waveguide BPF shown in Fig. 4, uses PPO for coupling matrix synthesis.

The design specifications are as follows:
1): Center frequency: f_0=3.0 GHz.
2): Fractional bandwidth: $\Delta f f_0 = 5\%$.
3): Transmission zero: 2780 and 3220 MHz.
4): Number of resonators: $N_R = 6$.
The dielectric constant of the dielectric waveguide filter is 20.5.

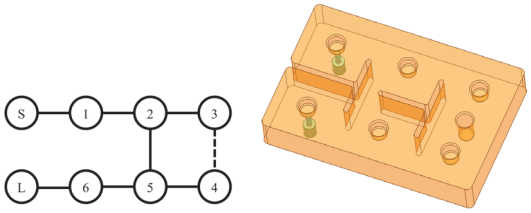

(a) (b)

Fig. 4. (a) Sixth order filter topology with symmetric transmission zeros, and (b) 3D model.

B. Concrete realization

During the coupling matrix synthesis process, when the intelligent agent interacts with the environment, the first step involves acquiring the current state. In this case, a sixth-order filter with a center frequency of 3 GHz and a bandwidth of 150 MHz is employed. Based on the symmetry of the coupling matrix, there are a total of eight nonzero values in the current state. The role of the intelligent agent is to modify these eight values by either increasing or decreasing them, with the values along the diagonal of the coupling matrix ranging from [0.5,1.3]. The range for the cross-coupling $m_{2,5}$ is [−0.5,0.5].

According to the symmetry of the coupling matrix, the agent has a total of 10 different actions, which are expressed as follows:

$$A = \{m_{0,1}\pm, m_{1,2}\pm, m_{2,3}\pm, m_{3,4}\pm, m_{2,5}\pm\}, \quad (8)$$

$$m_{(x,x)}\pm = \max\left(\min\left(m_{(x,x)} \pm change, \max M\right), \min M\right), \quad (9)$$

where $m_{(x,x)}$ refers to the currently adjusted matrix element.

After the agent performs an action, it transitions to a new state. In this process, the environment provides the agent with rewards for the action based on the old state and the new state. As described in section II, these rewards are utilized by the agent through the use of a reward function to select actions for coupling matrix synthesis, thus adjusting the direction and objectives for the coupling matrix. During the agent's training process, the PPO network gradually learns the relationship between *S*-parameters and the adjustment of the coupling matrix. The agent continues to explore in search of better solutions. Upon training completion, the agent is capable of identifying coupling matrices that meet the specified requirements.

C. Design results

In this paper, a PPO algorithm is used to optimize the eighth order coupling matrix for 2 minutes, which is a relatively long value in the optimization process because the PPO algorithm itself has randomness. The comprehensive process is shown in Figs. 5 (a)-(c). The eight nonzero coupling coefficients M of this sixth-order filter are $M = \{M_{0,1} = M_{6,7} = 1.009, M_{1,2} = M_{5,6} = 0.851, M_{2,3} = M_{4,5} = 0.617, M_{3,4} = 0.61, M_{2,5} = -0.025\}$. As can be seen from Fig. 5 (c), the S parameters meet the in-band return loss and insertion loss, and generate two transmission zeros near the specified frequency. In addition, according to the synthesized coupling matrix, a full-wave simulation was performed in simulation software Ansys HFSS, and the simulation result is shown in Fig. 5 (d). The simulation result is basically consistent with the S parameters of the filter synthesized by the coupling matrix.

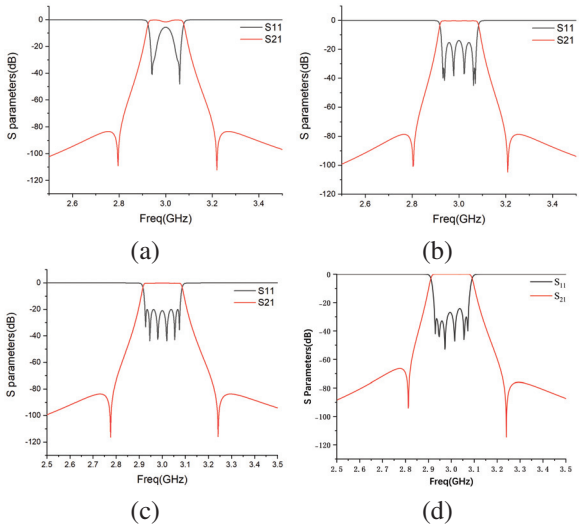

Fig. 5. (a)-(c) Coupling matrix synthesis process based on PPO algorithm, and (d) full-wave simulation result.

IV. CONCLUSION

In this paper, a PPO algorithm in deep reinforcement learning is introduced, and an Actor-Critic network for coupling matrix synthesis is constructed and designed with unique action function and reward function. The coupling matrix of a six-order filter is synthesized by using PPO, and the corresponding full-wave simulation is performed after obtaining the coupling matrix. It is proved that the S parameters of the coupling matrix synthesis and the full-wave simulation results corresponding to the coupling matrix are basically consistent. The feasibility and generality of the PPO algorithm are verified. In the proposed PPO comprehensive coupling matrix in this paper, although the synthesis time for complex coupling matrices is relatively long, this algorithm not only synthesizes traditional common coupling matrices but also can synthesize some special coupling matrices. That is, it can synthesize uncommon coupling structures.

ACKNOWLEDGMENT

This work was supported in part by the Fundamental Research Funds for the Central Universities under Grant A03019023801088, Sichuan Province Science and Technology Support Program,(No.2022YFS0193) and Fundamental Research Funds for the Central Universities(No.ZYGX 2021YGLH025).

REFERENCES

[1] D. Liang, X. Zhang, B. Yang, and D. Young, "Overview of base station requirements for RF and microwave filters," in *2021 IEEE MTT-S International Microwave Filter Workshop (IMFW)*, pp. 46-49, 2021.

[2] R. J. Cameron, C. M. Kudsia, and R. R. Mansour, *Microwave Filters for Communication Systems: Fundamentals, Design, and Applications*. Hoboken, NJ: John Wiley & Sons, 2018.

[3] F. Feng, C. Zhang, J. Ma, and Q.-J. Zhang, "Parametric modeling of EM behavior of microwave components using combined neural networks and pole-residue-based transfer functions," *IEEE Transactions on Microwave Theory and Techniques*, vol. 64, no. 1, pp. 60-77, 2016.

[4] M. Ohira, A. Yamashita, Z. Ma, and X. Wang, "Automated microstrip bandpass filter design using feedforward and inverse models of neural network," in *2018 Asia-Pacific Microwave Conference (APMC)*, pp. 1292-1294, 2018.

[5] M. Ohira, K. Takano, and Z. Ma, "A novel deep-Q-network-based fine-tuning approach for planar bandpass filter design," *IEEE Microwave and Wireless Components Letters*, vol. 31, no. 6, pp. 638-641, 2021.

[6] M. Ohira, A. Yamashita, Z. Ma, and X. Wang, "A novel eigenmode-based neural network for fully automated microstrip bandpass filter design," in *2017 IEEE MTT-S International Microwave Symposium (IMS)*, pp. 1628-1631, 2017.

[7] B. Liu, H. Yang, and M. J. Lancaster, "Global optimization of microwave filters based on a surrogate model-assisted evolutionary algorithm," *IEEE Transactions on Microwave Theory and Techniques*, vol. 65, no. 6, pp. 1976-1985, 2017.

[8] J. L. Chvez-Hurtado and J. E. Rayas-Snchez, "Polynomial-based surrogate modeling of RF and microwave circuits in frequency domain exploiting the multinomial theorem," *IEEE Transactions on Microwave Theory and Techniques*, vol. 64, no. 12, pp. 4371-4381, 2016.

[9] L. Bi, W. Cao, W. Hu, and M. Wu, "Intelligent tuning of microwave cavity filters using granular multi-swarm particle swarm optimization," *IEEE Transactions on Industrial Electronics*, vol. 68, no. 12, pp. 12901-12911, 2021.

[10] S. Koziel, J. Meng, J. W. Bandler, M. H. Bakr, and Q. S. Cheng, "Accelerated microwave design optimization with tuning space mapping," *IEEE Transactions on Microwave Theory and Techniques*, vol. 57, no. 2, pp. 383-394, 2009.

[11] Q. S. Cheng, J. W. Bandler, and S. Koziel, "Space mapping design framework exploiting tuning elements," *IEEE Transactions on Microwave Theory and Techniques*, vol. 58, no. 1, pp. 136-144, 2010.

[12] J. Schulman, F. Wolski, P. Dhariwal, A. Radford, and O. Klimov, "Proximal policy optimization algorithms," *arXiv preprint arXiv:1707.06347*, 2017.

[13] M. A. Nielsen, Neural Networks and Deep Learning, vol. 25. San Francisco, CA: Determination Press, 2015.

[14] S. Hochreiter, "The vanishing gradient problem during learning recurrent neural nets and problem solutions," *International Journal of Uncertainty, Fuzziness and Knowledge-Based Systems*, vol. 6, no. 02, pp. 107-116, 1998.

[15] Y. Lecun, Y. Bengio, and G. Hinton, "Deep learning," *Nature*, vol. 521, no. 7553, p. 436, 2015.

[16] X. Glorot, A. Bordes, and Y. Bengio, "Deep sparse rectifier neural networks," *Journal of Machine Learning Research*, vol. 15, pp. 315-323, 2011.

[17] G. E. Dahl, T. N. Sainath, and G. E. Hinton, "Improving deep neural networks for LVCSR using rectified linear units and dropout," in *2013 IEEE International Conference on Acoustics, Speech and Signal Processing*, pp. 8609-8613, 2013.

Dongdong Fan was born in Shanxi, China,in 1996. He received the B.E. degree in Optoelectronic information science and engineering from the Nanyang Institute of Technology of China, in 2019, where he is currently pursuing the M.E. degree in electronic information engineering with the School of Physics. His current research interests include radio-frequency circuit and filter.

Shuai Ding received the Ph.D. degree in radio physics from the University of Electronic Science and Technology of China (UESTC), Chengdu, in 2013. From 2013 to 2014, he was a Postdoctoral Associate with the cole Polytechnique de Montral, Montral, QC, Canada.

In 2015, he joined UESTC, where he is currently an Associate Professor. He has authored or coauthored over 80 publications in refereed journals and international conferences/symposia. His current research interests include time-reversed electromagnetics and its applications to communication and energy transmission, phased array, analog signal processing, and microwave circuits. He has served as a TPC Member for various conferences and a reviewer for several peer-reviewed periodicals and international conferences/symposia.

Haotian Zhang was born in Henan, China,in 1998. He is received the M.E. degree in physics with the School of Physics from the University of Electronic Science and Technology of China, in 2023. His current research interests include machine learning, antenna arrays, and filter.

Weihao Zhang was born in Handan, China,in 1995. He received theB.E. degree in fundamental science (mathematics and physics) from the University of Electronic Science and Technology of China, in 2018, where he is currently pursuing the Ph.D.degree in Electronic Information Materials and Components with University of Electronic Science and Technology of China, ChengDu, China. His current research interests include integrated magnetic devices and fabrication technologies, filter, filtering antenna, metasurface, antenna array.

Qingsong Jia was born in Sichuan, China,in 1997. He received the B.E. degree in electronic information science and technology from the University of Electronic Science and Technology of China, in 2019, where he is currently pursuing the Ph.D.degree in electromagnetic field and microwave technology with the School of Physics. His current research interests include metasurface, antenna arrays, and the application of radio OAM vortex wave.

Xu Han was born in Sichuan, China, in 1995. He received the B.E. degree in electronic information science and technology from the University of Electronic Science and Technology of China, in 2018, where he is currently pursuing the Ph.D.degree in electromagnetic field and microwave technology with the School of Physics. His current research interests include metasurface, antenna arrays, and phase array.

Hao Tang was born in Hebei, China, in 1998. He received the B.E. degree in Internet of Things Engineering from the Chengdu University of Technology of China,in 2020, where he is currently pursuing the Ph.D. degree in physics with the School of Physics. His current research interests include metasurface and antenna arrays.

Zhaojun Zhu was born in Sichuan, China, in 1978. He received the B.S. degree and the Ph.D.degree in physical electronics from the University of Electronic Science and Technology of China(UESTC), Chengdu, in 2002 and 2007, respectively. Since 2012, he has been an Associate Professor with UESTC. His research interests include the design of microwave and millimeter-wave circuits.

Yuliang Zhou received the B.S. degree in applied physics from the University of Electronic Science and Technology of China, Chengdu, China, in 2012, where he is currently pursuing the Ph.D. degree in communication and information systems. From 2017 to 2018, he was with the Microwave Laboratory, University of Pavia, Pavia, Italy. His current research interests include substrate integrated circuits, leaky-wave antennas, and systems for wireless communication.

Additional Acceleration of Antenna Optimal Characterization with Modeling Support

Ahmet Uluslu

Department of Electronics and Automation
Istanbul University-Cerrahpaşa, Istanbul, 34500, Turkey
auluslu@iuc.edu.tr

Abstract – Optimal characterization is assumed to provide the best solution for the designed cost function among the possible solutions within the specified range. These processes can take a long time depending on the applications and computer hardware used. Here, the optimization process is supported by ANN modeling in order to shorten the current optimization processes as much as possible. For this purpose, the selection of design parameters of the bowtie patch antenna (BPA) is presented as a multi-dimensional, multi-objective modeling-supported design optimization problem. The operating frequency of the proposed antenna is 28 GHz, which is the standard for millimeter wave band and 5G technologies. To overcome this challenging design optimization, a new, fast and powerful optimization algorithm was used by modifying the non-dominant sorting genetic algorithm (NSGA)-III, and the optimal characterization of the microwave antenna design was achieved. Although the proposed method gives the same results compared to the existing process, it takes much less time. Therefore, it is possible to shorten the process and reduce costs without the need for extra applications or hardware. As a whole, the proposed design optimization process is an efficient, fast and reliable solution for all design problems.

Index Terms – Accelerated optimal characterization, antenna applications, modeling support, non-dominated sorting genetic algorithm, optimization.

I. INTRODUCTION

In recent years, antenna design for 5G systems has become very popular in the communication world and has become one of the most demanded topics. As a result of the developments so far, this technology will be used almost all over the world by the end of 2024 [1] (delay may occur due to pandemic conditions). International Mobile Telecommunications (IMT) and International Telecommunications Association (ITU) boards have stated their requirements for 5G. In addition, in the final statement of the 2019 World radiocommunication conference, the operating frequencies of 5G antennas were reported as 25, 38 or 66 GHz [2]. In another statement, the Federal Communications Board (FCC) specified the operating frequencies of 5G antennas as 28 or 38 GHz, and for open source and unlicensed work, 37 or 64-71 GHz [3, 4]. It has been reported that the channel bandwidth of the system should be a minimum of 1000 MHz for 6 GHz and above and a minimum of 100 MHz for a frequency below 6 GHz [5, 6].

Pareto optimal characterization for microwave elements has been demonstrated in [7]. In a similar study, the optimal characterization of a microwave transistor was addressed as a multi-objective optimization problem [8]. The older version of the algorithm used in the study was non-dominated sorting genetic algorithm (NSGA)-II [9, 10], which is a method used in antenna design optimization problems in the literature [11, 12]. Additionally, the other compared method, a multi-objective evolutionary algorithm based on decomposition (MOEA/D), is used for the pattern synthesis of a Vivaldi linear array [13], for the design of a compact broadband circularly polarized helical antenna [14], for the synthesis of the shaped beam pattern of an antenna array [15] used. NSGA-II and MOEA/D have been used to overcome the problems stated in conventional antenna design [16]. In [17], MOEA/D was proposed for antenna design. In another study, a simple base station antenna using two bow-tie dipoles has been proposed [18], developed for a compact log-periodic dipole array [19], and proposed as an automation design scheme for compact, high-isolation multiplex systems [20]. However, a modeling-assisted optimization problem solving method has not yet been found. Bowtie patch antenna (BPA) different frequencies [21, 22] and different design types pi- and U-shaped [23, 24] are available in the literature.

As an optimization technique, NSGA-III uses the MATLAB 2021a toolbox. The basic framework of the proposed multi-purpose NSGA-III algorithm is similar to that of NSGA-II, although it incorporates significant changes [25]. Keeping variety among population members in NSGA-III, on the other hand, helps by supplying

Submitted On: April 20, 2024
Accepted On: July 1, 2024

https://doi.org/10.13052/2024.ACES.J.390503

and adaptively updating a collection of well-distributed reference points, as detailed in [25, 26]. The ideal characterization of the NSGA-III, a new, quick, and powerful optimization technique, is considered to be obtained in this work to handle the tough optimization problem of the 5G-28 GHz microwave antenna design. Furthermore, the Method of Moments (MoM) was employed to precisely quantify the gain and S_{11} performance measurements of the antenna design when the geometric design parameters changed. The acquired performance measure was then utilized to generate a cost function for use in the design optimization issue. By using the MATLAB 2021a application at 28 GHz, the design problem for 5G antennas in accordance with the 5G criteria mentioned above has been solved.

The remainder of this paper is briefly structured as follows. Section II discusses the antenna design parameters and geometric form. The objective and cost function of the multi-objective optimization problem are discussed in Section III. Section IV discusses the functioning component. Literature comparison and self-criticism are made in Section V. Section VI concludes the paper.

II. ANTENNA ARCHITECTURE

A planar variation of bionic dipole antennas is the bowtie antenna. Bowtie antennas are one of the most commonly used antenna types for communication systems and ground penetrating radar (GPR) applications. Bowtie antennas offer several advantages such as small weight, cheap cost, low profile and symmetrical emission pattern. It also offers ultra-wideband solutions with high bandwidth [21]. There are design possibilities in different shapes and geometries, for example, there are modified examples with U [23] and pi [24] shaped slots. The frequency value can go up to 28 GHz, which is the candidate standard for 5G technologies [22]. The reflection coefficient is defined as the ratio of the amplitude of the reflected signal to the amplitude of the transmitted signal. Determining antenna performance is the most basic parameter. Directivity, another important parameter, is the ratio of the power density in the direction where the antenna radiates maximum radiation to the power density of an isotropic antenna of the same power at the same distance. Directional antennas are antennas that can emit very strong radiation and receive very strong signals when receiving. The gains of such antennas are large wherever they are directed. Where it is not directed, it is very low. Thus, unwanted noise or broadcasts are prevented. The measure of the directivity ability of a lossless antenna is the antenna gain. This value is closely related to the directivity of the antenna. Unlike the directivity of the antenna, which only describes its directivity characteristics, antenna gain also includes the efficiency of its antenna and therefore also represents the actual radiated power. This power is usually less than the power provided by the sender. However, since measuring this power is easier than measuring directivity, antenna gain is more often used as directivity. Assuming that the antenna is a lossless antenna, the directivity can be taken equal to the antenna gain. However, the performance measurements of the design largely depend on the geometric design values. Bowtie antenna design can therefore be considered a multi-purpose, multi-dimensional design optimization issue. A triangular-shaped microstrip bowtie antenna is considered in this study on the application of the NSGA-III algorithm for Pareto optimization of antenna design. Figure 1 and Table 1 show the diagram of the antenna design and its design parameters.

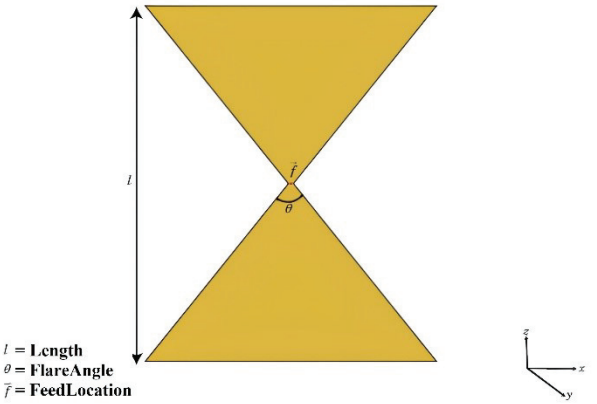

Fig. 1. Bowtie antenna.

Table 1: Antenna design parameters

Parameter	Value	Definition
Length (meters)	0.001-0.04	Planar bowtie length
Flare angle (degrees)	5-90	Planar bowtie flare angle
Conductor	PEC	Type of metal material
Tilt	0	Tilt angle of antenna

The design optimization of bowtie antenna is performed by NSGA-III algorithm using the optimization variables given in Table 1. All these processes were performed by a computer with 8th generation Intel Core i7 CPU, 3.20 GHz processor and 8 GB RAM.

III. MULTI-OBJECTIVE OPTIMIZATION

Evolutional multi-objective optimization methods have proven their age in finding many successful combined and diversified non-dominant solutions in optimization problems with two or more goals since the early 90s. Of course, in problems involving multiple goals and

functions, there are usually many optimization problems with three or more input and output values [27, 28]. For this reason, evolutional multi-objective optimization algorithms are expected to research and develop by addressing this problem for the last five years. Many objective issues pose difficulties in an evolutional multi-objective optimization algorithm as with any optimization algorithm. The most significant of them is the presence of a high number of non-dominant solutions in the solution set, which expands the archive solution set. If these non-dominant solutions occupy a large place in the solution set, the algorithm may have great difficulty in dominating a sufficient number of new solutions. This situation significantly slows down the search process of the algorithm [29, 30]. Another challenge is that enacting a large-scale problem can be a challenging task, so evaluating the performance of the algorithm used in later decision-making situations can be misleading and difficult. For this reason, performance evaluation criteria hyper volume measure [31] and other criteria [29, 32] are computationally meaningless or too costly. Using the diversity protection operator crowd-distance [25], clustering [33] operators as a third challenge, the solution can increase the cost in terms of computation.

It is feasible to solve multi-objective optimization issues by using evolutional optimization procedures, which typically involve two or more goals. To address the multi-objective optimization issue in this article, a modified NSGA-III method will be employed.

A. Multi-objective optimization for generic formulation

A minimized multi-objective optimization problem with N goals is defined as follows:

$$\text{Minimize } \overrightarrow{y} = F(\overrightarrow{x}) = [f_1\overrightarrow{x}, f_2\overrightarrow{x}, \ldots, f_N\overrightarrow{x}]^T,$$
$$\text{subject to } g_j(\overrightarrow{x}) \le 0, \quad j = 1,2,\ldots,M,$$
$$\text{where } \overrightarrow{x} = [x_1, x_2, \ldots, x_p]^T \varepsilon\, \Omega.$$

The variable $\vec{y}$ is an objective vector, the variable g_j represent restrictions, and the variable $\vec{x}$ is a P-dimensional vector expressing choice variables inside a parameter space Ω. The area filled by objective vectors is referred to as objective space. The relevant space is the subspace of goal vectors meeting the requirements [7, 34, 35].

B. Non-dominated sorting genetic algorithm accelerated by modeling

Since the current optimization processes are undesirably long and hardware upgrades or other tools will increase the cost, optimization is supported by modeling. For this purpose, it was modeled using a multi-layer perceptron (MLP) with reduced data using the Latin hypercube sampling (LHS) method before optimization. There is a similar study in the literature [36]. Then, the modeled parts will be included in the optimization process and a unified structure will be created.

We use a reference point-based multi-objective evolutionary algorithm following the NSGA-II framework. This highlights population members that are not dominant but are close to a set of provided reference points. The NSGA-III used can be applied to multi-objective testing problems containing 2 to 15 targets. mNSGA-III was used in this study by making a series of modifications on the existing NSGA-III. First of all, a cutoff point was added among the results found. For results that fall outside the desired limits, the cost is shown to be high and the algorithm is forced to find the desired results. Subsequently, after calculating the targets, before creating the solution archive, ANN modeling is added and the solution archive is multiplied. By reducing the number of iterations to reach the minimum cost value, less costly results can be obtained in terms of optimization time. In addition, a feasible solution set was created by combining all the results found in each step and the selection process was made from that set. A version of this converted into a mathematical model is shown in Fig. 2. As defined in Fig. 2, the process begins with the definition of algorithm parameters, especially population size, maximum iteration and weight coefficients. Here, the most important innovation, ANN model support, is specified externally. Thus, a decrease of up to 8 times in optimization time was observed. Again, as can be seen in Fig. 2, if the ANN contains a model, this time saving is achieved by skipping the calculation part. All of this results in achieving optimal characterization.

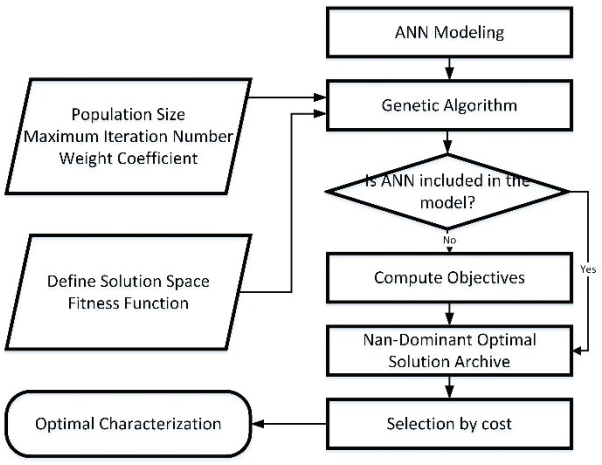

Fig. 2. Flow chart of microwave antenna by modeling accelerated non-dominant sorting genetic algorithm (NSGA)-III optimal solution modification.

C. Objective and cost functions

Among the antenna measurement functions, S_{11} and 90-degree directivity, which are among the most basic

parameters determining the performance of the antenna explained in detail in the previous section, were chosen as reference points. Since multi-objective optimization problems try to converge the two selected objective function values to zero at the same time, functions that will keep the directivity parameter high and the S_{11} parameter low are tried to be selected. According to all these, the following objective functions are defined.

Objective functions:

$$OF_1 = \min\{e^{-\frac{directivity}{wc_1}}\}, \quad (1)$$

$$OF_2 = \min\{e^{\frac{S_{11}}{wc_2}}\}. \quad (2)$$

Here, the maximum reference points are given as directivity$\geq$0 and the minimum reference points are given as S_{11} <=0. Thus, the algorithm will try to optimize both performance parameters at the same time according to the importance of the determined weight coefficients (wc_{1-2}). The objective functions used in the optimization of the algorithm are collected to determine the cost function that will be used to demonstrate the success of the results in comparison with each other and are used to create the cost function:

$$cost = OF_1 + OF_2. \quad (3)$$

Objective functions (1-2) to be used in the optimization process have been selected since analysis is required for predefined performance parameters at a frequency of 28 GHz. It was tried to determine the result with the minimum average cost (3) taken over 10 runs with the determined goal functions.

In this optimization process, the decision variables are antenna length (meters) and flare angle (degrees), respectively. Since the importance of the requirements is different, trials have been made for different weight coefficients (wc_1, wc_2).

IV. RESULTS

A. Comparison of ANN aided and unaided NSGA-III and MOEA/D

First, the performance of NSGA-III was compared with a recently proposed MOEA/D procedure. The default parameters of the algorithm used (MOEA/D) are given as crossover percentage (P_c)=0.5, maximum iteration=30, archive=100 and population (N)=100. The default parameters of the proposed algorithm (NSGA-III) are given as percentage of crossover used (P_c)=0.5, mutation (P_m)=0.5, maximum iterations=30 and population (N)=80. Experiments were conducted for four different conditions in total. The results of two different algorithms are presented, with and without modeling support. Figure 3 shows typical cost and function evaluation number (FEN) variations with a repeat of the best performance. It was selected from 10 different studies for MOEA/D and NSGA-III with and without ANN support. As seen in the figure, the proposed algorithm showed more successful results than its rival. With ANN support, the steps to reach the MOEA/D minimum cost were reduced from 26 to 23. Similarly, NSGA-III also decreased from 16 to 13. Thus, the optimum was reached approximately 20% earlier in NSGA-III. In addition, since the ANN modeling part added to the very beginning of the application shown in Fig. 2 and the archive part created with these models skipped the calculation part of the lenses, there was an approximately 8-fold decrease in the total time.

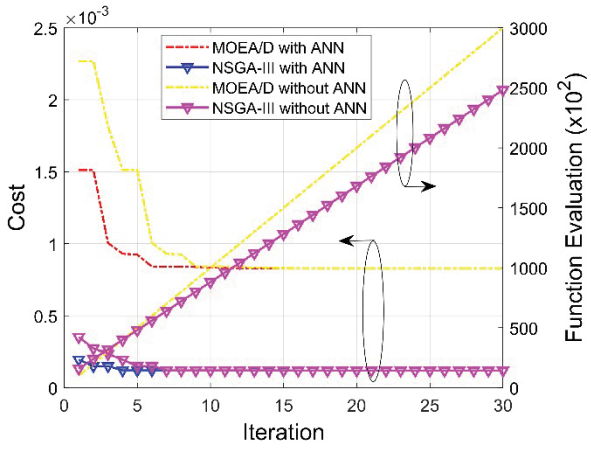

Fig. 3. Typical cost and FEN variations with iteration of the best performance of NSGA-III and MOEA/D algorithms selected from 10 runs for multi-objective optimization.

B. Optimal parameter set selection for optimization

Instead of starting from a single point, genetic algorithms seek from a collection of points. It is vital to select the algorithm settings that are best for this purpose. The algorithm's default settings are supplied as follows: population (N)=80; crossover percentage (P_c)=0.5; mutation (P_m)=0.5; maximum iterations (I)=30. For the 28 GHz algorithm, tests with various population characteristics have been conducted. With a duplicate of the best performance chosen from 10 distinct runs with crossover percentage (P_c)=0.5, mutation (P_m)=0.5 and population (N)=30, 50, 80. Figure 3 displays typical cost and FEN fluctuations. Additionally, a numerical summary of the cost and FEN changes from Fig. 4 is provided in Table 2. The best parameter set was determined to be crossover percentage (P_c)=0.5, mutation (P_m)=0.5, maximum iteration=30 and population (N)=50 based on the graph and table. The chosen optimal parameters will be used to continue the investigation in the next section.

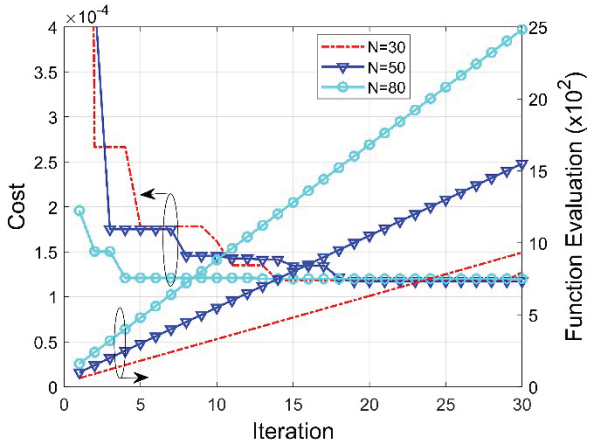

Fig. 4. Typical cost and FEN variations with iteration of the best performance of the algorithm selected out of 10 runs for optimization by population: crossover percentage (P_c)=0.5, mutation (P_m)=0.5 and maximum iteration=30.

Table 2: Performance evaluations of the algorithm by population for optimization: crossover percentage (P_c) = 0.5, mutation (P_m) = 0.5 and maximum iteration = 30

Population (N)		**Minimum**	**Maximum**	**Mean**
30	Cost	0.119×10^{-3}	2.307×10^{-3}	0.220×10^{-3}
	FEN	450	60	930
50	Cost	0.117×10^{-3}	0.454×10^{-3}	0.157×10^{-3}
	FEN	1000	100	1550
80	Cost	0.119×10^{-3}	0.196×10^{-3}	0.125×10^{-3}
	FEN	2480	160	2480

C. Weight coefficient selection for cost

Determining the weight coefficients inside the cost (3) function is crucial since the working concept of the algorithm aims to obtain the solution with the lowest cost. Weight coefficient-1 (wc_1) represents the directivity parameter in the cost function, while weight coefficient-2 (wc_2) represents the parameter S_{11}. The best performance, chosen from 10 distinct runs, is shown in Fig. 4 along with its repeating typical cost and FEN variations for wc_{1-2}=0.3, 0.5 and 0.7, respectively. Additionally, a numerical summary of the cost and FEN changes from Fig. 5 is provided in Table 3.

D. S_{11} for bowtie antenna

Figure 6 shows the typical magnitude and frequency variations at 25-32 GHz for S_{11} of three antennas with the best performance for percent transition (P_c)=0.5, mutation (P_m)=0.5, and population (N)=30, 50 and 80. Additionally, the variations in magnitude and frequency

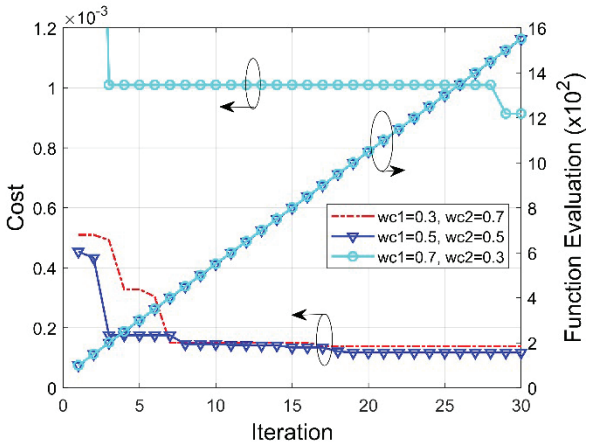

Fig. 5. Typical cost and FEN variations with iteration of the best performance of the selected algorithm over 10 runs for optimization by weight coefficients: crossover percentage (P_c)=0.5, mutation (P_m)=0.5, maximum iteration=30 and population (N)=50.

Table 3: Performance evaluations of the algorithm according to the weight coefficients for optimization: crossover percentage (P_c)=0.5, mutation (P_m)=0.5, maximum iteration=30 and population (N)=50

wc 1	**wc 2**		**Minimum**	**Maximum**	**Mean**
0.3	0.7	Cost	0.138×10^{-3}	0.509×10^{-3}	0.197×10^{-3}
		FEN	900	100	1550
0.5	0.5	Cost	0.117×10^{-3}	0.454×10^{-3}	0.157×10^{-3}
		FEN	1000	100	1550
0.7	0.3	Cost	0.914×10^{-3}	4.79×10^{-3}	1.20×10^{-3}
		FEN	1500	100	1550

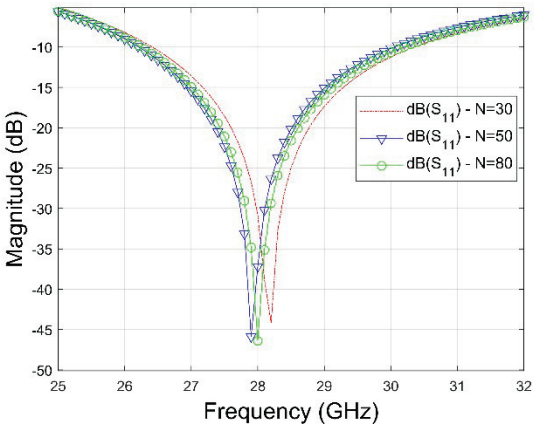

Fig. 6. S_{11} of antenna for the best performance selected among different population values: P_c=0.5, P_m=0.5 and maximum iteration=30.

in Fig. 6 are given in Table 4 as a numerical table. As a result, the increase in the population value gives more result value and increases the cost of optimization. Figure 7 shows the three best performances for population (N)=50, wc_1=0.3, 0.5 and 0.7, and wc_2=0.3, 0.5 and 0.7, in addition to the parameters used in Fig. 6. The S_{11} of the antenna shows typical angle and frequency variations between 25 and 32 GHz. Additionally, the variations of angle and frequency in Fig. 7 are given in Table 5 as a numerical table. It is seen that increasing the weight coefficient of S_{11} is reflected in the results. According to the results in Figs. 6 and 7, it can be said that the bandwidth of the antennas is 26-30 GHz. In addition, using the population (N)=80, wc_1=0.5 and wc_2=0.5 parameters given in Fig. 6, the best result is -47.96 dB S_{11}. Directivity for the result is shown in Fig. 8, and the most successful design parameters were obtained using the 3D EM simulation tool CST Microwave studio. In Fig. 9, the variation of S_{11} is given as typical amplitude-frequency.

Table 4: Numerical form of frequency and S_{11} values in Fig. 6

Population (N)	**Frequency (GHz)**	**S_{11} (dB)**
30	28.1	−43.41
50	27.9	−47.27
80	28	−47.96

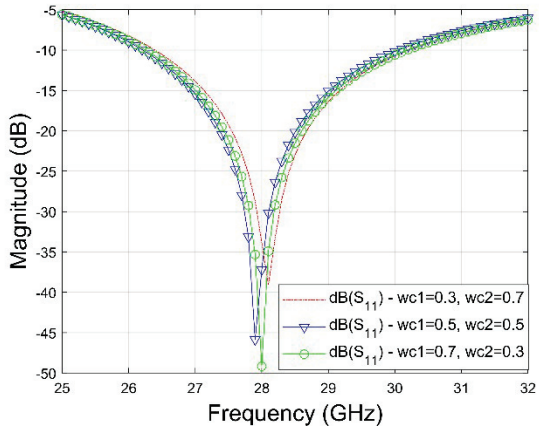

Fig. 7. S_{11} of antenna for the best performance selected among different weight coefficients values: P_c=0.5, P_m=0.5, N=50 and maximum iteration=30.

Table 5: Numerical form of frequency and S_{11} values in Fig. 7

wc_1-wc_2	**Frequency (GHz)**	**S_{11} (dB)**
0.3-0.7	28.1	−36.86
0.5-0.5	27.9	−47.27
0.7-0.3	28	−48.96

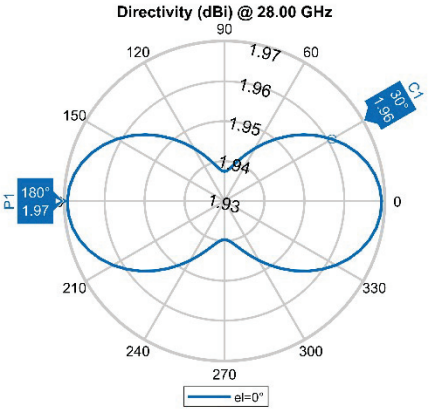

Fig. 8. Directivity of antenna for the best performance selected: P_c=0.5, P_m=0.5, N=80 and maximum iteration=30.

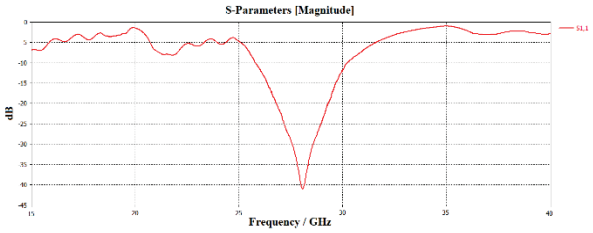

Fig. 9. S_{11} of the antenna from the results using CST (Substrate to RT/Duroid 5880).

V. DISCUSSION

In a similar study, it was stated that the proposed antenna had good performances operating at 28 GHz, with a S_{11} of -30 dB, VSWR below 2, good directivity and the radiation pattern of the proposed antenna providing a good match on the required frequency [22]. In our study, a S_{11} of -49 dB was obtained at 28 GHz. It is stated in detail in Table 6. In another study, two multi-objective optimization meta-heuristic strategies combined with the carrier model NSGA-II and MOEA/D are used to overcome the problems noted in conventional antenna design [16]. A total of 4 hours of process was reduced to 55 minutes with improvement. Thus, the process was made 4.4 times faster. In our study, it was seen that the time was made 8 times faster in total. It is stated in detail in Table 7. When compared with both similar studies, the success of the proposed method was once again confirmed.

At the very beginning of the study, modeling support was not added because the optimization processes for the

Table 6: Comparison of S_{11} values

	Frequency (GHz)	**S_{11} (dB)**
Current Study	28	−48.96
[22]	28	−30

Table 7: Comparison of optimization time

	Previous Working Time	**Subsequent Working Time**
Current Study	8X	1 X
[16]	8X	1.4 X

relevant model did not take very long. In similar studies or different models, it was observed that the optimization processes took undesirably long and this situation made optimization inextricable, and the flow of the study evolved in this direction. Architecturally, a longer lasting model could have been chosen. However, this would only prolong the processes and would not have any impact on the confirmation of the success of the application.

In future studies, the processes can be further accelerated by changing the network used in modeling support. Additionally, the suggested method can be tried on models that take more time, such as filter optimization.

VI. CONCLUSION

In the literature, the definition of optimal characterization is defined as the process of finding the optimal solution possible within the range specified by the user. This process may take an undesirably long time due to both the complexity of the problem and hardware inadequacies.

In this study, it has been shown that the current optimal characterization process can be reduced up to 8 times with only ANN support, without requiring any additional hardware or tools. Thus, this and similar optimization processes can be solved much more economically without any additional cost. The proposed ANN modeling addition is only a software add-on and does not require any additional budget. In the application part, compact microstrip single-band antenna designs that can operate in millimeter wave communication are formulated as a multi-objective optimization problem supported by ANN modeling, and are expressed in terms of dominant solutions and variation relations according to the geometric design parameters of the antennas. NSGA-III algorithm has been successfully applied to obtain optimum design values for desired cost functions using MOM technique. The fact that the originally designed system was supported by modeling caused the current optimization process to reach optimum by an additional 20% earlier. In addition to all these, the results in the study were compared with the MOEA/D, a recently proposed EMO algorithm, to compare the superiority of the problem and it was found to be more successful. When compared with similar studies in the literature, more effective results were obtained. As can be seen from the simulation results, the proposed NSGA-III-based design optimization method is an impact algorithm for generating optimal solutions of a microwave antenna in terms of geometric design parameters and performance criteria. In terms of verifying the results with a different program, the most successful design parameter was obtained using the 3D EM simulation tool CST Microwave studio.

In summary, the proposed modeling support can be successfully applied to any optimization algorithm processes and thus significant savings can be achieved in all other optimization processes.

REFERENCES

[1] T. Fisher, *5G availability around the world* [Online]. Available: https://www.lifewire.com/5g-availability-world-4156244

[2] W. Hong, Z. H. Jiang, C. Yu, J. Zhou, P. Chen, Z. Yu, H. Zhang, B. Yang, X. Pang, M. Jiang, Y. Cheng, M. K. T. Al-Nuaimi, Y. Zhang, J. Chen, and S. He, "Multibeam antenna technologies for 5G wireless communications," *IEEE Trans Antennas Propag*, vol. 65, no. 12, pp. 6231-6249, Dec. 2017.

[3] H. Jaafar, M. T. Ali, S. Subahri, A. L. Yusof, and M. K. M. Salleh, "Improving gain performance by using air substrate at 5.8GHz," in *2012 International Conference on Computer and Communication Engineering (ICCCE)*, *IEEE*, July 2012, pp. 95-98.

[4] J. Bang and J. Choi, "A SAR reduced mm-wave beam-steerable array antenna with dual-mode operation for fully metal-covered 5G cellular handsets," *IEEE Antennas Wirel Propag Lett*, vol. 17, no. 6, pp. 1118-1122, June 2018.

[5] *5G spectrum GSMA public policy position* [Online]. Available: https://www.gsma.com/latinamerica/resources/5g-spectrum-gsma-public-policy-position-2/

[6] A. Sharma, S. Khah, and S. Rawat, "Compact Y-shaped antenna with partial and meandered ground for WLAN/Wi-Max Applications," *Scientia Iranica*, 2022.

[7] F. Gunes, A. Uluslu, and P. Mahouti, "Pareto optimal characterization of a microwave transistor," *IEEE Access*, vol. 8, pp. 47900-47913, 2020.

[8] F. Kiani, A. Seyyedabbasi, and P. Mahouti, "Optimal characterization of a microwave transistor using grey wolf algorithms," *Analog Integr Circuits*

Signal Process, vol. 109, no. 3, pp. 599-609, Dec. 2021.

[9] J. O. Yang, Q. R. Yuan, F. Yang, H. J. Zhou, Z. P. Nie, and Z. Q. Zhao, "Synthesis of conformal phased array with improved NSGA-II algorithm," *IEEE Trans Antennas Propag*, vol. 57, no. 12, pp. 4006-4009, Dec. 2009.

[10] G. Li, S. Yang, Q. Feng, X. L. Zhao, and X. Yin Zhang, "Dual-polarized differential-fed phased array antenna with sidelobe suppression based on NSGA-II for 5G millimeter wave application," in *2020 International Conference on Microwave and Millimeter Wave Technology (ICMMT)*, *IEEE*, pp. 1-3, Sep. 2020.

[11] C. Zhang and A. Qing, "Sidelobe level and sideband suppression in time-modulated linear arrays by NSGA-II," in *2017 IEEE International Symposium on Antennas and Propagation & USNC/URSI National Radio Science Meeting*, *IEEE*, pp. 531-532, July 2017.

[12] J. Moreno, I. Gonzalez, and D. Rodriguez, "Using simulation and the NSGA-II evolutionary multiobjective algorithm in the design of a compact dualband equatorial helix antenna," in *2017 6th International Conference on Space Mission Challenges for Information Technology (SMC-IT)*, *IEEE*, pp. 56-60, Sep. 2017.

[13] H. Li, Y. Chen, and S. Yang, "Pattern synthesis of a time-modulated Vivaldi linear array with MOEA/D algorithm," in *2019 IEEE International Conference on Computational Electromagnetics (ICCEM)*, *IEEE*, pp. 1-3, Mar. 2019.

[14] D. Ding, Y. Tu, Y. Lin, and X. Ding, "Design of dielectric-loaded compact broadband circularly-polarized helix antenna by using multiobjective evolutionary algorithm based on decomposition (MOEA/D)," in *2017 IEEE 2nd Information Technology, Networking, Electronic and Automation Control Conference (ITNEC)*, *IEEE*, pp. 1504-1507, Dec. 2017.

[15] W. Feng, N. Zhao, S. Ao, J. Tang, X. Zhang, Y. Fu, D. K. C. So, and K. Wong, "Joint 3D trajectory and power optimization for UAV-aided mmwave MIMO-NOMA networks," *IEEE Transactions on Communications*, vol. 69, no. 4, pp. 2346-2358, Apr. 2021.

[16] M. C. De Melo, P. B. Santos, E. Faustino, C. J. A. Bastos-Filho, and A. Cerqueira Sodre, "Computational intelligence-based methodology for antenna development," *IEEE Access*, vol. 10, pp. 1860-1870, 2022.

[17] X. Wang, G. Wang, D. Wang, and Q. Zhang, "Ensemble-learning-based multiobjective optimization for antenna design," *IEEE Trans Antennas Propag*, vol. 71, no. 2, pp. 1295-1303, Feb. 2023.

[18] D. Lu and J. Zhao, "Design of high-isolation fragment-type 5G base station antennas with MOEA/D-GO," in *2020 International Symposium on Antennas and Propagation (ISAP)*, *IEEE*, pp. 467-468, Jan. 2021.

[19] Q.-Q. Li, Q.-X. Chu, Y.-L. Chang, and J. Dong, "Tri-objective compact log-periodic dipole array antenna design using MOEA/D-GPSO," *IEEE Trans Antennas Propag*, vol. 68, no. 4, pp. 2714-2723, Apr. 2020.

[20] Q.-Q. Li, Q.-X. Chu, and Y.-L. Chang, "Design of compact high-isolation MIMO antenna with multiobjective mixed optimization algorithm," *IEEE Antennas Wirel Propag Lett*, vol. 19, no. 8, pp. 1306-1310, Aug. 2020.

[21] K. Y. Yazdandoost and R. Kohno, "Slot antenna for ultra wideband system," in *IEEE/ACES International Conference on Wireless Communications and Applied Computational Electromagnetics 2005*, *IEEE*, pp. 212-216, 2005.

[22] B. Babayiğit and A. İ. N. Al-Husseın, "5G slotted bow-tie antenna design," *Gazi Mühendislik Bilimleri Dergisi*, vol. 4, no. 2, pp. 99-107, Aug. 2018.

[23] K. Singh, Y. Kumar, and S. Singh, "A modified bow tie antenna with U-shape slot for wireless applications," *International Journal of Emerging Technology and Advanced Engineering*, vol. 2, no. 10, pp. 158-162, Oct. 2012.

[24] W. Kueathaweekun, P. Jearapraditkul, N. Anantrasirichai, O. Sangaroon, and T. Wakabayashi, "Wide-band CPW-fed slot antenna with tuning stub and pi-strip for WLAN/WiMAX application," in *International Symposium on Intelligent Signal Processing and Communications Systems, IEEE*, pp. 1-4, Feb. 2009. doi:10.1109/ISPACS.2009.4806771.

[25] K. Deb, A. Pratap, S. Agarwal, and T. Meyarivan, "A fast and elitist multiobjective genetic algorithm: NSGA-II," *IEEE Transactions on Evolutionary Computation*, vol. 6, no. 2, pp. 182-197, Apr. 2002.

[26] K. Deb and H. Jain, "An evolutionary many-objective optimization algorithm using reference-point-based nondominated sorting approach, part I: Solving problems with box constraints," *IEEE Transactions on Evolutionary Computation*, vol. 18, no. 4, pp. 577-601, Aug. 2014.

[27] O. Chikumbo, E. Goodman, and K. Deb, "Approximating a multi-dimensional Pareto front for a land use management problem: A modified MOEA with an epigenetic silencing metaphor," in *2012 IEEE Congress on Evolutionary Computation*, *IEEE*, pp. 1-9, June 2012.

[28] C. A. C. Coello and G. B. Lamont, *Applications of Multi-Objective Evolutionary Algorithms*, World Scientific Publishing, 2004.

[29] K. Deb, *Multi-objective Optimization Using Evolutionary Algorithms*. Chichester: Wiley, 2001.

[30] K. Deb and D. Saxena, "Searching for Pareto-optimal solutions through dimensionality reduction for certain large-dimensional multi-objective optimization problems," in *Proceedings of the World Congress on Computational Intelligence (WCCI-2006)*, pp. 3352-3360, 2006.

[31] E. Zitzler and L. Thiele, "Multiobjective evolutionary algorithms: A comparative case study and the strength Pareto approach," *IEEE Transactions on Evolutionary Computation*, vol. 3, no. 4, pp. 257-271, 1999.

[32] E. Zitzler, L. Thiele, M. Laumanns, C. M. Fonseca, and V. G. da Fonseca, "Performance assessment of multiobjective optimizers: an analysis and review," *IEEE Transactions on Evolutionary Computation*, vol. 7, no. 2, pp. 117-132, Apr. 2003.

[33] E. Zitzler, M. Laumanns, and L. Thiele, "SPEA2: Improving the strength Pareto evolutionary algorithm for multiobjective optimization," in *SPEA2: Improving the Strength Pareto Evolutionary Algorithm for Multiobjective Optimization*, Sep. 2001.

[34] A. Uluslu, "Chameleon swarm algorithm assisted optimization of U-slot patch antenna for quad-band applications," *IEEE Access*, vol. 10, pp. 74152-74163, 2022.

[35] A. Uluslu, "Fitting nonlinear mathematical models to the cost function of the quadrafilar helix antenna optimization problem," *Analog Integr Circuits Signal Process*, vol. 115, no. 3, pp. 307-318, June 2023.

[36] A. Uluslu, "Application of artificial neural network base enhanced MLP model for scattering parameter prediction of dual-band helical antenna," *The Applied Computational Electromagnetics Society Journal (ACES)*, Sep. 2023.

Ahmet Uluslú received his Ph.D. from Istanbul Yıldız Technical University Electronics and Communication Engineering Department in 2020. He completed his master's degree at the Department of Electromagnetic Fields and Microwave Techniques from the same university. He is working as an associate professor at Istanbul University - Cerrahpaşa Electronics and Automation Department. His current research areas are microwave circuits, especially optimization techniques of microwave circuits, antenna design optimization-modeling, surrogate-based optimization and artificial intelligence algorithm applications.

An Approach to the Implementation of Laplace and a Broadband Helmholtz Fast Multipole Method as an Application Independent Library

Sanjay Velamparambil

Ansys Inc., 1995 N. 57th Court, Suite 100, Boulder, CO-80301, USA
sanjay.velamparambil@ansys.com

Abstract **–** In this paper, we propose an approach to develop an application independent library of Laplace and Helmholtz fast multipole method (FMM) that can be used in different applications. For this purpose, we consider a generalized problem and a corresponding canonical problem (defined below). In the first main contribution, we show that it is possible to capture the essential characteristics of the canonical summation from sampling the values of certain potentials or signature functions. In the second main contribution, we show that partial derivatives of arbitrary orders acting on the far field can be represented as product of sparse matrices within the library, transparent to the user. Combining the two ideas, we show that once the FMM is configured to compute the canonical summation, the same setup can be used to work with a much wider, general class of problems.

Index Terms **–** Fast multipole methods, integral equations.

I. INTRODUCTION

In this paper, we describe an approach to develop a *stand-alone, application independent library* of the fast multipole method (FMM) [1–3] to be used in different physical applications and developed by multiple teams with differing backgrounds. In particular, we are concerned with the evaluation of summations of the form:

$$y_m = \sum_{n=1}^{N} A_{mn} x_n, \quad 1 \le m \le M, \tag{1a}$$

with:

$$A_{mn} = \int_{\Omega} g_m(\vec{x}) \mathcal{M}_u \int_{\Omega'} f_n(\vec{x}') \mathcal{L}'_v G(\vec{x},\vec{x}')\, d\Omega' d\Omega, \tag{1b}$$
$$u, v = x, y, z;\ \vec{x}, \vec{x}' \in \mathbb{R}^3,$$

where $\mathcal{M}_u$ and $\mathcal{L}_v$ are linear partial differential operators with constant coefficients and:

$$G(\vec{x},\vec{x}') = \begin{cases} \frac{1}{\|\vec{x}-\vec{x}'\|} & \text{for the Laplace Equation} \\ \frac{e^{ik\|\vec{x}-\vec{x}'\|}}{\|\vec{x}-\vec{x}'\|} & \text{for the Helmholtz Equation.} \end{cases} \tag{1c}$$

Note that, in general, $\Omega' \neq \Omega$. Furthermore, following the terminology used by the method of moments (MoM) practitioners in electromagnetics, we shall refer to $f_j(\vec{x})$ and $g_i(\vec{x})$ as the *basis* and *testing* functions, respectively, with the understanding that they can be Dirac δ-functions to represent "point" particles.

Such computations can arise from a wide variety of applications, such as electromagnetics, acoustics and elastic wave scattering. Since its development in the 1980s [4, 5] for the Laplace equation to the elegant extension to the Helmholtz and Maxwell equations in the 1990s [2, 3, 6], FMM and its multilevel variants have transformed computational physics, especially, computational electromagnetics. It is beyond the scope of this paper to provide a comprehensive overview of these remarkable developments. Instead, we refer the reader to the recent review by He *et al.* [7].

Although the theory of FMM has been well established and many high quality implementations exist, both in the public domain and in proprietary products, the development of an application independent library is still a challenging problem due to various *practical* constraints such as:

- Different formulations and physics lead to different choices for $\mathcal{M}_u$ and $\mathcal{L}_v$.
- Different domain and geometry; the integrals could be defined over surfaces or volumetric regions, discretized with surface elements such as flat or curvilinear triangles and/or quadrilaterals and volume elements such as tetrahedra. It is also possible to have mixed formulations involving both surface elements and volume elements. The quality of such a mesh can often be poor, with highly non-uniform elements.
- Different basis and testing procedures in reducing the integral equations to a matrix equation; note that each basis and testing function can be supported by one or more mesh elements.
- Familiarity/background knowledge of the library user. Even though one can expect the users to have a sound understanding of the integral equation and the underlying physics, it is not necessary that they

Submitted On: August 9, 2023
Accepted On: July 8, 2024

https://doi.org/10.13052/2024.ACES.J.390504

have a sufficient understanding of FMM to develop the components needed to integrate their code with a library.

We illustrate this with an example. In an implementation of Laplace FMM that uses spherical harmonics, the library user may have to provide the multipole coefficients of basis/testing functions. Although standard implementations of spherical harmonics are available, it may be tricky to ensure consistency between third party implementation of spherical harmonics and the ones used in the FMM implementation.

One of the ways to address these issues is to replace the basis and testing functions with weighted (point) "particles" as shown in Fig. 1. Although this approach simplifies the implementation of the library, it has several drawbacks. First, as illustrated in Fig. 1, replacing mesh elements and basis/testing functions with weighted particles generally leads to *incompatible partitioning* of the geometry, requiring error-prone bookkeeping, complicated data interchange between the application and the library, and messy corrections in the near field. In addition, given that the number of quadrature points is generally larger than the number of basis/testing functions, the matrix as seen by the library tends to be larger as well, potentially affecting the performance.

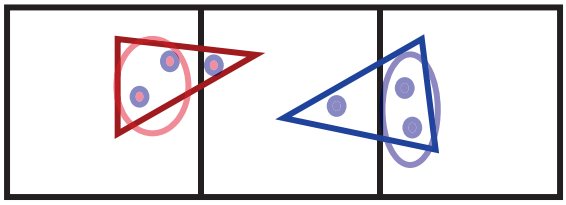

Fig. 1. The two triangles are near to each other, but some of the quadrature points can still be well separated (shown in ellipses) leading to tricky bookkeeping and near field corrections.

Therefore, the objective of this paper is to present an approach that can handle a wide class of problems through the use of good *abstractions* to capture the physics, the formulation and the discretization. The main contributions of this work are:

- Abstractions to characterize the geometry of the elements in a way that allows consistent handling of non-uniform meshes.
- A technique to compute required multipole coefficients of the shape/basis and testing functions from *sampled values* of their corresponding potentials or signature functions which are easy to define and simple to evaluate, without involving any special functions.
- We show that the partial derivatives of the far field, represented by multipole or plane wave expansions, can be represented as products of sparse matrices independent of the basis and testing functions allowing the user to compute these derivatives without having to directly work with multipole expansions.

Finally, we demonstrate that once the library is integrated into an existing code to compute what we call the *canonical problem*, defined in equation (4), the same implementation can be used to evaluate summations in equation (1) without modifying the library and without adding new subroutines to the application code.

II. PRELIMINARIES

A. General class of problems

We assume that the reader is familiar with the basic mathematical formulation and the octree based computational structure of the Laplace and Helmholtz multi-level fast multipole methods (MLFMM). Except when specificity is needed, we shall use the abbreviation MLFMM to refer to either of the two versions.

In the context of MLFMM, we begin by noting that if g_m and f_n in equation (1) belong to well separated boxes, the Green's function in equation (1) does not involve any singularities. Since:

$$\frac{\partial G}{\partial u} = -\frac{\partial G}{\partial u'}, u = x, y, z, \tag{2}$$

whenever $\vec{x} \neq \vec{x}'$, the differential operator $\mathcal{L}'_v$ appearing on the source point $\vec{x}'$ can be transferred to the observation point $\vec{x}$ when g_m and f_n are *geometrically well separated*. Therefore, for far field computations, it is possible to transform equation (1b) to a linear combination of integrals of the form:

$$A_{mn} = \int_{\Omega} g_m(\vec{x}) \mathcal{D}_{pqr} \int_{\Omega'} f_n(\vec{x}') G(\vec{x}, \vec{x}')\, d\Omega' d\Omega, \tag{3a}$$

$$\text{where } \mathcal{D}_{pqr} = \frac{\partial^{p+q+r}}{\partial x^p \partial y^q \partial z^r}, \vec{x} \neq \vec{x}', \tag{3b}$$

with p, q and r being non-negative integers.

One of the key results presented in this work is that the differential operator $\mathcal{D}_{pqr}$ can be *exactly* represented as a product of certain sparse matrices in the calculation of far interactions. Anticipating this result, we define a new summation:

$$y_m = \sum_{n=1}^{N} P_{mn} x_n, \quad 1 \leq m \leq M, \tag{4a}$$

$$\text{where } P_{mn} = \int_{\Omega} g_m(\vec{x}) \int_{\Omega'} f_n(\vec{x}') G(\vec{x}, \vec{x}')\, d\Omega' d\Omega, \tag{4b}$$

and refer to it as the *canonical problem*.

B. Some notations and definitions

If $r = \|\vec{x}\|$ and $\hat{\mathbf{x}} = \frac{\vec{x}}{\|\vec{x}\|}$ for $\vec{x} \in \mathbb{R}$, we shall often write $\vec{x} = (r, \hat{\mathbf{x}}) = (r, \theta, \phi)$ in spherical coordinates. We shall

denote the unit sphere centered at the origin by $\Omega_0 = \{\vec{r} \in \mathbb{R}^3 : |\vec{r}| = 1\}$ and will typically use the symbol $\hat{\mathbf{s}} = (1, \theta, \phi)$ to denote a vector on Ω_0.

Following [8, 9], we define the associated Legendre function $P_n^m(x)$ of *degree* $n > 0$ and *order* $-n \leq m \leq n$ and by the formula:

$$P_n^m(x) = (-1)^m \frac{(1-x^2)^{m/2}}{2^n n!} \frac{d^{n+m}}{d^{n+m}x}(x^2-1)^n. \tag{5a}$$

Following Messiah [9], we define the spherical harmonic $Y_n^m(\theta,\phi)$ of degree n and order m by the relation:

$$Y_n^m(\theta,\phi) = \left[\frac{2n+1}{4\pi}\right]^{1/2} \left[\frac{(n-m)!}{(n+m)!}\right]^{1/2} P_n^m(\cos\theta) e^{im\phi}. \tag{5b}$$

We have:

$$Y_n^{-m}(\theta,\phi) = (-1)^m [Y_n^m(\theta,\phi)]^*, \tag{5c}$$

$$\int_0^{\pi}\int_0^{2\pi} Y_n^m(\theta,\phi) Y_{n'}^{m'*}(\theta,\phi) \sin\theta \, d\theta d\phi = \delta_{nn'}\delta_{mm'}, \tag{5d}$$

where * denotes the complex conjugate.

Let $\vec{x} = r\hat{\mathbf{x}} = (r,\theta,\phi) \in \mathbb{R}$. We define *inner and outer* multipole functions for the Laplace equation by the formulae [10]:

$$O_n^m(\vec{x}) = \sqrt{\frac{4\pi}{2n+1}} \frac{(-1)^n i^{-m}}{A_n^m} \frac{Y_n^m(\theta,\phi)}{r^{n+1}}, \tag{6a}$$

$$I_n^m(\vec{x}) = \sqrt{\frac{4\pi}{2n+1}} i^m A_n^m r^n Y_n^m(\theta,\phi), \tag{6b}$$

$$\text{where } A_n^m = \frac{(-1)^n}{\sqrt{(n-m)!(n+m)!}}. \tag{6c}$$

Similarly, for the Helmholtz equation, we define the inner and outer functions, denoted by $\tilde{I}_n^m(\vec{x})$ and $\tilde{O}_n^m(\vec{x})$, respectively, by the formulae [10]:

$$\tilde{I}_n^m(\vec{x}) = j_n(kr) Y_n^m(\hat{\mathbf{x}}), \tag{7a}$$

$$\tilde{O}_n^m(\vec{x}) = h_n(kr) Y_n^m(\hat{\mathbf{x}}), \tag{7b}$$

where $j_n(kr)$ and $h_n(kr)$ are, respectively, spherical Bessel and Hankel functions of the first kind and of order n.

III. ABSTRACTIONS FOR THE FAR FIELD COMPUTATIONS

We first develop the abstractions needed to evaluate the canonical summation in equation (4). Assuming the existence of an octree structure, let B_s and B_r be the boxes in which the basis function f_j and the testing function g_i, respectively, reside. [1] Referring to Fig. 2, let:

$$B_s \subset D_s \stackrel{\text{def}}{=} \{\vec{x} \in \mathbb{R}^3 \big| |\vec{x} - \vec{c}_s| < R_s\}, \tag{8}$$

$$B_r \subset D_r \stackrel{\text{def}}{=} \{\vec{x} \in \mathbb{R}^3 \big| |\vec{x} - \vec{c}_r| < R_r\}. \tag{9}$$

We assume that $\operatorname{supp} f_j \subset D_s$ and $\operatorname{supp} g_i \subset D_r$ and that $\bar{D}_s \cap \bar{D}_r = \emptyset$.

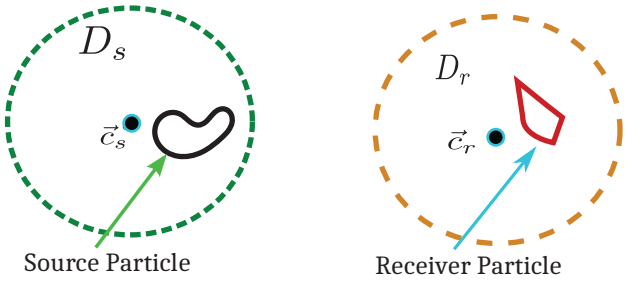

Fig. 2. The basis function, f_j, and the testing function, g_i, ("generalized particles") are enclosed in spheres D_s, with center at $\vec{c}_s$ and D_r, with center at $\vec{c}_r$, respectively, under the condition that $D_s \cap D_r = \emptyset$.

To represent the matrix element in equation (4), we first let:

$$\psi_j(\vec{x}) = \int_{\operatorname{supp} f_j} f_j(\vec{x}') G(\vec{x},\vec{x}') \, d\vec{x}', \tag{10a}$$

$$P_{ij} = \int_{\operatorname{supp} g_i} g_i(\vec{x}) \psi_j(\vec{x}) \, d\vec{x}. \tag{10b}$$

For a given accuracy $\varepsilon > 0$, let $N \geq 0$ be given. Let $\mathcal{O}_n^m(\vec{x})$ and $\mathcal{I}_n^m(\vec{x})$, respectively, denote the outer and inner multipoles of either Laplace or Helmholtz kernel. Then, we recall the following foundational results from the theory of MLFMM [2, 10]:

1. The potential $\psi_j(\vec{x})$ can be approximated by a finite *outer* multipole series valid *outside* D_s:
$$\psi_j(\vec{x}) \approx \sum_{n=0}^{N} \sum_{m=-n}^{n} \alpha_n^m \mathcal{O}_n^m(\vec{x} - \vec{c}_s), \; \vec{x} \notin \bar{D}_s. \tag{11a}$$
2. The potential $\psi_j(\vec{x})$ can be approximated as an *inner* multipole series valid *inside* D_r:
$$\psi_j(\vec{x}) \approx \sum_{n=0}^{N'} \sum_{m=-n}^{n} \beta_n^m \mathcal{I}_n^m(\vec{x} - \vec{c}_r), \; \vec{x} \in D_r. \tag{11b}$$
3. There exists a linear operator, $\mathcal{T}$, called a translation operator, relating the coefficients $\{\alpha_n^m\}$ and $\{\beta_n^m\}$ by:
$$\beta_n^m = \sum_{p=0}^{N} \sum_{q=-p}^{q} \mathcal{T}(n,m;p,q) \alpha_p^q. \tag{11c}$$

[1] Note that we are not providing a strict definition for the term "reside." It is simply a rule that the user provides to determine if a given basis/testing function can be considered as belonging to a given box. For example, in the case of point particles, if the location of the particle falls into a box, it can be considered to be a resident of that box.

4. To evaluate P_{ij}, we substitute equation (11b) into equation (10b), and obtain:

$$P_{ij} \approx \sum_{n=0}^{\min\{N,N'\}} \sum_{m=-n}^{n} \beta_n^m \rho_n^m, \tag{11d}$$

$$\rho_n^m \stackrel{\text{def}}{=} \int_{\operatorname{supp} g_i} g_i(\vec{x}) \mathcal{I}_n^m(\vec{x}-\vec{c}_r)\, d\vec{x}. \tag{11e}$$

Borrowing the terminology from Laplace FMM parlance, we shall refer to α_n^m as the "Q2M" coefficients and ρ_n^m as the "L2P" coefficients.

Expressing the Q2M and L2P coefficients in terms of multipole functions presents a challenge to implementation when multiple teams are involved. For example, a team developing a stand-alone library of FMM, to be used by multiple product teams, may not be deeply familiar with the applications themselves. On the other hand, a product team, although experts in, say, integral equations, may have little or no familiarity with FMM. Given that it is these coefficients that couple the application side (integral equation) with the FMM implementation, it is imperative that they are evaluated correctly and efficiently.

An obvious way to do this is to let the FMM library be aware of the basis and testing functions, and thus let the library evaluate these functions. This has the advantage that if the library decides to change, say, the definitions of inner functions, it will remain transparent to the application. However, this approach has the severe disadvantage that the library is deeply tied to a particular class of basis and testing functions. It is then left with the task of potentially adding a new class of basis and testing functions for every new application. This is inefficient and will eventually make the code unmaintainable.

A second approach is to let the application evaluate the coefficients (α_n^m, ρ_n^m) using formulae similar to those in equation (11d) and then hand-over the results to the FMM kernel. This has the great advantage that the FMM library remains completely decoupled from the application. However, this approach has the disadvantage that the application team must have some familiarity with FMM and multipoles. This may not always be the case.

Therefore, our goal is to evaluate the coefficients α_n^m and ρ_n^m within the library without exposing the functions $(\mathcal{O}_n^m, \mathcal{I}_n^m)$ to the application.

We now present an approach that eliminates these difficulties and it is inspired by ideas from [11–14].

A. Evaluation of Q2M and L2P coefficients for the Laplace equation

We begin by noting the basis function f_j is defined by the application and that the application "knows" how to evaluate $\psi_j(\vec{x})$ in equation (10a) at any point $\vec{x} \in \mathbb{R}^3$. Moreover, if $\vec{x} \notin \operatorname{supp} f_j$, the integral can be accurately evaluated using simple quadrature.

Consider a sphere $S \stackrel{\text{def}}{=} \{\vec{x} \in \mathbb{R}^3 \,\big|\, |\vec{x}-\vec{c}_s| = R > R_s\}$ so that $S \cap \operatorname{supp} f_j = \emptyset$. Let $\vec{x} \in S$. Then $\vec{x} = \vec{c}_s + R\hat{\mathbf{s}}$ where $\hat{\mathbf{s}} \in \Omega_0$. Then, substituting the definition of O_n^m from equation (6a) into equation (11a) and using the orthogonality of $Y_n^m(\hat{\mathbf{s}})$ from equation (5d), we obtain the well known relation (see, for example [14, equations 4-5]):

$$\alpha_n^m = i^m \sqrt{\frac{2n+1}{4\pi(n-m)!(n+m)!}} R^{n+1} \cdot \int_{\Omega_0} \psi_j(\vec{c}_s + R\hat{\mathbf{s}}) Y_n^{m*}(\hat{\mathbf{s}})\, d\Omega_s. \tag{12}$$

Now assume that the degree of approximation used in the FMM is $p > 0$. Then, the maximum degree of spherical harmonics under the integral that is relevant to the computations is $2p$. Therefore, if we use a quadrature, such as a composite Gauss-Legendre-Trapezoidal rule, that can integrate spherical harmonics of degree $2p$ exactly, we will be able to compute the coefficients exactly as well. Let N_q be the number of quadrature points, $\{(\hat{\mathbf{s}}_k, w_k)\}$, be quadrature points and their corresponding weights on Ω_0, respectively, and let $\vec{x}_k = \vec{c}_s + R\hat{\mathbf{s}}_k$, for $1 \le k \le N_q$. Then, equation (12) can be approximated as:

$$\tilde{\alpha}_n^m \approx i^m \sqrt{\frac{2n+1}{4\pi(n-m)!(n+m)!}} R^{n+1} \cdot \sum_{k=1}^{N_q} w_k \psi_j(\vec{x}_k) Y_n^{m*}(\hat{\mathbf{s}}_k). \tag{13}$$

Therefore, to compute the coefficients α_n^m, all the library needs are the values of $\psi_j(\vec{x})$, given by equation (10), at a set points on a specified sphere, which the application can readily supply. As remarked earlier, since the observation points $\vec{x}_k$ are chosen to be far away from the support of f_j, the integrand in (10a) is non-singular and hence $\psi_j(\vec{x}_k)$ can be evaluated using simple quadrature rules.

Using the addition theorem [10]:

$$\frac{1}{\|\vec{x}-\vec{x}'\|} = \sum_{n=0}^{\infty} \sum_{m=-n}^{n} (-1)^n I_n^{-m}(\vec{x}'-\vec{c}_s) O_n^m(\vec{x}-\vec{c}_s), \tag{14a}$$

for $\|\vec{x}-\vec{c}_s\| > \|\vec{x}'-\vec{c}_s\|$ in equation (10a) and comparing with equation (11a), it is easy to see that:

$$\alpha_n^m = (-1)^n \int_{\operatorname{supp} f_j} f_j(\vec{x}') I_n^{-m}(\vec{x}'-\vec{c}_s)\, d\vec{x}'. \tag{14b}$$

Comparing equation (14b) with the definition of ρ_n^m in equation (11d), we see that:

$$\rho_n^m = (-1)^n \alpha_n^{-m}, \tag{15}$$

for the f_j if it were also used as a testing function in a Galerkin MoM. Since:

$$\int_{\Omega} g_m(\vec{x}) \int_{\Omega'} f_n(\vec{x}') G(\vec{x},\vec{x}')\, d\Omega' d\Omega = \int_{\Omega'} f_n(\vec{x}') \int_{\Omega} g_m(\vec{x}) G(\vec{x},\vec{x}')\, d\Omega d\Omega',$$

it follows that we can use exactly the same technique (equations (12) and (13)) for computing ρ_n^m of any testing function g_i by evaluating the corresponding Q2M coefficients and using the relation in equation (15).

By this process, we have thus decoupled the application and the library for computing the L2P and Q2M coefficients for the Laplace equation: the application does not have to work with I_n^m functions and the library does not have to know the nature of the basis and testing functions, (f_j, g_i).

A.1. Comparison of performance

Given a multipole degree $p > 0$ and using a composite Gauss-Trapezoidal rule with $2(p+1)^2$ quadrature points, it is easy to see that the standard approach to computing Q2M (and L2P) coefficients and the potential based approach proposed above have the same asymptotic complexity. However, the proposed method has a larger constant associated with it. We now demonstrate that this additional cost for engineering a simplified interface is negligible in the context of the much larger initialization time (the time for the matrix-vectors are not affected).

To do this, we have taken 30 distinct triangular meshes ranging in size from 200 to about 1.2 million. They were generated by Ansys Q3D Extractor for different test cases and do not share a common geometry. For our purposes, it is sufficient to replace the triangles with point sources at their centroids. The canonical matrix in equation (4) is then constructed with a multipole degree of $p = 5$ which gives roughly 4 digits of accuracy in the matrix vector products. All the computations were done on a single core of a virtual machine with two Intel(R) Xeon(R) 6238R @2.20GHz processors with 182GB of RAM. In Fig. 3, we compare the time for evaluating the Q2M coefficients using the standard approach and from the potential samples.

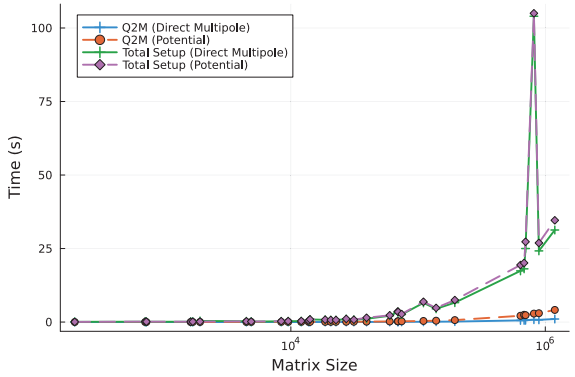

Fig. 3. Comparing the time for evaluating Q2M coefficients using standard ("Direct Multipole") and using sampled potentials ("Potential") for various test cases. We have also plotted the total setup time to provide the larger context.

It is important to note that the bulk of the initialization/setup time is spent in computing the near matrix and that the near matrix evaluation for concentrated sources gives the least possible time. This is because the commonly used basis functions require more expensive handling of singularities and near singularities. In other words, we are comparing the cost of Q2M evaluations against the best case scenario for the rest of the initialization. It is clear from Fig. 3 that although the proposed method is slightly more expensive, the increase is negligible when compared with the overall setup time. We have also compared the accuracy of the computed matrix vector products and the largest $2-$norm error observed was less than 2×10^{-4}, which is comparable to the overall precision of the matrix-vector products corresponding to the degree of multipole approximation $p = 5$.

B. Evaluation of Q2P and L2P coefficients for the Helmholtz equation

In the case of Helmholtz FMM that uses only multipole expansions involving $\tilde{O}_n^m$ and $\tilde{I}_n^m$, it is clear that an approach analogous to the one described in section A can be readily developed. However, most applications of Helmholtz FMM involves electrically large structures where a diagonalized form is employed [2, 10], often combined with multipole expansions to handle multiscale structures [15]. For such a mixed-form FMM, it is simpler to compute signature functions [10] rather than work with potentials. We now show how signature functions can be used to decouple the FMM library from the applications.

The *signature function* of the potential $\psi_j(\vec{x})$ of equation (10a), now with the Green's function for the Helmholtz equation (1), is defined by formula [10]:

$$\tilde{\psi}_j(\hat{\mathbf{s}}) = \lim_{r\to\infty} kre^{-ikr}\psi(\vec{c}_s + r\hat{\mathbf{s}}), \tag{16a}$$

which when approximated by equation (11a) with $\mathcal{O}_n^m = \tilde{O}_n^m$, can be shown to be:

$$\tilde{\psi}_j(\hat{\mathbf{s}}) = \sum_{n=0}^{\infty}\sum_{m=-n}^{m} \alpha_n^m \frac{Y_n^m(\hat{\mathbf{s}})}{i^{n+1}}. \tag{16b}$$

Therefore, given a signature function $\tilde{\psi}(\hat{\mathbf{s}})$, the orthogonality of spherical harmonics implies that we can recover the coefficients of the multipole expansion in equation (11a), α_n^m, using the formula [16]:

$$\alpha_n^m = i^{n+1}\int_{\Omega_0} \tilde{\psi}_j(\hat{\mathbf{s}}) Y_n^{m*}(\hat{\mathbf{s}})\, d\Omega_s. \tag{17}$$

It is well known that [2, 10] the signature function of the Green's function $G(\vec{r},\vec{r}') = \frac{e^{ik|\vec{r}-\vec{r}'|}}{|\vec{r}-\vec{r}'|}$ for $\vec{r}' \in D_s$ is given by:

$$\tilde{G}(\hat{\mathbf{s}}) = ke^{ik\hat{\mathbf{s}}\cdot(\vec{c}_s-\vec{r}')}.$$

Therefore, it follows that signature function of $\psi_j(\vec{x})$ of the canonical problem in equation (10a) is given by:

$$\tilde{\psi}_j(\hat{\mathbf{s}}) = k \int_{\text{supp}\, f_j} f_j(\vec{r'}) e^{ik\hat{\mathbf{s}}\cdot(\vec{c}_s - \vec{r'})}\, d\vec{r'}, \tag{18}$$

and we define the signature of the *basis function* f_j by $\tilde{f}_j(\hat{\mathbf{s}}) = \tilde{\psi}_j(\hat{\mathbf{s}})$.

Using the representation [9, 10]:

$$\tilde{I}_n^m(\vec{x} - \vec{c}) = \frac{1}{4\pi i^n} \int_{\Omega_0} e^{ik(\vec{x}-\vec{c})\cdot\hat{\mathbf{s}}} Y_n^m(\hat{\mathbf{s}})\, d\Omega_s, \tag{19a}$$

it is easy to show that the L2P coefficients:

$$\rho_n^m = \frac{1}{4\pi i^n} \int_{\Omega_0} \tilde{g}_i(\hat{\mathbf{s}}) Y_n^m(\hat{\mathbf{s}})\, d\Omega_s \tag{19b}$$

$$\text{where } \tilde{g}_i(\hat{\mathbf{s}}) \stackrel{\text{def}}{=} \int_{\text{supp}\, g_i} g_i(\vec{x}) e^{ik(\vec{x}-\vec{c})\cdot\hat{\mathbf{s}}}\, d\vec{x}, \tag{19c}$$

are defined by the signature function of the *testing function* g_i [2].

Hence, in a mixed-form broadband FMM that uses both diagonalized and (possibly scaled) multipole expansions, the user only has to provide the signature functions in equation (18) and equation (19c) for setting up the far field calculations in Helmholtz FMM. Furthermore, these functions are easy to define and easy to calculate.

IV. COMPUTATION OF THE DERIVATIVES OF THE FAR FIELD

We claimed in the introduction that it is possible to represent the derivatives of far fields as product of sparse matrices. In this section, we shall demonstrate this claim. The approach relies on the following observation for the Helmholtz equation (A similar argument can be made for the Laplace equation by setting $k = 0$ and replacing $\tilde{I}_n^m$ with I_n^m.)

Consider the potential field $\psi_j(\vec{x})$ due to sources in D_s having an approximation of the form in equation (11b):

$$\psi_j(\vec{x}) = \sum_{n=0}^{N} \sum_{m=-n}^{n} \beta_n^m \tilde{I}_n^m(\vec{x} - \vec{c}_r),\ \vec{x} \in D_r. \tag{20a}$$

Since:

$$\nabla^2 \frac{\partial \psi_j}{\partial u} + k^2 \frac{\partial \psi_j}{\partial u} = \frac{\partial}{\partial u}\left\{\nabla^2 \psi_j + k^2 \psi_j\right\} = 0,\ u = x, y, z, \tag{20b}$$

it follows that $\frac{\partial \psi_j}{\partial u}$ also must have an expansion of the form:

$$\frac{\partial \psi_j(\vec{x})}{\partial u} = \sum_{n=0}^{N'} \sum_{m=-n}^{n} \delta_n^m \tilde{I}_n^m(\vec{x} - \vec{c}_r),\ \vec{x} \in D_r, \tag{20c}$$

and that the coefficients $\{\beta_n^m\}$ and $\{\delta_n^m\}$ must be related through a linear operator T_u so that:

$$\psi_j \mapsto \frac{\partial \psi_j}{\partial u} \implies \{\beta_n^m\} \mapsto \{\delta_n^m\} = T_u(\{\beta_n^m\}).$$

[2] Compare with equation (18) for subtle differences.

Thus, for non-negative integers $p, q, r \geq 0$, an inductive reasoning shows that:

$$\psi_j \mapsto \frac{\partial^{p+q+r} \psi_j}{\partial x^p \partial y^q \partial z^r} \implies \{\beta_n^m\} \mapsto \{\delta_n^m\} = T_z^r T_y^q T_x^p(\{\beta_n^m\}).$$

Therefore:

$$\int_{\text{supp}\, g_i} g_i(\vec{x}) \frac{\partial^{p+q+r} \psi_j}{\partial x^p \partial y^q \partial z^r}\, d\vec{x}$$

$$= \sum_{n=0}^{N'} \sum_{m=-n}^{n} \delta_n^m \cdot \int_{\text{supp}\, g_i} g_i(\vec{x}) \tilde{I}_n^m(\vec{x} - \vec{c}_r)\, d\vec{x} \tag{21a}$$

$$= \sum_{n=0}^{N'} \sum_{m=-n}^{n} \delta_n^m \rho_n^m, \tag{21b}$$

where ρ_n^m are the same receiving coefficients defined in equation (11d). Thus, we see that partial derivatives of arbitrary order manifest as product of linear operators that can be applied to the local expansion coefficients β_n^m transparent to the application/user.

So far, we have not said anything about the nature of T_u. In the next three sections, we shall demonstrate that the finite dimensional representation of T_u is a sparse matrix for the Laplace and low frequency Helmholtz FMM that use explicit multipole expansions and a diagonal matrix for the high frequency Helmholtz FMM that uses signature functions.

A. Derivatives for the Laplace kernel

Let $\vec{x} = (r, \theta, \phi) \in \mathbb{R}^3$. We begin with the integral representation of the inner function $I_n^m(\vec{x})$ derived in [10, equation 2.33]:

$$I_n^m(\vec{x}) = \frac{(-1)^{n+m}}{n!} \frac{1}{2\pi} \cdot \int_{-\pi}^{\pi} (z + ix\cos\alpha + iy\sin\alpha)^n e^{im\alpha}\, d\alpha. \tag{22}$$

Without the loss of generality, consider the case of $\frac{\partial I_n^m(\vec{x})}{\partial x}$. From Appendix A, we have:

$$\frac{\partial I_n^m(\vec{x})}{\partial x} = \frac{i}{2}\left(I_{n-1}^{m+1}(\vec{x}) + I_{n-1}^{m-1}(\vec{x})\right). \tag{23}$$

Substituting equation (23) into equation (20a), we get:

$$\frac{\partial \psi_j(\vec{x})}{\partial x} = \sum_{n=0}^{N} \sum_{m=-n}^{n} \beta_n^m \frac{\partial I_n^m(\vec{x} - \vec{c}_r)}{\partial x}$$

$$= \sum_{n=0}^{N} \sum_{m=-n}^{n} \beta_n^m \cdot \frac{i}{2}\left(I_{n-1}^{m+1}(\vec{x} - \vec{c}_r) + I_{n-1}^{m-1}(\vec{x} - \vec{c}_r)\right). \tag{24a}$$

Since $I_n^m = 0$ if $n < 0$ or $|m| > n$, the above equation can be rewritten as:

$$\frac{\partial \psi(\vec{x})}{\partial x} = \sum_{n=0}^{N-1} \sum_{m=-n}^{n} \frac{i}{2}(\beta_{n+1}^{m-1} + \beta_{n+1}^{m+1}) I_n^m(\vec{x} - \vec{c}_r). \tag{24b}$$

Identifying:

$$\delta_n^m = \frac{i}{2}(\beta_{n+1}^{m-1} + \beta_{n+1}^{m+1}),$$

and $N' = N - 1$ in equation (20c), we see that the matrix representation of T_x has *at most two non-zero entries per row*. It is clear from Appendix A that a similar reasoning can be made for T_y and T_z as well.

B. Derivatives for the Helmholtz kernel with multipoles

Without the loss of generality, we consider the partial derivative with respect to x. Then, it can be shown that $\frac{\partial \tilde{I}_n^m}{\partial x}$ can be expressed as a four-term recurrence of the form (see Appendix B for the derivation and for the explicit expressions):

$$\frac{\partial \tilde{I}_n^m(\vec{x})}{\partial x} = \sum_{\substack{\nu=|n-1| \\ \nu \neq n}}^{n+1} \sum_{p=-1,1} T_\nu^{m+p} \tilde{I}_\nu^{m+p}(\vec{x}). \tag{25a}$$

A reasoning similar to that made in the previous section shows that each row of the matrix representation of T_x has at most four entries, once again showing that the derivative can be represented as a sparse matrix. Furthermore, a closer look at equation (25a) shows that if equation (20a) has degree N, then equation (20c) will have degree $N' = N + 1$. However, if the degree of the "L2P" coefficients ρ_n^m is truncated to N, then the summation in equation (21b) will be truncated to degree N and we can set $N' = N$.

C. Derivatives for the Helmholtz kernel in diagonalized form

A potential field $\psi_j(\vec{x})$ having an approximation of the form in (20a), can also be represented as [2, 10]:

$$\psi_j(\vec{x}) = \frac{i}{4\pi} \int_{\Omega_0} \tilde{\psi}_j(\hat{\mathbf{s}}) \cdot e^{ik(\vec{x}-\vec{c}_r)\cdot\hat{\mathbf{s}}}\, d\Omega_s, \tag{26a}$$

$$\text{where } \tilde{\psi}_j(\hat{\mathbf{s}}) \stackrel{\text{def}}{=} \sum_{n=0}^{N} \sum_{m=-n}^{m} \beta_n^m \frac{Y_n^m(\hat{\mathbf{s}})}{i^{n+1}}, \tag{26b}$$

so that:

$$\begin{aligned} P_{ij} &= \int_{\text{supp}\, g_i} g_i(\vec{x})\, \psi_j(\vec{x})\, d\vec{x} \\ &= \frac{i}{4\pi} \int_{\Omega_0} \tilde{g}_i(\hat{\mathbf{s}}) \cdot \tilde{\psi}_j(\hat{\mathbf{s}})\, d\Omega_s, \end{aligned} \tag{26c}$$

$$\text{where } \tilde{g}_i(\hat{\mathbf{s}}) = \int_{\text{supp}\, g_i} g_i(\vec{x}) e^{ik(\vec{x}-\vec{c}_r)\cdot\hat{\mathbf{s}}}\, d\vec{x}, \tag{26d}$$

and we recognize $\tilde{g}_i(\hat{\mathbf{s}})$ as the signature function defined in equation (19c). Since:

$$\frac{\partial \psi_j(\vec{x})}{\partial x} = \frac{i}{4\pi} \int_{\Omega_0} (iks_x) \cdot \tilde{\psi}_j(\hat{\mathbf{s}}) \cdot e^{ik(\vec{x}-\vec{c}_r)\cdot\hat{\mathbf{s}}}\, d\Omega_s, \tag{26e}$$

from equation (26a), it follows that:

$$\begin{aligned} &\int_{\text{supp}\, g_i} g_i(\vec{x})\, \frac{\partial \psi_j(\vec{x})}{\partial x}\, d\vec{x} \\ &\quad = \frac{i}{4\pi} \int_{\Omega_0} \tilde{g}_i(\hat{\mathbf{s}}) \cdot (iks_x) \cdot \tilde{\psi}_j(\hat{\mathbf{s}})\, d\Omega_s, \end{aligned} \tag{26f}$$

demonstrating that the partial differential operator appears as a *diagonal* modification to the incoming signature function $\tilde{\psi}_j(\hat{\mathbf{s}})$.

Note that this result has been known from the very early days of FMM and has been effectively used for computing with derivatives [17]. The novelty in our approach is that we are using it to transfer the *responsibility of computing the derivative* to the library instead of requiring the application do it.

V. A PSEUDO-EXAMPLE FOR A LIBRARY INTERFACE

We now discuss how the results from sections III and IV can be used to develop an application independent library of Laplace and Helmholtz FMM. Our objective is not to describe a concrete implementation, but to discuss the essential functionality.

To that end, we divide the library functionality into two parts: the matrix build/initialization functions and matrix apply ("matrix-vector" product) functions. During the initialization, we expect the user to provide what are called "call-back" functions. The library, in turn, repeatedly calls these functions to get the information needed to complete matrix initialization. After the matrix is built, the library provides the functionality to evaluate matrix-vector products, potentially involving different combinations of derivatives.

A. Matrix initialization

Building the matrix consists of three phases:

- The tree construction phase
- The evaluation of the near interactions
- The evaluation of the far field representations ("Q2M" and "L2P" coefficients).

A.1. Constructing the tree

Rationale:

In general, each source/receiver can be assigned a "center" and a spatial extent. The former can be captured as a array of three floating point numbers. Given that the mesh used in the discretization can be extremely non-uniform in practical cases, it is often necessary to take the spatial extent into account to ensure sufficient accuracy. This can lead to non-uniform trees with internal nodes also "hosting" sources and/or receivers. The following listing shows an example of an interface.

```
1 function get_center(particle_index, center[])↩
      ;
2 function get_bounding_box(particle_index, ↩
      xyzMin[], xyzMax[]);
```

A.2. Computing near interactions with multiple matrices

Rationale:

With the ability to compute arbitrary derivatives of the far field, it becomes necessary to handle multiple

matrices as well. As a simple example, consider the following summations:

$$f(\vec{x}_i) = \sum_{j=1}^{N} a_j G(\vec{x}_i, \vec{x}_j), \tag{27a}$$

$$\vec{F}(\vec{x}_i) = \sum_{j=1}^{N} a_j \nabla G(\vec{x}_i, \vec{x}_j). \tag{27b}$$

Although potential and the derivatives of the far field can be computed from a single FMM representation, the four components of the near matrix must be stored simultaneously. In other words, the library needs to allow for the possibility of multiple matrix entries resulting from each pair-wise interaction. If we assume that every pair-wise near interaction results in the same number of matrix entries (although there are exceptions, this usually the case), the following interface would be adequate for most purposes.

```
function get_matrix_element(receiver_index, ↩
    source_index, elements[]);
```

In the above example, `dim(elements)=4` and a user can return the Green's function and its gradient as:

$$\texttt{elements} = \left[G, \frac{\partial G}{\partial x}, \frac{\partial G}{\partial y}, \frac{\partial G}{\partial z}\right].$$

A.3. Computing Q2M and L2P coefficients

Rationale:

In section III, we have shown that the required Q2M and L2P coefficients can be evaluated from sampled potential values or signature functions. For the Laplace equation, this can be implemented in the following way. Given a node with sources (or receivers) in it, we can construct a sphere with center, $\vec{c}_s$ at the center of the box and a sufficiently large radius, $R >> d$ where d is the box length, and introduce a Gauss-Trapezoidal rule as discussed in section A. Then, a function of the following nature can be invoked repeatedly to evaluate the potential, as defined by equation (10a) at each integration point $\vec{x}_k = \vec{c}_s + R\hat{\mathbf{s}}_k$ in equation (13).

```
function P(xk) = get_potential(particle_index↩
    , xk[]);
```

For the Helmholtz equation, we expect the user to return the signature function, defined by equation (18).

```
function F(sk) = get_signature(particle_index↩
    , cs[], sk[]);
```

Note that in this case, we need both the center of the box $\vec{c}_s$ and the direction vector $\hat{\mathbf{s}}_k$ passed to the application.

B. Evaluating matrix-vector products

In order to offer maximum flexibility, we split the evaluation of the matrix-vector products (MVP) into three steps:

- `multipole_pass`: performs all the source-to-multipole (Q2M), outer-to-outer (M2M, aggregation), outer-to-inner (M2L) and inner-to-inner (L2L) translations in the standard FMM flow. This is a pre-requisite for calling the far field evaluation step below.
- `far_axpy`: evaluates (the integral of) the potential (or its derivative) for every testing function using the results in Section IV.
- `near_axpy`: evaluates the contribution due the near interaction matrix selected by the user (if there are multiple matrices involved).

The library can offer a functionality similar to the following one to accomplish these tasks:

```
/* takes the input vector X and performs M2M,↩
    M2L and L2L passes of FMM
 * Must be called before calling far_axpy.
 */
function multipole_pass(input_x);

/* near_matrix_index lets the user select the↩
    correct near matrix */
function near_axpy(near_matrix_index, input_x↩
    ,output_y);

/* the input array deriv tells the library to↩
    apply the desired derivatives
 * to the far field coefficients before ↩
    evaluating the potential */
function far_axpy(deriv[], output_y);
```

where the array `deriv` specifies the orders of the partial derivatives. For example:

$$\texttt{deriv}[1,2,2] \implies \frac{\partial^2}{\partial z^2}\frac{\partial^2}{\partial y^2}\frac{\partial}{\partial x}.$$

The motivation for this is best illustrated by an example. Towards this, consider the evaluation of the two sums in equation (27). A psuedo-code is given below.

```
/* Let X denote the input vector and P, dPx, ↩
    dPy and dPz, respectively denote the ↩
    potential and
 * the three components of the gradient
 */

  /* do M2M, M2L and L2L */
  multipole_pass(X);

  /* compute P = A * X for potential; matrix ↩
      index 0 ==> Green's function */
  near_axpy(0,X,P);
```

```
deriv = [0,0,0]; /* no partial derivatives */
far_axpy(deriv,P);

/* compute dPx = dAx * X for partial derivative with respect to x */
near_axpy(1, X,dPx);  /* matrix index 1 ==> partial derivative with respect to x */
deriv = [1, 0, 0];    /* partial derivative with respect to x */
far_axpy(deriv,dPx);
```

Computation of the partial derivatives with respect y and z can be done analogously. Note that the `multipole_pass` is usually the most dominant part during a matrix-vector evaluation and it is invoked only once.

VI. SUMMARY AND CONCLUSIONS

In this paper, we have proposed an approach to developing a stand-alone, application independent library of Laplace and Helmholtz FMM. Towards this end, we have demonstrated a technique to capture the essential characteristics of the problem needed for setting up the FMM – the basis and testing functions, mesh etc. – using samples of either potentials or the signature functions of a *canonical problem*. Furthermore, we have shown that it is possible to transfer the responsibility of computing the partial derivatives of the far field to the library, instead of burdening the user to implement complicated integrals. This is accomplished by representing partial derivatives of arbitrary orders as product of certain sparse matrices. We have also outlined a pseudo interface that illustrates how the methods can be used.

Within Ansys Inc., we have developed a flexible library, called `Q3Dfastmvpack` incorporating these ideas and it is currently being used by multiple Ansys products.

ACKNOWLEDGEMENTS

I would like to thank my colleagues Andy Mathis, Dalian Zheng, Eric Bracken and Indranil Chowdhury for the many discussions. I would also like to thank Werner Thiel for supporting this work.

APPENDICES

A. Partial derivatives of I_n^m

Let $h(\alpha;\vec{x}) = (z + ix\cos\alpha + iy\sin\alpha)$ in equation (22). Consider:

$$\begin{aligned}
\frac{\partial I_n^m(\vec{x})}{\partial x} &= \frac{(-1)^{n+m}}{(n-1)!}\frac{i}{2\pi}\int_{-\pi}^{\pi} h(\alpha;\vec{x})^{n-1}e^{im\alpha}\cos\alpha\, d\alpha \\
&= \frac{(-1)^{n+m}}{(n-1)!}\frac{i}{2\pi}\int_{-\pi}^{\pi} h(\alpha;\vec{x})^{n-1}e^{im\alpha}\frac{e^{i\alpha}+e^{-i\alpha}}{2}\, d\alpha \\
&= \frac{i}{2}\frac{(-1)^{n+m}}{(n-1)!}\frac{1}{2\pi}\left\{\int_{-\pi}^{\pi} h(\alpha;\vec{x})^{n-1}e^{i(m+1)\alpha}\, d\alpha\right. \\
&\left. + \int_{-\pi}^{\pi} h(\alpha;\vec{x})^{n-1}e^{i(m-1)\alpha}\, d\alpha\right\} \\
&= \frac{i}{2}\frac{(-1)^{n+m}}{(n-1)!}\frac{1}{2\pi}\int_{-\pi}^{\pi} h(\alpha;\vec{x})^{n-1}e^{i(m+1)\alpha}\, d\alpha \\
&\quad + \frac{i}{2}\frac{(-1)^{n+m}}{(n-1)!}\frac{1}{2\pi}\int_{-\pi}^{\pi} h(\alpha;\vec{x})^{n-1}e^{i(m-1)\alpha}\, d\alpha \\
&= \frac{i}{2}\left(I_{n-1}^{m+1}(\vec{x}) + I_{n-1}^{m-1}(\vec{x})\right),
\end{aligned}$$

where we have used the facts $n-1+m-1 = n+m$ and that $(-1)^{n+m-2} = (-1)^{n+m}$. The following results can be similarly derived:

$$\begin{aligned}
\frac{\partial I_n^m(\vec{x})}{\partial y} &= \frac{1}{2}\left(I_{n-1}^{m+1}(\vec{x}) - I_{n-1}^{m-1}(\vec{x})\right), \\
\frac{\partial I_n^m(\vec{x})}{\partial z} &= -I_{n-1}^{m}(\vec{x}).
\end{aligned}$$

B. Partial derivatives of $\tilde{I}_n^m(\vec{x})$

We have, from equation (19a):

$$\begin{aligned}
&\frac{\partial^{p+q+r}}{\partial x^p \partial y^q \partial z^r} I_n^m(\vec{x}) \\
&= \frac{(ik)^{p+q+r}}{4\pi i^n}\int_{\Omega_0} s_x^p s_y^q s_z^r e^{ik\vec{x}\cdot\hat{\mathbf{s}}} Y_n^m(\hat{\mathbf{s}})\, d\Omega_s, \qquad (28)
\end{aligned}$$

where $\hat{\mathbf{s}} = (s_x, s_y, s_z) = (\sin\theta\cos\phi, \sin\theta\sin\phi, \cos\theta)$. Noting that:

$$\sin\theta e^{i\phi} = (-)\sqrt{\frac{8\pi}{3}}Y_1^1(\hat{\mathbf{s}}), \qquad (29)$$

from the definition of spherical harmonics $Y_n^m(\theta,\phi)$ in equation (5b), and using equation (5c), we get:

$$\sin\theta\cos\phi = (-)\sqrt{\frac{2\pi}{3}}\left[Y_1^1(\hat{\mathbf{s}}) - Y_1^{-1}(\hat{\mathbf{s}})\right] \qquad (30a)$$

$$\sin\theta\sin\phi = i\sqrt{\frac{2\pi}{3}}\left[Y_1^1(\hat{\mathbf{s}}) + Y_1^{-1}(\hat{\mathbf{s}})\right] \qquad (30b)$$

$$\cos\theta = \sqrt{\frac{4\pi}{3}}Y_1^0(\hat{\mathbf{s}}). \qquad (30c)$$

Let:

$$\mathcal{V}_p(\vec{x}) = \frac{1}{4\pi i^n}\int_{\Omega_0} Y_1^p(\hat{\mathbf{s}})e^{ik\vec{x}\cdot\hat{\mathbf{s}}}Y_n^m(\hat{\mathbf{s}})\, d\Omega_s, p = -1, 0, 1. \qquad (31)$$

Then, substituting equation (30) into equation (28) and using equation (31), we get:

$$\frac{\partial I_n^m(\vec{x})}{\partial x} = (-)ik\sqrt{\frac{2\pi}{3}}\left(\mathcal{V}_1(\vec{x}) - \mathcal{V}_{-1}(\vec{x})\right) \qquad (32a)$$

$$\frac{\partial I_n^m(\vec{x})}{\partial y} = (-)k\sqrt{\frac{2\pi}{3}}\left(\mathcal{V}_1(\vec{x}) + \mathcal{V}_{-1}(\vec{x})\right) \qquad (32b)$$

$$\frac{\partial I_n^m(\vec{x})}{\partial z} = ik\sqrt{\frac{4\pi}{3}}\mathcal{V}_0(\vec{x}). \qquad (32c)$$

Now, substituting the following well known addition theorem [9, 10]:

$$e^{ik\vec{x}\cdot\hat{\mathbf{s}}} = \sum_{n'=0}^{\infty}\sum_{m'=-n'}^{n'} 4\pi i^{n'} j_{n'}(kx) Y_{n'}^{m'*}(\hat{\mathbf{x}}) Y_{n'}^{m'}(\hat{\mathbf{s}}),$$

into equation (31), we can express:

$$\mathcal{V}_p(\vec{x}) = \frac{1}{4\pi i^n}\sum_{\nu=0}^{\infty}\sum_{\mu=-\nu}^{\nu} 4\pi i^{\nu}(-1)^{\mu} j_{\nu}(k\|\vec{x}\|) Y_{\nu}^{-\mu}(\hat{\mathbf{x}})\cdot$$

$$\int_{\Omega_0} Y_1^p(\hat{\mathbf{s}}) Y_{\nu}^{\mu}(\hat{\mathbf{s}}) Y_n(\hat{\mathbf{s}})\, d\Omega_s \tag{33a}$$

$$= \sum_{\nu=0}^{\infty}\sum_{\mu=-\nu}^{\nu} i^{\nu-n}(-1)^{\mu} j_{\nu}(k\|\vec{x}\|) Y_{\nu}^{-\mu}(\hat{\mathbf{x}})\gamma\begin{pmatrix}\nu & 1 & n\\ \mu & p & m\end{pmatrix}, \tag{33b}$$

where γ is the Gaunt coefficient defined as

$$\gamma\begin{pmatrix}n_1 & n_2 & n_3\\ m_1 & m_2 & m_3\end{pmatrix} \stackrel{\text{def}}{=} \int_{\Omega_0} Y_{n_1}^{m_1}(\hat{\mathbf{s}}) Y_{n_2}^{m_2}(\hat{\mathbf{s}}) Y_{n_3}^{m_3}(\hat{\mathbf{s}})\, d\Omega_s, \tag{33c}$$

for integers $n_i \geq 0$ and $-n_i \leq m_i \leq n_i$ for $i = 1,2,3$. Using the properties of Gaunt coefficients [9], for $\gamma \neq 0$, we have to have $|n-1| \leq \nu \leq n+1$, $\nu+n+1$ even and $\mu + m + p = 0$. Thus, $\nu = |n-1|$ and $\nu = n+1$ and therefore:

$$\mathcal{V}_p(\vec{x}) = \sum_{\substack{\nu=|n-1|\\ \nu\neq n}}^{n+1} i^{\nu-n}(-1)^{m+p} j_{\nu}(k\|\vec{x}\|) Y_{\nu}^{m+p}(\hat{\mathbf{x}})$$

$$\gamma\begin{pmatrix}\nu & 1 & n\\ -(m+p) & p & m\end{pmatrix} \tag{33d}$$

$$= (-1)^{m+p}\sum_{\substack{\nu=|n-1|\\ \nu\neq n}}^{n+1} i^{\nu-n}\cdot$$

$$\gamma\begin{pmatrix}\nu & 1 & n\\ -(m+p) & p & m\end{pmatrix} I_{\nu}^{m+p}(\vec{x}), \tag{33e}$$

showing that the right hand sides of equations (32a)-(32c) have at most four non-zero terms.

REFERENCES

[1] L. Greengard, "The rapid evaluation of potential fields in particle systems," Ph.D. thesis, Yale University, 1987.

[2] V. Rokhlin, "Diagonal forms of translation operators for the Helmholtz equation in three dimensions," *Applied and Comp. Harmonic Analysis*, vol. 1, pp. 82-93, 1993.

[3] W. C. Chew, J.-M. Jin, E. Michielssen, and J. M. Song, *Fast and Efficient Algorithms in Computational Electromagnetics*, chap. 9, Boston: Artech House, 2001.

[4] V. Rokhlin, "Rapid solution of integral equations of classical potential theory," *Journal Of Computational Physics*, vol. 60, pp. 187-207, 1985.

[5] J. Carrier, L. Greengard, and V. Rokhlin, "A fast adaptive multipole algorithm for particle simulations," *SIAM Journal on Scientific and Statistical Computing*, vol. 9, no. 4, pp. 669-686, July 1988.

[6] V. Rokhlin, "Rapid solution of integral equations of scattering theory in two dimensions," *Journal Of Computational Physics*, vol. 86, pp. 414-439, 1990.

[7] W.-J. He, X.-W. Huang, M.-L. Yang, and X.-Q. Sheng, "Massively parallel multilevel fast multipole algorithm for extremely large-scale electromagnetic simulations: A review," *Progress In Electromagnetics Research*, vol. 173, pp. 37-52, 2022.

[8] F. W. J. Olver, D. W. Lozier, R. F. Boisvert, and C. W. Clark, *NIST Handbook of Mathematical Functions*, Cambridge: Cambridge University Press, Cambridge, 2010.

[9] A. Messiah, *Quantum Mechanics*, New York: Dover Publications, Inc., 2014.

[10] M. A. Epton and B. Dembart, "Multipole translation theory for the three dimensional Laplace and Helmholtz equations," *SIAM J. of Scientific Computing*, vol. 16, no. 4, pp. 865-897, July 1995.

[11] C. R. Anderson, "An implementation of the fast multipole method without multipoles," *SIAM Journal of Scientific and Statistical Computing*, vol. 13, no. 4, pp. 923-947, July 1992.

[12] T. Eibert, "A diagonalized multilevel fast multipole method with spherical harmonics expansion of the k-space Integrals," *IEEE Transactions on Antennas and Propagation*, vol. 53, no. 2, pp. 814-817, Feb. 2005.

[13] B. Dembart and E. Yip, "A 3D Fast multipole method for electromagnetics with multiple levels," *11th Annual Review of Progress in Applied Computational Electromagnetics, Monterey, CA*, vol. 1, pp. 621-628, Mar. 1995.

[14] J. Phillips and J. White, "A precorrected-FFT method for electrostatic analysis of complicated 3-D structures," *IEEE Transactions on Computer-Aided Design of Integrated Circuits and Systems*, vol. 16, no. 10, pp. 1059-1072, 1997.

[15] J.-S. Zhao and W. C. Chew, "Integral equation solution of Maxwell's equations from zero frequency to microwave frequencies," *IEEE Transactions on Antennas and Propagation*, vol. 48, no. 10, pp. 1635-1645, Oct. 2000.

[16] B. Dembart and E. Yip, "The accuracy of fast multipole methods for Maxwell's equations," *IEEE Computational Science and Engineering*, vol. 5, no. 3, pp. 48-56, 1998.

[17] J. M. Song and W. C. Chew, "Multilevel fast multipole algorithm for solving combined field integral equations of electromagnetic scattering," *Micro. Opt. Tech. Lett.*, vol. 10, no. 1, pp. 14-19, Sep. 1995.

Sanjay Velamparambil I obtained a Ph.D. in Engineering from the Indian Institute of Science, Bangalore, in 1997. My doctoral work was in the then nascent field of fast multipole methods (FMM). Subsequently, working with Dr. Weng Chew at the University of Illinois at Urbana-Champaign, I pioneered the parallelization of Helmholtz FMM on distributed memory computers.

I was with Ansoft Corporation (currently Ansys Inc.) from 2002-2005 working on fast integral equation methods for signal integrity applications. In 2007, I joined Acceleware Corporation, Calgary, and worked on linear algebraic algorithms for GPU computing. In 2010, I joined Apache Design Solutions, which was later acquired by Ansys. I have been working on fast integral equation methods for several Ansys products such as Ansys Q3D Extractor® and SIwave™ since 2010.

I enjoy long bicycle rides, especially mountainous routes, running, and generally love the outdoors. I am married and we are fortunate enough to live in the foothills of the majestic Rocky Mountains in Northern Colorado.

Development and Simulation of 26 GHz Beamforming Systems and Antenna Array 5G Network Base Stations

Abd Al Menam A. Alazzawi, Mohamad Kamal A. Rahim, and Osman Ayop

Advanced RF & Microwave Research Group (ARFMRG)
Faculty of Electrical Engineering, University Technology Malaysia (UTM), 81310 UTMJB Johor, Malaysia
abdalmenamahmed6@gmail.com, mdkamal@utm.my, osmanayop@utm.my

Abstract – This paper focuses on designing a new structure of beamforming networks with an array antenna to control the beams. The 3×4 array antenna structure connects to the 3×3 Rotman lens beamformers to achieve this goal. The middle time delay line is around 14 mm. The design allows the *x*-axis to cover +25, 0, −25 degrees. Therefore, this work targets fifth generation (5G) application, which necessitates coverage in all directions by other base stations or users. Computer Simulation Technology (CST) microwave software facilitates the simulation process. The design begins with a single microstrip patch antenna, designed to function as an array antenna resonating at 26 GHz. The half-lambda separation (λ/2) among antennas gives 13.8 dBi gain with S11< −10 dB. The final structure for beamforming networks has a gain of 14 dBi. This work uses the Roger 5880 substrate, which has a dielectric constant of 2.2, a loss tangent of 0.0009, and a thickness of 0.127 mm.

Index Terms – array antenna, CST studio, mm-wave, Rotman lens, series feed antenna.

I. INTRODUCTION

The introduction of fifth generation (5G) wireless communication technology marks a significant advancement in mobile wireless communication systems [1]. Positioned as a notable improvement over previous generations, 5G aims to enhance data transmission rates, reduce latency, and increase the capacity for interconnected devices. Engineered to support various applications such as virtual reality, autonomous vehicles, smart cities, and the Internet of Things (IoT), 5G technology integrates high-frequency radio waves, advanced antenna technologies, and network virtualization [2, 3]. An important challenge faced by array antennas equipped with beamforming circuits relates to coverage direction, particularly in addressing blind angles and optimizing beamforming for wider radiation. In response, series-feed array antennas offer a flexible solution by allowing the adjustment of beam patterns through modulation of signal phase and amplitude, often with the assistance of a beamformer. Furthermore, integrating a Rotman lens (an effective microwave lens capable of directing electromagnetic waves) can improve the performance of series-fed array antennas [4]. The effectiveness of Rotman lens design relies on careful consideration of factors such as frequency range, lens geometry, material composition, and relevant parameters. When combined with a series-fed array antenna, the Rotman lens is typically positioned at the array's focal point to concentrate electromagnetic waves emitted by array elements, thereby enhancing antenna system gain and directivity [5]. Series-fed array antennas with Rotman lenses find applications in various fields, including 5G wireless communication, radar systems, and remote sensing, especially in scenarios requiring precise energy transmission or reception [6, 7].

This paper delves into the design of series-fed array antennas integrated with Rotman lenses, specifically resonating at 26 GHz, for application in fifth-generation wireless communication networks. The primary objective is to address unseen and blind angles within the coverage area. Computer Simulation Technology (CST) software is employed for simulation and prototype design purposes. The substrate material selected for this simulation is Rogers 5880, featuring a thickness of 0.127 mm.

II. PROPOSED ROTMAN LENS DESIGN

Rotman lenses play a pivotal role in microwave engineering, facilitating precise manipulation of electromagnetic waves through focusing and beam steering mechanisms [8]. Researchers extensively utilize a sophisticated set of equations to ascertain crucial aspects of the lens, including its geometry, dimensions, material composition, and thickness [9, 10]. These calculations are indispensable for attaining the desired performance parameters necessary for optimal functionality and efficiency in various applications [11, 12]. Figure 1 illustrates how the link technique demonstrates the connections between different components in the system, offering insightful information on the internal mechanisms of Rotman lens-integrated setups [13, 14].

The design process of the printed Rotman lens began by establishing the dimensions of the transmission line,

Submitted On: May 2, 2024
Accepted On: June 13, 2024

https://doi.org/10.13052/2024.ACES.J.390505

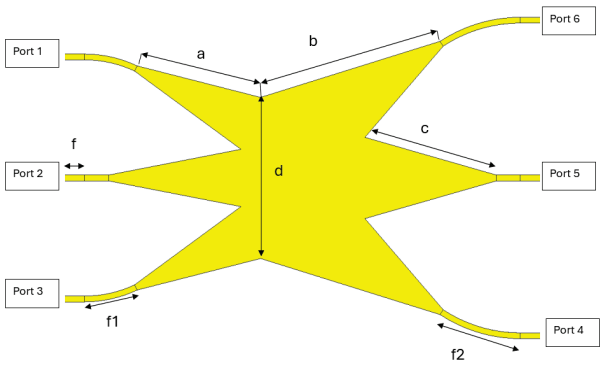

(a)

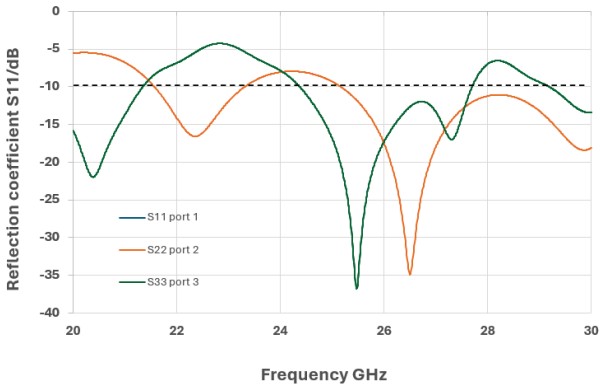

(b)

Fig. 1. (a) Structure of a 3×3 Rotman lens and (b) reflection coefficient for the Rotman lens's input ports.

denoted as Wr (transmission line width) and Lr (transmission line length):

$$Wr = \frac{(c*2*f)}{\sqrt{\varepsilon r} - (\sin 2\theta\ )}, \tag{1}$$

$$Lr = \frac{(c*2*f)}{(2*\sqrt{\varepsilon r} - \sin 2\theta\ )}, \tag{2}$$

$$d = L*\sqrt{n} - 1). \tag{3}$$

Equation (3) determines the position of the feed network by calculating the distance between it and the first transmission line. This calculation involves considering the width (Wr) and length (Lr) of the transmission line, the speed of light (c), the operating frequency (f), the relative permittivity of the substrate (εr), and the beam scanning angle (θ):

$$S = Wr*\tan\left(\frac{\theta}{2}\right). \tag{4}$$

The position of the radiating elements is determined using equation (4), where S represents the element spacing, Wr is the width of the transmission line, and θ denotes the beam scanning angle. This equation plays a crucial role in establishing the precise placement of the radiating elements in the system, ensuring optimal performance and functionality:

$$x = (n-1)*S*\sin(\theta)\ . \tag{5}$$

The position of the i-th radiating element, denoted by x, in an array of n transmission lines with an element spacing of S is crucial in determining the beam scanning angle, represented by θ as shown in equation (5). The relationship between these parameters is fundamental to the design and analysis of antenna arrays for various applications in wireless communication and radar systems [15, 16]. The precise calculation and adjustment of these values in Table 1 are essential to achieving the antenna array's desired radiation pattern and beam steering capabilities.

Table 1: Dimension of Rotman lens design structure (all dimensions are in mm)

Dimensions	Value (mm)
a	8.67
b	12.78
c	9.30
d	10.94
f	1.63
f1	3.66
f2	5.70

III. SERIES FEED ARRAY ANTENNA DESIGN AT 26 GHz

A. Microstrip patch antenna

A pre-established formula is implemented during the fabrication process of microstrip antennas. Equations (6–10) provide a representation of the antenna's equation:

$$wp = \frac{c}{2fo\sqrt[2]{\frac{(\varepsilon r+1)}{2}}}, \tag{6}$$

$$Leff = \frac{c}{2fo\sqrt[2]{\varepsilon reff}}, \tag{7}$$

$$\varepsilon reff = \frac{\varepsilon r+1}{2} + \frac{\varepsilon r-1}{2}\left[1+12\frac{h}{wp}\right]^{-\frac{1}{2}}, \tag{8}$$

$$\Delta L = 0.412h\frac{(\varepsilon reff+0.3)\left(\frac{wp}{h}+0.264\right)}{(\varepsilon reff-0.258)\left(\frac{wp}{h}+0.8\right)}, \tag{9}$$

$$Lp = Leff - 2\Delta L. \tag{10}$$

Initially, equation (6) is employed to determine the width of the patch, denoted as Wp, predicated on key parameters such as the resonant frequency (fr), relative permittivity (εr), and substrate height (h). Subsequently, equation (8) is utilized to derive the effective permittivity, ε_{reff}, crucial for computing the length extension, ΔLp, attributed to fringing fields, contingent upon the condition $Wp/h>1$ as delineated in equation (9). Finally,

equation (10) facilitates the calculation of the patch length, *Lp*, completing the design process with meticulous precision.

B. Series feed array antenna

To successfully integrate a Rotman lens with a series-fed array antenna operating at 26 GHz, it is crucial to meticulously assess the antenna's frequency range and bandwidth, along with the configuration of the array consisting of four elements spaced at half a wavelength. The choice of elements in the array significantly influences the antenna's performance metrics such as gain, directivity, and bandwidth [17, 18].

Figure 2 and Table 2 provides insight into the (W_p *x* L_p) series feed structure and its corresponding equivalent circuit with 3.89 mm separation distance which is λ/2. It's printed over Roger 5880 substrate with 2.2 dielectric constant and 0.127 mm substrate thickness to radiate at 26 GHz.

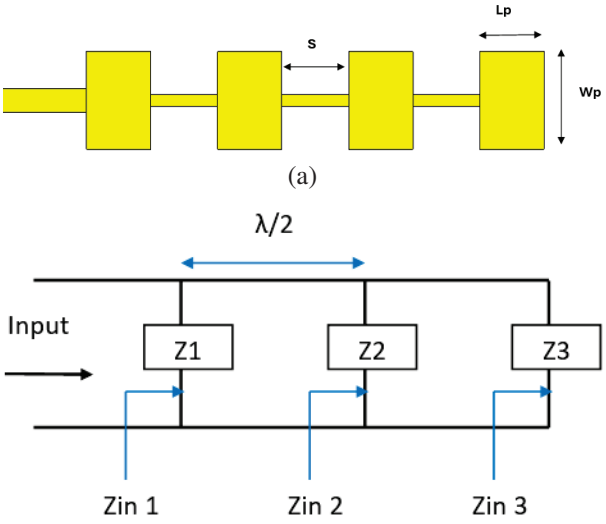

Fig. 2. Microstrip series feed patch antenna (a) 1×4 series feed antenna and (b) equivalent circuit of series feed antenna.

Employing a series feed array configuration yielded a substantial gain enhancement, elevating the gain from approximately 8.5 dBi to approximately 14 dBi.

Table 2: Microstrip series feed array antennas dimensions (all dimensions in mm)

Dimensions	Value (mm)	Explanation
Wp	4.80	Patch Width
Lp	3.65	Patch Length
S	3.89	Elements Spacing
h	0.127	Substrate Hight
εr	2.2	Epsilon

Additionally, fine-tuning of the bandwidth allocation facilitated the generation of a single beam transmitting at 26 GHz, thereby enhancing signal efficiency. These advancements are visually elucidated in the accompanying schematic in Fig. 3 (a,b).

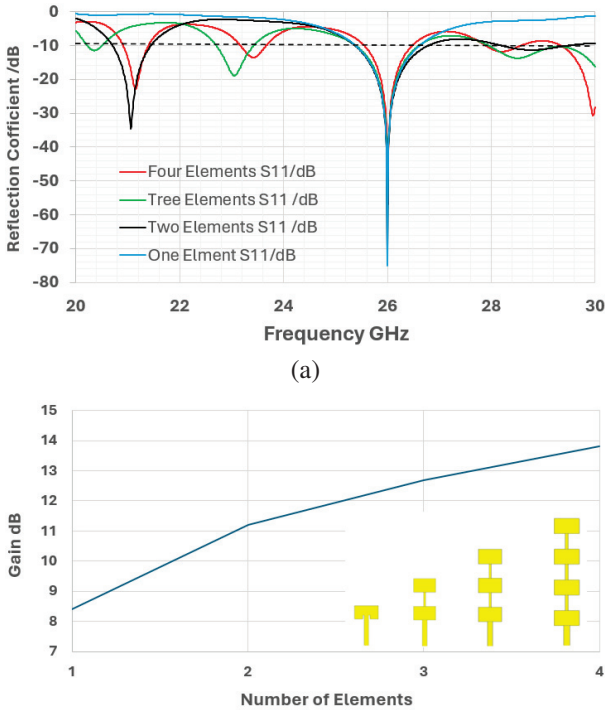

Fig. 3. (a) Reflection coefficient for single patch to four series feed antennas and (b) gain of single patch to four elements series feed antennas.

IV. RESULTS AND DISCUSSIONS

In the design process, the series feed antennas are fabricated using Roger 5880 material to ensure resonance at 26 GHz. In order to verify the accuracy of the antenna fabrication, the reflection coefficient and radiation pattern were measured, as shown in Fig. 4 (a, b).

The proposed structure is simulated using CST software, and the performance is monitored by the reflection coefficient (S11), gain, bandwidth, and radiation pattern. Figure 5 shows the integration of an array antenna with a Rotman lens over 80 by 31 mm using a 13-14 mm delay line to achieve a phase difference based on the True Time Delay (TDD) concept of the Rotman lens [19, 20]. Figure 6 shows the reflection coefficient S11 of the integrated final structure. From the analysis, the reflection coefficient is less than 15 dB. Synchronization between the array antennas and the beamforming network is achieved by a 3×3 Rotman lens set by resonating at the same frequency. The connected Rotman lens was

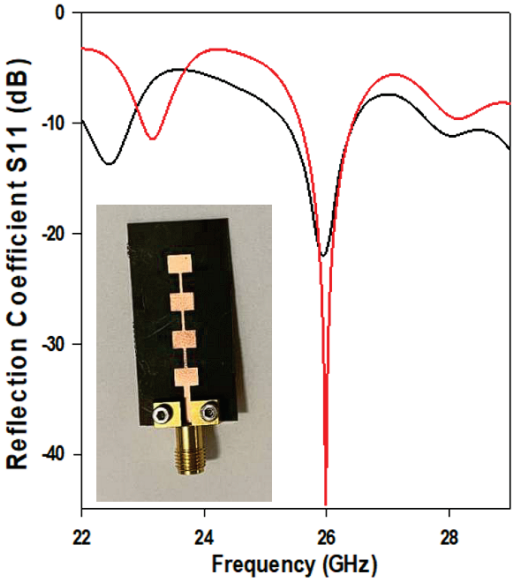

(a)

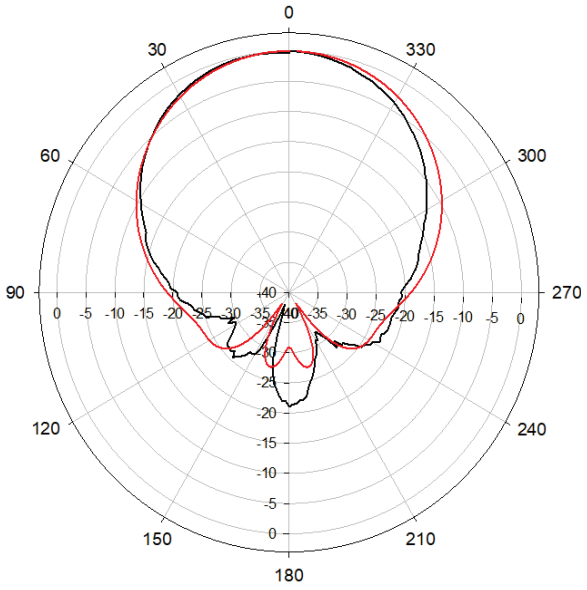

(b)

Fig. 4. (a) Fabricated series feed array antennas with reflection coefficient and (b) radiation pattern comparison (phi=0).

prepared to shift the phase at −25, 0, +25 degrees. The array antennas have connected single-layer 0.127 mm Rotman beamformers to allow the beam to cover blinded angles efficiently [21, 22].

The radiation pattern of the proposed final structure depicted in Fig. 7 is analyzed at 26 GHz with Phi=0 deg. The beam is observed to have a beam at −25, 0, and +25 degrees, with the gain of ports 1 to 3 around 14.2 dBi. The beams exhibit an angular width (3 dB) ranging from 20 to 30 degrees.

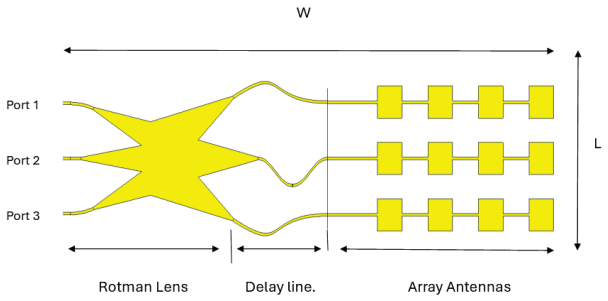

Fig. 5. Integrated structure of 3×3 Rotman lens and 3×4 array antennas.

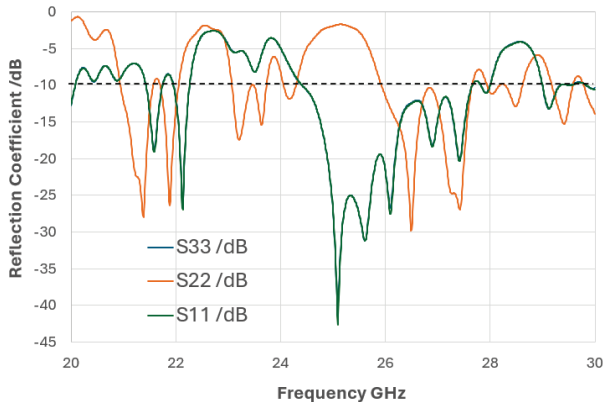

Fig. 6. Reflection coefficient S11 of integrated final structure of Rotman lens and array antennas.

The results presented in Table 3 exhibit a strong alignment with prominent references in the field, showcasing the efficiency of this particular structure in identifying broad blinded angles that were previously unaddressed by alternative designs. Notably, the comparison highlights the remarkable capability of this configuration to attain 0 and ±25 degrees utilizing merely three input ports. This significant breakthrough accentuates

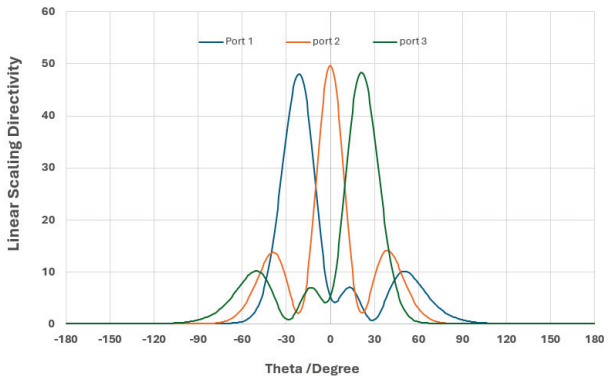

(a)

Fig. 7. (*Continued.*)

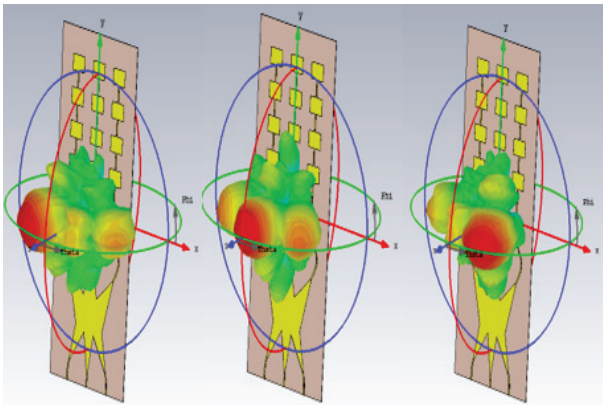

(b)

Fig. 7. Radiation pattern of final structure (a) directivity using Cartesian coordinate and (b) 3D radiation pattern.

the considerable potential for further advancements and the implementation of optimizations tailored to specific applications.

Table 3: Performance of final structure in comparison with other references

Variables	This Work	Ref (11)	Ref (13)	Ref (16)
Frequency GHz	26	6-18	60	10-14
Return Loss dB	20	16	12	25
Gain dB (Max)	14.2	-	-	11.37
Beam angle (deg)	0±25	0±28	0±25	0±16
Subs thickness (mm)	0.127	-	0.127	0.0027
No. of input ports	3	8	5	11

V. CONCLUSION

The microstrip series feed patch antenna is operated at 26 GHz with a separation of half lambda. A single-series-fed patch antenna is enhanced into a 3×4 array antenna configuration. To widen the coverage angle and improve sensitivity, 3×3 Rotman lenses were designed. A beamforming network circuit was meticulously devised to match the array of antenna ports, incorporating a delay line with 14 mm separations. This novel structure aims to eliminate blind angles effectively. The array antennas demonstrated a gain of 14 dBi and a reflection coefficient of 20 dB or less, showcasing their high performance. The precise beam control of the array, coupled with the Rotman lenses, enables coverage of angles from −25 to +25 degrees along the *x*-axis. This advancement makes the antennas suitable for applications in 5G and automotive radar systems. For future improvements, integrating a programmable controller chip could further optimize beam characteristics based on specific application requirements.

ACKNOWLEDGMENT

The authors thank, Research Management Center (RMC), Universiti Teknologi Malaysia (UTM), Faculty of Electrical Engineering for the support of the research under grant the Ministry of Higher Education (MOHE) for supporting the research work under grant no FRGS/1/2021/STG04/UTM/01/1 and UTM matching grant 04M37.

REFERENCES

[1] N. Kou, S. Yu, Z. Ding, and Z. Zhang, "One-dimensional beam scanning transmitarray lens antenna fed by microstrip linear array," *IEEE Access*, vol. 7, pp. 90731-90740, 2019.

[2] N. Kalva and B. M. Kumar, "Feedline design for a series-fed binomial microstrip antenna array with no sidelobes," *IEEE Antennas Wirel. Propag. Lett.*, vol. 22, no. 3, pp. 650-654, 2023.

[3] B. A. Nia, L. Yousefi, and M. Shahabadi, "Integrated optical-phased array nanoantenna system using a plasmonic Rotman lens," *J. Light. Technol.*, vol. 34, no. 9, pp. 2118-2126, 2016.

[4] Q. Liang, B. Sun, and G. Zhou, "Miniaturization of Rotman lens using array port extension," *IEEE Antennas Wirel. Propag. Lett.*, vol. 22, no. 3, pp. 541-545, 2023.

[5] H. T. Chou and Z. C. Tsai, "Near-field focus radiation of multibeam phased array of antennas realized by using modified Rotman lens beamformer," *IEEE Trans. Antennas Propag.*, vol. 66, no. 12, pp. 6618-6628, 2018.

[6] M. Heino, C. Icheln, J. Haarla, and K. Haneda, "PCB-based design of a beamsteerable array with high-gain antennas and a Rotman lens at 28 GHz," *IEEE Antennas Wirel. Propag. Lett.*, vol. 19, no. 10, pp. 1754-1758, 2020.

[7] J. W. Lian, Y. L. Ban, H. Zhu, and Y. J. Guo, "Reduced-sidelobe multibeam array antenna based on SIW Rotman lens," *IEEE Antennas Wirel. Propag. Lett.*, vol. 19, no. 1, pp. 188-192, 2020.

[8] S. Christie, R. Cahill, N. B. Buchanan, V. F. Fusco, N. Mitchell, Y. V. Munro, and G. Maxwell-Cox, "Rotman lens-based retrodirective array," *IEEE Trans. Antennas Propag.*, vol. 60, no. 3, pp. 1343-1351, 2012.

[9] H. Cho, J. H. Lee, J. W. Yu, and B. K. Ahn, "Series-fed coupled split-ring resonator array antenna with wide fan-beam and low sidelobe level for millimeter-wave automotive radar," *IEEE Trans. Veh. Technol.*, vol. 72, no. 4, pp. 4805-4814, 2023.

[10] S. D. Joseph and E. A. Ball, "Series-fed millimeter-wave antenna array based on microstrip line

structure," *IEEE Open J. Antennas Propag.*, vol. 4, no. pp. 254-261, 2023.

[11] A. Darvazehban, O. Manoochehri, M. A. Salari, P. Dehkhoda, and A. Tavakoli, "Ultra-wideband scanning antenna array with Rotman lens," *IEEE Trans. Microw. Theory Tech.*, vol. 65, no. 9, pp. 3435-3442, 2017.

[12] B. Wang, Z. Zhao, K. Sun, C. Du, X. Yang, and D. Yang, "Wideband series-fed microstrip patch antenna array with flat gain based on magnetic current feeding technology," *IEEE Antennas Wirel. Propag. Lett.*, vol. 22, no. 4, pp. 834-838, 2023.

[13] A. Attaran, R. Rashidzadeh, and A. Kouki, "60 GHz low phase error Rotman lens combined with wideband microstrip antenna array using LTCC technology," *IEEE Trans. Antennas Propag.*, vol. 64, no. 12, pp. 5172-5180, 2016.

[14] S. Ogurtsov and S. Koziel, "A conformal circularly polarized series-fed microstrip antenna array design," *IEEE Trans. Antennas Propag.*, vol. 68, no. 2, pp. 873-881, 2020.

[15] G. Sacco, P. D'Atanasio, and S. Pisa, "A wideband and low-sidelobe series-fed patch array at 5.8 GHz for radar applications," *IEEE Antennas Wirel. Propag. Lett.*, vol. 19, no. 1, pp. 9-13, 2020.

[16] H. T. Chou and C. Y. Chang, "Application of Rotman lens beamformer for relatively flexible multibeam coverage from electrically large-phased arrays of antennas," *IEEE Trans. Antennas Propag.*, vol. 67, no. 5, pp. 3058-3066, 2019.

[17] A. Eid, J. G. D. Hester, and M. M. Tentzeris, "Rotman lens-based wide angular coverage and high-gain semipassive architecture for ultralong range mm-wave RFIDs," *IEEE Antennas Wirel. Propag. Lett.*, vol. 19, no. 11, pp. 1943-1947, 2020.

[18] Karki, S. K., Varonen, M., Kaunisto, M., Rantala, A., Lahti, M., Lamminen, A., & Viikari, V. "Beam-reconfigurable antenna based on vector modulator and Rotman lens on LTCC," *IEEE Access*, vol. 9, pp. 52872-52882, 2021.

[19] J. Y. Deng, Y. Bin Liu, Z. Chen, and W. Lin, "Compact multibeam antenna using miniaturized slow-wave substrate-integrated waveguide Rotman lens for satellite-assisted internet of vehicles," *IEEE Internet Things J.*, vol. 11, no. 4, pp. 6848-6856, 2024.

[20] Y. Liu and M. C. E. Yagoub, "Compact omnidirectional millimeter-wave antenna array fed in series by a novel feed network," *IEEE Trans. Antennas Propag.*, vol. 69, no. 11, pp. 7604-7612, 2021.

[21] Q. Liang, B. Sun, G. Zhou, J. Zhao, and G. Zhang, "Design of compact Rotman lens using truncated ports with energy distribution slots," *IEEE Access*, vol. 7, pp. 120766-120773, 2019.

[22] Y. Kang, E. Noh, and K. Kim, "Design of traveling-wave series-fed microstrip array with a low side-lobe level," *IEEE Antennas Wirel. Propag. Lett.*, vol. 19, no. 8, pp. 1395-1399, 2020.

Abd Al Menam A. Alazzawi earned his B.Eng. degree in Telecommunications from the University of Diyala, IRAQ, in 2015, followed by an M.Eng. degree in Electronics (Telecommunications) from the University of Technology Melaka Malaysia (UTeM) in 2018. Currently, he is pursuing a Ph.D. at the University of Technology Malaysia (UTM) in Johor Bahru city. He is currently conducting research on millimeter waves, base station array antennas, and beamforming circuits.

Mohamad Kamal A. Rahim received the B.Eng. degree in electrical and electronic engineering from the University of Strathclyde, UK, in 1987, the M.Eng. degree in science from the University of New South Wales, Australia, in 1992, and the Ph.D. degree in electrical engineering from the University of Birmingham, UK, in 2003. From 1987 to 1989, he worked as a management trainee with Sime Tyres Mer Gong Alor Star Kedah and as a production supervisor with Sime Shoes, Kulim, Kedah. In 1989, he became an assistant lecturer at the Department of Communication Engineering, Faculty of Electrical Engineering, University Technology Malaysia, Kuala Lumpur. The faculty appointed him as an associate professor. He is currently a professor of RF and antennas at University Technology Malaysia's Faculty of Electrical Engineering.

Osman Ayop earned his B.Eng. degree in electrical engineering, with a major in telecommunication, his M.Eng. degree in RF & Microwave, and his Ph.D. degree in electrical engineering from University Technology Malaysia (UTM) in 2007, 2010, and 2016, respectively. In 2013, he had completed his attachment at Uppsala University, Sweden, under the supervision of Prof. Dr. Vernon Cooray. He is currently a senior lecturer with the Department of Communication Engineering, School of Electrical Engineering, UTM. He is also an active researcher with the Advanced RF and Antenna Research Group (ARFMRG).

Pulse Radiation Characteristics Prediction Method of Vivaldi Antenna based on Dipole Array

Binwen Wang, Hui Ning, Hao Cai, Qilong Liu, Yan Wang, and Youjie Yan

Northwest Institute of Nuclear Technology
Xi'an 710024, China
srxh_bingwen@aliyun.com, ninghuisun@aliyun.com, 1178818032@qq.com, 820091469@qq.com, 1278206596@qq.com, pine976@163.com

***Abstract* –** This paper presents a theoretical method to estimate the pulse radiation characteristics of Vivaldi antennas. Based on the surface current distribution and the ultra-wideband radiation principle, Vivaldi antenna is equivalently modeled as a dipole array, and the pulse radiation characteristics of a single Vivaldi antenna are brought out utilizing the spatial superposition approach. Then, the influences and results of the Vivaldi antenna pulse characteristics prediction with different construction ways of the dipole array and element numbers are furthermore investigated. Next, a quadratic spatial superposition technique is employed to complete the theoretical prediction for time-domain radiation characteristics of Vivaldi antenna arrays. Experiments and simulations are conducted separately to verify the proposed method for both single Vivaldi antenna and array. The validated results demonstrate that the dipole array-based theoretical prediction method can effectively capture the pulse radiation characteristics for both individual Vivaldi antenna and array operating in different modes, thereby addressing challenges associated with estimating radiation characteristics in ultra-wideband pulse applications.

***Index Terms* –** Antenna array, beam scanning, dipole array, pulse radiation characteristics, Vivaldi antenna.

I. INTRODUCTION

The Vivaldi antenna, also known as the tapered slot antenna, is a planar end-fire antenna initially proposed by Gibson in 1979 [1]. Owing to its exceptional characteristics of ultra-wideband operation, high gain, low profile and excellent directivity, it has garnered significant attention and extensive applications in the field of radio communication technology [2–10]. Particularly, the attributes of stable phase center behavior, easy integration capability and cost-effectiveness exhibited by the Vivaldi antenna render it highly suitable for time domain radiation applications such as through-wall radar [11–12], ground-penetrating radar [13–14], non-destructive testing [8, 15] and biomedical imaging [16–18]. In comparison to traditional pulse radiation antennas like TEM horn antennas [19–20] or IRA [21–22], the Vivaldi antenna offers numerous advantages. Furthermore, akin to most antennas, Vivaldi antenna can be employed as array elements. Radiation gain enhancement can be achieved while enabling functionalities like beamforming and beam-scanning through precise control of excitation timing [23–34]. However, despite the remarkable advantages mentioned above, this type of antenna also encounters several technical challenges. Foremost among them is accurately calculating the radiation characteristics of Vivaldi antenna array in time domain. The absence of clear field distribution function poses difficulties for large-scale synthesis and beamforming operations on Vivaldi antenna arrays [25], thereby significantly limiting the engineering realization and practical application.

The computational electromagnetics methods and commercial electromagnetic simulation software can accurately compute the radiation characteristics of the array antennas [26–28]. However, when dealing with very short excited pulses and excessively large array scales, the computation grid number becomes too large, leading to significant consumption of computing resources and time due to limitations in computer hardware conditions. Consequently, the calculation efficiency becomes extremely low or even impractical. In order to address this challenging issue associated with calculating radiation characteristics for large-scale array antennas, Pozar proposed the active element pattern method [29], which predicts the total radiation field by combining the active patterns of each array element using superposition principles. Building upon this approach, Yang introduced the subarray equivalent extrapolation method [30] to enhance computational efficiency for determining array antenna radiation characteristics. Zhang et al. applied the active element pattern method to calculate time-domain patterns for TEM horn antenna arrays [31]. Although widely utilized and validated, employing the

Submitted On: April 5, 2024
Accepted On: July 3, 2024

https://doi.org/10.13052/2024.ACES.J.390506

active element pattern method requires extensive data measurement efforts that are labor-intensive, costly and tedious. Additionally, when there are changes in excitation pulse waveforms, re-measurements become necessary. Theoretical predictions have also been explored in relevant studies. For instance, Mikheev et al. derived an electric field calculation formula based on electromagnetic tensor methods for arbitrary wire antennas [32], enabling prediction of radiation characteristics for wire antenna arrays through superposition principles. Reference [33] has employed multiple reflection theory-based estimations to determine time-domain radiation characteristics of bowtie antennas. Theoretical methods, however, are confined to a subset of radiating antennas with relatively simplistic structures that lend themselves to analytical solutions.

To summarize, the theoretical prediction method stands out as the most cost-effective and ideal approach, primarily based on calculating the time-domain radiation field of a single antenna and employing spatial superposition principles. The spatial superposition process takes into account the influence of array factors, thereby eliminating the need for additional extraction of array factor. Therefore, accurately predicting the radiation characteristics of an array antenna in the time domain hinges upon precisely calculating the radiation field of the array element. This paper proposes a dipole array-based theoretical method for predicting radiation characteristics of Vivaldi antennas and their array in time-domain, building upon surface current distribution and wideband radiation principles, and verified by experiments and numerical simulation. This paper is organized as follows. The first section is the introduction, the second section outlines prediction concepts and implementation processes, the third section presents the verification, and the final section is the conclusion.

II. PREDICTION METHOD

Figure 1 illustrates the typical Vivaldi antennas, coplanar Vivaldi and antipodal Vivaldi [34], respectively. The sole distinction lies within the feeding structures, while the radiation principle remains unaltered. In accordance with the theory of time-domain electromagnetics, the pulse radiation characteristics of the antenna can be acquired utilizing the Maxwell's equations and time-domain retarded potential after determining the antenna surface current distribution. However, for most UWB pulse radiating antennas, the time-domain surface current distribution is so complicated that there are challenges in providing an analytical solution. Therefore, it is imperative to reasonably approximate and solve for the current distribution in order to address this prediction problem.

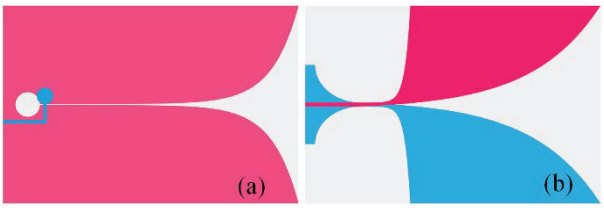

Fig. 1. Typical Vivaldi antennas: (a) coplanar Vivaldi and (b) antipodal Vivaldi.

Firstly, the investigation focuses on the antenna surface current distribution. Figure 2 illustrates the current distribution at typical frequency points of the two Vivaldi antennas, obtained using the time-domain finite integral techniques.

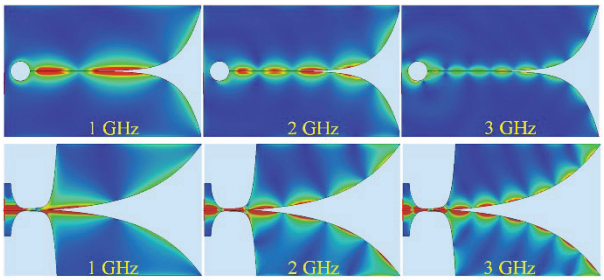

Fig. 2. Current distributions of the Vivaldi antennas in typical frequency points.

Figure 2 qualitatively demonstrates that the surface current of the Vivaldi antenna is primarily concentrated along the exponential gradient edge of the radiation patch, with minimal contribution from other positions on the patch. Consequently, it can be inferred that the primary path of the surface current flow corresponds to this exponential gradient line. Therefore, the Vivaldi antenna can be considered as a curvilinear radiator composed of two exponential gradient lines, as illustrated in Fig. 3.

The simplification of the solution difficulty is greatly facilitated by the equivalence based on surface current distribution. Upon examining the operating principle and radiation process of Vivaldi antenna, it becomes apparent that the ultra-wideband feature stem from the varied length between the gradient slots, radiating electromagnetic waves with distinct wavelengths while preserving relatively stable phase centers [35]. Thus, the equivalent curvilinear radiator shown in Fig. 3 can be further modeled by a dipole antenna array, as plotted in Fig. 4.

In order to elucidate the estimation idea more clearly, Fig. 4 only employs an array consisting of three dipole elements to simulate the Vivaldi antenna. It is worth noting that the array with multiple elements can also be utilized, wherein the curvilinear radiator is

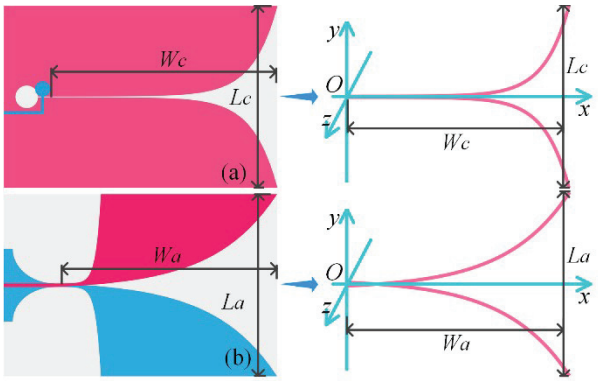

Fig. 3. Vivaldi antennas and the equivalent curvilinear radiators: (a) coplanar Vivaldi and (b) antipodal Vivaldi.

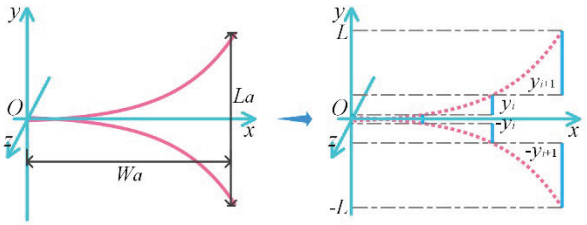

Fig. 4. Utilizing the dipole array to model the curvilinear radiator and the primary path of the surface current flow.

divided into several segments and each segment corresponds to an equivalent dipole antenna at the respective position. However, it should be emphasized that this dipole array differs from the conventional arrays in terms of the spatial distribution of the array elements, which follows the exponential gradient lines of the Vivaldi antenna. Moreover, unlike independently feeding elements in traditional arrays, current propagates along the previous dipole element towards the end and then continues into the subsequent dipole element. The total length of all elements of the dipole array matches that of the dimensions in the E-plane of the Vivaldi antenna. Overall, this equivalence effectively divides a dipole antenna with the length identical to the E-plane size of Vivaldi antenna into smaller dipoles, distributed according to the exponential gradient line structure characteristics of Vivaldi antenna. From the perspective of current element, when the element number of the dipole array is sufficient, the dipole array can be regarded as a collection of current elements, which is equal to solve the radiation characteristics of Vivaldi antenna utilizing the current element analysis. In fact, the Vivaldi antenna is considered as the dipole array in y direction, disregarding the x component current of the curvilinear radiator. This is because, from an external viewpoint, the current flows in the x-direction on the upper and lower poles of the curvilinear radiator are opposite, and the contribution to the field on the yoz plane is zero. For other field points, the contribution of the x component remains negligible.

The above-mentioned equivalence simplifies the radiation characteristics prediction of the Vivaldi antenna to the calculation of the radiated field of a dipole array in time-domain, the foundation of which is the pulse radiation of a single dipole antenna. Figure 5 illustrates the radiation process of the dipole antenna, which is positioned along the y axis. To differentiate the source point and field point, the coordinates of source points are attached by a superscript s.

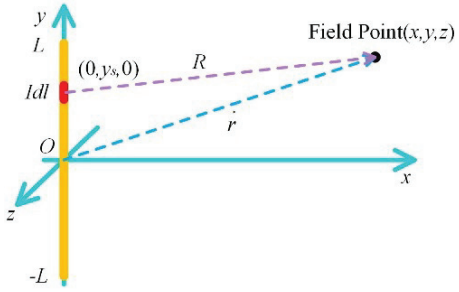

Fig. 5. Radiation process of the dipole antenna.

According to the theory of multiple reflections, the frequency domain current distribution of dipole antenna can be elegantly expressed as [36]:

$$\overrightarrow{I}(l,\omega) = I_0(\omega)\frac{e^{-jkl}+\Gamma_2 e^{-jk(2L-l)}}{1-\Gamma_1\Gamma_2 e^{-jk2L}}, \tag{1}$$

where I_0 represents the amplitude of excitation current, k is the propagation constant, l refers to the distance between the current element and the feeding point of dipole, L denotes the length of dipole arm, and Γ_1 and Γ_2 stand for the reflection coefficients at the feeding and terminal end, respectively.

The current distribution reveals that the magnetic vector potential in the y-direction at the field point $\overrightarrow{r}$ is:

$$\overrightarrow{A}(\overrightarrow{r},\omega) = \frac{\mu_0 I_0(\omega)}{4\pi}\int_{2L}\frac{e^{-jkl}+\Gamma_2 e^{-jk(2L-l)}}{1-\Gamma_1\Gamma_2 e^{-jk2L}}\frac{e^{-jkR}}{R}dl, \tag{2}$$

where R is the distance between field and source points:

$$R = \sqrt{(x-x_s)^2+(y-y_s)^2+(z-z_s)^2}\Big|_{x_s=0,z_s=0}^{\text{for dipole}}. \tag{3}$$

The magnetic field at the field point can be derived from equation (2), thereby enabling us to ascertain the components of the electric field in each direction:

$$\overrightarrow{E}(\overrightarrow{r},\omega)_x = \frac{I_0(\omega)(x-x_s)}{j4\pi\omega\varepsilon_0}\int_{-L}^{L} i(R,l)(y-y_s)a_R dl, \tag{4}$$

$$\begin{aligned}\vec{E}(\vec{r},\omega)_y = &\frac{I_0(\omega)}{j2\pi\omega\varepsilon_0}\int_{-L}^{L} i(R,l)b_R dl \\ &-\frac{I_0(\omega)z^2}{j4\pi\omega\varepsilon_0}\int_{-L}^{L} i(R,l)a_R dl \\ &-\frac{I_0(\omega)(x-x_s)^2}{j4\pi\omega\varepsilon_0}\int_{-L}^{L} i(R,l)a_R dl,\end{aligned} \tag{5}$$

$$\overrightarrow{E}(\overrightarrow{r},\omega)_z = \frac{I_0(\omega)z}{j4\pi\omega\varepsilon_0}\int_{-L}^{L} i(R,l)(y-y_s)a_R dl, \tag{6}$$

where the mentioned functions are designated as:

$$\begin{cases} i(R,l) = \dfrac{e^{-jk(R+l)}+\Gamma_2 e^{-jk(2L+R-l)}}{1-\Gamma_1\Gamma_2 e^{-jk2L}} \\ a_R = -k^2R^{-3}+3jkR^{-4}+3R^{-5} \\ b_R = jkR^{-2}+R^{-3} \end{cases}. \tag{7}$$

By performing the inverse Fourier transform on equations (4-6), the corresponding radiation field in time-domain of the dipole antenna can be acquired, and the electric field in y direction is the principle polarized component, which is the subsequent focus to be investigated.

A simple verification to the theoretical calculation of the radiation field for dipole antenna is presented below, employing the time-domain finite integral techniques. As marked in Fig. 5, a dipole is positioned along the y direction with the pole length of 15 cm and the feeding gap of 4 mm. Utilizing a Gaussian pulse with pulse width of 0.6 ns shown in Fig. 6 as the excitation, the principle polarized electric field at the field point (5,0,0) is obtained, as plotted in Fig. 7.

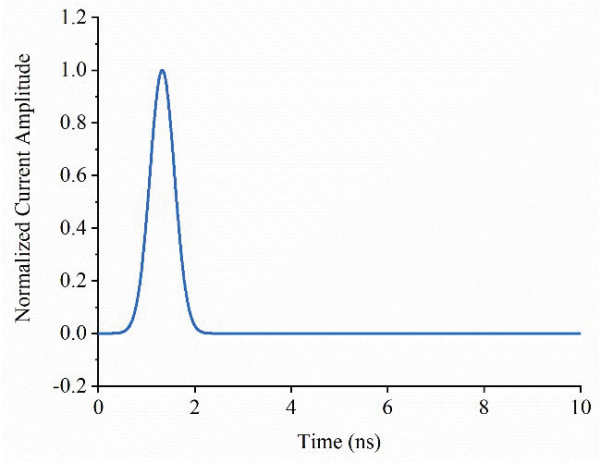

Fig. 6. Excitation pulse with pulse width of 0.6 ns.

The radiated electric field waveforms of the dipole antenna obtained by the prediction method, as depicted in Fig. 7, exhibits remarkable concordance with the numerical results with the pulse mean square error of 0.43. Only a slight discrepancy in pulse duration is observed. This variation is primarily attributed to the pole radius of the dipole. Current concentration occurs along the dipole axis during the equivalence process, while the practical current is distributed across the dipole surface, thereby inducing a certain degree of broadening on the radiated electric field waveform.

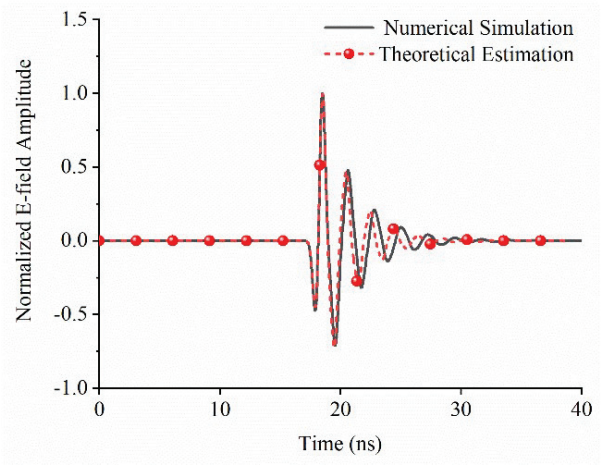

Fig. 7. The normalized principle polarized electric field waveform at the field point (5,0,0).

The pulse radiation characteristics of a dipole array can be obtained by combining the radiation field of a single dipole with the principle of spatial superposition. However, for the dipole antenna array proposed and constructed in this paper, slight deviations in the calculation of radiation field arise due to differences in feeding ways and structure. These deviations are manifested in the integral range. For the i_{th} element in Fig. 4, the integral range of [-L,L] in equation (5) should be replaced by [-y_{i+1},-y_i] and [y_i,y_{i+1}], while the pole length L remains unchanged. That means, the current distribution of the i_{th} element is equal to that on the corresponding position of the dipole with total length of 2L, reflections resulted by the feeding gap and the terminal end of the dipole with length of 2L has been taken into account. Moreover, the reflections present in the current distribution on the i_{th} element are generated by both the feeding gap of the first element dipole and the terminal end of the n_{th} element dipole. And the positional difference among array elements has already been considered through R in equation (5).

According to the radiation process, there exist two approaches for calculating the radiation field of the proposed dipole array. The first approach involves direct superposition, whereby the radiation field generated by each individual dipole element at the designated point is considered. Consequently, the overall radiation field of

the dipole array can be determined:

$$\vec{E}_a(\vec{r},t)=\sum_{i=1}^{n}\vec{E}_i(\vec{r}_i,t), \tag{8}$$

where $\vec{r}_i$ refers to the position vector of the field point $\vec{r}$ relative to the feeding center of the i_{th} element.

A more sophisticated approach involves treating the dipole array as an individual dipole, thus solving the radiation field of each segment. Subsequently, spatial superposition is performed while considering the time delays determined by the actual distance between field and source point:

$$\vec{E}_a(\vec{r},t)=\sum_{i=1}^{n}\vec{E}_{di}(\vec{r},t-t_{di}), \tag{9}$$

where t_{di} indicates the relative time delays of the array elements.

Take an antipodal Vivaldi antenna with the dimensions of 200 mm ×300 mm as an example. Figure 8 illustrates the antenna model and the excitation pulse with the upper frequency limit of 3 GHz.

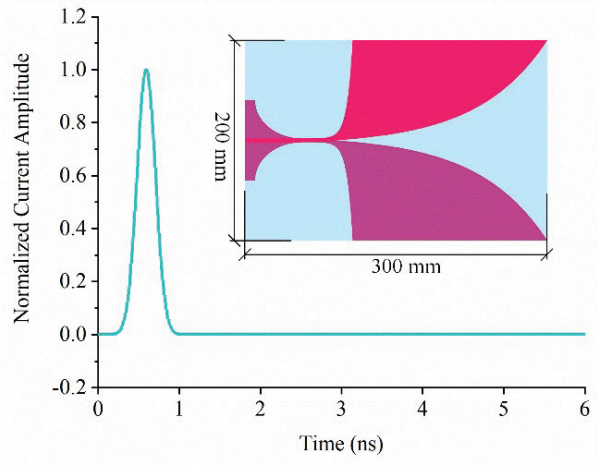

Fig. 8. Antipodal Vivaldi antenna and the excitation pulse.

Employing the aforementioned prediction method, the normalized electric field waveform in the principle polarized direction at the distance of 5 m along the main axis of the Vivaldi antenna is obtained, as depicted in Fig. 9. Subsequently, a comparison was made with the numerical results.

As observed in Fig. 9, the main pulse features of the predicted radiation waveform are in good agreement with the simulated results, except for a slight discrepancy in the tail oscillation. The corresponding pulse mean square error is 0.28. This can be attributed to the different treatment of the reflections at the feeding and terminal end in the simplified equivalent process, compared to the actual radiation. However, these predictions adequately meet the requirements for capturing the primary

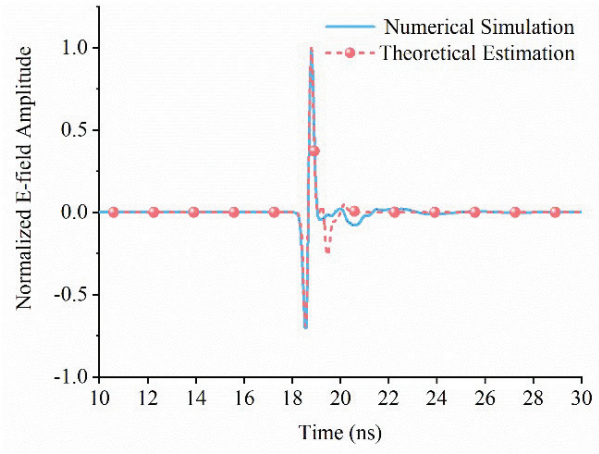

Fig. 9. Normalized radiated waveform at a distance of 5 m along the main axis of the Vivaldi antenna.

pulse characteristics. Furthermore, the impact of various dipole array elements on the radiation field of Vivaldi antenna is investigated. As depicted in Fig. 10, a comparative analysis is conducted to examine the predicted results of the radiation field with different dipole array elements.

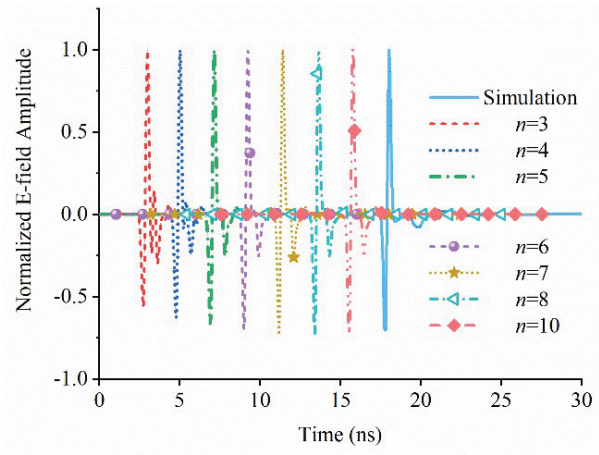

Fig. 10. Radiation field waveforms estimated by dipole array with different element numbers.

As illustrated in Fig. 10, the discrepancy between the theoretically estimated radiation waveforms and the numerical results diminishes with the increase of the dipole array element number, denoted as n. This convergence can be attributed to the increasing equivalence between the proposed dipole array and the gradient curve, aligning with expectations. It is well established that the time-domain radiation waveform of an antenna is determined by its current distribution. The duration of the radiation field waveform pulse is not only related

to the excitation pulse but also to the relative position of the current elements. As the number of equivalent dipole array elements increases, the positional equivalence becomes more pronounced. In essence, when the element number of the dipole array becomes sufficiently large, it approximates decomposing the gradient curve into an adequate number of elementary currents. It should be noted that a larger number of array elements leads to increased computational complexity, hence, the element number of the dipole array should be not overmuch in practical calculations and applications.

The dipole arrays utilized in the prediction process are uniform arrays with equidistant spacing along the *x*-axis. However, it is worth noting that non-uniform arrays can also be employed for an equivalent purpose. Figure 11 illustrates the schematic diagram of both a uniform dipole array and a non-uniform dipole array with the same element number of n=6. In the case of the non-uniform dipole array, the spacing along the *x*-axis adheres to a relationship of equal proportional variation, where q represents the common ratio.

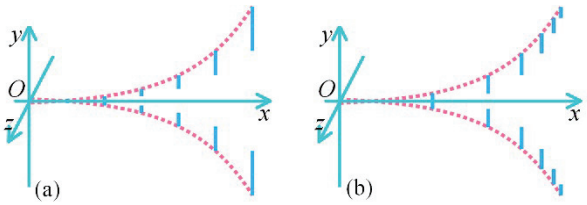

Fig. 11. Modeling methods of the curvilinear radiator: (a) uniform dipole array and (b) non-uniform dipole array.

The normalized radiation waveforms at the distance of 5 m along the main axis of the Vivaldi antenna obtained through the utilization of both uniform and non-uniform arrays is depicted in Fig. 12.

Figure 12 reveals that the non-uniform dipole array can also achieve a good prediction of Vivaldi antenna radiation field waveform. Specifically, for Vivaldi antennas, the initial section of the exponential gradient slot line primarily facilitates current propagation with minimal contribution to radiation, while it is the sharply changing length in *y*-direction in the end part of the exponential gradient slot line that plays a crucial role in generating radiation. In other words, the terminal part can be considered as the main radiating section. However, given that an excessive number of segments would lead to a significant increase in computational load, non-uniform segmentation allows for a more precise focus on the principal radiating components of the antenna. This precisely highlights the advantages offered by the non-uniform dipole array depicted in Fig. 11.

This section presents the concept and methodology of the dipole array-based prediction, while also analyzing the impact of array construction ways and element number on prediction effectiveness. Moreover, it should be noted that the discrete equivalent approach described herein can also be applied to antennas with more intricate structures as well as for estimating time domain radiation characteristics. In the following section, experiments and simulations are employed to further validate the prediction method.

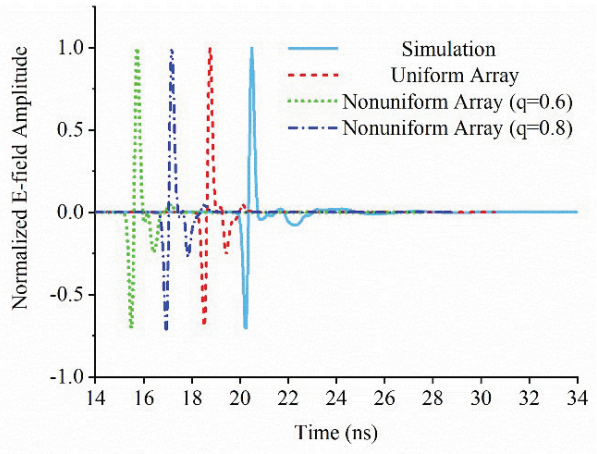

Fig. 12. Normalized radiated waveforms estimated by uniform dipole array and non-uniform dipole arrays.

III. VALIDATION AND DISCUSSION

A. Fabrication and measurement of antipodal Vivaldi

To validate the proposed theoretical prediction method, an antipodal Vivaldi antenna is designed and fabricated, as depicted in Fig. 13, which is printed on a FR-4 dielectric substance with thickness of 2 mm, relative dielectric constant of 4.3 and loss tangent of 0.025.

Firstly, the S11 of the antipodal Vivaldi antenna is measured within the frequency range of 10 MHz to 6 GHz, employing a vector network analyzer of KEYSIGHT E5080B. Figure 14 presents the measured curves, compared with numerical results obtained by finite integral techniques.

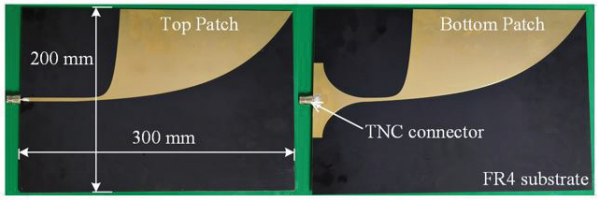

Fig. 13. The designed and fabricated antipodal Vivaldi antenna.

As depicted in Fig. 14, the measured results exhibit excellent agreement with the numerical simulations. The measured lower cut-off frequency (S11≤-10 dB) is 0.64

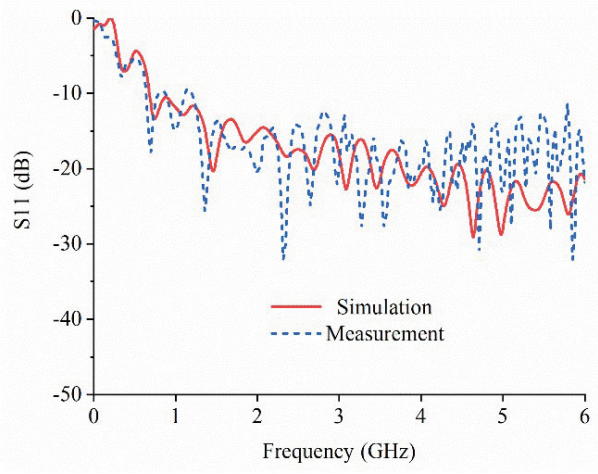

Fig. 14. Comparison of the measured and simulated S11 parameter.

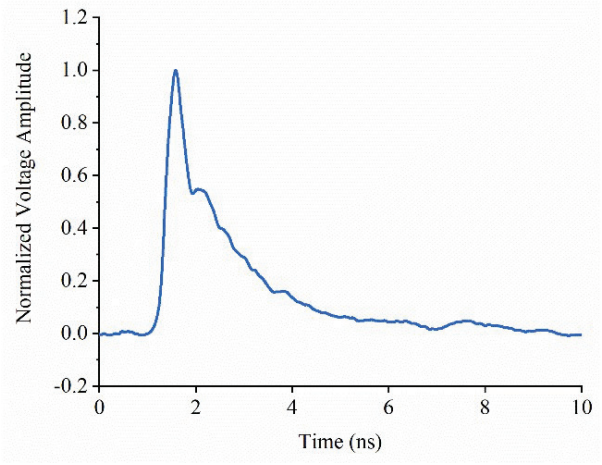

Fig. 15. The measured excitation pulse generated by the solid-state pulse generator.

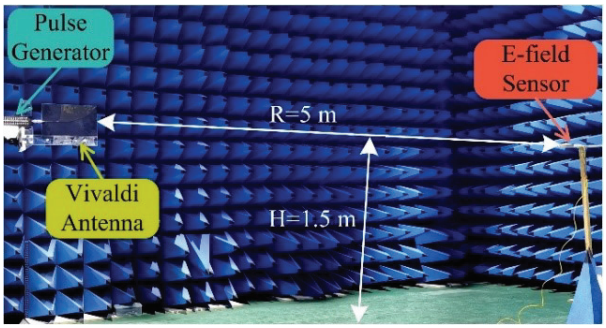

Fig. 16. Experimental setup for antipodal Vivaldi antenna.

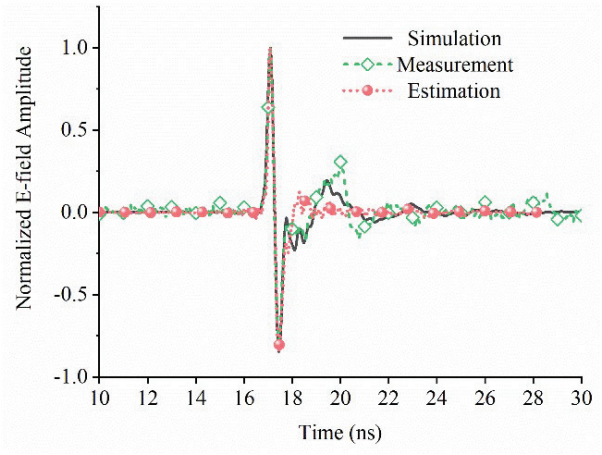

Fig. 17. Comparison of the measured radiated field waveforms of Vivaldi antenna with theoretical prediction and numerical results.

GHz. Aperture width is about $0.43\lambda_0$ where λ_0 is the maximum operating wavelength. The measured frequency upper limit exceeds 6 GHz, resulting in a proportional bandwidth close to 10, proving that the fabricated antipodal Vivaldi antenna is a typical ultra-wideband antenna.

Secondly, the time-domain radiation characteristics of the antipodal Vivaldi antenna are demonstrated. The excitation pulses utilized in the second section are all ideal Gaussian pulses, which is too difficult to implement. Hence, an ultra-wideband solid-state pulse generator based on avalanche transistor is designed and employed to output the excitation pulse for the Vivaldi antenna. The measured excitation pulse is shown in Fig. 15. Then, a testing apparatus is established to measure the radiation field waveform of the antipodal Vivaldi antenna. Figure 16 illustrates the experimental setup. The antipodal Vivaldi antenna is feeding via TNC coaxial cable which is connected to the solid-state pulse generator. The field measurement system comprises a monopole probe and photoelectric module with the bandwidth up to 3 GHz and response time less than 150 ps. An oscilloscope of TELEDYNE LECROY 806Zi-B with the bandwidth of 6 GHz and sampling rater of 20 GSa/s is utilized. The measured radiation field waveform at the distance of 5 m along the main axis of the antenna is presented in Fig. 17, which is compared against theoretical estimation and numerical results.

As observed from Fig. 17, the radiated electric field waveforms are bipolar pulses under the excitation of the pulse depicted in Fig. 15. It is evident that the measured bipolar pulse accurately matches both the numerical and theoretical estimated results, demonstrating the effectiveness of the proposed prediction method for Vivaldi antenna radiation field. Comparatively speaking, there are no related studies on the prediction of the radiated electric field for Vivaldi antenna in previous references, which further emphasizes the innovation

and significance of this work. Additionally, the proposed method and the conducted work in this paper offer a novel approach to analyze Vivaldi antennas. For instance, the theoretical prediction method enables quick examination of the impact of antenna dimensions on the radiation field, which is beneficial for antenna design and UWB pulse generator development. The time-domain pattern of single Vivaldi antenna is not particularly significant and was not elaborated here. In the subsequent section, the temporal pattern of the Vivaldi array will be analyzed and predicted.

B. Antipodal Vivaldi antenna array

The prediction of pulse radiation characteristics of Vivaldi antenna array primarily relies on the spatial superposition of the radiation field of each element antenna, in which the array factor has been incorporated. To differentiate with the aforementioned spatial superposition, the new spatial superposition in this step is referred as the quadratic spatial superposition. Assuming a $M\times N$ Vivaldi antenna array with a relative delay sequence between excitation pulses of each element represented by matrix τ, the radiation field waveform at any field point of the array can be obtained using the quadratic spatial superposition:

$$\vec{E}_{AC}(\vec{r},t)=\sum_{i=1,j=1}^{M,N}\vec{E}_{i,j}(\vec{r}_{i,j},t-\tau_{i,j}), \qquad (10)$$

where $\vec{r}_{i,j}$ stands out the position vector of the field point $\vec{r}$ with respect to the (i,j) element, $\vec{E}_{i,j}$ refers to the radiated electric field of the (i,j) element antenna.

For cost reasons, numerical simulation is employed to validate the prediction method to the pulse radiation characteristics of antenna array. A 6×12 array is constructed using the antipodal Vivaldi antenna in previous part as the array element, as shown in Fig. 18, with spacing of 250 mm in E-plane between each element and spacing of 200 mm in H-plane.

The excitation pulse of each element in the array remains as the measured output waveform from the pulse generator, as depicted in Fig. 15. First consider synchronous excitation, where the time delay sequence matrix is set to zero. The theoretical prediction approach is utilized to obtain the radiated waveforms at the distance of 10 m along the main axis of the array antenna, as illustrated in Fig. 19, and then a comparison is made with numerical results acquired by finite integral techniques. Additionally, Fig. 20 presents the predicted temporal patterns for both E-plane and H-plane under synchronous excitation of the Vivaldi antenna array.

As observed in Fig. 19, the theoretical predicted electric field waveform exhibits excellent agreement with the numerical results, which indicates that the proposed prediction method is capable of achieving accurate predictions for the array antenna radiation field waveform. In fact, this outcome is inevitable due to ideal conditions where the waveforms at the main axis field point of an array antenna are essentially identical to those of a single antenna under synchronous excitation. The array antenna beam exhibits a higher degree of concentration and achieves greater gain compared to an individual antenna array element, therefore, it places greater emphasis on its time domain pattern. As depicted in Fig. 20, it can be clearly observed that the theoretically predicted patterns in both E-plane and H-plane for the array antenna align closely with numerical results across a wide range of angles. Notably for the concerned 3-dB beam width, the errors remain below 5%. These findings demonstrate that the proposed theoretical approach also yields effective predictions for the time domain pattern of the Vivaldi antenna array.

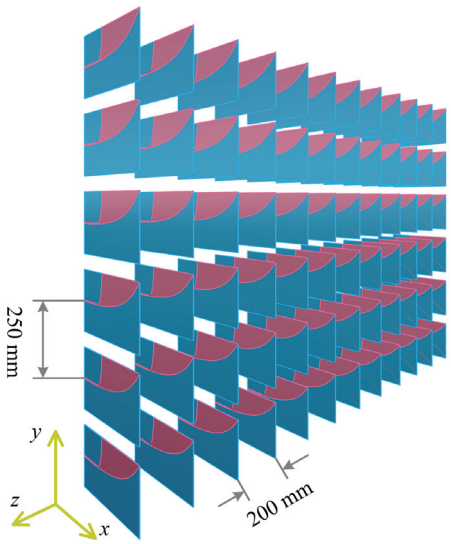

Fig. 18. A 6×12 Vivaldi antenna array.

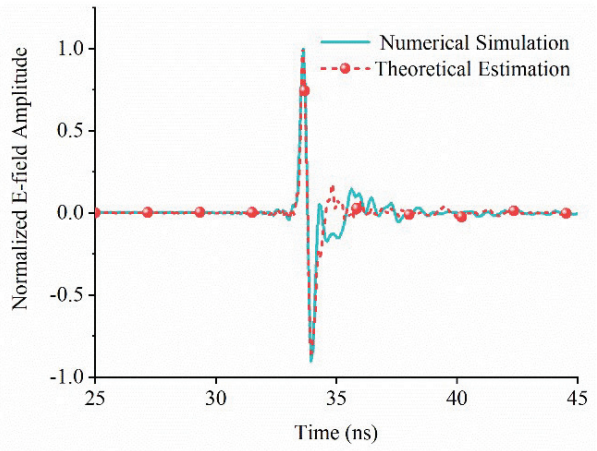

Fig. 19. Radiated waveforms at 10 m along the main axis of the Vivaldi antenna array.

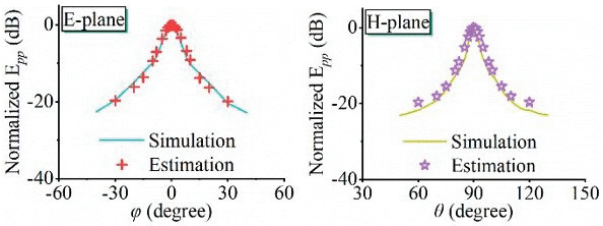

Fig. 20. Temporal patterns of the Vivaldi antenna array in E-plane and H-plane under synchronous excitation.

The beam width of the antenna is determined by the size of the radiating aperture. As evident from both the array aperture dimension and the obtained time-domain patterns, the temporal pattern of the 6×12 array in H-plane appears relatively narrow, necessitating beam scanning in most application scenarios. Beam scanning operates on the principle of configuring the time delay sequence based on the desired scanning angle and spacing between array elements, thereby controlling the excitation timing for each element within the array to deflect the radiation beam, ensuring optimal spatial superposition at the desired angle. Here, employing the theoretical prediction method to obtain the H-plane temporal patterns in different scanning angles, compared with the numerical results, is depicted in Fig. 21.

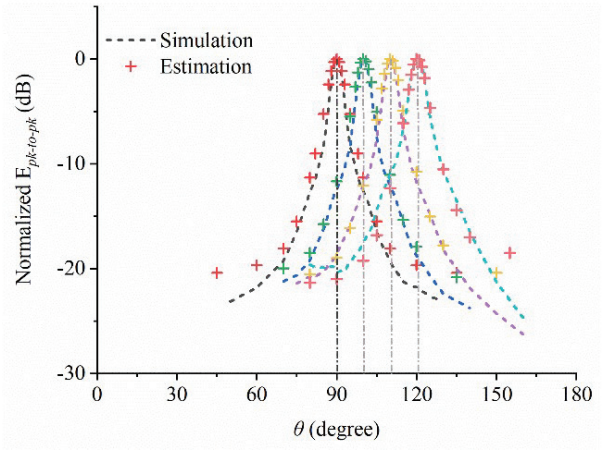

Fig. 21. Temporal patterns on H-plane within different scanning angles.

As demonstrated in Fig. 21, the time-domain pattern of the array can still be effectively predicted when operating in the beam scanning mode, which further validates the correctness and effectiveness of the proposed theoretical prediction method. Based on the proposed prediction method, the time-domain radiation characteristics of the array under different excitation delay sequences can be thoroughly studied and analyzed, leading to significant cost reduction and facilitating the design, development and engineering implementation of array antennas. Moreover, the issues of pattern synthesis for antenna arrays become feasible by integrating global optimization algorithms and the proposed prediction method. This approach can offer guidance and convenience for radiation characteristics measurements of array via advance prediction.

IV. CONCLUSION

Vivaldi antenna is a widely used ultra-wideband pulse radiating antenna. Estimating the time-domain radiation characteristics of Vivaldi antennas holds significant importance for antenna design, array development and engineering realization. This paper presents a theoretical method for predicting the radiation characteristics of Vivaldi antennas in time-domain, in which the dipole array is employed to model the Vivaldi antenna. By superimposing the pulsed radiation electric fields of dipole antennas, the time-domain radiated field of Vivaldi antenna is obtained. The influence of the construction way and element number of the dipole array on the estimation effect of Vivaldi antenna radiation field in time-domain is investigated, and the specific implementation process of the theoretical estimation method is presented. Additionally, quadratic spatial superposition is employed to incorporate the array factor, enabling the realization of pulsed radiation characteristics of the Vivaldi antenna array. The measurement of a fabricated antipodal Vivaldi antenna is conducted, which demonstrates that the proposed dipole array-based method can accurately predict the radiation field waveform of the Vivaldi antenna. Furthermore, numerical simulation to the Vivaldi antenna array also indicates that this approach effectively enables estimation of radiation field waveform and time-domain patterns of Vivaldi array operating on synchronous excitation and beam scanning mode. This methodology serves as a foundation for array temporal pattern synthesize and contributes to designing and characteristics measurements of the Vivaldi array.

REFERENCES

[1] P. J. Gibson, "The Vivaldi aerial," *IEEE 9th European Microwave Conference*, Brighton, UK, pp. 101-105, Sep. 1979.

[2] A. Hossain and A. V. Pham, "A novel gain-enhanced miniaturized and lightweight Vivaldi antenna," *IEEE Trans. Antennas Propagat.*, vol. 71, no. 12, pp. 9431-9439, Dec. 2023.

[3] Z. Qiao, Z. Wang, T. Loh, S. Gao, and J. Miao, "A compact minimally invasive antenna for OTA testing," *IEEE Antennas Wirel. Propag. Lett.*, vol. 18, no. 7, pp. 1381-1385, July 2019.

[4] R. Cicchetti, V. Cicchetti, A. Faraone, L. Foged, and O. Testa, "A compact high-gain wideband lens

Vivaldi antenna for wireless communications and through-the-wall imaging," *IEEE Trans. Antennas Propagat*., vol. 69, no. 6, pp. 3177-3192, June 2021.

[5] N. O. Parchin, M. Shen, and G. F. Pedersen, "Small-size tapered slot antenna (TSA) design for use in 5G phased array applications," *Appl. Comput. Electromagn. Soc. J.*, vol. 32, no. 3, pp. 193-202, Mar. 2017.

[6] F. B. Zarrabi, N. P. Gandji, R. Ahmadian, H. Kuhestani, and Z. Mansouri, "Modification of Vivaldi antenna for 2-18 GHz UWB application with substrate integration waveguide structure and comb slots," *Appl. Comput. Electromagn. Soc. J.*, vol. 30, no. 8, pp. 844-849, Aug. 2017.

[7] B. Biswas, R. Ghatak, and D. R. Poddar, "A fern fractal leaf inspired wideband antipodal Vivaldi antenna for microwave imaging system," *IEEE Trans. Antennas Propagat*., vol. 65, no. 11, pp. 6126-6129, Nov. 2017.

[8] S. M. Kameli, S. S. Refaat, H. Abu-Rub, A. Darwish, A. Ghrayeb, and M. Olesz, "Ultra-wideband Vivaldi antenna with an integrated noise-rejecting parasitic notch filter for online partial discharge detection," *IEEE Trans. Instrum. Meas*., vol. 73, pp. 1-10, 2024.

[9] B. Wang, H. Ning, Y. Yan, C. Cao, and Q. Liu, "Antipodal Vivaldi antenna with resistance loading on bent terminal," *Int. Conf. Microw. Millim. Wave Technol., ICMMT - Proc.*, Harbin, CN, pp. 1-3, Aug. 2022.

[10] A. S. Dixit, S. Kumar, S. Urooj, and A. Malibari, "A highly compact antipodal Vivaldi antenna array for 5G millimeter wave applications," *Sensors*, vol. 21, no. 7, pp. 2360(1-15), Mar. 2021.

[11] J. Zhang, H. Lan, M. Liu, and Y. Yang, "A handheld Nano through-wall radar locating with the gain-enhanced Vivaldi antenna," *IEEE Sens. J*., vol. 20, no. 8, pp. 4420-4429, Apr. 2020.

[12] Z. Hu, Z. Zeng, K. Wang, W. Feng, J. Zhang, Q. Lu, and X. Kang, "Design and analysis of a UWB MIMO radar system with miniaturized Vivaldi antenna for through-wall imaging," *Remote Sensing*, vol. 11, no. 16, pp. 1867(1-20), Aug. 2019.

[13] Z. Tahar, X. Derobert, and M. Benslama, "An ultra-wideband modified Vivaldi antenna applied to through the ground and wall Imaging," *Prog. Electromagn. Res. C*, vol. 86, pp. 111-122, Aug. 2018.

[14] D. N. Elsheakh and E. A. Abdallah, "Compact ultra-wideband Vivaldi antenna for ground-penetrating radar detection applications," *Microw. Opt. Technol. Lett*., vol. 61, no. 5, pp. 1268-1277, Feb. 2019.

[15] J. Zhang, X. Zhang, and S. Xiao, "Antipodal Vivaldi antenna to detect UHF signals that leaked out of the joint of a transformer," *Int. J. Antennas Propag*., vol. 2017, pp. 1-13, June 2017.

[16] M. Ren, Z. Cheng, L. Wu, H. Zhang, S. Zhang, X. Chen, D. Xing, and H. Qin, "Portable microwave-acoustic coaxial thermoacoustic probe with miniaturized Vivaldi antennas for breast tumor screening," *IEEE Trans. Biomed. Eng*., vol. 70, no. 1, pp. 175-181, Jan. 2023.

[17] A. M. de Oliveira, A. M. de Oliveira Neto, M. B. Perotoni, N. Nurhayati, H. Baudrand, A. de Carvalho, and J. F. Justo, "A fern antipodal Vivaldi antenna for near-field microwave imaging medical applications," *IEEE Trans. Antennas Propagat*., vol. 69, no. 12, pp. 8816-8829, Dec. 2021.

[18] U. Rafique, S. Pisa, R. Cicchetti R, O. Testa, and M. Cavagnaro, "Ultra-wideband antennas for biomedical imaging applications: A survey," *Sensors*, vol. 22, no. 9, pp. 3230(1-38), Apr. 2022.

[19] V. M. Fedorov, M. V. Efanov, V. Y. Ostashev, V. P. Tarakanov, and A. V. UI'yanov, "Antenna array with TEM-horn for radiation of high-power ultrashort electromagnetic pulses," *Electronics*, vol. 10, no. 9, pp. 1011(1-18), Apr. 2021.

[20] J. Shao, G. Fang, J. Fan, Y. Ji, and H. Yin, "TEM horn antenna loaded with absorbing material for GPR applications," *IEEE Antennas Wirel. Propag. Lett*., vol. 13, pp. 523-527, Mar. 2014.

[21] A. Ha, M. H. Chae, and K. Kim, "Beamwidth control of an impulse radiating antenna using a liquid metal reflector," *IEEE Antennas Wirel. Propag. Lett*., vol. 18, no. 4, pp. 571-575, Apr. 2019.

[22] S. Xiao, S. Altunc, P. Kumar, C. E. Baum, and K. H. Schoenbach, "A reflector antenna for focusing subnanosecond pulses in the near field," *IEEE Antennas Wirel. Propag. Lett*., vol. 9, pp. 12-15, Jan. 2010.

[23] C. Pfeiffer and J. Massman, "An UWB hemispherical Vivaldi array," *IEEE Trans. Antennas Propagat*., vol. 70, no. 10, pp. 9214-9224, Oct. 2022.

[24] A. M. de Oliveira, J. R. B. Garay, J. P. de Souza, A. M. da Silva, M. B. Perotoni, W. Beccaro, and J. F. Justo, "Active Vivaldi antenna timed-array for ultra-wideband 3D beamforming," *Recent Pat. Eng.*, vol. 10, no. 2, pp. 121-127, Aug. 2016.

[25] X. Jiang, Y. Yan, L. Meng, B. Wang, L. Bi, and Y. Yin, "Theoretical study on directivity of ultra-wideband time-domain antenna array based on 3D impulse point sources," *National Conference on Antennas*, Harbin, CN, pp. 816-818, Aug. 2023.

[26] K. Zhang, L. Wang, R. Liu, M. Wang, C. Fan, H. Zheng, and E. Li, "Low-dispersion leapfrog WCS-FDTD with artificial anisotropy parameters and simulation of hollow dielectric resonator antenna array," *IEEE Trans. Antennas Propagat*., vol. 69, no. 9, pp. 5801-5811, Sep. 2021.

[27] S. E. Bankov and M. D. Duplenkova, "Transformation of the electromagnetic field in an UWB array of TEM horns," *Proc. IEEE All-Russian Microw. Conf., RMC*, Moscow, RU, pp. 178-181, Nov. 2022.

[28] K. N. Klimov, K. I. Konov, A. M. Belevtsev, I. K. Epaneshnikova, and A. S. Boldyreff, "Electromagnetic modeling of the ultra-wideband antenna array radiator," *Conf. Proc. Radiat. Scatt. Electromagn. Waves, RSEMW*, Divnomorskoe, RU, pp. 232-235, Aug. 2023.

[29] D. M. Pozar, "The active element pattern," *IEEE Trans. Antennas Propagat*., vol. 42, no. 8, pp. 1176-1178, Aug. 1994.

[30] X. Yang, H. Qian, B. Z. Wang, and S. Xiao, "Radiation pattern computation of pyramidal conformal antenna array with active-element pattern technique," *IEEE Antennas Propag. Mag*., vol. 53, no. 1, pp. 28-37, Feb. 2011.

[31] M. Zhang, C. Liao, Z. Ye, J. Feng, and Q. Liu, "A rapid method for calculating the pulsed antenna arrays including mutual coupling effects," *Chinese Journal of Radio Science*, vol. 30, no. 5, pp. 864-869, Oct. 2015.

[32] O. V. Mikheev, S. A. Podosenov, K. Y. Sakharov, A. A. Sokolov, and V. A. Turkin, "Approximate calculation methods for pulse radiation of a TEM-horn array," *IEEE Trans. Electromagn. Compat*., vol. 43, no. 1, Feb. 2001.

[33] B. Wang, Q. Liu, C. Cao, Y. Yan, and T. Jiang, "A method for predicting time-domain radiation characteristics for bowtie antenna," *Int. Appl. Comput. Electromagn. Soc. Symp., ACES-China*, Hangzhou, CN, pp. 1-3, Aug. 2023.

[34] A. Bhattacharjee, A. Bhawal, A. Karmakar, A. Saha, and D. Bhattacharya, "Vivaldi antennas: A historical review and current state of art," *Int. J. Microw. Wirel. Technol*., vol. 13, no. 8, pp. 833-850, Oct. 2021.

[35] A. S. Arezoomand, R. A. Sadeghzadeh, and M. Naser-Moghadasi, "Novel techniques in tapered slot antenna for linearity phase center and gain enhancement," *IEEE Antennas Wirel. Propag. Lett*., vol. 16, pp. 270-273, June 2016.

[36] В. И. Кошелев, В. П. Беличенко, and Ю. И. Буянов, "Ultra-wideband electromagnetic radiation technology," National Defense Industry Press, CN, 2018.

Binwen Wang was born in Gansu, China, in 1993. He received his B.S. degree in Nuclear Science from Xi'an Jiaotong University, Xi'an, China, in 2015, and his M.S. degree in Electromagnetic Field and Microwave Techn-ology from the Northwest Institute of Nuclear Techn-ology, Xi'an, China, in 2017. He is currently an Engineer at the Northwest Institute of Nuclear Technology. His research interests include time-domain electromagnetics and ultra-wideband antenna.

Hui Ning was born in Zhejiang, China, in 1969. He received his M.S. and Ph.D. degrees in Nuclear Science and Technology from Tsinghua University, Beijing, China, in 1997 and 2001, respectively. He is currently a Professor at the Northwest Institute of Nuclear Technology, Xi'an, China, specializing in time-domain electromagnetics and the pulse power technique and its applications.

Hao Cai was born in Henan, China, in 1997. He received his B.S. and M.S. degree in Electromagnetic Field and Microwave Technology from the National Defense University of Science and Technology, Chang-sha, China, in 2019 and 2021. He is currently an Engineer at the Northwest Institute of Nuclear Technology, specializing in ultra-wideband pulse generator.

Qilong Liu was born in Hubei, China, in 1997. He received his B.S. degree in Power System and Automation from the Army Engineering University of PLA, Shijiazhuang, China, in 2019. He is currently an Assistant Engineer at the Northwest Institute of Nuclear Technology, specializing in ultra-wideband antenna.

Yan Wang was born in Ningxia, China, in 2000. She received her B.S. degree in Electromagnetic Field and Microwave Technology from the National Defense University of Science and Technology, Chang-sha, China, in 2022. She is currently an Engineer at the Northwest Institute of Nuclear Technology, specializing in ultra-wideband pulse generator.

Youjie Yan was born in Henan, China, in 1982. He received the B.S. degree in electronical information science and technology from Xidian University, Xi'an China, in 2005, the M.S. degree in electromagnetic field and microwave technology from the Northwest Institute of Nuclear Technology, Xi'an, China, in 2008, and the Ph.D. degree in plasma physics from the University of Electronic Science and Technology of China, Chengdu, China. He is currently a Professor level senior engineer. His research interests include the time-domain electromagnetics and the electromagnetic compatibility.

Compact-size Lightweight Beam-reconfigurable ESPAR Antenna with Parasitic Elements for UAV Applications

Min-Jae Kang[1], Yu-Seong Choi[2], and Wang-Sang Lee[1,*]

[1]Department of Electrical Engineering
Gyeongsang National University (GNU), B405-401, 501, Jinju-daero, Jinju-si, Gyeongnam, 52828, Republic of Korea
hunt0919@gnu.ac.kr, wsang@gnu.ac.kr
*Corresponding author

[2]Korea Aerospace Industries (KAI), Ltd
78, Gongdan 1-ro, Sanam-myeon, Sacheon-si, Gyeongnam, 52529, Republic of Korea
cys4140@gnu.ac.kr

Abstract – This paper presents a compact lightweight beam-reconfigurable antenna system for unmanned aerial vehicles (UAVs). The antenna system consists of a central active monopole element surrounded by eight parasitic elements, which can be controlled using PIN diodes to switch the beam across four elevation angles and eight azimuth beams. This beam-reconfigurable antenna system has several advantages over traditional UAV antennas, including light weight, efficiency, and compactness. The antenna system operates at 5.09 GHz and achieves a measured peak gain of 4.55 dBi, with a remarkably low weight of 9 g and a size of $1.00\lambda_0 \times 1.00\lambda_0 \times 0.22\lambda_0$.

Index Terms – Beam-reconfigurable, compact, electronically steerable parasitic array radiator (ESPAR) antenna, PIN didoes, UAV applications.

I. INTRODUCTION

Unmanned aerial vehicles (UAVs) are increasingly being used in various military applications and mission scenarios, as they offer several advantages over traditional aircraft, including flexibility, maneuverability, and cost-effectiveness. In the context of the Fourth Industrial Revolution, UAVs are expected to play an even more critical role in diverse fields such as logistics, disaster relief, and environmental monitoring. One of the key challenges in designing UAVs is developing efficient and compact communication systems. Reconfigurable antennas offer a promising solution to this challenge, as they can dynamically adjust their radiation patterns to adapt to changing environmental conditions and communication requirements [1–8].

Electronically Steerable Parasitic Array Radiator (ESPAR) is a well-known type of reconfigurable antenna that has been widely studied for UAV applications. ESPAR antennas consist of a central active radiating element surrounded by passive radiating elements. The passive elements play a crucial role in reflecting or re-radiating the waves emitted by the central active element. The re-radiation process is controlled by variable loads or switches that are connected to each passive element. By adjusting the loads applied to the passive elements, it is possible to alter the phase of the re-radiated waves. This allows for precise control over the radiation pattern and direction of the entire antenna array [9–19].

In this paper, we propose a modified ESPAR antenna design for UAV applications. The modified design enables precise control over both azimuth and elevation angles, facilitating enhanced beam steering capabilities at a center frequency of 5.09 GHz.

II. BACKGROUND THEORY

This section provides the theoretical foundation to comprehend the fundamental principles behind the functioning of the proposed antenna. To begin with, there are three mechanisms responsible for the mutual coupling in a multi-element ESPAR antenna, as depicted in Fig. 1 (a) [20]. These mechanisms include (1) direct spatial coupling between elements, (2) indirect coupling that can occur through scattering from nearby objects, such as support towers, and (3) a feed network that provides a pathway for coupling. Furthermore, there are elements in the multi-element antenna that do not generate their own current. Instead, they have significant currents induced by radiation from neighboring elements. These elements are referred to as parasitic elements, which have a significant impact on the performance of an antenna system that includes them. Let's consider ESPAR antenna consisting of one active element and (N-1) passive elements (a total of N elements). This ESPAR antenna can be represented as an N-port network, as shown in Fig. 1 (b).

Submitted On: May 17, 2024
Accepted On: July 5, 2024

https://doi.org/10.13052/2024.ACES.J.390507

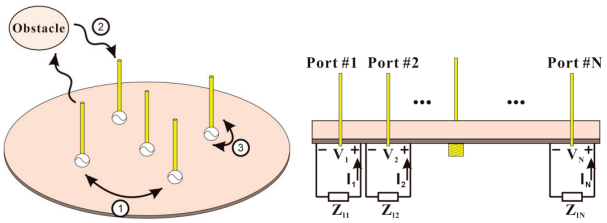

(a) (b)

Fig. 1. (a) Mechanisms for coupling between elements of a multi-element antenna and (b) a side view of the multi-port network representing the mutual coupling between active and parasitic elements.

The voltages and currents at the feeding point of each element can be defined using the following equation:

$$\begin{aligned} V_1 &= Z_{11}I_1 + Z_{12}I_2 + \cdots + Z_{1N}I_N, \\ V_2 &= Z_{21}I_1 + Z_{22}I_2 + \cdots + Z_{2N}I_N, \\ \vdots &= \qquad\qquad\qquad \vdots \\ V_N &= Z_{N1}I_1 + Z_{N2}I_2 + \cdots + Z_{NN}I_N, \end{aligned} \tag{1}$$

where V_k, I_k, and Z_{kk} represent the voltage, current, and self-impedance of the kth element, and Z_{ki} represents the mutual impedance between the kth and ith elements. The variables k and $i = 1, 2, \ldots N$. In ESPAR antenna, the parasitic elements are typically terminated with reactive loads, short circuits (SC), or open circuits (OC). Therefore, in a general form, we can consider them loaded with complex impedances denoted as Z_L. Thus, the voltage of parasitic ports is expressed as:

$$V_k = -I_k Z_{L,k}, \tag{2}$$

where $Z_{L,k}$ represents the impedance load of the kth element. By substituting (2) into (1), the matrix form can be obtained as in (3):

$$\begin{bmatrix} V_1 \\ 0 \\ 0 \\ \vdots \\ 0 \end{bmatrix} = \begin{bmatrix} Z_{11} & Z_{12} & Z_{13} & \cdots & Z_{1N} \\ Z_{21} & Z_{22}+Z_{L,2} & Z_{23} & \cdots & Z_{2N} \\ Z_{31} & Z_{32} & Z_{33}+Z_{L,3} & \cdots & Z_{3N} \\ \vdots & \vdots & \vdots & \ddots & \vdots \\ Z_{N1} & Z_{N2} & Z_{N3} & \cdots & Z_{NN}+Z_{L,N} \end{bmatrix} \begin{bmatrix} I_1 \\ I_2 \\ I_3 \\ \vdots \\ I_N \end{bmatrix}, \tag{3}$$

The Method of Moments (MoM) and the Finite Element Method (FEM) are the most commonly used numerical methods for computing the mutual impedance matrix in (3) then the elements' currents can be determined as given in (4):

$$\begin{bmatrix} I_1 \\ I_2 \\ I_3 \\ \vdots \\ I_N \end{bmatrix} = \begin{bmatrix} Z_{11} & Z_{12} & Z_{13} & \cdots & Z_{1N} \\ Z_{21} & Z_{22}+Z_{L,2} & Z_{23} & \cdots & Z_{2N} \\ Z_{31} & Z_{32} & Z_{33}+Z_{L,3} & \cdots & Z_{3N} \\ \vdots & \vdots & \vdots & \ddots & \vdots \\ Z_{N1} & Z_{N2} & Z_{N3} & \cdots & Z_{NN}+Z_{L,N} \end{bmatrix}^{-1} \begin{bmatrix} V_1 \\ 0 \\ 0 \\ \vdots \\ 0 \end{bmatrix}. \tag{4}$$

The mutual impedance matrix governs the magnitude, phase, and distribution of the elements' currents for the ESPAR antenna. The total field pattern of an N-element ESPAR antenna is the superposition of all elements' radiation patterns and can be obtained by (5). In this ESPAR antenna, the parasitic elements are arranged in a circular pattern around the active element [21]:

$$a(\theta,\phi) = E_1(\theta,\phi) + \sum_{k=2}^{N} I_k E_k(\theta,\phi) e^{j\left(\beta \cdot d \cdot \widehat{R}) sin\theta \; cos(\; \varphi - \varphi_k)\right)}, \tag{5}$$

where the angular position of the kth element is denoted by $\varphi_k = \frac{2\pi(k-1)}{N-1}$ represents the position vector of the kth element is the unit vector toward the observation point. $E_1(\theta,\phi)$ is the radiation patteren of the active element $E_k(\theta,\phi)$ is the field pattern of the single kth element. β is the phase constant. d is the distance between the active element and each passive element. I_k is the complex current excitation coefficient of the kth element. This current coefficient includes both magnitude and phase information, enabling precise control of the antenna's radiation pattern. The phase of these current coefficients determines the direction of maximum power radiation, while the magnitude influences the directivity, gain, and coverage characteristics of the antenna. In this paper, four different modes (Mode A, Mode B, Mode C, and Mode D) have been developed to generate multiple beams in the azimuth and elevation directions. Each mode can be constructed by activating one or more of the PIN diodes connected to the passive elements. The activation of the PIN diode connected to the *kth* passive element impacts its complex load impedance. Therefore, its complex current excitation coefficient I_k varies, resulting in different beam directions as described in (5).

III. ANTENNA CONFIGURATION

The proposed antenna consists of a central active element, which is a monopole, surrounded by passive elements, as illustrated in Figs. 2 (a-c). The active element at the center is fed by an RF signal, while the neighboring passive elements can either be connected or disconnected to the ground using the PIN diodes. The PIN diodes (SMP1331-079LF), which have a forward bias voltage of 0.8 V and reverse current of 10 μA have been selected for implementation with the passive elements due to their high-power handling, switching, and low insertion loss characteristics [22, 23]. Figure 2 (e) shows the equivalent circuit of the PIN diode. The resistance in the ON state (1.7 Ω) can cause RF losses. In ESPAR antennas, beam steering can be achieved by configuring the passive elements using the PIN diodes. The passive elements consist of bow-tie-shaped HPEs and monopole-shaped VPEs forming an antenna structure. Each of these elements is controlled by PIN diodes. Crucial parameters for impedance matching include the distance between the active element and VPEs, as well as the height of the VPEs. Increasing the distance improves the reflection

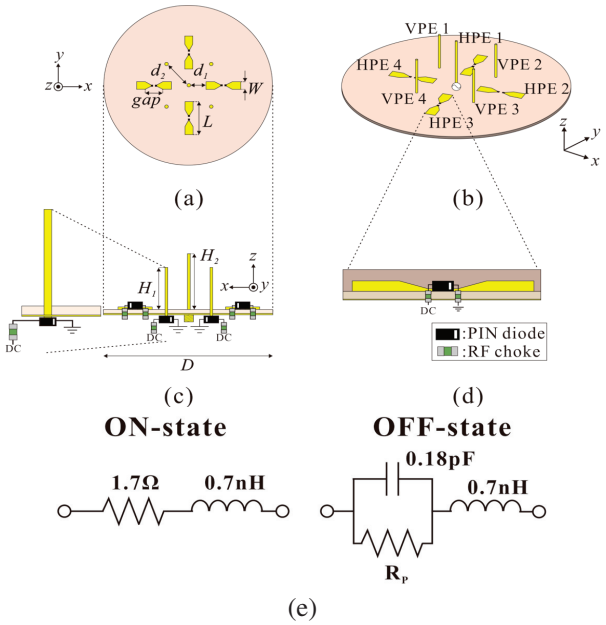

Fig. 2. Proposed antenna configuration: (a) a top view, (b) a perspective view, (c) a side view, (d) a HPE cutting plane view with a diode junction diagram, and (e) on/off equivalent model of the PIN diode.

coefficient, while increasing the height raises the operational frequency and narrows the bandwidth. When the PIN diodes are activated, the HPEs' arms connect, resulting in resonance at 5.09 GHz. These effectively act as reflectors. Similarly, when the PIN diodes of the VPEs are activated, they act as directors.

Figures 3 and 4 show that the number of activated passive elements controlled by PIN diodes determines the mode, and the simulated 3D gain patterns for Modes A, B, C, and D.

The primary difference among modes lies in the elevation angle. In Mode A, the antenna uses a single

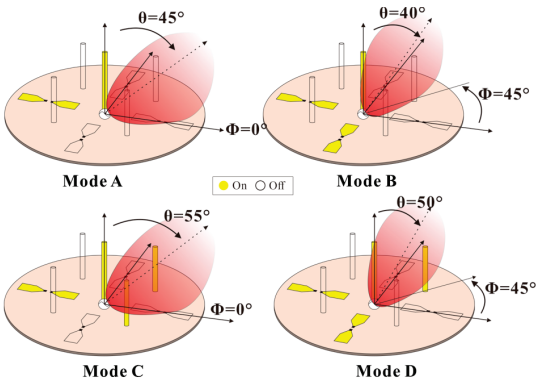

Fig. 3. Schematic diagram according to the operation of parasitic elements.

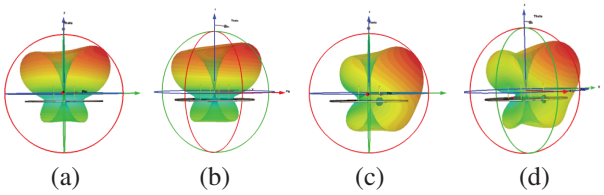

Fig. 4. Simulated 3-D realized gain patterns of different modes: (a) Mode A, (b) Mode B, (c) Mode C, and (d) Mode D.

HPE for beam steering and achieves azimuth angles of 0°, 90°, 180°, and 270°. The key feature of Mode A is that HPEs act as reflectors. In this mode, the antenna steers the beam in four different azimuth directions while maintaining an elevation angle of 45°. This means that the antenna's beam is tilted 45° upward from the horizontal plane. Mode B offers specific beam steering capabilities, using only two HPEs for achieving azimuth angles of 45°, 135°, 225°, and 315°. Similar to Mode A, Mode B maintains a consistent 40° elevation. Mode C employs one HPE and two VPEs for beam steering, achieving azimuth angles of 0°, 90°, 180°, and 270°. The presence of two VPEs helps to provide more precise beam direction while maintaining a relatively higher elevation angle of 55°. Mode D, the final operating mode, uses two HPEs and one VPE for beam steering at azimuth angles of 45°, 135°, 225°, and 315°. Similar to Mode B, this mode allows for diagonal beam steering, providing directional flexibility. This is particularly valuable when the target or communication point is not aligned with the primary azimuth points. One of the challenges in antenna design, especially when incorporating active components like PIN diodes, is managing potential interference between DC and RF signals. Such interference can degrade antenna performance, resulting in inconsistent radiation patterns and reduced efficiency. Figure 2 (d) shows how to address this challenge by integrating a chip inductor into the antenna design. This inductor, known as an RF choke, is connected in parallel to the HPE arm. Its purpose is to facilitate the smooth flow of the DC signal required to control the PIN diode while isolating it from the RF signal. This separation ensures that the DC signal does not interfere with the RF signal, enabling consistent and optimal antenna performance. The antenna's design philosophy prioritizes both performance and structural simplicity. A simple design expedites manufacturing, reduces potential points of failure, and often leads to cost savings. To align with this philosophy, the placement of the RF choke inductor has been carefully selected. Instead of introducing an external component or a complex network, the inductor was positioned directly on the substrate. This was achieved by drilling a via at the junction of the HPE arm and the PIN diode. This strategic placement minimizes the

length of the signal path, thereby reducing signal losses and ensuring efficient operation. Additionally, this placement contributed to a compact design.

IV. RESULTS AND DISCUSSION

For the experimental verification, the substrate of the proposed antenna is used in the TACONIC RF-35 which has a dielectric constant (ε_r) of 3.5, and loss tangent (tan δ) of 0.0018. The substrate has a thickness of 0.76 mm, and the thickness of the copper layer is 0.018 mm. Figure 5 shows the fabricated proposed antenna. The optimal parameters of the proposed antenna are shown in Table 1. These design parameters define the structure of the proposed antenna, which has a significant impact on its radiation pattern and frequency response. For instance, d_1 and d_2 represent the distances between elements in the proposed antenna, while H_1 and H_2 denote the height of the elements. *D, L, and W* determine the size and shape of the antenna, and the selection of these parameters is crucial in achieving the desired antenna performance. In Figs. 6 (a-b), simulation results are presented based on design parameters related to the most critical aspect of the proposed antenna, namely VPE. As the distance (d_2) between the central active element and VPE increases, the reflection coefficient improves. Additionally, when the height of VPE (H_1) is increased, the operating frequency shifts to higher frequency bands, resulting in a narrower bandwidth. The comparison of simulated

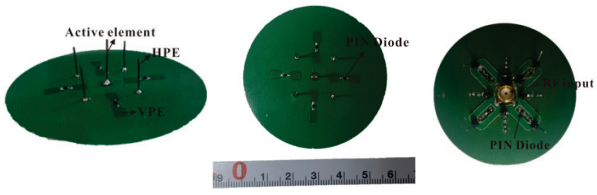

(a) (b) (c)

Fig. 5. Fabricated proposed antenna: (a) a perspective view, (b) a top view, and (c) a bottom view.

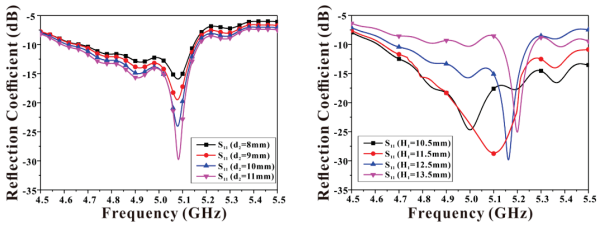

(a) (b)

Fig. 6. Simulated impedance characteristics of the proposed antenna with regard to the design parameters: (a) impedance characteristics in regard to the distance (d_2) between active element and VPE and (b) impedance characteristics in regard to the height (H_1) of VPE.

Table 1: Geometric design parameters of the proposed antenna (unit = mm)

d_1	d_2	W	L
6	13	2.8	12.28
gap	H_1	H_2	D
6	10.5	13.3	58.93

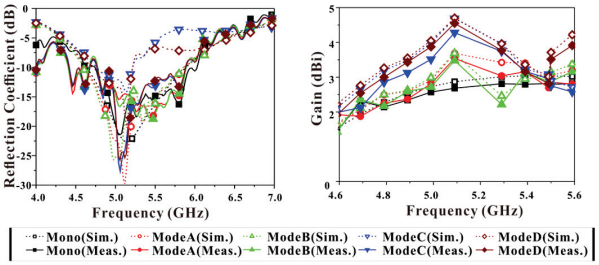

(a) (b)

Fig. 7. The characteristics of the proposed antenna at operating mode.

and measured results for various operating modes of the proposed antenna underscores its versatility and flexibility. Figure 7 (a) illustrates the measured 10-dB bandwidth of the proposed antenna, which spans from 4.61 GHz to 5.86 GHz. The operating frequency range of the proposed antenna makes it suitable for a wide range of applications. The measurements of the *S*-parameters were carried out using a vector network analyzer by Rohde & Schwarz (RS-ZND 40). The simulated and measured gains are shown in Fig. 7 (b), a peak gain of approximately 4.55 dBi can be obtained when Mode D is selected. The discrepancy between the simulated and measured results is attributed to the use of PIN diodes. PIN diodes exhibit non-ideal behavior in real-world applications, including parasitic inductance, resistance, and capacitance, which are often simplified or neglected in simulations. Consequently, PIN diodes can introduce additional impedance variations and losses that are difficult to accurately model in simulations. Modes C and D exhibit higher discrepancies between the simulated and measured results because they utilize more PIN diodes compared to the other proposed modes.

Figures 8 (a-d) illustrates the comparison between simulation and measurement values for the azimuth angles for each mode. In each operational mode, the configuration was systematically classified based on distinct azimuth angles. These radiation patterns in Modes A to D demonstrate the antenna's ability to steer the beam in specific directions, offering precise directionality required in various application scenarios.

Modes A and C exhibit azimuth angles of 0°, 90°, 180°, and 270°, while Modes B and D show angles of 45°, 135°, 225°, and 315°. As previously mentioned, equivalent resistors in the PIN diodes cause RF losses.

Table 2: Comparison of the proposed antenna parameters with other antenna designs

Antenna Parameters		[14]	[15]	[16]	[17]	[18]	Prop.
$f_c(GHz)$		2.055	2.45	2.484	2.44	5.09	**5.09**
BW (%)		2.6	16	N/A	N/A	8.6	**12.7**
Peak gain (dBi)		4.58	N/A	5.3	8.1	4.9	**4.55**
Num. of Az. Beams		2	15	12	6	8	**8**
Num. of Ele. Beams		2	3	1	3	1	**4**
Num. of Act. Elem.		4	1	1	1	1	**1**
Num. of Para. Elem.		4	8	12	12	8	**8**
Elect.Size (λ_0^3)	L (λ_0)	1.21	1.63	1.26	1.06	1.00	**1.00**
	W (λ_0)	1.17	1.63	1.26	1.06	1.00	**1.00**
	H (λ_0)	0.05	0.26	0.25	0.36	0.25	**0.22**

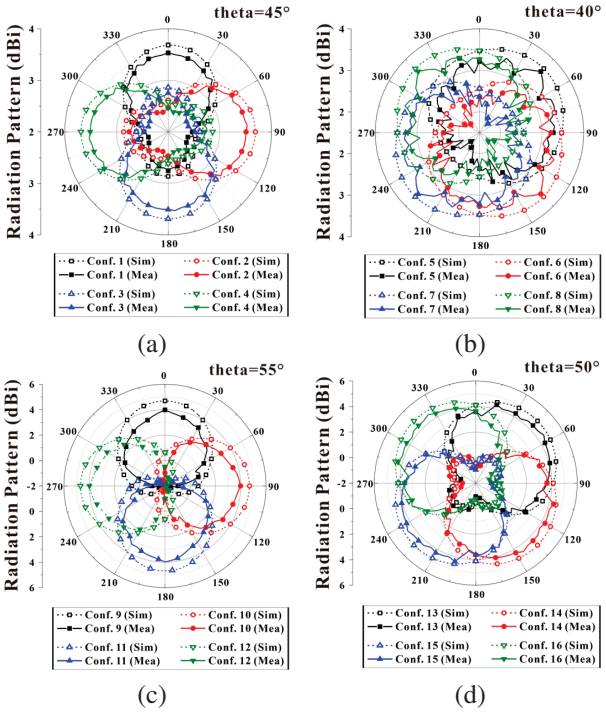

Fig. 8. Radiation pattern with regard to the operating modes at 2D cutting plane: (a) Mode A at $\theta = 45^\circ$, (b) Mode B at $\theta = 40^\circ$, (c) Mode C at $\theta = 55^\circ$, and (d) Mode D at $\theta = 50^\circ$.

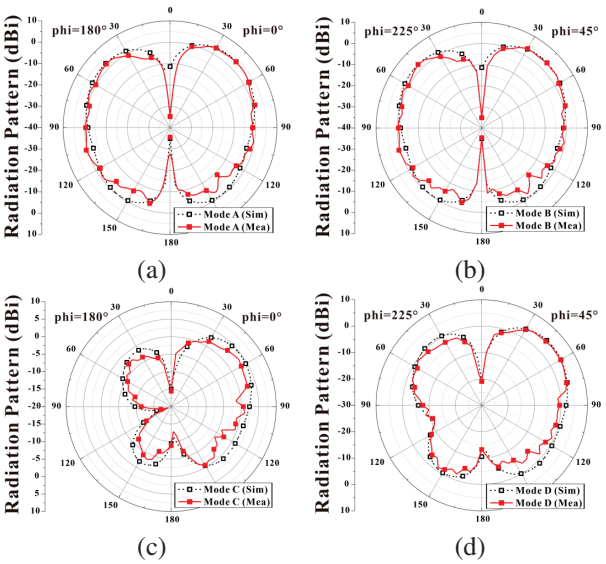

Fig. 9. Radiation pattern by operating mode at 2D cutting plane: (a) Mode A, (b) Mode B, (c) Mode C, and (d) Mode D.

Since the proposed antenna utilizes up to three PIN diodes in a single mode, the actual measured gain of the antenna exhibits some discrepancies from the simulated gain. Figs. 9 (a-d) illustrate a comparison of elevation angles for all beam patterns from Mode A to Mode D. With a single reflector (HPE), Mode A has an elevation angle of 45°. Mode C with added VPEs achieves a maximum elevation angle of 55°. Mode B, with two reflectors, maintains a 40° elevation angle, while Mode D, featuring an additional VPE, reaches an elevation angle of 50°. The proposed antenna has the highest number of elevation-beams compared to the other antenna designs. Furthermore, the performance of the proposed antenna, in terms of compact size, wide bandwidth, high gain, simple structure, and a high number of azimuth-beams, is comparable to that of the previous antenna designs, as indicated in Table 2. Compared to the other antenna designs in Table 2, the proposed antenna has the smallest size. When compared to [17] and [18], which also utilize

a single active element, the proposed antenna uses fewer parasitic elements while achieving control over two additional azimuth angles and one additional elevation angle compared to [17]. Despite having the same number of parasitic elements as [18], the proposed antenna can control four elevation angles, unlike [18], which cannot control elevation angles.

V. CONCLUSION

A 5.09 GHz beam-reconfigurable antenna for U2X communications is presented in this paper. The proposed antenna consists of VPEs and HPEs parasitic elements, each using PIN diodes, and it switches the beam direction to eight azimuth and four elevation angles. This indicates that fewer parasitic elements are used compared to the number of reconfigurable modes, while still using a small number of active elements. The RF choke of this antenna is inserted through via in the substrate, making it more compact and reducing signal loss, thus increasing efficiency. The antenna was fabricated and tested in an anechoic chamber, and the results show that the antenna achieves a peak gain of 4.55 dBi and a low weight of 9 g. The proposed antenna design has the potential to significantly improve the communication, radar, and search and rescue capabilities of UAVs. It is also lightweight and compact, making it ideal for UAV applications.

ACKNOWLEDGMENT

This work was supported in part by the Korean Government (MSIT) through the National Research Foundation of Korea, South Korea, under Grant RS-2024-00338277, in part by the Institute of Information & Communications Technology Planning & Evaluation (IITP) grant funded by the Korea government (MSIT), under Grant RS-2022-00156409 (ICT innovation human resources 4.0).

REFERENCES

[1] F. Grimaccia, F. Bonfante, M. Battipede, P. Maggiore, and E. Filippone, "Risk analysis of the future implementation of a safety management system for multiple RPAS based on first demonstration flights," *Electronics*, vol. 6, no. 3, pp. 50, 2017.

[2] H. Baek and J. Lim, "Design of future UAV-relay tactical data link for reliable UAV control and situational awareness," *IEEE Communications Magazine*, vol. 56, no. 10, pp. 140-150, 2018.

[3] H. Ullah, N. G. Nair, A. Moore, C. Nugent, P. Muschamp, and M. Cuevas, "5G communication: An overview of vehicle-to-everything, drones, and healthcare use-cases," *IEEE Access*, vol. 7, pp. 37251-37268, 2019.

[4] R. Kovalchukov, D. Moltchanov, A. Samuylov, and A. Ometov, "Analyzing effects of directionality and random heights in drone-based mmwave communication," *IEEE Transactions on Vehicular Technology*, vol. 67, no. 10, pp. 10064-10069, 2018.

[5] S. A. R. Naqvi, S. A. Hassan, H. Pervaiz, and Q. Ni, "Drone-aided communication as a key enabler for 5G and resilient public safety networks," *IEEE Communications Magazine*, vol. 56, no. 1, pp. 36-42, 2018.

[6] M. S. Sharawi, O. A. Rawashdeh, and D. N. Aloi, "Performance of an embedded monopole antenna array in a UAV wing structure," in *Melecon 2010 - 2010 15th IEEE Mediterranean Electrotechnical Conference*, Valletta, Malta, pp. 835-838, 2010.

[7] X. Miao, W. Wan, Z. Duan, and W. Geyi, "Design of dual-mode arc-shaped dipole arrays for indoor base-station applications," *IEEE Antennas and Wireless Propagation Letters*, vol. 18, no. 4, pp. 752-756, 2019.

[8] C. U. Lee, G. Noh, B. Ahn, J.-W. Yu, and H. L. Lee, "Tilted-beam switched array antenna for UAV mounted radar applications with 360° coverage," *Electronics*, vol. 8, no. 11, pp. 1240, 2019.

[9] M. Taromaru and T. Ohira, "Electronically steerable parasitic array radiator antenna: Principle control theory and its applications," *Proc. Int. Union of Radio Science General Assembly*, 2005.

[10] R. Harrington, "Reactively controlled directive arrays," *IEEE Transactions on Antennas and Propagation*, vol. 26, no. 3, pp. 390-395, 1978.

[11] T. Ohira and K. Iigusa, "Electronically steerable parasitic array radiator antenna," *Electronics and Communications in Japan (Part II: Electronics)*, vol. 87, no. 10, pp. 25-45, 2004.

[12] C. Sun, A. Hirata, T. Ohira, and N. C. Karmakar, "Fast beamforming of electronically steerable parasitic array radiator antennas: Theory and experiment," *IEEE Transactions on Antennas and Propagation*, vol. 52, no. 7, pp. 1819-1832, 2004.

[13] J. Costantine, Y. Tawk, S. E. Barbin, and C. G. Christodoulou, "Reconfigurable antennas: Design and applications," *Proceedings of the IEEE*, vol. 103, no. 3, pp. 424-437, 2015.

[14] S. V. S. Nair and M. J. Ammann, "Reconfigurable antenna with elevation and azimuth beam switching," *IEEE Antennas and Wireless Propagation Letters*, vol. 9, pp. 367-370, 2010.

[15] Z. Shi, R. Zheng, J. Ding, and C. Guo, "A novel pattern-reconfigurable antenna using switched printed elements," *IEEE Antennas and Wireless Propagation Letters*, vol. 11, pp. 1100-1103, 2012.

[16] M. Groth, M. Rzymowski, K. Nyka, and L. Kulas, "ESPAR antenna-based WSN node with DoA estimation capability," *IEEE Access*, vol. 8, pp. 91435-91447, 2020.

[17] M. Rzymowski and L. Kulas, "Two-row ESPAR antenna with simple elevation and azimuth beam switching," *IEEE Antennas and Wireless Propagation Letters*, vol. 20, no. 9, pp. 1745-1749, 2021.
[18] Y.-S. Choi and W.-S. Lee, "Reconfigurable beam switching antenna with horizontal parasitic element reflector (HPER) for UAV applications," in *2020 IEEE International Symposium on Antennas and Propagation and North American Radio Science Meeting*, Montreal, QC, Canada, pp. 433-434, 2020.
[19] H. Kawakami and T. Ohira, "Electrically steerable passive array radiator (ESPAR) antennas," *IEEE Antennas Propag. Mag.*, vol. 47, no. 2, pp. 43-50, Apr. 2005.
[20] R. Movahedinia, "Low-cost beam steerable antennas using parasitic elements," Dissertation, Concordia University, 2018.
[21] C. A. Balanis, *Antenna Theory: Analysis and Design*. Hoboken, NJ: Wiley, 2016.
[22] C. G. Christodoulou, Y. Tawk, S. A. Lane, and S. R. Erwin, "Reconfigurable antennas for wireless and space applications," *Proceedings of the IEEE*, vol. 100, no. 7, pp. 2250-2261, 2012.
[23] D. Piazza, P. Mookiah, M. D'Amico, and K. R. Dandekar, "Experimental analysis of pattern and polarization reconfigurable circular patch antennas for MIMO systems," *IEEE Transactions on Vehicular Technology*, vol. 59, no. 5, pp. 2352-2362, 2010.

Min-Jae Kang received the B.S. degrees in electronic engineering from Gyeongsang National University (GNU), Jinju, South Korea, in 2023. His research interests are reconfigurable antennas for unmanned aeronautics, wireless power transfer, high-power microwave systems, and communications systems, RFID/IoT sensors, and RF/microwave circuit and antenna designs.

Yu-Seong Choi received the B.S. and the M.S. degrees in electronic engineering from Gyeongsang National University (GNU), Jinju, South Korea, in 2019 and 2021, respectively. Since 2022, he is currently working in Korea Aerospace Industries.

His research interests include reconfigurable antenna design & analysis, RF/Microwave circuits and systems, and RFID/IoT sensors.

Wang-Sang Lee received the B.S. degree from Soongsil University, Seoul, South Korea, in 2004, and the M.S. and Ph.D. degrees in electrical engineering from the Korea Advanced Institute of Science and Technology (KAIST), Daejeon, South Korea, in 2006 and 2013, respectively.

From 2006 to 2010, he was with the Electromagnetic Compatibility Technology Center, Digital Industry Division, Korea Testing Laboratory (KTL), Ansan-si, South Korea, where he was involved in the international standardization for radio frequency identification (RFID) and photovoltaic systems as well as electromagnetic interference (EMI)/EMC analysis, modeling, and measurements for information technology devices. In 2013, he joined the Korea Railroad Research Institute (KRRI), Uiwang-si, South Korea, as a Senior Researcher, where he was involved in the position detection for high-speed railroad systems and microwave heating for low-vibration rapid tunnel excavation system. Since 2014, he has been an Associate Professor with the Department of Electronic Engineering, Gyeongsang Nat'l University (GNU), Jinju, South Korea. From 2018 to 2019, he was a Visiting Scholar with the ATHENA Group, Georgia Institute of Technology, Atlanta, GA, USA. His current research interests include near- and far-field wireless power and data communications systems, RF/microwave antenna, circuit, and system design, RFID/Internet of Things (IoT) sensors, and EMI/EMC.

Dr. Lee is a member of IEC/ISO JTC1/SC31, KIEES, IEIE, and KSR. He was a recipient of the Best Paper Award at IEEE RFID in 2013, the Kim Choong-Ki Award Electrical Engineering Top Research Achievement Award at the Department of Electrical Engineering, KAIST, in 2013, the Best Ph.D. Dissertation Award at the Department of Electrical Engineering, KAIST, in 2014, the Young Researcher Award at KIEES in 2017, and the Best Paper Awards at IEIE in 2018 and KICS in 2019.

A Low Profile Polarization-insensitive Multiple-band Metamaterial Absorber using a Slotted Octagonal Unit Cell

Mohamed Elhefnawy[1,2], KyoungHun Kim[1], Tae-Hyeon Kim[1], and Wang-Sang Lee[1]

[1]Department of Electronic Engineering
Gyeongsang National University, Jinju, 52828, South Korea
wsang@gnu.ac.kr

[2]Department of Electrical Engineering
October 6 University, Egypt

Abstract **–** This paper introduces a thin, polarization-insensitive (PI), and multiple-band electromagnetic metamaterial absorber (MMA). The unit cell of the MMA consists of a slotted octagonal metallic patch printed on an FR4 dielectric substrate, backed by a grounded metallic layer, and notably does not incorporate resistive lumped elements. The proposed MMA exhibits measured absorption, exceeding 75% for normal incidence, across frequency bands ranging from 2.22–2.38 GHz, 6.86–7.24 GHz, 11.68–12.71 GHz, 14.1–14.8 GHz, and 15.47–16 GHz. The proposed MMA unit cell has dimensions of $0.21\lambda_0 \times 0.21\lambda_0$ and a thickness of $0.001\lambda_0$, where λ_0 represents the wavelength corresponding to the lowest frequency at 2.22 GHz. The performance of the proposed MMA is simulated using CST Microwave Studio and MATLAB, and subsequently validated through experimental measurements.

Index Terms **–** Absorption, metamaterial absorber (MMA), metasurface absorber, polarization-insensitive (PI), transmission line (TL) model.

I. INTRODUCTION

Absorbers are commonly utilized in various applications, including stealth technology and anechoic chambers. The wedge-tapered absorber is the most commonly used type of electromagnetic absorber, often employed in anechoic chambers. However, this pyramid-shaped array absorber is susceptible to damage and has large dimensions [1]. One of the most widely used absorbers is the Salisbury absorber, which is composed of three layers. The first layer consists of a thin resistive sheet, the middle layer is a low-loss dielectric with a thickness equal to an odd multiple of the quarter wavelength, and the bottom layer is a perfect electric conductor (PEC) located behind the dielectric slab. The odd multiples of the quarter-wavelength thickness of the dielectric material result in the transformation of a short circuit at the bottom layer into an open circuit at the top resistive layer. The effective impedance of the Salisbury structure is determined by the impedance of the top resistive layer. Impedance matching occurs when the impedance of the resistive layer matches that of free space. However, the Salisbury screen is limited by two primary constraints: its thickness and operational bandwidth. Furthermore, the Salisbury absorber maintains a bulky structure, especially when operating at lower frequencies. To address the problem of limited bandwidth, the Jaumann absorber has been developed to provide a wider absorption bandwidth by using a multi-layered design, while still maintaining a significant thickness similar to previous absorbers. The circuit analog absorber (CAA) consists of a periodic arrangement of conductive metal instead of a resistive sheet. The challenge of thickness persists in the CAA due to the middle layer's thickness being approximately one-quarter of the wavelength. Metamaterials can be used as absorbers because they have the potential to effectively prevent the reflection and transmission of incident waves within specific frequency bands and polarizations. The metamaterial absorber (MMA) consists of periodic unit cells, with each cell comprising a dielectric substrate positioned between a top metallic layer and a ground layer at the bottom [2–4]. MMA may exhibit negative permeability and permittivity, or a negative refractive index. The negligible transmission through the absorber is attributed to the existence of a copper ground at the bottom of each unit cell [5]. The thin structure of the metamaterial can be classified as a metasurface [6]. Metasurface absorbers exhibit unique characteristics due to their artificial sub-wavelength structure. In the metasurface configuration, the surface currents present on the top resonance layer induce an electric resonance. Furthermore, the top resonance structure has the ability to interact with the ground layer, leading to the creation of anti-parallel currents that produce

Submitted On: March 13, 2024
Accepted On: June 18, 2024

https://doi.org/10.13052/2024.ACES.J.390508

magnetic resonance [7]. The permittivity and permeability can be manipulated by utilizing the induced electric and magnetic resonances, respectively. As a result, it is possible to achieve impedance matching between the metasurface absorber and free space [8, 9]. There are many approaches that can be used to enhance the bandwidth of the electromagnetic absorber. One strategy is to incorporate lossy materials, such as resistive sheets, lumped resistors, or high-loss substrates. Another approach is to introduce multiple absorption bands and combine them to create a broader absorption bandwidth. Additionally, the pin diodes can be integrated with electromagnetic absorbers to switch between different frequency bands. For instance, in [10], a wide fractional bandwidth absorber was constructed by symmetrically placing eight 100 Ω chip resistors along a 16-sided loop. Notably, there is a gap between the substrate layer and the ground in this configuration. In [11], the unit cell of the periodic structure contains two bow-tie dipoles, along with an additional resistive load. In [12], a low-profile absorber with ultrawideband capabilities was developed by incorporating a resistive frequency selective surface (FSS) layer on a ground-backed substrate. The utilization of single- and double-layer resistive FSS was introduced in [13]. Additionally, a design for an absorber using concentric circular rings loaded with lumped resistances was presented in [14]. A low-cost, extremely thin, and angularly stable metallic high-impedance FSS absorber was presented in [15]. In [16], a configuration of three interconnected hexagonal split-ring resonators was introduced to create an MMA with a negative refractive index. Additionally, the design of metamaterial unit cells with matching permittivity and permeability was presented in [17] to generate an absorber with an impedance equal to that of free space. In [18], a periodic arrangement of double-split ring resonators was presented. This MMA demonstrated the ability to absorb electromagnetic waves regardless of their polarization. The relative permeability was controlled by inducing magnetic resonance, which was caused by the generation of surface currents flowing in opposite directions between the top and bottom layers. Furthermore, the dielectric constant was manipulated by the induced electric field in the capacitive gap on the top layer. In [19], it was observed that the intense concentration of electromagnetic fields leads to the absence of reflection, causing the incident EM wave to be absorbed. In [20], two FSS layers positioned on either side of a dielectric substrate were utilized to create a dual-sided absorber. In [21], an ultra-thin MMA was designed to minimize the in-band radar cross-section (RCS) of a waveguide slot antenna. This absorber comprised two metal layers separated by a lossy dielectric spacer. The top layer consisted of an etched oblique cross-gap patch arranged in a periodic pattern, while the bottom layer was made of solid metal. Additionally, in [22], a C-band microwave absorber based on complementary split-ring resonators (CSRR) was introduced. In [23], the FSS unit cell design allows for the integration of PIN diodes between neighboring unit cells to facilitate switching between the X-band and C-band for RF shielding applications.

This research presents a novel MMA design, notable for its capacity to support a greater number of frequency bands when compared to designs of similar size and low profile. Unlike prior studies that relied on complex structures or resistive lumped elements, the proposed MMA design utilizes a new simple structure consisting of a slotted octagonal unit cell with a symmetrical configuration to ensure remarkable polarization insensitivity and offers high absorptivity for both TE and TM polarizations.

II. THEORETICAL BACKGROUND

In this section, an overview is presented on the theoretical foundation for the mathematical modeling of MMA. Two approaches are employed for the modeling of these absorbers. The first approach involves manipulating the permittivity and permeability of the MMA, whereas the second approach is based on applying transmission line (TL) theory to model the MMA.

A. Mathematical modeling of MMA based on permittivity and permeability

The input impedance of the MMA (Z_{MM}) can be adjusted by controlling its complex relative permittivity (ε_r) and complex relative permeability (μ_r). This can be expressed as follows:

$$Z_{MM}(\omega) = \sqrt{\frac{\mu_o \mu_r(\omega)}{\varepsilon_o \varepsilon_r(\omega)}}. \tag{1}$$

The reflection coefficients for perpendicular and parallel polarizations at oblique incidence are provided by the following equations:

$$\Gamma_{\perp} = \frac{Z_{MM}\cos(\theta_i) - Z_o\cos(\theta_t)}{Z_{MM}\cos(\theta_i) + Z_o\cos(\theta_t)}, \tag{2}$$

$$\Gamma_{\parallel} = \frac{Z_{MM}\cos(\theta_t) - Z_o\cos(\theta_i)}{Z_{MM}\cos(\theta_t) + Z_o\cos(\theta_i)}. \tag{3}$$

Where θ_i and θ_t are the incident and transmission angles, respectively. Z_o is the free space impedance. By adjusting the geometry of the MMA unit cell, it is possible to tailor the absorber's permittivity and permeability. As a result, the impedance of the MMA will match that of free space, leading to the absence of reflection of the incident electromagnetic waves from the absorber. The reflection coefficients will change as the incident and transmitted angles are varied. When an electromagnetic wave hits the surface of the MMA, it is reflected and transmitted. To achieve high absorption, it is important to minimize both the reflection coefficients ($\Gamma_{\perp}$ and

$\Gamma_{\parallel}$) and transmission coefficient (T). This is because the absorption (A) can be determined as:

$$A = 1 - \left[|\Gamma_{\perp}|^2 + |\Gamma_{\parallel}|^2\right] - |T|^2. \quad (4)$$

B. Mathematical modeling of MMA based on transmission line theory

The MMA can be represented using a TL model. In this model, the straight metallic strip is represented as an inductor (L), while the gap between the metallic strips is represented as a capacitor (C). Additionally, the losses of the conductor and substrate, as well as any lumped resistors that may be utilized, can be modeled by a resistor (R). It is important to note that the dielectric losses increase as the number of metallic gaps increases [2]. The TL model only considers the capacitances that are aligned with the incident electric field, while disregarding those in other orientations. The specific values of inductances, capacitances, and resistors depend on the configuration and structure of the MMA unit cell and can be calculated using various mathematical formulas [2, 5, 13, 15, 16, 22–26]. The number of RLC resonant circuits that can be created in the TL model is determined by the number of current paths in the MMA [2]. The equivalent impedance for the ground and substrate layers is denoted by Z_1 as indicated in Fig. 1.

$$Z_1 = Z_{o1} \tanh(\gamma h). \quad (5)$$

Where $\left(Z_{o1} = Z_o \sqrt{\frac{\mu_{rc}}{\varepsilon_{rc}}}\right)$ represents the characteristic impedance of the substrate, and h is the substrate thickness. ($\gamma = \alpha + j\beta$) represents the propagation constant in the dielectric substrate layer, while α represents the attenuation constant, and β denotes the phase constant. f and c denote the frequency and speed of light, respectively. Also, the complex relative permeability in the substrate is denoted as μ_{rc}, and the complex relative permittivity inside the substrate is represented by ($\varepsilon_{rc} = \varepsilon_r - j\frac{\sigma}{2\pi f \varepsilon_o}$), where ε_r and σ represent the relative permittivity and the conductivity of the substrate, respectively. ε_o represents the permittivity of free space. The impedance of the resonant layer of the MMA (Z_{MMA}) is given as:

$$Z_{MMA} = \sum_{n=1}^{M} R_n + j2\pi f L_n + \frac{1}{j2\pi f C_n}. \quad (6)$$

The total number of RLC resonant circuits in the TL model is represented by M. The input impedance of the MMA can be expressed as follows:

$$Z_{MM} = Z_{MMA} \parallel Z_1. \quad (7)$$

Equations (2), (3), and (4) can also be applied similarly to the TL model to determine the absorptivity of the MMA.

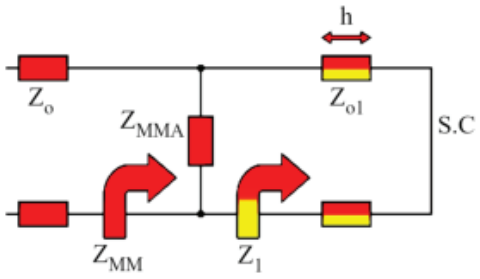

Fig. 1. TL model for the MMA.

III. RESULTS AND DISCUSSION

The proposed MMA unit cell consists of the top layer featuring a slotted octagonal metallic patch printed on an FR-4 dielectric substrate, backed by a grounded metallic layer. The relative permittivity of FR-4 is 4.3, with a thickness of 1.6 mm, and a loss tangent of 0.025. The FR-4 substrate was selected for the proposed MMA due to its high-loss characteristics. Both the top and bottom metallic layers are constructed from copper, each with a thickness of 0.035 mm. The octagonal shape was selected for constructing the unit cell to achieve symmetry. The dimensions of the unit cell were determined based on the desired operational frequency. Incorporating slots into the octagonal shape induces resonances at the desired frequency bands. By selecting the octagonal shape for the unit cell, optimizing its geometry, and utilizing slots within the octagonal shape, it is possible to control the values of permittivity and permeability of the MMA unit cell, thereby improving the absorption properties of the MMA. The proposed unit cell size is 28.854 mm $\times$ 28.854 mm; the dimension parameters are shown in Fig. 2.

The absorptivity of the proposed MMA was simulated using the S-parameters obtained from the frequency domain solver in CST MWS. In the frequency domain solver, the periodic boundary conditions and Floquet port excitation were adopted to approximate the periodic structure of the MMA as shown in Fig. 3. The proposed MMA unit cell was excited with two Floquet modes: TE and TM. In the TE mode, the incident wave propagates in the z-direction, with the electric field polarized in the y-direction, while the magnetic field is directed in the x-direction. On the other hand, in the case of the TM mode, the incident wave also propagates in the z-direction, with the electric field polarized in the x-direction and the magnetic field in the y-direction.

To extract the material properties of the proposed MMA, a time domain solver with two TE ports is used in CST simulation to obtain the reflection coefficient (S_{11}^{TE}) and transmission coefficient (S_{21}^{TE}), as illustrated in Fig. 4. Here, S_{11}^{TE} defines the reflection coefficient when the reflected and incident waves are at port 1, while S_{21}^{TE} represents the transmission coefficient for reflected

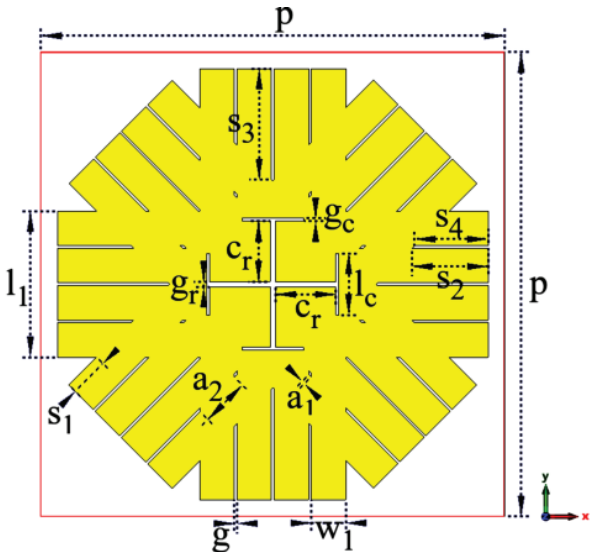

Fig. 2. Geometry of the proposed MMA unit cell. (p = 28.854 mm, s_1 = 2.426 mm, s_2 = 4.734 mm, s_3 = 6.963 mm, s_4 = 4.574 mm, w_1 = 2.148 mm, g = 0.16 mm, a_1 = 0.226 mm, a_2 = 3.038 mm, l_1 = 9.073 mm, l_c = 3.833 mm, c_r = 3.76 mm, g_r = 0.325 mm, g_c = 0.175 mm).

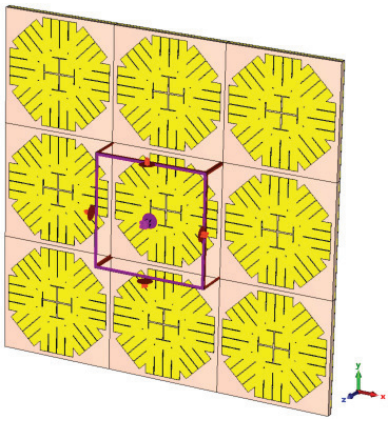

Fig. 3. CST simulation for the proposed MMA using frequency domain solver.

and incident waves at ports 2 and 1, respectively. The permeability, permittivity, refractive index, and normalized impedance of the proposed MMA have been simulated using MATLAB. The MATLAB simulations utilized the extracted S-parameters obtained from the time domain solver in CST, with mathematical formulations provided in [27].

The real part of the refractive index exhibits negative values around the resonance frequencies of 2.245 GHz, 6.76 GHz, 12 GHz, and 14.88 GHz, demonstrating the metamaterial properties of the proposed absorber, as illustrated in Fig. 5 (a). Moreover, the imaginary part of the permeability has higher values near the resonance

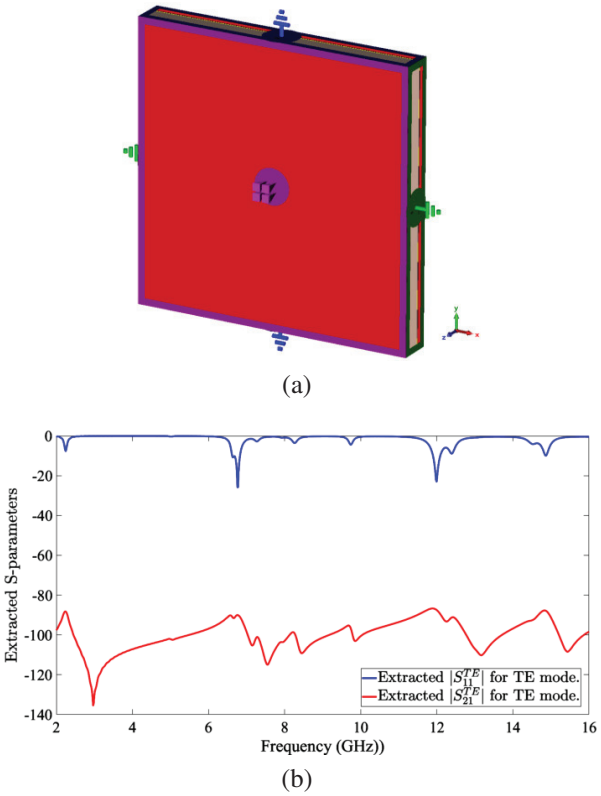

Fig. 4. CST model with two TE ports to extract the S-parameters of the proposed MMA unit cell: (a) CST model and (b) extracted S-parameters.

frequencies as shown in Fig. 5 (b). Furthermore, the value of the imaginary part of the permittivity increases in the vicinity of the resonance frequencies, as shown in Fig. 5 (c). The proposed MMA unit cell will be matched at frequencies of 2.245 GHz, 6.76 GHz, 12 GHz, and 14.88 GHz. This occurs when the real part of the normalized impedance tends to have high values, while the imaginary part is close to 0, as illustrated in Fig. 5 (d).

The electric field and surface current distributions for the proposed MMA were simulated using CST at 2.35 GHz, 6.97 GHz, and 11.87 GHz under TE and TM wave excitations to analyze the absorption mechanism in the proposed MMA unit cell. In TE mode excitation, the electric field on the top layer is more concentrated along the y-direction. The electric field intensity decreases at the center of the MMA unit cell as the resonance frequency increases as shown in Figs. 6 (a), 6 (e), and 6 (i). Additionally, on the bottom layer, the electric field concentration becomes more weakened as the resonance frequency increases, leading to a greater reduction in capacitive leakage loss as indicated in Figs. 6 (b), 6 (f), and 6 (j). In the TM mode, the electric field distribution remains the same as in the TE mode, but the electric

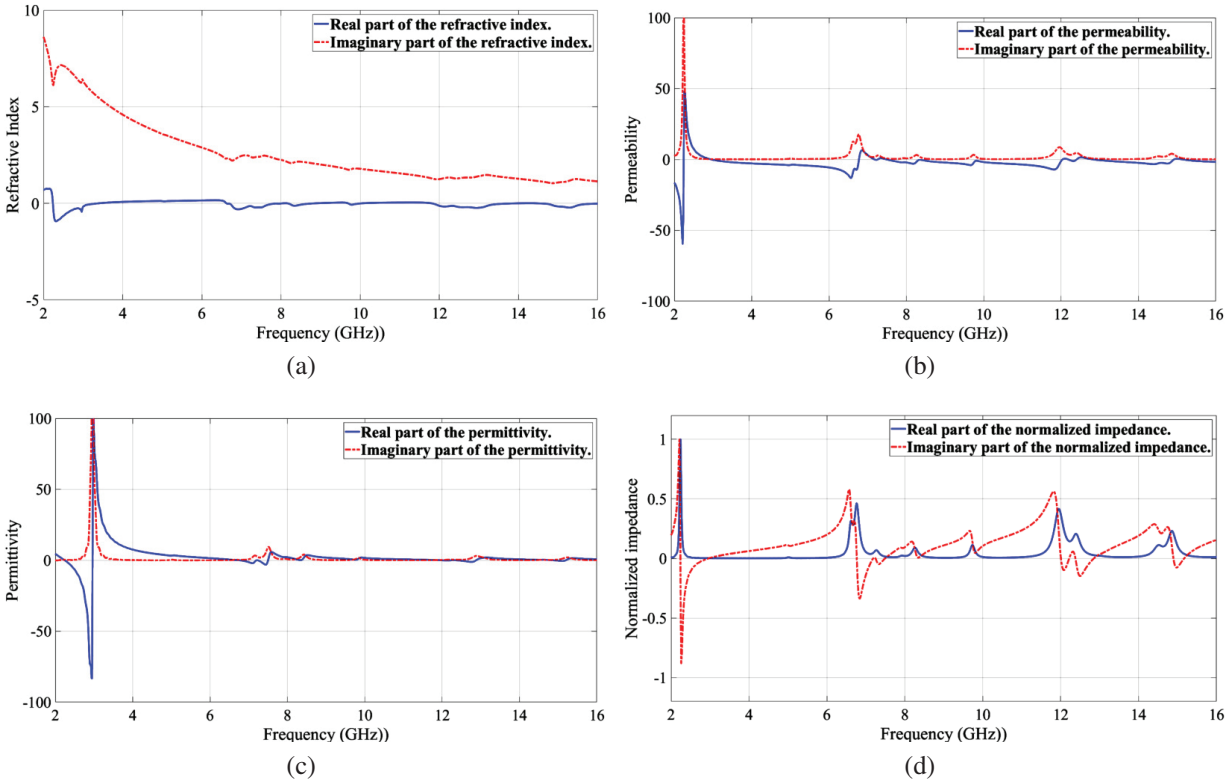

Fig. 5. MATLAB simulation for the material properties of the proposed MMA unit cell: (a) refractive index, (b) permeability, (c) permittivity, and (d) normalized impedance.

field is concentrated along the x-axis on the top and bottom layers as shown in Figs. 7 (a), 7 (b), 7 (e), 7 (f), 7 (i), and 7 (j). As the resonance frequency increases, there is a corresponding increase in the number of metallic gaps, which consequently leads to higher dielectric losses [2]. However, there is a greater decrease in the concentration of the electric field across a larger area on the top and bottom layers, thereby causing a reduction in capacitive leakage losses. The increase in resonance frequency results in an overall-decrease in losses and the imaginary part value of permittivity associated with electric field distribution under both TE and TM as indicated in Fig 5 (c). In the TE mode excitation at 2.35 GHz, surface currents on the top and bottom layers flow in opposite directions, creating cyclic current loops in the y-axis direction as shown in Figs. 6 (c) and 6 (d).

This leads to high permeability due to magnetic resonances along the y-axis. With increasing resonance frequency, these current loops gradually shift away from the y-axis and begin to flow in multiple directions, as depicted in Figs. 6 (g), 6 (h), 6 (k), and 6 (l), leading to reduced magnetic resonances and a decrease in the imaginary part value of permeability as shown in Fig. 5 (b). Similarly, in the TM mode, cyclic current loops are formed in the x-axis direction, with the imaginary part value of permeability decreasing as the resonance frequency increases as illustrated in Figs. 7 (c), 7 (d), 7 (g), 7 (h), 7 (k), and 7 (l).

Figure 8 shows the fabricated prototype of the proposed MMA consisting of 9 $\times$ 9 unit cells. The experimental setup for the proposed MMA is shown in Fig. 9. The experimental setup utilizes a pair of double-ridged waveguide horn antennas operating in the frequency band of 0.8–18 GHz. The S-parameters were measured using a Rohde & Schwartz ZNB 40 vector network analyzer. Initially, the S-parameters of a metallic sheet were measured as a reference. Subsequently, the metallic sheet was replaced with the fabricated prototype, and the S-parameters were remeasured and normalized. The S-parameter corresponding to the reflection coefficient with the reflected and transmitted waves in TE mode (S_{11co}) is used to determine the perpendicular polarization reflection coefficient as $\Gamma_{\perp} = S_{11co}$. Furthermore, the cross S-parameter representing the reflection coefficient with the reflected wave in the TE mode and the

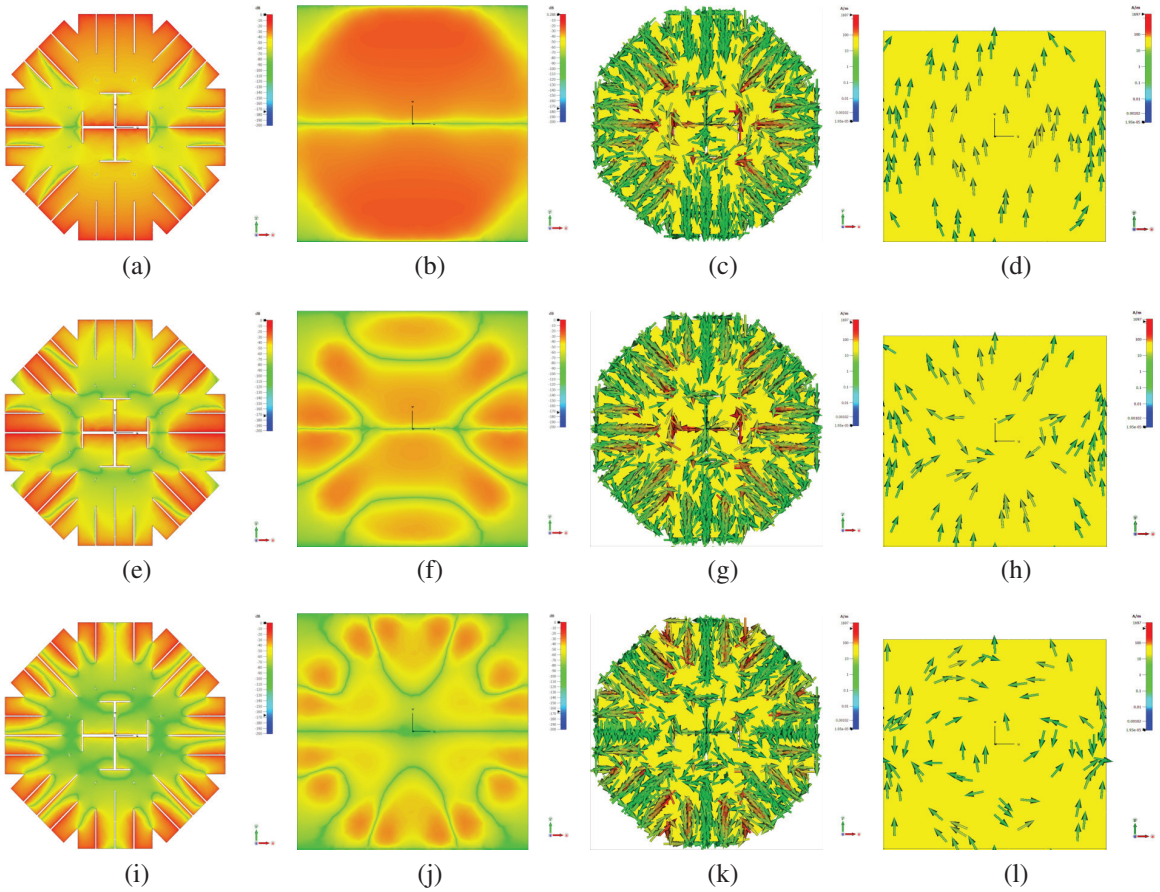

Fig. 6. Electric field and surface current distributions for the proposed MMA under TE mode excitation: (a) TE mode - top layer (E-field at 2.35 GHz), (b) TE mode - bottom layer (E-field at 2.35 GHz), (c) TE mode - top layer (surface current at 2.35 GHz), (d) TE mode - bottom layer (surface current at 2.35 GHz), (e) TE mode - top layer (E-field at 6.97 GHz), (f) TE mode - bottom layer (E-field at 6.97 GHz), (g) TE mode - top layer (surface current at 6.97 GHz), (h) TE mode - bottom layer (surface current at 6.97 GHz), (i) TE mode - top layer (E-field at 11.87 GHz), (j) TE mode - bottom layer (E-field at 11.87 GHz), (k) TE mode - top layer (surface current at 11.87 GHz), and (l) TE mode - bottom layer (surface current at 11.87 GHz).

incident wave in the TM mode $S_{11cross}$ is used to calculate the reflection coefficient for parallel polarization as $\Gamma_{\parallel} = S_{11cross}$. In order to measure the S_{11co} parameter, the alignment of the transmitting and receiving horn antennas is crucial, with both antennas being oriented vertically and parallel to the y-axis as indicated in Fig. 9. Furthermore, the transmitting horn antenna will be horizontally positioned, while the receiving antenna will be vertically positioned to measure the $S_{11cross}$ parameter. The simulated and measured magnitudes of the S-parameters S_{11co} and $S_{11cross}$ are depicted in Fig. 10 (a).

Absorptivity, also known as absorption, refers to the ability of a designed structure to absorb electromagnetic radiation that is incident upon it within a specific frequency range. For the proposed MMA, the absorption can be expressed as: $A = 1 - |S_{11co}|^2 - |S_{11cross}|^2$. Figure 10 (b) shows the simulated and measured absorption at normal incidence for the proposed MMA. The measured results indicate that across the frequency bands of 2.22–2.38 GHz, 6.86–7.24 GHz, 11.68–12.71 GHz, 14.1–14.8 GHz, and 15.47–16 GHz, the measured absorption exceeds 75%, indicating the multiple-band absorption characteristics for the proposed MMA. Although the decrease in losses is observed within the proposed MMA structure at higher resonance frequencies, the proposed MMA exhibits higher measured absorption in the frequency ranges of 6.86–7.24 GHz and 11.68–12.71 GHz due to better matching and lower values of the reflection coefficient (S_{11co}). The absorption

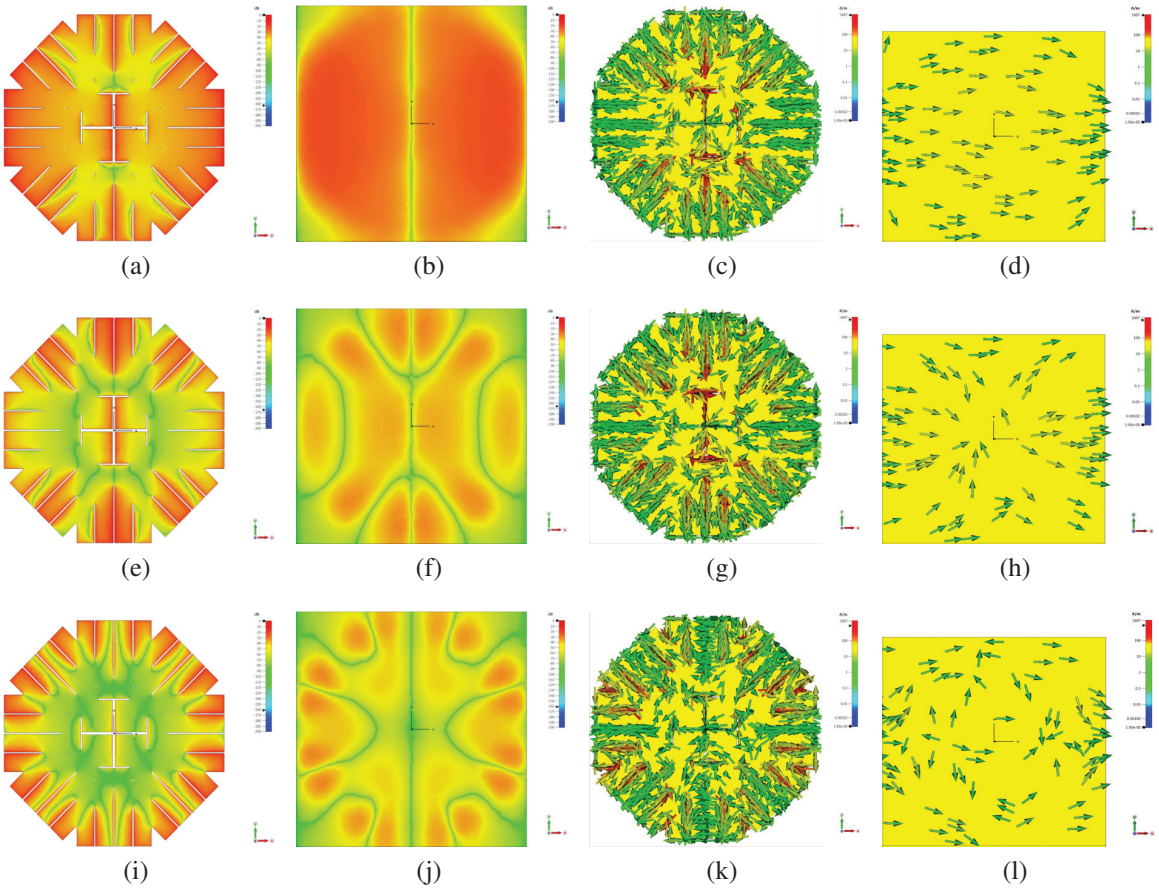

Fig. 7. Electric field and surface current distributions for the proposed MMA under TM mode excitation: (a) TM mode - top layer (E-field at 2.35 GHz), (b) TM mode - bottom layer (E-field at 2.35 GHz), (c) TM mode - top layer (surface current at 2.35 GHz), (d) TM mode - bottom layer (surface current at 2.35 GHz), (e) TM mode - top layer (E-field at 6.97 GHz), (f) TM mode - bottom layer (E-field at 6.97 GHz), (g) TM mode - top layer (surface current at 6.97 GHz), (h) TM mode - bottom layer (surface current at 6.97 GHz), (i) TM mode - top layer (E-field at 11.87 GHz), (j) TM mode - bottom layer (E-field at 11.87 GHz), (k) TM mode - top layer (surface current at 11.87 GHz), and (l) TM mode - bottom layer (surface current at 11.87 GHz).

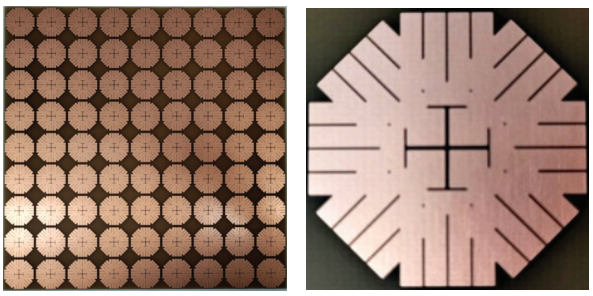

Fig. 8. Fabricated prototype of the proposed MMA: (a) 9 $\times$ 9 unit cells and (b) enlarged unit cell.

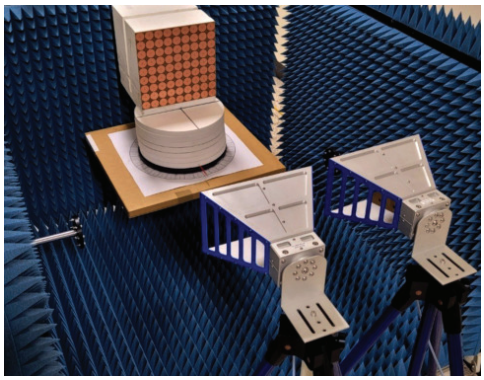

Fig. 9. Experimental setup for the proposed MMA.

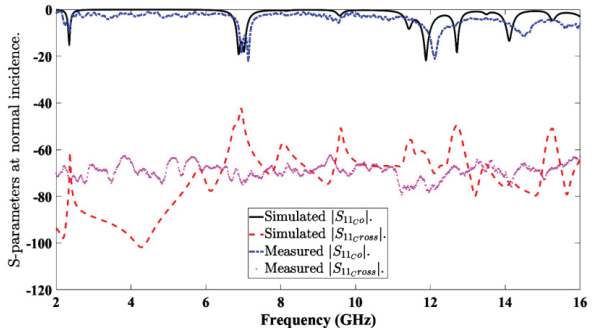

(a)

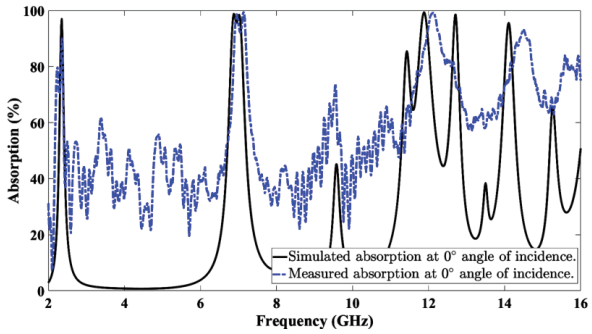

(b)

Fig. 10. Simulated and measured S-parameters and absorption at normal incidence for the proposed MMA: (a) simulated and measured magnitudes of the S-parameters at normal incidence and (b) simulated and measured absorption at normal incidence.

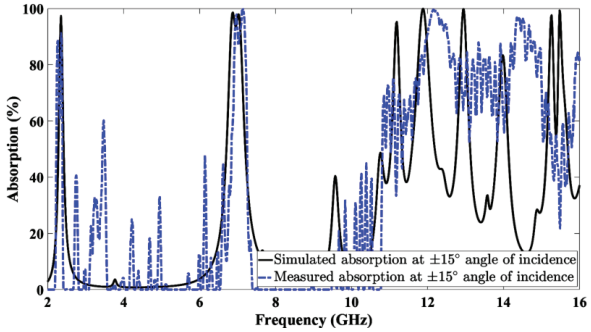

(a)

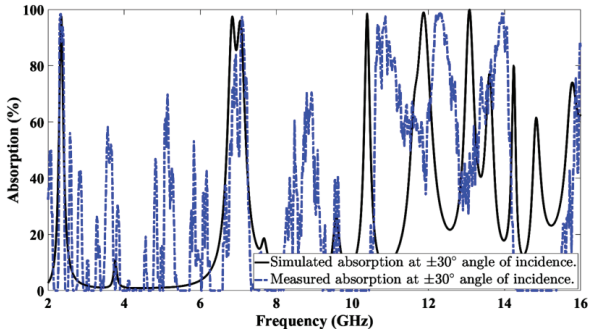

(b)

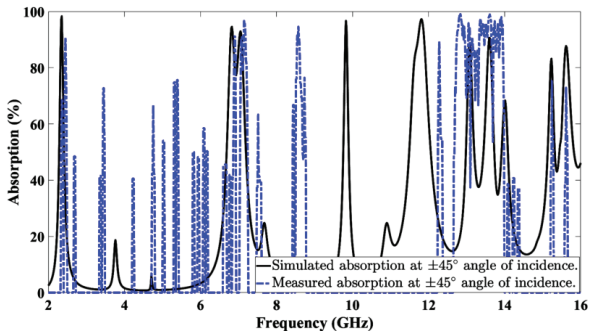

(c)

Fig. 11. Simulated and measured absorption at oblique incidence for the proposed MMA: (a) simulated and measured absorption at ±15° angle of incidence, (b) simulated and measured absorption at ±30° angle of incidence, and (c) simulated and measured absorption at ±45° angle of incidence.

characteristics of the proposed MMA depend on the incident angle. At ±15° angle of incidence, the frequency bands exhibiting absorption exceeding 75% are almost the same as those observed under normal incidence, as shown in Fig. 11 (a). Conversely, when the incident angle is increased to ±30°, the frequency bands with absorption rates exceeding 75% will shift to be 2.29–2.41GHz, 6.9–6.95 GHz, 7.05–7.21 GHz, 10.6–11.14 GHz, 12.09–12.6 GHz, 13.71–14.09 GHz, and 15.96–16 GHz as indicated in Fig. 11 (b). Additionally, the frequency bands with absorption rates higher than 75% vary as the angle of incidence increases, as indicated in Fig. 11 (c).

The variations observed between the simulated and measured results can mainly be attributed to the small size of the fabricated sample. The proposed MMA can be valuable in a wide range of practical applications across various fields. This is particularly relevant in situations where normal or near-normal incidence is prevalent, and where efficient absorption is crucial. The developed MMA could be utilized in the future for wireless energy harvesting applications.

Table 1 presents a comparison between the proposed MMA and the previously published works on MMA. The proposed MMA offers a simple symmetrical structure characterized by a compact size, low profile, and insensitivity to polarization. Moreover, the proposed MMA

Table 1: Comparison of the proposed MMA with recently published studies on metamaterial absorbers

Ref	Structure	Unit Cell Size	Thickness	Center Freq. (GHz)	Absorption Bandwidth (at -3 dB)	PI
[2]	An FSS hexagonal unit cell based on an inter-digital capacitor pattern.	0.49 λ_0 × 0.49λ_0	0.058λ_0	9.61 10.35	10% 10%	yes
[4]	Two resonators printed on the upper surface of dual side copper coated Fr-4 epoxy glass substrate.	0.11λ_0 × 0.11λ_0	0.011λ_0	4.195 9.345 11.48	4% 3.75% 4.12%	yes
[5]	Modified segmented split-ring-based symmetric metamaterial.	0.34λ_0 × 0.34λ_0	0.059λ_0	11.23 14.18 17.37 19.18	1.74% 2.92% 2.8% 3.7%	yes
[9]	An octagonal ring, cross-wires, and cut-off circle artificial structure.	0.423λ_0 × 0.423λ_0	0.031λ_0	12.2	0.05%	yes
[25]	Two split rings and two arms with outer square split-ring resonator.	0.08λ_0 × 0.08λ_0	0.013λ_0	2.5 4.9 6	3.2% 3.54% 3.57%	no
[26]	Modified square split ring resonator structure with a cross-strip line.	0.44λ_0 × 0.44λ_0	0.088λ_0	4.62 16.3	2.5% 2.7%	yes
[28]	Four groups of dipoles lying around a metallic ring connected by four groups of pins.	0.12λ_0 × 0.12λ_0	0.022λ_0	3.25 9.45 10.9	5.6% 4.3% 4.6%	yes
[29]	Top of the unit cell consists of eight circular sector.	0.31λ_0 × 0.31λ_0	0.025λ_0	9.26	5.5%	yes
[30]	Metallic split ring resonators surrounded by E-shaped fractals.	1.73λ_0 × 1.73λ_0	0.08λ_0	24	33.3%	yes
[31]	MMA unit cell with three elongated patch resonators of identical size and shape.	0.82λ_0 × 0.82λ_0	0.068λ_0	16.919 21.084 25.266	4.73% 2.37% 3.96%	yes
This work	MMA unit cell features a symmetrical structure with a slotted octagonal metallic patch.	0.21λ_0 × 0.21λ_0	0.001λ_0	2.3 7.05 12.19 14.45 15.73	6.96% 5.39% 8.45% 4.84% 3.37%	yes

exhibits a greater number of absorption bands compared to previous studies published on MMA.

IV. CONCLUSION

In this study, a new design has been proposed to achieve a compact, thin, polarization-insensitive, and multiple-band MMA using an FR4 substrate without resistive lumped elements. The proposed MMA features a symmetrical structure with a slotted octagonal metallic patch printed on an FR4 dielectric substrate, backed by a grounded metallic layer. Furthermore, the simulations and experimental results indicate that the proposed MMA can efficiently absorb incident waves. The proposed MMA can provide five absorption bands with measured absorptivity exceeding 75%. The developed absorber structure has the potential for use in various wireless communication and defense applications.

ACKNOWLEDGMENT

This work was supported in part by the Korean Government (MSIT) through the National Research Foundation of Korea, South Korea, under Grant 2019R1C1C1008102 and in part by the Institute of Information & Communications Technology Planning & Evaluation (IITP) grant funded by the Korea government (MSIT), under Grant RS-2022-00156409 (ICT innovation human resources 4.0).

REFERENCES

[1] I. Catalkaya and S. Kent, "An optimized microwave absorber geometry based on wedge absorber," *Applied Computational Electromagnetics Society (ACES) Journal*, vol. 32, no. 7, pp. 621-627, 2017.

[2] J. Lee, M. Yoo, and S. Lim, "A study of ultra-thin single layer frequency selective surface microwave absorbers with three different bandwidths using double resonance," *IEEE Transactions on Antennas and Propagation*, vol. 63, no. 1, pp. 221-230, 2014.

[3] F. Erkmen, T. S. Almoneef, and O. M. Ramahi, "Scalable electromagnetic energy harvesting using frequency-selective surfaces," *IEEE Transactions on Microwave Theory and Techniques*, vol. 66, no. 5, pp. 2433-2441, 2018.

[4] N. Mishra, D. K. Choudhary, R. Chowdhury, K. Kumari, and R. K. Chaudhary, "An investigation on compact ultra-thin triple band polarization independent metamaterial absorber for microwave frequency applications," *IEEE Access*, vol. 5, pp. 4370-4376, 2017.

[5] S. Hannan, M. T. Islam, N. M. Sahar, K. Mat, M. E. Chowdhury, and H. Rmili, "Modified-segmented split-ring based polarization and angle-insensitive multi-band metamaterial absorber for X, Ku and K band applications," *IEEE Access*, vol. 8, pp. 144051-144063, 2020.

[6] K. Lee and S. K. Hong, "Rectifying metasurface with high efficiency at low power for 2.45 GHz band," *IEEE Antennas and Wireless Propagation Letters*, vol. 19, no. 12, pp. 2216-2220, 2020.

[7] W. Xin, Z. Binzhen, W. Wanjun, W. Junlin, and D. Junping, "Design and characterization of an ultrabroadband metamaterial microwave absorber," *IEEE Photonics Journal*, vol. 9, no. 3, pp. 1-13, 2017.

[8] Y. Wei, J. Duan, H. Jing, Z. Lyu, J. Hao, Z. Qu, J. Wang, and B. Zhang, "A multiband, polarization-controlled metasurface absorber for electromagnetic energy harvesting and wireless power transfer," *IEEE Transactions on Microwave Theory and Techniques*, vol. 70, no. 5, pp. 2861-2871, 2022.

[9] M. J. Uddin, M. H. Ullah, and S. Z. Islam, "A broadband polarized metamaterial absorber driven by strong insensitivity and proximity effects," *IEEE Access*, vol. 9, pp. 131672-131684, 2021.

[10] M. D. Banadaki, A. A. Heidari, and M. Nakhkash, "A metamaterial absorber with a new compact unit cell," *IEEE Antennas and Wireless Propagation Letters*, vol. 17, no. 2, pp. 205-208, 2017.

[11] F. Erkmen and O. M. Ramahi, "A scalable, dual-band absorber surface for electromagnetic energy harvesting and wireless power transfer," *IEEE Transactions on Antennas and Propagation*, vol. 69, no. 10, pp. 6982-6987, 2021.

[12] D. Kundu, S. Baghel, A. Mohan, and A. Chakrabarty, "Design and analysis of printed lossy capacitive surface-based ultrawideband low-profile absorber," *IEEE Transactions on Antennas and Propagation*, vol. 67, no. 5, pp. 3533-3538, 2019.

[13] M. Hossain, N. Nguyen-Trong, K. Sayidmarie, and A. Abbosh, "Equivalent circuit design method for wideband nonmagnetic absorbers at low microwave frequencies," *IEEE Transactions on Antennas and Propagation*, vol. 68, no. 12, pp. 8215-8220, 2019.

[14] S. Sambhav, J. Ghosh, and A. K. Singh, "Ultra-wideband polarization insensitive thin absorber based on resistive concentric circular rings," *IEEE Transactions on Electromagnetic Compatibility*, vol. 63, no. 5, pp. 1333-1340, 2021.

[15] F. Costa, S. Genovesi, A. Monorchio, and G. Manara, "Low-cost metamaterial absorbers for sub-GHz wireless systems," *IEEE Antennas and Wireless Propagation Letters*, vol. 13, pp. 27-30, 2013.

[16] M. S. Islam, M. Samsuzzaman, G. K. Beng, N. Misran, N. Amin, and M. T. Islam, "A gap coupled hexagonal split ring resonator based metamaterial for S-band and X-band microwave applications," *IEEE Access*, vol. 8, pp. 68239-68253, 2020.

[17] X. Duan, X. Chen, and L. Zhou, "A metamaterial electromagnetic energy rectifying surface with high harvesting efficiency," *AIP Advances*, vol. 6, no. 12, pp. 1-7, 2016.

[18] P. Zuo, T. Li, M. Wang, H. Zheng, and E.-P. Li, "Miniaturized polarization insensitive metamaterial absorber applied on EMI suppression," *IEEE Access*, vol. 8, pp. 6583-6590, 2019.

[19] M. M. Zargar, A. Rajput, K. Saurav, and S. K. Koul, "Single-layered flexible dual transmissive rasorbers with dual/triple absorption bands for conformal applications," *IEEE Access*, vol. 9, pp. 150426-150442, 2021.

[20] M. A. Shukoor and S. Dey, "Novel dual-mode polarization insensitive wide angular stable circular ring based deca-band absorber for RCS and EMI shielding applications," *IEEE Transactions on*

Electromagnetic Compatibility, vol. 64, no. 5, pp. 1337-1345, 2022.

[21] T. Liu, X. Cao, J. Gao, Q. Zheng, W. Li, and H. Yang, "RCS reduction of waveguide slot antenna with metamaterial absorber," *IEEE Transactions on Antennas and Propagation*, vol. 61, no. 3, pp. 1479-1484, 2012.

[22] A. F. Almutairi, M. S. Islam, M. Samsuzzaman, M. T. Islam, N. Misran, and M. T. Islam, "A complementary split ring resonator based metamaterial with effective medium ratio for C-band microwave applications," *Results in Physics*, vol. 15, pp. 1-10, 2019.

[23] U. Farooq, A. Iftikhar, M. F. Shafique, M. S. Khan, A. Fida, M. J. Mughal, and D. E. Anagnostou, "C-band and X-band switchable frequency-selective surface," *Electronics*, vol. 10, no. 4, pp. 1-15, 2021.

[24] S. Dey and S. Dey, "Conformal multifunction FSS with enhanced capacitance loading for high angle stable stopband filtering and microwave absorption," *IEEE Transactions on Electromagnetic Compatibility*, vol. 64, no. 2, pp. 315-326, 2022.

[25] M. L. Hakim, M. T. Islam, T. Alam, S. K. Abdul Rahim, B. Bais, M. S. Islam, and M. S. Soliman, "Triple-band square split-ring resonator metamaterial absorber design with high effective medium ratio for 5G sub-6 GHz applications," *Nanomaterials*, vol. 13, no. 2, pp. 1-15, 2023.

[26] M. L. Hakim, T. Alam, M. S. Soliman, N. M. Sahar, M. H. Baharuddin, S. H. Almalki, and M. T. Islam, "Polarization insensitive symmetrical structured double negative (DNG) metamaterial absorber for Ku-band sensing applications," *Scientific Reports*, vol. 12, no. 1, pp. 479-497, 2022.

[27] Z. Szabó, G.-H. Park, R. Hedge, and E.-P. Li, "A unique extraction of metamaterial parameters based on Kramers–Kronig relationship," *IEEE Transactions on Microwave Theory and Techniques*, vol. 58, no. 10, pp. 2646-2653, 2010.

[28] H. Zhai, C. Zhan, Z. Li, and C. Liang, "A triple-band ultrathin metamaterial absorber with wide-angle and polarization stability," *IEEE Antennas and Wireless Propagation Letters*, vol. 14, pp. 241-244, 2014.

[29] T. T. Nguyen and S. Lim, "Wide incidence angle-insensitive metamaterial absorber for both TE and TM polarization using eight-circular-sector," *Scientific Reports*, vol. 7, no. 1, pp. 3204-3215, 2017.

[30] R. M. H. Bilal, M. A. Baqir, P. K. Choudhury, M. Karaaslan, M. M. Ali, O. Altıntas, A. A. Rahim, E. Unal, and C. Sabah, "Wideband microwave absorber comprising metallic split-ring resonators surrounded with E-shaped fractal metamaterial," *IEEE Access*, vol. 9, pp. 5670-5677, 2021.

[31] H. Wu, S. Ji, J. Zhao, Z. Luo, and H. Dai, "Design and analysis of a triple-band non-zonal polarization electromagnetic metamaterial absorber," *Applied Computational Electromagnetics Society (ACES) Journal*, vol. 36, no. 6, pp. 697-706, 2021.

Mohamed Elhefnawy received B.S. and M.S. Degrees in Electronics and Communications Engineering from Tanta University and the Arab Academy for Science & Technology, Egypt, in 1999 and 2005, respectively. He received a Ph.D. degree in Communications Engineering from USM University, Malaysia, in 2010. Since 2023, he has been working as a senior researcher in the Department of Electronic Engineering at Gyeongsang National University (GNU) in Jinju, South Korea. He is currently on leave from the Department of Electrical Engineering at the Faculty of Engineering, October 6 University, Egypt. He has a strong academic background that includes electromagnetic field theory, wave propagation, antenna theory, and RF/Microwave engineering. His research interests include the design and development of antennas and RF/microwave components.

KyoungHun Kim received B.S. Degree in Electronics Engineering from Gyeongsang National University (GNU), Jinju, South Korea, in 2023. He is currently an M.S. student in the Department of Electronic Engineering at Gyeongsang National University (GNU) in Jinju, South Korea. His research interests include antenna design and the development of wireless power transfer systems.

Tae-Hyeon Kim received B.S. Degree in Electronics Engineering from Gyeongsang National University (GNU), Jinju, South Korea, in 2023. He is currently an M.S. student in the Department of Electronic Engineering at Gyeongsang National University (GNU) in Jinju, South Korea. His research interests include the design and development of antennas and measurement and improve electrical performance of aircraft radome.

Wang-Sang Lee received the B.S. degree from Soongsil University, Seoul, South Korea, in 2004, and the M.S. and Ph.D. degrees in electrical engineering from the Korea Advanced Institute of Science and Technology (KAIST), Daejeon, South Korea, in 2006 and 2013, respectively. From 2006 to 2010, he was with the Electromagnetic Compatibility Technology Center, Digital Industry Division, Korea Testing Laboratory (KTL), Ansan-si, South Korea, where he was involved in the international standardization for radio frequency identification (RFID) and photovoltaic systems as well as electromagnetic interference (EMI)/EMC analysis, modeling, and measurements for information technology devices. In 2013, he joined the Korea Railroad Research Institute (KRRI), Uiwang-si, South Korea, as a Senior Researcher, where he was involved in the position detection for high-speed railroad systems and microwave heating for low-vibration rapid tunnel excavation systems. Since 2014, he has been a Professor with the Department of Electronic Engineering, Gyeongsang National University (GNU), Jinju, South Korea. From 2018 to 2019, he was a Visiting Scholar with the ATHENA Group, Georgia Institute of Technology, Atlanta, GA, USA. His current research interests include near- and far-field wireless power and data communications systems, RF/microwave antenna, circuit, and system design, RFID/Internet of Things (IoT) sensors, and EMI/EMC. Dr. Lee is a member of IEC/ISO JTC1/SC31, KIEES, IEIE, and KSR. He was a recipient of the Best Paper Award at IEEE RFID in 2013, the Kim Choong-Ki Award Electrical Engineering Top Research Achievement Award at the Department of Electrical Engineering, KAIST, in 2013, the Best Ph.D. Dissertation Award at the Department of Electrical Engineering, KAIST, in 2014, the Young Researcher Award at KIEES in 2017, and the Best Paper Awards at IEIE in 2018 and KICS in 2019.

Introducing a 12/10 Induction Switched Reluctance Machine (ISRM) for Electric Powertrains

M. Joodi, M. Abbasian, and M. Delshad

Department of Electrical Engineering
Islamic Azad University, Khorasan (Isfahan) Branch, Isfahan, Iran
joodi@khuisf.ac.ir, m.abbasian@khuisf.ac.ir, delshad@khuisf.ac.ir

Abstract – The induction switched reluctance machine (ISRM) is a novel electric machine that integrates the switched reluctance machine (SRM) with rotor inductive conductors to enhance performance in electric vehicle (EV) powertrain applications. In this topology, the rotor conductors act as a magnetic shield, diverting magnetic flux and preventing magnetic field lines from penetrating the rotor body. By engineering this design, short magnetic flux paths are created in both the stator and rotor of the electric machine. Since its recent introduction, the ISRM represents an emerging technology in the early stages of development. Similar to conventional SRMs, the ISRM can take on various topologies with different stator and rotor pole numbers. Minimizing rotor copper loss is a critical consideration in the ISRM design process. This paper examines two distinct ISRM topologies (12/10 and 12/8), and their characteristics are analyzed using the finite element method. Simulation results, including power density, torque density, efficiency, and copper loss, are presented and compared. Finally, the optimal ISRM topology is proposed for hybrid electric powertrains.

Index Terms – Electric vehicle, electromagnetic induction, reluctance machines, torque.

I. INTRODUCTION

Electric vehicles (EVs) and hybrid electric vehicles (HEVs) have been demonstrated to be an imminent technology and an outstanding alternative to gasoline and diesel vehicles. EVs have an electric motor instead of an internal combustion engine, and the engine size of HEVs is smaller than conventional vehicles. As a result, they generate less emissions and have better fuel economy [1]. Traditionally, batteries on HEVs can only be recharged through regenerative braking or slowing, meaning that most of the work is carried out by the combustion engine [2]. Another breed of HEVs, called PHEVs, are equipped with a dedicated charging socket which enables the batteries to be charged using external charging equipment [3].

Automobile designers and engineers have been working on EVs and HEVs since 1900s, and most car manufacturers have launched their HEV or EV prototypes or even mass-produced them. However, due to the technical challenges and high mass production costs, their popularity in the market has been lower than what expected. EVs and HEVs account for less than 5% of worldwide vehicle production**.** Therefore, a lot of work still needs to be done. The main challenges that negatively impact the adoption rate of EVs consists of high initial cost, lack of charging stations, and charging time [4].

Electric machines employed in HEVs are required to have features including high torque, high power density, high reliability, high efficiency, low level of noise and vibration, and reasonable cost. Permanent magnet synchronous motors (PMSMs) are widely used in the powertrain of EVs and HEVs [5]. Some HEV powertrain systems, such as Toyota Prius, implement two PMSMs for traction and generator application.

PMSM benefits from high torque and power density, but permanent magnet materials employed in this machine are the major source of concern. Permanent magnet materials contain rare earth materials, such as neodymium. In recent years, the rare earth materials price has ramped up and suffered fierce fluctuations [6].

Engineers and researchers have conducted many efforts to eliminate or at least reduce permanent magnet materials from electric machines employed in HEVs and EVs propulsion systems. Induction machines (IMs) are another option that has been used in electric powertrains. For instance, the first models of Tesla EV powertrains were engineered using IMs. Compared to PMSM, IMs have lower efficiency and torque density. This leads more car manufacturers to consider PMSM as the first option for EV and HEV applications [7].

Extensive efforts have been dedicated to the advancement of electric machines that eliminate the need for permanent magnets, focusing on the generation of reluctance torque [8]. One promising alternative for powertrains in EVs and HEVs is the switched reluctance

Submitted On: November 18, 2023
Accepted On: June 9, 2024

https://doi.org/10.13052/2024.ACES.J.390509

machine (SRM). SRM works on the principle of variable reluctance: the rotor of this motor constantly tries to align through the lowest reluctance lane. The formation of the rotary magnetic field can be done using the circuit of power electronics switching. SRM has no permanent magnet or rare earth materials. It is a robust machine that has better operation at high temperatures and high rotational speeds, compared to PMSM.

Several references have proposed conventional SRM for HEV and EV propulsion systems. Conventional SRM suffers from low torque and high level of noise and vibration [9]. In recent decades, scientists have been working to design and develop new SRM topologies with higher torque density and lower noise and vibration. For instance, a high torque SRM was proposed for HEV powertrain application in [10]. In [11], a bipolar SRM was designed for automotive applications. It was shown that this machine produces higher torque and lower noise and vibration compared to conventional SRM.

Researchers have been working on developing revolutionary SRM topologies to overcome SRM problems. For instance, a short magnetic flux path SRM, named segmental SRM, was proposed by Mecrow [12]. An improved version of this novel machine with single tooth windings was presented in [13]. In 2013, an 80-kw segmental rotor SRM was designed for EV application [14].

Short magnetic flux path SRM is a category of SRMs which benefits from a magnetic flux path that does not circle entire stator and rotor yoke. This leads to lower iron loss, lower noise and vibration, and higher torque density. Segmental SRMs can be designed in different configurations. Some of them have segmental stator and non-segmental rotor, but some other topologies have non-segmental stator and segmental rotors [15].

Segmental SRMs can generate torque up to 50% more than conventional SRMs with the same volume. The reason is that the magnetic flux lines in segmental SRMs are oriented more in the motional direction. Moreover, the radial forces have lower amplitude, and the machine experiences lower noise and vibration. This is a great achievement in the field of SRM design, but there is an important drawback that prohibits the development of segmental SRMs. The problem is that the rotor or the stator of segmental SRMs is comprised of several ferromagnetic poles which are installed in a non-ferromagnetic housing. This structure hardens the machine production, and particularly prevents achieving a very small and uniform airgap between the stator and the rotor. If the segmental SRM does not benefit from a very small airgap, the phase inductance in the aligned position will not be large enough to produce very high torque levels. In addition, the process of the segmental rotor or stator assembly during mass production of the machine may cause airgap non-uniformity, that leads to unbalanced radial forces. The unbalanced forces are the main source of vibration in the electric machines.

This discussion clarifies that the segmental SRMs are not ideal options to take the place of the conventional SRMs. A new configuration of segmental SRM, called double stator switched reluctance machine (DSSRM) was invented in 2010 [16]. This machine comprises one segmental rotor which is installed between two stators. DSSRM can generate torque two times more than a conventional SRM with the same volume. In addition, this machine has very low noise and vibration level. DSSM has been proposed in several references as a considerable option for EV and HEV powertrains. Double rotor switched reluctance machine (DRSRM) with very high torque density is another novel SRM which was presented in [17].

As discussed above, engineering novel SRM topologies has been a trend over the years. Some researchers have been working to develop optimized versions of conventional SRM in terms of shape optimization or control drive system [18]. Most of these attempts are based on artificial intelligence, genetic algorithm, and neural networks. The objectives used in these optimization algorithms are based on maximum torque density, maximum torque per ampere, and maximum torque per motor loss [19]. In some works, vibration and torque ripple of switched reluctance motors are mitigated through current profile optimization [20].

The induction switched reluctance machine (ISRM) is a novel electric machine that has a conventional structure, and benefits from short magnetic flux path and high torque density [21]. The machine consists of two ferromagnetic parts, the stator and the rotor, which are not segmental (unlike segmental SRMs). The novelty is based on the arrangement of conductors on the rotor which act like a magnetic shield and prevent the magnetic flux entering the rotor poles. This novel topology potentially helps ISRM to generate torque density approximately two times more than conventional SRMs [22]. In addition, the short flux path results in lower copper loss in the machine at high speeds, which is the dominant loss. The results which are comprehensively presented and discussed in [22] confirm that, despite the rotor copper loss due to the rotor windings, the efficiency of ISRM is higher than conventional SRMs.

ISRM can be designed and developed in various stator and rotor pole numbers and phase numbers. Each configuration requires a specific rotor and stator winding topology in terms of winding pitch. In this paper, two different 3-phase ISRM, 12/8 and 12/10, will be considered. The magnetic flux path of each machine is determined, and the copper loss and efficiency of them are calculated using finite element method (FEM). A comprehensive

competition between these two ISRMs is performed, and the results are presented.

II. 12/8 INDUCTION SWITCHED RELUCTANCE MACHINE

Various stator and rotor pole numbers can be considered for ISRM. To achieve the best configuration in terms of efficiency and power density, different configurations should be studied and compared. In order to design an ISRM, firstly the number of phases should be considered. Then, based on the stator and rotor winding pitches, the number of rotor and stator poles should be chosen. In this paper, 3-phase ISRMs are considered. As a result, the stator pole numbers should be a multiple of 6. Like conventional SRMs, the simplest 3-phase configuration of ISRM has 6 stator poles and 4 rotor poles.

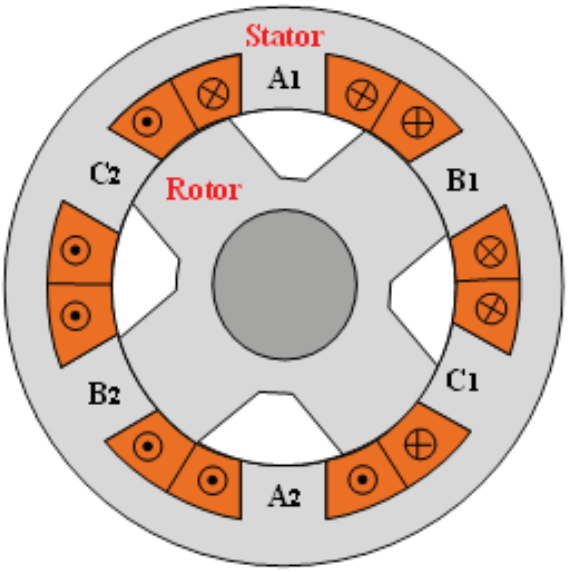

Fig. 1. Cross-section of a conventional 6/4 SRM.

There is an important difference between the stator winding topology of ISRM and conventional SRM. In conventional 6/4 SRM, the phase windings are concentrated and each coil is wound around each stator pole, as shown in Fig. 1. In 6/4 ISRM, the coil span is 180^o and the phase windings are full pitch, as shown in Fig. 2. This leads to a considerable end winding, and consequently higher copper loss and higher motor length in 6/4 ISRM, compared to 6/4 SRM. In order to mitigate this drawback of ISRM, other ISRM configurations with smaller end windings should be considered. 12/8 ISRM is a candidate that can be considered for this purpose.

The 12/8 ISRM is a 3-phase ISRM with the stator coil span of 90^o. This leads to a smaller end winding, because each phase coil is distributed between 4 slots, rather than 2 slots, which is the case in 6/4 ISRM. As

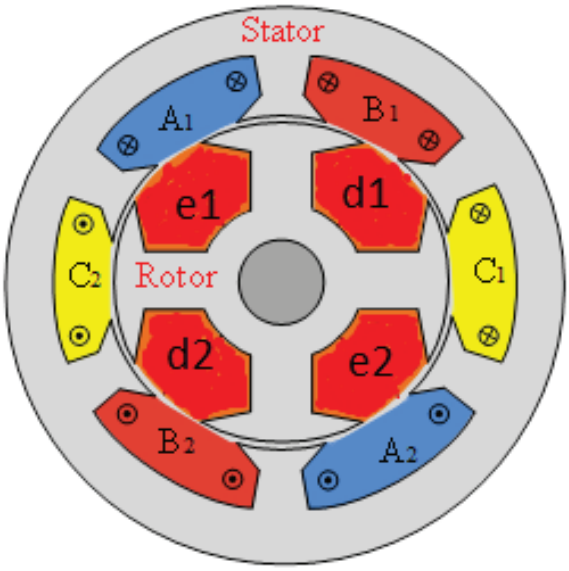

Fig. 2. Cross-section of a 6/4 ISRM.

a result, the number of conductors which overlap at the end sides of the 12/8 ISRM is half of the 6/4 ISRM. Fortunately, the rotor windings of 12/8 ISRM are concentrated, and this is a merit for 12/8 ISRM. In 6/4 ISRM, the rotor windings are long pitch with a coil span of 180^o, which increases the final rotor length and rotor copper loss. In 12/8 ISRM, two coils per phase are connected in series to form each phase. For instance, a_1a_2 and a_3a_4 form phase A. This is also the case for phase B and phase C. The winding strategy of the rotor is completely different. On the rotor, one isolated short-circuited concentrated winding is wound around each rotor pole (f_1f_2, g_1g_2, h_1h_2, g_1g_2, h_1h_2, i_1i_2, j_1j_2, h_1h_2). Like conventional SRM, pulsed DC is required to excite each phase.

In [21], a 12/8 ISRM was designed and analyzed and compared with a conventional 12/8 SRM. The results confirmed that the 12/8 ISM has higher torque density and efficiency, compared to conventional 12/8 SRM.

In order to investigate the flux path and output characteristics of 12/8 ISRM, a 12/8 ISRM with the parameters presented in Table 1 is considered and simulated. The machine configuration is shown in Fig. 3. First, the flux path of the machine is studied. Due to the effect of induction phenomenon on the rotor windings, transient FEM simulation must be performed to analyze the performance of ISRM. For this purpose, one phase is excited with a constant current for 15 degrees, from unaligned position to aligned position, while the rotor is running at a constant speed of 1500 rpm. The magnetic flux path of the machine is extracted when the rotor is on the verge of full alignment, as shown in Fig. 4. Figure 5 shows

Table 1: Characteristics of the ISRMs

Stator Outer Radius	115 mm
Stack length	90 mm
Airgap	0.5 mm
Number of stator poles	12
Number of rotor poles	8 or 10
Turn number of stator and rotor windings	40
Rated current	200 A
Maximum current density of windings	20 A/mm^2
Motor core material	M19
Rated power	80 kW
Slot fill factor	60%
Motor length (12/8)	209 mm
Motor length (12/10)	152 mm
Cooling method	Oil spray

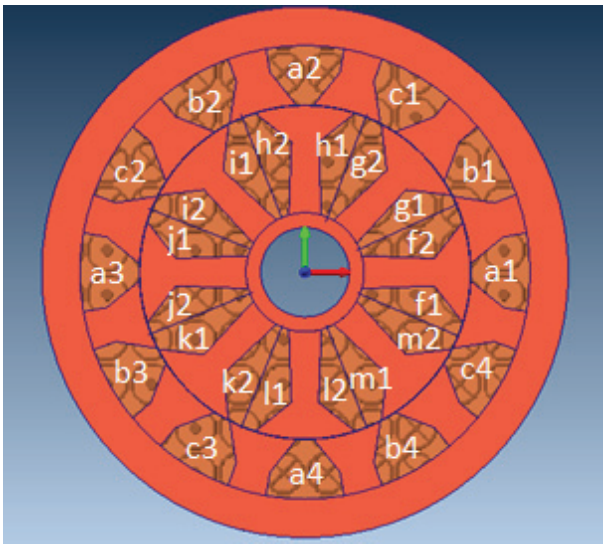

Fig. 3. Cross-section of a 12/8 ISRM.

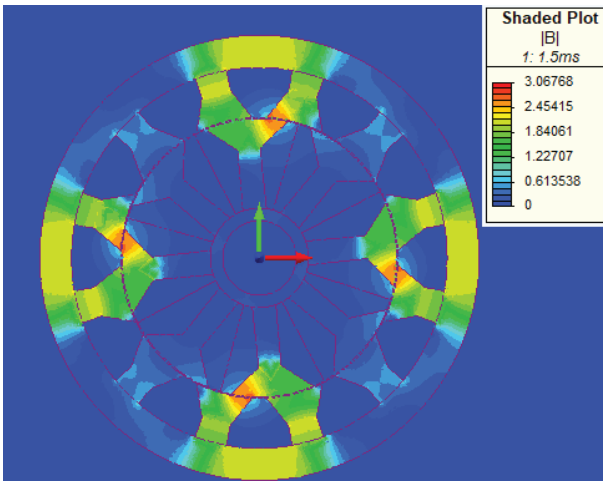

Fig. 4. Flux distribution in 12/8 ISRM.

the magnetic flux path and the current density of the stator and rotor windings. It is clear that a short flux path is created around each excited winding of phase A. The induced currents in the rotor windings are also observable in Fig. 5. As shown in Fig. 5, the current is induced in all of the rotor coils, which leads to high level of rotor copper loss. This can increase the rotor ohmic loss and the rotor temperature, which hardens the rotor cooling process.

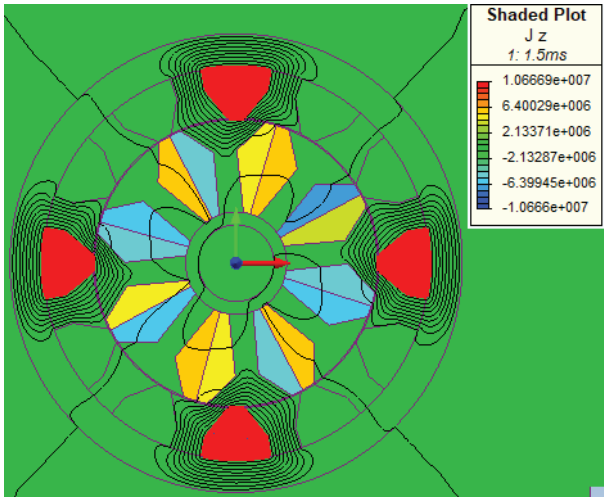

Fig. 5. Current density in 12/8 ISRM.

III. 12/10 INDUCTION SWITCHED RELUCTANCE MACHINE

Due to the presence of conductors on the rotor of ISRM, a magnetic short flux path is created in the machine and, hence, high torque is achieved. However, rotor conductors will be a major source of copper loss and heat in ISRM. Direct liquid cooling systems, such as oil spray cooling (which is used in the Toyota Prius), can cool down the internal parts of the machine, but designing an ISRM with lower rotor copper loss can alleviate the need for such a cooling system and increase the efficiency of the machine. In addition, in the 12/8 ISRM the stator windings are long pitch with a coil span of 90^o, which increases the final stator length and stator copper loss. This urges researchers to design an ISRM stator with short pitch windings. In conclusion, the best ISRM has short pitch windings on both stator and rotor. This brings up the subject of an ISRM with less copper loss and length.

In this section a 12/10 ISRM is introduced. Its configuration is shown in Fig. 6. This electric machine benefits from short pitch concentrated windings on the rotor and stator. There are two types of stator poles with different widths in this machine. The width of the thick poles is two times greater than the width of the thin poles. The

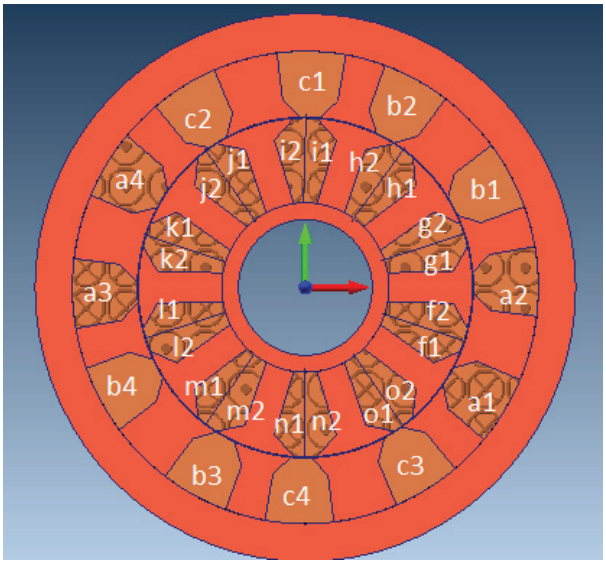

Fig. 6. Cross-section of a 3-phase 12/8 ISRM.

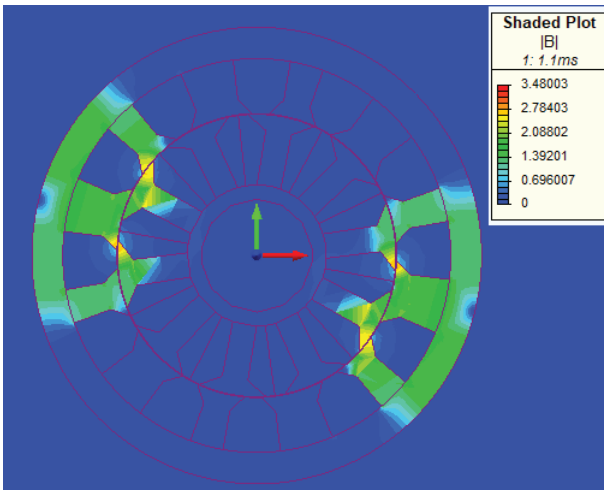

Fig. 7. Flux distribution in 12/10 ISRM.

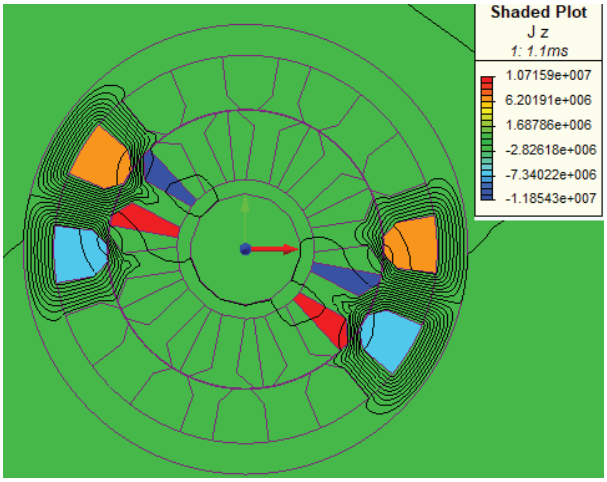

Fig. 8. Current density in 12/10 ISRM.

stator coils are wound around thick poles, as shown in Fig. 6. This machine has three phases: phase A is comprised of $a_1a_2a_3a_4$, phase B is comprised of $b_1b_2b_3b_4$, and phase C is comprised of $c_1c_2c_3c_4$. On the rotor side, the width of all poles is the same, and one coil is wound around each rotor pole. It should be mentioned that all rotor windings are separately short circuited and are not connected together. The result is that there are 10 isolated short-circuited windings on the rotor (f_1f_2, g_1g_2, h_1h_2, i_1i_2, j_1j_2, k_1k_2, l_1l_2, m_1m_2, n_1n_2, o_1o_2).

A 12/10 ISRM with the characteristics presented in Table 1 is analyzed and compared with the 12/8 ISRM. The stator outer diameter, the stator stack length, and the slot fill factor of the 12/10 ISRM is the same as the 12/8 ISRM which was analyzed in the previous section. The final motor length of the 12/10 ISRM is 27% less than the 12/8 ISRM.

A transient finite element model of the machine is created and solved in Magnet Infolytica. In this simulation, phase A is excited with a constant current, while the rotor is running with the speed of 1500 rpm from unalignment to alignment position. The magnetic flux path of the machine is extracted and drawn as shown in Fig. 7 when the rotor is on the verge of full alignment. Moreover, Fig. 8 shows the magnetic flux path and the current density of the stator and rotor windings. The figures show that a short flux path is created around each excited winding of phase A. The induced currents in the rotor windings are shown in Fig. 8. Dissimilar to 12/8 ISRM, the current is not induced in all of the rotor coils of 12/10 ISRM. This leads to a lower level of rotor copper loss, compared to 12/8 ISRM. This will be fully considered and investigated in the next section of this paper.

IV. COMPARISION OF 12/8 ISRM AND 12/10 ISRM

Rotor windings play a very important role in the correct operation of ISRM by preventing the flux line from entering the rotor yoke of the machine and creating a short magnetic flux path. This phenomenon is based on the Faraday law of induction and Lenz law. This leads to induced electric current in the rotor windings, which is a source of copper loss and heat in the rotor of the ISRM. Rotor copper loss is a crucial aspect of ISRM that must be considered in the optimum design of the machine.

Designing an ISRM with maximum torque density and minimum possible rotor loss is a key issue in the applicability of this novel machine. In this section, using finite element analysis, the torque capability of the 12/8 ISRM and 12/10 ISRM, along with the induced current in the rotor windings of the machines, are studied

and compared. In these simulations one phase of the machines is excited by a constant current, while the rotor is running from unaligned position to aligned position, with a constant speed of 1500 rpm.

After completing the simulation, the results are displayed. Firstly, phase A of the machines is excited with a constant current 0f 100 A. The output torque of the two machines is calculated and presented in Fig. 9. The simulation is repeated for different currents (from 0 A to 200 A) at a speed of 1500 rpm, and the average output torque is calculated and presented in Fig. 10. Results show that the output torque of the 12/10 ISRM is higher than the output torque of the 12/8 ISRM, especially at higher phase currents. For instance, at the current phase of 200 A, the average torque of 12/10 ISRM is 14% higher than the average torque of 12/8 ISRM.

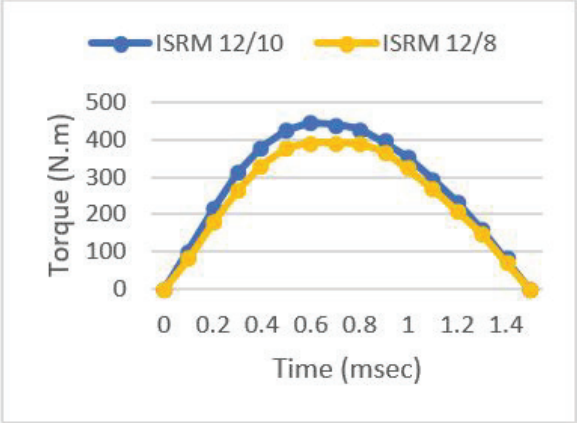

Fig. 9. Torque profile of the 12/10 ISRM compared to torque profile of the 12/8 ISRM.

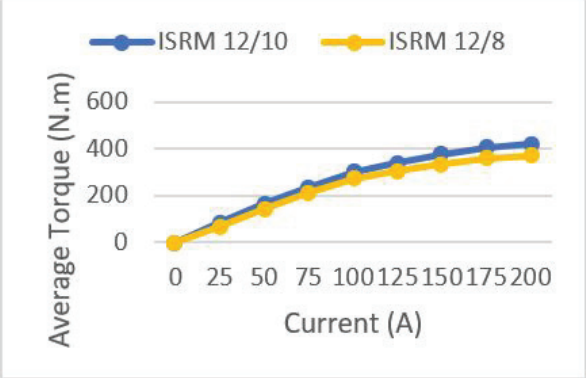

Fig. 10. Average torque of the 12/10 ISRM compared to average torque of the 12/8 ISRM.

As mentioned before, the 12/10 ISRM benefits from concentrated windings which are coiled around the stator poles. As shown in Fig. 6, there are two types of stator poles in terms of thickness, and the windings are placed around the thick stator poles. This winding strategy leads to a smaller end winding, compared to 12/8 ISRM. As a result, the final motor length and the volume of 12/10 is less than 12/8 ISRM. The stack length of the 12/8 ISRM and the 12/10 ISRM are the same, and equal to 90 mm. Considering the end windings, the final motor length of the 12/8 ISRM is 209 cm, while the final motor length of the 12/10 ISRM is 152 cm. As a result, the volume of the 12/8 ISRM is 36% higher than the volume of the 12/10 ISRM.

Using these resultant data, the average torque per volume of the 12/8 ISRM and the 12/10 ISRM for different currents (from 0 A to 200 A) is calculated and the results are presented in Fig. 11. The results show that, at high currents, the torque density of the 12/10 ISRM is about 50% higher than the torque density of the 12/8 ISRM.

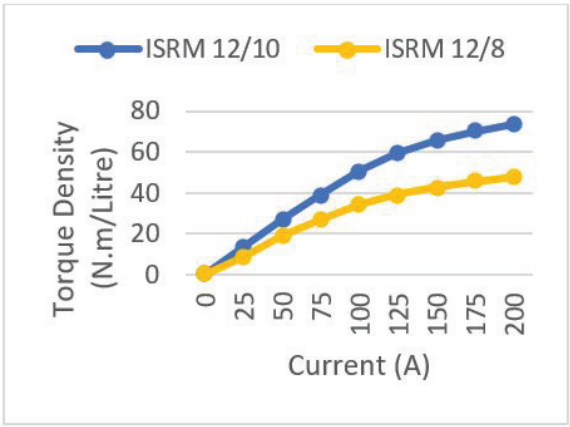

Fig. 11. Torque density of the 12/10 ISRM compared to torque density of the 12/8 ISRM.

Rotor copper loss is a crucial aspect of ISRM that should be studied in the optimum design of the machine. In this section, using finite element analysis, the induced current in the rotor windings of the 12/8 ISRM and the 12/10 ISRM is calculated and presented. In these simulations, the rotor is running from unalignment to alignment position with a speed of 1500 rpm, and the phases are excited by the constant current of 70 A. Figure 12 shows the induced current in the four rotor windings of 12/8 ISRM (f to i, see Fig. 3). The four other rotor windings of the 12/8 ISRM (j to m) have the same current as Fig. 12. In addition, the induced current in the five rotor windings of 12/10 ISRM (f to j, see Fig. 6) is shown in Fig. 13. The five other rotor windings of the 12/10 ISRM (k to o) have the same shape as Fig. 13, but with negative values.

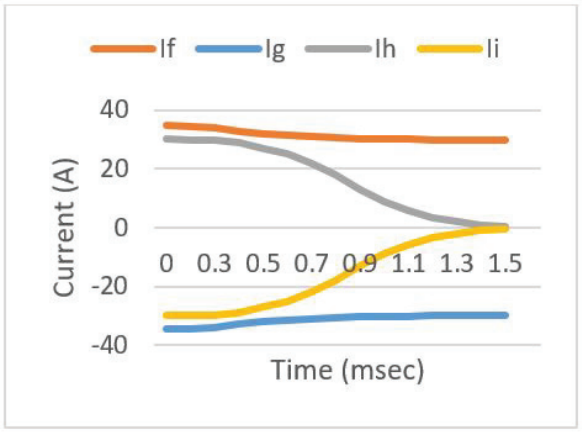

Fig. 12. Rotor winding currents of the 12/8 ISRM.

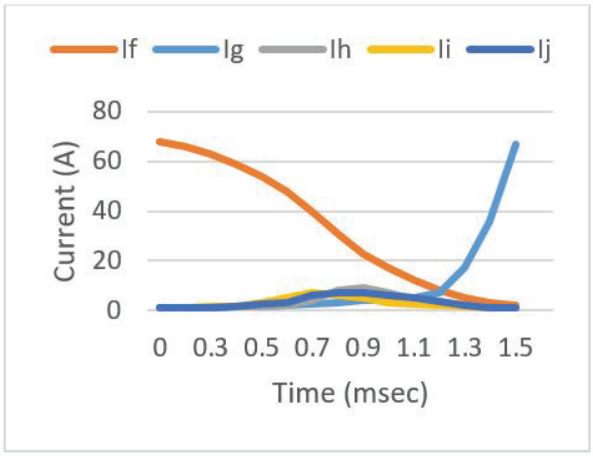

Fig. 13. Rotor winding currents of the 12/10 ISRM.

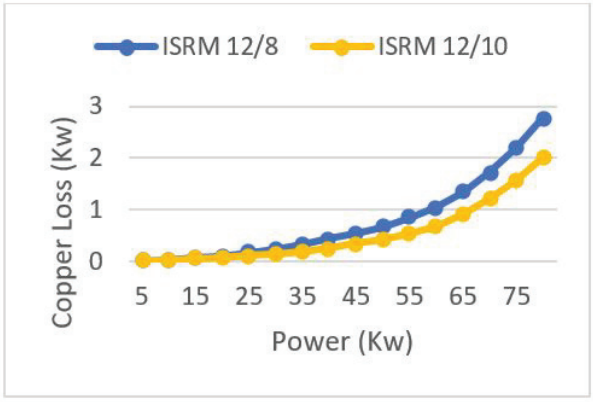

Fig. 14. Copper loss of the 12/10 ISRM compared to copper loss of the 12/8 ISRM.

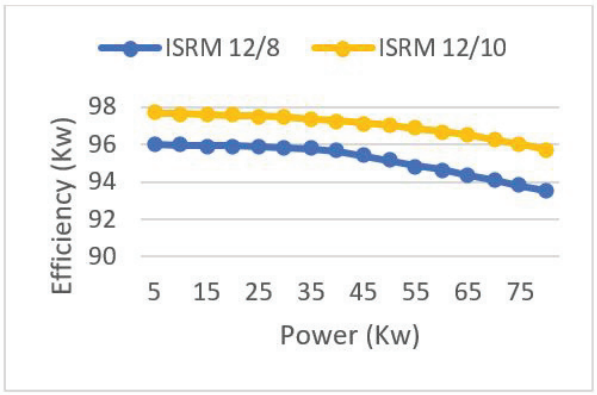

Fig. 15. Efficiency of the 12/10 ISRM compared to efficiency of the 12/8 ISRM.

For each machine, the simulation is redone for different phase currents, and the rotor winding currents are extracted. Using these data, the total machine copper loss is calculated in different output powers and the results are presented in Fig. 14. The results confirm that the 12/10 ISRM has lower copper loss, compared to the 12/8 ISRM. This is an important point, specially at high power where copper loss plays an important negative role in appropriate operation and efficiency of the machine. Designing an ISRM with a lower level of copper loss is a significant achievement which can boost the efficiency of the machine. The efficiency of the 12/10 ISRM and the 12/8 ISRM is calculated in different powers, and the results are presented in Fig. 15. The results show that 12/10 ISRM enjoys higher efficiency, which is an important merit for electric powertrain systems.

In ISRMs, similar to SRMs, the stator phases are excited by sequences of DC voltage pulses. These pulses create a magnetic field that interacts with the rotor windings. This interaction not only induces a motional EMF due to the relative motion between the stator and rotor but also a transformer EMF resulting from the changing magnetic field linked with the rotor coils. Unfortunately, it is not feasible to separately quantify the transformer EMF and motional EMF using FEM simulations. The primary challenge lies in the complex nature of the problem and the mutual interactions between these two EMFs. Both EMFs are inherently interlinked, and their combined effect influences the overall performance of the ISRMs. Given the intertwined nature of transformer and motional EMFs, the induced currents in the rotor coils are a result of both phenomena. These currents contribute to Joule losses.

Although it is challenging to separate the individual contributions of transformer and motional EMFs, we expect that the transformer-induced currents might have a more significant impact at lower speeds where the rate of change of the magnetic field is higher. Conversely, motional-induced currents could dominate at

higher speeds due to increased rotor movement. Understanding the balance between these losses will help in optimizing the design and control strategies for ISRMs, ultimately improving their efficiency.

V. CONCLUSIONS

In this paper, a 12/10 induction switched reluctance machine (ISRM), was introduced for electric powertrains. In this topology, the rotor windings create a magnetic shield, and divert the magnetic flux and prevent the magnetic field lines from passing into the rotor body. As a result, a short magnetic flux path is created around each excited phase of the machine. In order to evaluate the capability of the 12/10 ISRM, it was compared with a 12/8 ISRM which has been presented in previous research works. The characteristics of the 12/10 ISRM and the 12/8 ISRM, including torque profile, average torque, torque density, rotor currents, copper loss, and efficiency, were extracted using FEM analysis. Simulation results for both machines were presented and compared. Results confirm that the 12/10 ISRM has more torque density and efficiency, compared to the 12/8 ISRM. Moreover, copper loss of the 12/10 ISRM is less than copper loss of the 12/8 ISRM, which alleviates the cooling system of the electric machine.

REFERENCES

[1] L. Liu, Y. Huang, M. Zhao, and Y. Ruan, "Parametric modeling and optimization of switched reluctance motor for EV," *Applied Computational Electromagnetic Society (ACES) Journal*, vol. 37, no. 9, pp. 948-958, 2022.

[2] H. Tu, H. Feng, S. Srdic, and S. Lukic, "Extreme fast charging of electric vehicles: A technology overview," *IEEE Trans. Transport. Electrific.*, vol. 5, no. 4, pp. 861-878, Dec. 2019.

[3] M. Yilmaz and P. T. Krein, "Review of battery charger topologies charging power levels and infrastructure for plug-in electric and hybrid vehicles," *IEEE Trans. Power Electron.*, vol. 28, no. 5, pp. 2151-2169, May 2013.

[4] M. Popescu, J. Goss, D. A. Staton, D. Hawkins, Y. C. Chong, and A. Boglietti, "Electrical vehicles: Practical solutions for power traction motor systems," *IEEE Trans. Ind. Appl.*, vol. 54, no. 3, pp. 2751-2762, May/June 2018.

[5] E. Ayciecek, N. Bekiroglu, I. Senol, and Y. Oner, "Rotor configuration for cogging torque minimization of open-slot axial flux permanent magnet synchronous motors," *Applied Computational Electromagnetic Society (ACES) Journal*, vol. 30, no. 4, 2015.

[6] G. Pellegrino, A. Vagati, P. Guglielmi, and B. Boazzo, "Performance comparison between surface-mounted and interior PM motor drives for electric vehicle application," *IEEE Trans. Ind. Electron.*, vol. 59, no. 2, pp. 803-811, Feb. 2012.

[7] X. Sun, Z. Shi, G. Lei, Y. Guo, and J. Zhu, "Analysis and design optimization of a permanent magnet synchronous motor for a campus patrol electric vehicle," *IEEE Trans. Veh. Technol*, vol. 68, no. 11, pp. 10535-10544, Nov. 2019.

[8] B. Khan, F. Khan, W. Ullah, M. Umair, and S. Hussain, "Slot filling factor calculation and electromagnetic performance of single phase electrically excited flux switching motors," *Applied Computational Electromagnetic Society (ACES) Journal*, vol. 35, no. 8, pp. 922-928, 2020.

[9] M. Abdalmagid, E. Sayed, M. Bakr, and A. Emadi, "Geometry and topology optimization of switched reluctance machine: A review," *IEEE Access*, vol. 10, pp. 5141-5170, Jan. 2022.

[10] Z. Yang and F. Shang, "Development of a rare-earth-free SR motor with high torque density for hybrid vehicles," *IEEE Trans. Energy Convers.*, vol. 30, no. 3, pp. 132-143, Mar. 2015.

[11] C. S. Edrington, M. Krishnamurthy, and B. Fahimi, "Bipolar switched reluctance machines: A novel solution for automotive applications," *IEEE Trans. Veh. Technol.*, vol. 54, no. 3, pp. 795-808, May 2005.

[12] B. C. Mecrow, J. W. Finch, E. A. El-Kharashi, and A. G. Jack, "Switched reluctance motors with segmental rotors," *IEE Proc. Elect. Power Appl.*, vol. 149, no. 4, pp. 245-254, July 2002.

[13] B. C. Mecrow, J. W. Finch, and A. G. Jack, "Segmental rotor switched reluctance motors with single-tooth windings," *IEE Proc. Elect. Power Appl.*, vol. 150, no. 5, pp. 591-599, Sep. 2003.

[14] J. D. Widmer, R. Martin, and B. C. Mecrow, "Optimization of an 80-kW segmental rotor switched reluctance machine for automotive traction," *Proc. IEMDC*, pp. 427-433, July 2013.

[15] Emine Bostanci, Mehdi Moallem, Amir Parsapour, and Babak Fahimi, "Opportunities and challenges of switched reluctance motor drives for electric propulsion: A comparative study," *IEEE Trans. Transportation Electrification.*, vol. 3, no. 1, pp. 58-75, Mar. 2017.

[16] M. Abbasian, M. Moallem, and B. Fahmi, "Double stator switched reluctance motors: Fundamentals and magnetic force analysis," *IEEE Trans. Energy Convers.*, vol. 25, no. 3, pp. 589-597, Dec. 2010.

[17] T. Guo, T. Shofield, and A. Emadi, "Double segmented rotor switched reluctance machine with shared stator back-iron for magnetic flux passage," *IEEE Trans. Energy Convers.*, vol. 31, no. 4, pp. 1278-1286, Dec. 2016.

[18] S. Li, S. Zhang, T. G. Habetler, and R. G. Harley, "Modeling, design optimization, and applications of switched reluctance machines: A review," *IEEE Trans. Ind. Appl.,* vol. 55, no. 3, pp. 2660-2681, May 2019.

[19] A. Bentounsi, F. Rebahi, and R. E. H. Bouchekara, "Multi-objective optimization design of 8/6 switched reluctance motor using GA and PSO algorithms," *J. Electr. Eng. Technol*., vol. 15, no. 4, pp. 168-175, 2015.

[20] C. Ma, L. Qu, R. Mitra, P. Pramod, and R. Islam, "Vibration and torque ripple reduction of switched reluctance motors through current profile optimization," in *Proc. IEEE Appl. Power Electron. Conf. Expo. (APEC),* pp. 3279-3285, Mar. 2016.

[21] M. Abbasian, "Induction switched reluctance motor," U.S. Patent, US20170370296A1, June 30, 2020.

[22] M. Azamian, M. Abbasian, and D. Gerling "Preliminary evaluation of induction switched reluctance motor for electric vehicle application," *IEEE Access*, May 30, 2021.

Mohammad Joodi was born in Maragheh, Iran, in 1976. He received the bachelor's degree and M.Sc. Degree in Electrical Engineering from IAU University, Tabriz, Iran, in 2007 and 2014, respectively. From 2016, he has been a PhD student at IAU University, Khorasgan, Isfahan, Iran.

Mohammadali Abbasian received the bachelor's degree, M.Sc. degree, and Ph.D. degree in Electrical Engineering from Isfahan University of Technology. He was with Renewable Energies and Vehicular Technologies, The University of Texas at Arlington, Arlington, Texas, USA, as Ph.D. exchange student. From 2017 to 2018, he was with the Bundeswehr University, Munich, Germany, as a research scientist. He was an assistant professor at the IAU University, Khorasgan, Isfahn, Iran.

Majid Delshad was born in Isfahan, Iran, in 1979. He received the B.S and M.S degrees in electrical engineering in 2001 and 2004 from Kashan University and Isfahan University of Technology, Iran, respectively. He received the Ph.D. degree in electrical engineering in Isfahan University of Technology. He is associate professor in Isfahan (Khorasgan) Branch, IAU. His research interest includes soft switching techniques in DC-DC converters and current-fed converters.

Efficient MAPoD via Least Angle Regression based Polynomial Chaos Expansion Metamodel for Eddy Current NDT

Yang Bao[1], Jiahao Qiu[1], Praveen Gurrala[2], and Jiming Song[3]

[1]College of Electronic and Optical Engineering
Nanjing University of Posts and Telecommunications, Nanjing, Jiangsu 210023, China
brianbao@njupt.edu.cn

[2]Micron Technology, Inc.
Boise, ID 83707, USA

[3]Department of Electrical and Computer Engineering
Iowa State University, Ames, IA 50011, USA

***Abstract* –** In this article, a metamodeling approach based on non-intrusive polynomial chaos expansion (PCE) with least angle regression (LAR) method is used in boundary element analysis for a model-assisted probability of detection (MAPoD) study of eddy current nondestructive testing (NDT) systems. The LAR-PCE metamodel represents the NDT system model responses by a set of coefficients with the polynomial basis functions in lieu of pure kernel degeneration accelerated boundary element method (KD-BEM) based physical model. Both the computational accuracy and efficiency of the LAR-PCE metamodel over the ordinary least squares (OLS) based PCE metamodel are demonstrated by testing the 3D eddy current NDT benchmarks with different system setups, flaw lengths and widths. The simulation results show two digits accuracy of the PoD metrics compared with the ones achieved by the KD-BEM based physical model as the benchmark. The LAR-PCE metamodel has remarkable improvements in computational efficiency over the OLS-PCE metamodel and accelerates the MAPoD study.

***Index Terms* –** Boundary element analysis, eddy current nondestructive testing (NDT), meta learning, model-assisted probability of detection (MAPoD), polynomial chaos expansions with least angle regression (LAR-PCE).

I. INTRODUCTION

Eddy current nondestructive testing (NDT) plays a critical role in testing for material damage and discontinuities (flaws) in components and in assessing the risk of component failure. Because it provides high sensitivity to small defects without needing to make direct contact with inspection samples, it has gained popularity in many industries such as aerospace, nuclear, railways, and special equipment [1]. In general, components need to be replaced if they have flaws whose sizes exceed a threshold value that is considered harmless [2]. Therefore, it is very important for NDT inspections to estimate the flaw sizes precisely. Imperfect estimation is primarily caused by measurement uncertainties (such as environmental conditions, human factors and protective clothing). Multiple output responses obtained repeatedly using the same (nominal) test parameters and conditions may vary significantly because of measurement uncertainties, thus impacting the reliability of the NDT system [3]. To quantify the reliability of NDT systems, the notion of probability of detection (PoD) is introduced [4]. PoD represents the probability of detecting a flaw as a function of flaw size. PoD study is applied to both eddy current and ultrasonic NDT by evaluating the presence of a flaw with the impedance variations and reflected signals, respectively. It is also applied to evaluate wall thinning due to backwall echo [5].

PoD assessments typically require performing a large number of tests accurately to quantify the impact of all uncertainties. It is challenging to perform a large number of measurements due to time and labor costs. Thus, accurate theoretical and numerical simulation models, which have been validated by experiment, are replacing physical measurements partly or entirely to get the required data for PoD analysis. This approach is called model assisted PoD (MAPoD) [6]. The simulation models used in the above process need to be accurate and efficient to ensure MAPoD analysis remains accurate without requiring large amounts of computer resources. Several simulation models have been proposed as forward solvers in eddy current NDT [7–10]. Generally, these solvers can be categorized into two types based on

Submitted On: February 12, 2024
Accepted On: July 2, 2024

https://doi.org/10.13052/2024.ACES.J.390510

the equation solved as the finite element method (FEM) and the boundary element method (BEM). Fast algorithms have been proposed to accelerate solving BEM matrix equations for large numbers of unknowns [11–14]. These fast algorithms are generally of two types: kernel independent and kernel dependent methods. In kernel dependent methods, such as multilevel fast multipole algorithm, different types of expansions are required for BEM kernel functions [11]. These methods, therefore, lack generality because the BEM kernels depend on the integral equation being solved. Kernel independent methods, such as the adaptive cross approximation algorithm and kernel degeneration (KD) algorithm, deal with the matrix entries directly and the existing codes can be reused for different kernels [12–14].

Unfortunately, the growing propagation of the uncertainties in the input parameters inside the NDT pushes the physical models toward their computational limits, thus very large numbers of simulations are needed in order to get the MAPoD curves. This drawback motivates the replacement of physical models by efficient and precise metamodels or surrogate models, which are data-driven mathematical approximations to the physical models [15–19]. Metamodels have been widely applied in NDT and included methods such as support vector regression, kriging interpolation, probabilistic collocation, polynomial chaos expansions (PCE) methods, and so on [15–18]. PCE was first introduced by Wiener to represent a random variable using expansions based on standard Gaussian random variables and their corresponding orthogonal basis functions: Hermite polynomials. PCE can be viewed as a spectral representation of random variables in terms of a set of polynomial basis functions that are orthogonal with respect to the joint distribution of the input variables, and it has advantages over other metamodels because it systematically guarantees convergence in distribution to the output random variable of interest if the latter has finite variance [17].

In contrast to the literatures mentioned above, this work is focused on non-intrusive polynomial chaos expansions with least angle regression (LAR-PCE) assisted by kernel degeneration accelerated boundary element method (KD-BEM) based physical model for MAPoD study of eddy current NDT systems. To our best knowledge, this is the first time that the LAR-PCE is applied to build the metamodel with the assisted KD-BEM physical model to accelerate the uncertainty propagation within MAPoD analysis for eddy current NDT systems. In the LAR-PCE metamodel, the NDT system model responses are represented by a set of coefficients with the polynomial basis functions in lieu of pure KD-BEM based physical model for PoD analysis. The LAR-PCE metamodel provides significant computational savings while still maintaining good accuracy compared with the OLS-PCE metamodel by taking the input parameter uncertainties into account in testing the eddy current NDT benchmarks.

II. METHODS

In this section, the methods used in this work are described in detail. It includes the KD-BEM based physical model in Section II, part A, the MAPoD analysis in Section II, part B, and the metamodel in Section II, part C.

A. KD-BEM based physical model

In BEM based physical models for 3D eddy current NDT, Stratton-Chu formulas are selected as the integral equation which has no low frequency breakdown issue. Expanding equivalent electric and magnetic surface currents using RWG vector basis functions and the normal component of the magnetic field using pulse basis functions, and selecting the Galerkin method as the testing method, the discretized impedance matrix is [20]:

$$\begin{bmatrix} 0.5\mathbf{T}-\mathrm{K}_1^{\times} & 0 & \mathbf{R}_1^{\times} \\ j\mu_2/\mu_1\mathbf{L}_2^{\times} & 0.5\mathbf{T}+\mathbf{K}_2^{\times} & 0 \\ \mu_2/\mu_1\mathbf{K}_2^{n} & -jk_2^2\mathbf{L}_2^{n} & 0.5\mathbf{D}-\mathbf{R}_2^{n} \end{bmatrix}, \quad (1)$$

where subscript $l = 1,\ 2$ stands for air or metal, the superscripts $\times$ and n denote the cross or dot product with the unit normal vector $\hat{\mathbf{n}}$, and give the tangential and normal components, respectively. The details of $\mathbf{K}$, $\mathbf{L}$, and $\mathbf{R}$ operators can be found in [20].

In BEM, the complexity of both CPU time and memory requirements are $O\left(N^2\right)$ when solved with iterative solvers using the full impedance matrix. Therefore, the KD algorithm is applied to accelerate the solution process by developing a low-rank approximation of the impedance matrix. It is well known that the entire impedance matrix is not rank deficient. Therefore, the octal tree structure is required to subdivide the bounding box of the object under inspection into blocks for applying the KD algorithm. The number of blocks is increased by $2^{level\times\mathrm{dim}}$, where 'dim' represents the dimension of the object. Near and far block pairs are defined based on the relative distances between the blocks. Near block pairs are the adjacent ones and calculated directly as full sub-matrices. Due to the nature of the Green function, BEM matrix elements corresponding to far block pairs are rank deficient matrices and can be approximated by the KD algorithm.

For a far block pair formed by blocks t and s with the dimensions T by Q, the kernel function and its gradient can be degenerated by the Lagrange polynomial interpolation [20]. The KD algorithm leads to memory savings because K^t and K^s are much smaller than T and Q. The KD algorithm can also be applied to other submatrices in the impedance matrix. The KD-BEM works as the efficient physical model for MAPoD analysis in a 3D eddy current NDT system.

B. MAPoD analysis

The KD-BEM based physical model makes estimations for MAPoD analysis. As we know, the PoD curve relates the probability of detecting flaws to the size. PoD calculations can be performed with two statistical methodologies: the "hit/miss" and the "$\hat{a}$ vs. a" regression analysis. In "hit/miss" analysis, NDT system responses larger than a defined threshold are regarded as 1 ("hit"), otherwise 0 ("missed"). This work focuses on the "$\hat{a}$ vs. a" regression analysis, where the flaw response ($\hat{a}$) is assumed to be proportional to the flaw size (a). PoD can be calculated by [3]:

$$PoD(a) = \Phi\left[\ln(a) - \mu/\sigma\right], \tag{2}$$

where Φ denotes the normal cumulative distribution function. Mean μ and standard deviation σ both on log scale can be represented as:

$$\mu = \left[\ln(\hat{a}_{th}) - \beta_0\right]/\beta_1, \tag{3}$$

$$\sigma = \sigma_r/\beta_1, \tag{4}$$

where $\hat{a}_{th}$ is the defined threshold value, and β_0, β_1 and σ_r can be estimated using the maximum likelihood method [21].

Although the KD-BEM physical model can simulate a single model response efficiently, applying it for uncertainty propagation within MAPoD analysis is still computationally intensive because of the need for evaluating a large number of model responses. This motivates the use of metamodels in lieu of the physical model to accelerate MAPoD analysis. A flowchart of the metamodel-accelerated MAPoD analysis is shown in Fig. 1.

The flowchart starts from the sampling process. Sampling is the process to draw the values randomly according to the probability distributions of random inputs that represent uncertainty parameters, which are proposed by NDT experts or statisticians. Two sampling strategies are applied in this work: Monte Carlo sampling (MCS) and Latin Hypercube sampling (LHS). In MCS, the sampling points can be anywhere within the range of random distributions. Thus, this strategy is applied for generating the validation and prediction points. LHS divides the cumulative curves into equal intervals on the cumulative probability scale and the sampling is generated randomly in each interval. LHS avoids the sampled values from being clustered. Therefore, LHS is selected to generate the training points for the metamodel.

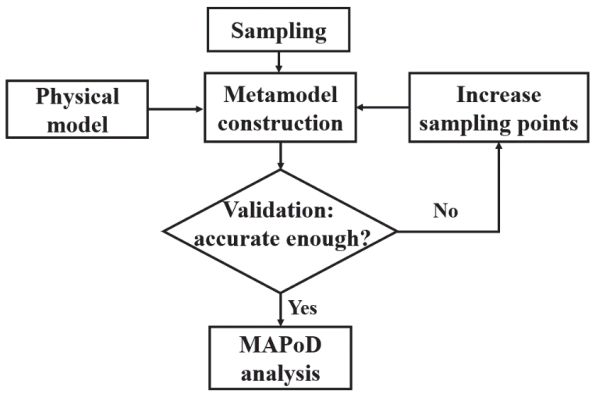

Fig. 1. Flowchart of metamodel accelerated MAPoD analysis.

Subsequently, the uncertainty is propagated through the physical model for different flaw sizes. In other words, selected training points are simulated by the KD-BEM based physical model to generate the model responses. These responses are used as inputs for constructing the metamodel. To validate the metamodel, the root mean squared error (RMSE) is defined as:

$$RMSE = \sqrt{\sum_{i=1}^{N_t}\left(\hat{Y}_i - Y_i\right)^2 \Big/ N_t}, \tag{5}$$

where N_t is the total number of validation points, and $\hat{Y}_i$ and Y_i are the prediction values and physical model responses, respectively. The normalized RMSE (NRMSE) is defined as RMSE divided by the scale of model response.

C. Metamodel

PCE is a type of stochastic metamodeling method for propagating uncertainty in the processes efficiently and can be viewed as a spectral representation of random variables in terms of polynomial basis functions which are orthogonal with respect to the probability density function of input random variables [15–17]. Based on whether it requires to reformulate or modify the existing governing equations, PCE can be categorized into intrusive and non-intrusive methods. Non-intrusive PCE considers the existing code or equations as a black box which makes it easy to implement for complex problems.

Consider a physical model represented by deterministic mapping $\boldsymbol{y} = M(\boldsymbol{x})$, where $\boldsymbol{x} = \{x_1, ..., x_n\}^T \in \mathbb{R}^n, n \geq 1$ is the vector of input variables, including parameters in the experiment setup and material properties. $\boldsymbol{y} = \{y_1, ..., y_Q\}^T \in \mathbb{R}^Q, Q \geq 1$ is the vector of the model response. Uncertainties in the input parameters arise during in-service inspections due to environmental conditions, human factors, and so on. In order to represent the reality of MAPoD analysis, statistical distributions of the uncertainties are introduced as inputs of the simulation model. Therefore, these uncertainties are considered in the input vector $\boldsymbol{x}$, which is represented by a random independent vector $\boldsymbol{X}$ with prescribed probability density function. The random variables of model responses are denoted by $\mathbf{Y} = M(\mathbf{X})$. In PCE, the model responses $\boldsymbol{Y}$ are expanded onto an orthogonal polynomial basis as [17]:

$$\boldsymbol{Y} = M(\boldsymbol{X}) = \sum_{i=1}^{\infty} a_i \psi_i(\boldsymbol{X}), \tag{6}$$

where ψ_i is the multivariate polynomial basis, i is the index of ith polynomial term, and a_i is the corresponding coefficient of the basis function needing to be determined. For inputs with uniform and normal distributions, the Legendre and Hermite basis are selected, respectively. In practice, a truncated form of PCE with sufficient number of terms satisfies the accuracy requirement.

The responses of a physical model are represented by a summation of PCE predictions at the same sampling points and corresponding residual:

$$\boldsymbol{Y} = \sum_{i=1}^{P} a_i \psi_i(\boldsymbol{X}) + \varepsilon_{PC} = \boldsymbol{a}^T \boldsymbol{\psi}(\boldsymbol{X}) + \varepsilon_{PC}, \tag{7}$$

where ε_{PC} is the corresponding residual which is minimized using least squares method and P is the required number of polynomial terms:

$$P = \frac{(p+n)!}{p!n!}, \tag{8}$$

where p is the required order of the PCE, n is the total number of random variables.

The LAR algorithm aims at selecting the predictors, which are the polynomial basis ψ, that have the greatest impacts on the model response. LAR provides not only a single PC metamodel but also a collection of PC representations. The steps in the LAR algorithm are as follows [17].

Step 1: Initialize the coefficients **a** as 0, which makes the initial residual equal to the output responses.

Step 2: Find the basis ψ_j that is most correlated with the current residual, increase or decrease the coefficient a_j of ψ_j just enough such that the updated residual has as much correlation with another predictor ψ_k as it does with ψ_j.

Step 3: Move jointly $\{\psi_j, \psi_k\}^T$ in the direction defined by their joint least-square coefficient of the current residual until the other predictor has as much correlation with the current residual.

Step 4: Continue this procedure until the number of the predictors reaches the required numbers of samples or responses. Thus, the metamodel associated with the greatest estimate is retained.

III. NUMERICAL RESULTS

The eddy current NDT case involves a coil with finite cross section placed above a thick plate with a surface flaw as shown in Fig. 2. MAPoD analysis for different ECNDT setups and different uncertain parameters are studied. In the first setup, the coil has an inner radius 9.34 mm, outer radius 18.4 mm, length 9 mm and number of turns 408. The thick plate has thickness 12.22 mm and conductivity 30.6 MS/m. For the surface flaw, depth is 5 mm, width is 0.28 mm, and length ranges from 0.1 to 0.5 mm with the interval 0.1 mm and from 1 to 5 mm with the interval 1 mm. In the second setup, the specimen, coil parameters and defect size are changed with regard to the first one. Coil has an inner radius 6.15 mm, outer radius 12.4 mm, length 6.15 mm, and number of turns 3790. The thick plate has thickness 5 mm and conductivity 30.3 MS/m. For the surface flaw, depth is 4 mm, length is 0.5 mm, and width ranges from 0.1 to 0.5 mm with the interval 0.1 mm. Width is 0.5 mm while the length ranges from 1.5 to 3.5 mm with the interval 0.5 mm. All cases are modeled after TEAM 15 benchmark problems [22], and the accuracy of KD-BEM method for modeling has been demonstrated in [20]. Only the single position with the peak response is simulated. The PoD metrics a_{50} and a_{90} represent that the flaw size is with 50% and 90% probabilities of detection, respectively.

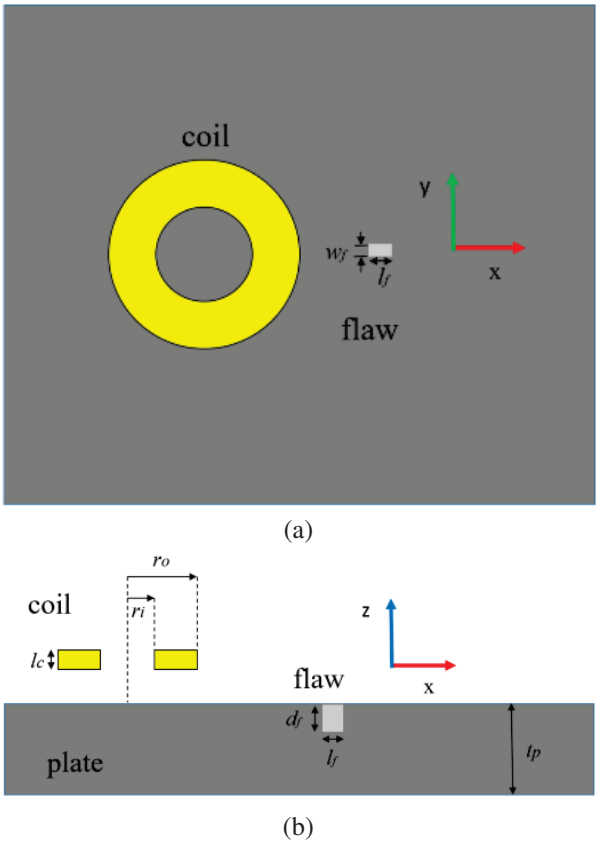

Fig. 2. Sketch of ECT problem: (a) top view and (b) sectional side view.

The relative x, y location, liftoff of the probe with respect to the flaw center, the inner and outer radius of the probe, and the tilt angle (the one between coil plane and xoy plane) are selected as the uncertain parameters with the distributions shown in Table 1. The operating frequency is 7 kHz in cases 1, 2, 4 and 5 with first setup, and 900 Hz in case 3 with second setup. In each case, 1000 MCS prediction points are generated for each flaw

Table 1: Distributions of the uncertain parameters

Parameters	CASE 1	CASE 2	CASE 3	CASE 4	CASE 5
Oper. Freq. (Hz)	7000	7000	900	7000	7000
x (mm)	N(13, 0.5)	U(12, 14)	N(9, 0.5)	N(14, 0.5)	U(12.5, 14.5)
y (mm)	N(0, 0.5)	U(-1, 1)	N(0, 0.5)	U(1.5, 1.5)	U(1.5, 1.5)
Liftoff (mm)	N(2, 0.5)	N(2, 1)	N(2, 0.5)	U(1.83, 2.23)	N(2, 0.7)

length/width and simulated through the KD-BEM physical model. In total (over all the flaw lengths), 5000 model responses are obtained in each case for MAPoD analysis. The model responses are the absolute values of the impedance variations which are treated in the metamodel fitting.

Convergence analysis and accuracy of proposed metamodels for surface flaw length ranges from 0.1 mm to 0.5 mm is studied in cases 1 and 2, and width ranges from 0.1 mm to 0.5 mm is studied in case 3. To test the performance of metamodels accelerated MAPoD analysis, the practical eddy current NDT cases are tested in cases 4 and 5. In cases 4 and 5, surface flaw length ranges from 1 mm to 5 mm are studied.

In case 1, to reach the predefined 1% accuracy in NRMSE and PoD metrics, the OLS-PCE method needs 500 LHS training points for each flaw length, while the LAR-PCE method needs only 150 LHS points. The computational costs are shown in Table 2. LAR-PCE only need to compute 30% physical model evaluations of OLS-PCE and the convergence of LAR-PCE is faster than OLS-PCE, which results in 72% training time savings. The NRMSE of LAR-PCE and OLS-PCE methods for flaw length ranges from 0.1 mm to 0.5 mm are shown in Fig. 3. NRMSE values are smaller than 1% for all flaw lengths. The regression line of the LAR-PCE metamodel can be found in "$\hat{a}$ vs. a" plot as shown in Fig. 4.

Table 2: Computation costs for case 1

Model	Training Points per Flaw Length	Total Training Time (s)
OLS-PCE	500	25
LAR-PCE	150	7
Pure physical model	1000	/

In Case 2, the OLS-PCE method needs 250 LHS training points, while the LAR-PCE method needs only 100 LHS training points to reach the predefined accuracy level for each flaw length. The computational costs are shown in Table 3. To reach the required accuracy level,

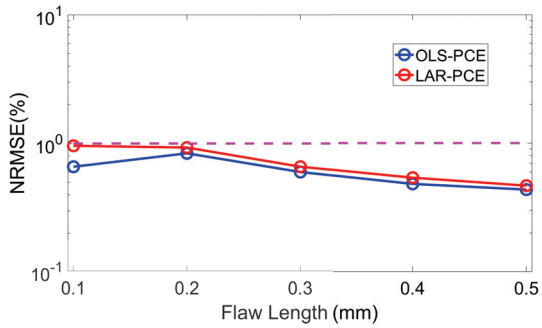

Fig. 3. NRMSE of OLS-PCE with 500 LHS training points and LAR-PCE with 150 LHS training points.

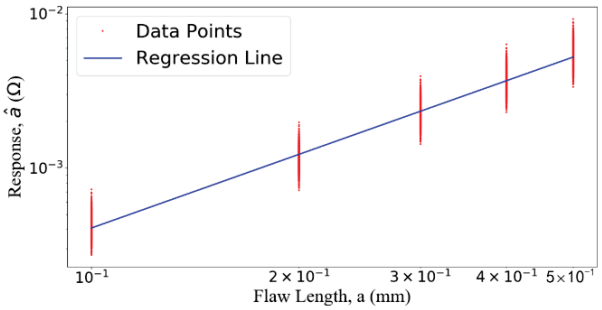

Fig. 4. Case 1: "$\hat{a}$ vs. a" plot with regression line of LAR-PCE metamodel.

the LAR-PCE method needs to compute 40% physical model evaluations with 63.6% training time savings over the OLS-PCE method. The regression line of the LAR-PCE metamodel can be found in "$\hat{a}$ vs. a" plot as shown in Fig. 5. Again, the LAR-PCE method accelerated physical model shows improved efficiency over the OLS-PCE method with well-maintained accuracy.

Table 3: Computation costs for case 2

Model	Training Points per Flaw Length	Total Training Time (s)
OLS-PCE	250	11
LAR-PCE	100	4
Pure physical model	1000	/

In case 3, flaw widths are analyzed to study the performance and accuracy of the LAR-PCE metamodel. LAR-PCE needs only 100 LHS training points while OLS-PCE needs 220 points to satisfy the accuracy level for each flaw width. Computational costs can be found in Table 4 that LAR-PCE requires 54.5% less physical model evaluations and 60% less training time than the OLS-PCE metamodel. The regression line of the LAR-PCE metamodel can be found in the "$\hat{a}$ vs. a" plot as

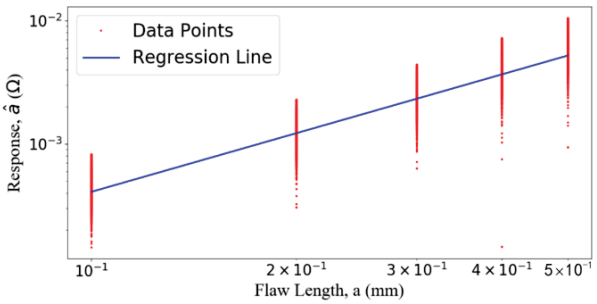

Fig. 5. Case 2: "$\hat{a}$ vs. a" plot with regression line of LAR-PCE metamodel.

shown in Fig. 6. Once more, the remarkable performance of the proposed LAR-PCE metamodel is demonstrated over the OLS-PCE metamodel.

Table 4: Computation costs for case 3

Model	Training Points per Flaw Length	Total Training Time (s)
OLS-PCE	220	15
LAR-PCE	100	6
Pure physical model	1000	/

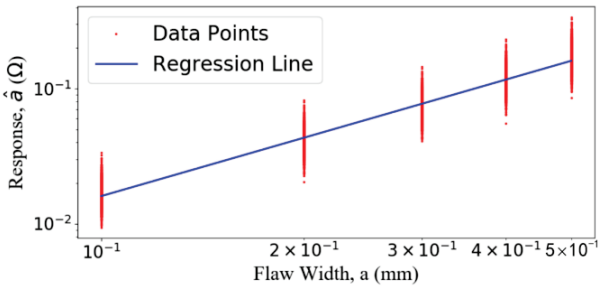

Fig. 6. Case 3: "$\hat{a}$ vs. a" plot with regression line of LAR-PCE metamodel.

The LAR-PCE metamodel shows advantages over the OLS-PCE metamodel in numbers of physical model evaluation needed and training time costed with faster convergence. The performance of metamodels accelerated MAPoD analysis for practical eddy current NDT problems are considered in the following cases. Flaw lengths ranging from 1 mm to 5 mm are studied in cases 4 and 5 with different uncertain parameters. The threshold value is 0.1 Ω.

In case 4, for each flaw length, LAR-PCE and OLS-PCE need 80 and 150 training points, respectively, to reach the required accuracy level with the computational costs shown in Table 5. The OLS-PCE metamodel needs 1.88 times computational cost and 1.43 times total training time of the LAR-PCE metamodel. PoD metrics achieved by the pure physical model, LAR-PCE and OLS-PCE metamodels are shown in Table 6. The relative differences among these metrics are smaller than 1%, which satisfy the accuracy requirement. PoD curves predicted by LAR-PCE for flaw lengths are shown in Fig. 7. Both the accuracy and efficiency of the LAR-PCE metamodel over OLS-PCE are demonstrated in the practical eddy current NDT problem.

Table 5: Computation costs for case 4

Model	Training Points per Flaw Length	Total Training Time (s)
OLS-PCE	150	10
LAR-PCE	80	7
Pure physical model	1000	/

Table 6: PoD metrics for case 4

Metrics	Pure Physical Model	OLS-PCE	LAR-PCE
μ	0.91626	0.91543	0.91564
σ	0.026475	0.027011	0.026402
a_{50}	2.4999	2.4978	2.4984
a_{90}	2.5862	2.5858	2.5844

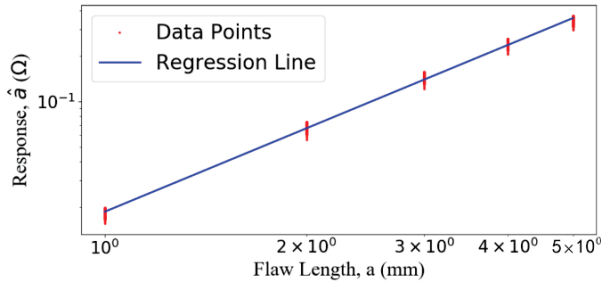

(a)

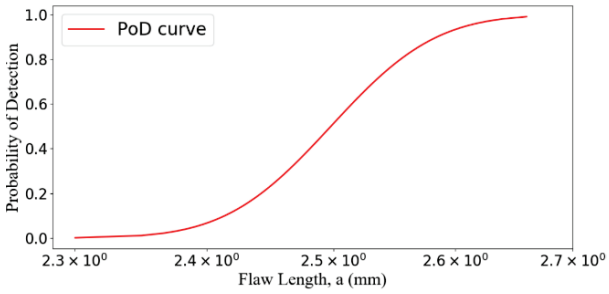

(b)

Fig. 7. Case 4 (a) "$\hat{a}$ vs. a" plot with regression line of LAR-PCE metamodel and (b) PoD curves.

In case 5, PoD metrics achieved by the LAR-PCE method with 150 LHS training points, the OLS-PCE

method with 500 LHS training points and the pure KD-BEM based physical model with 5000 MCS points are shown in Table 7. It can be seen that all PoD metrics predicted by the OLS-PCE and LAR-PCE agree well with those calculated by the pure physical model with the relative differences smaller than 1%. The relative differences of PoD metrics predicted by the LAR-PCE and pure physical model are 0.808%, 0.902%, 0.734% and 0.876% for μ, σ, a_{50} and a_{90}, respectively. The PoD curve predicted by LAR-PCE for flaw lengths is shown in Fig. 8. It can be concluded that, for case 5 to reach the required accuracy level 1% in the MAPoD analysis, the computational cost in LAR-PCE is just 30% of the OLS-PCE. This shows the advantage of applying LAR-PCE over OLS-PCE to replace the pure physical model in MAPoD analysis.

Table 7: PoD metrics for case 5

Metrics	Pure Physical Model	OLS-PCE	LAR-PCE
μ	0.90845	0.90116	0.90111
σ	0.12531	0.12449	0.12418
a_{50}	2.4805	2.4625	2.4623
a_{90}	2.9126	2.8884	2.8871

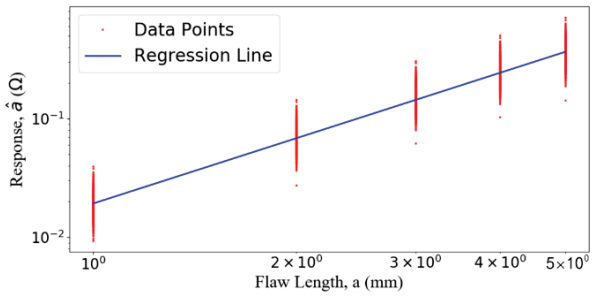

(a)

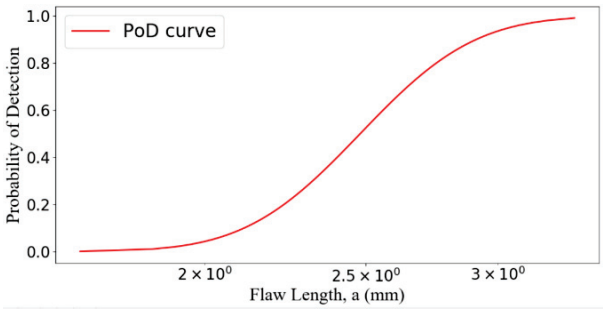

(b)

Fig. 8. Case 5 (a) "$\hat{a}$ vs. a" plot with regression line of LAR-PCE metamodel and (b) PoD curves.

IV. CONCLUSION

In this paper, the LAR-PCE method is proposed to accelerate eddy current MAPoD analysis based on the KD-BEM physical model. Both the accuracy and efficiency of the LAR-PCE metamodel are demonstrated by comparing the predicted PoD metrics with the ones achieved by the OLS-PCE metamodel and the pure physical model. Through numerical tests, which include different system setups and uncertain parameters, the results show that to ensure the relative differences of PoD metrics smaller than 1.1%, the LAR-PCE metamodel needs fewer training points than the OLS-PCE model. This makes LAR-PCE more efficient than the OLS-PCE metamodel in MAPoD analysis for eddy current NDT systems. The proposed LAR-PCE metamodel should work for accelerating the MAPoD analysis regardless of achieving the physical responses from experiment or simulation only, or from both. The uncertainties considered in this study do not significantly influence the relative efficiencies of the two metamodeling techniques we compared. In other words, regardless of the uncertainties considered, the LAR-PCE based metamodel performed better than OLS-PCE, as evident from the simulation time and accuracy values. Also, it can find merits in MAPoD study in other NDT areas such as ultrasound, eddy current thermography and so on which could be the future work.

REFERENCES

[1] A. Sophian, G. Tian, D. Taylor, and J. Rudlin, "Electromagnetic and eddy current NDT: A review," *Insight*, vol. 43, no. 5, pp. 302-306, 2001.

[2] J. Schijve, *Fatigue of Structures and Materials*. Dordrecht: Springer, 2009.

[3] M. R. Bato, A. Hor, A. Rautureau, and C. Bes, "Experimental and numerical methodology to obtain the probability of detection in eddy current NDT method," *NDT&E International*, vol. 114, pp. 1-13, 2020.

[4] A. Moskovchenko, M. Švantner, V. Vavilov, and A. Chulkov, "Analyzing probability of detection as a function of defect size and depth in pulsed IR thermography," *NDT&E International*, vol. 130, pp. 1-9, 2022.

[5] N. Yusa, H. Song, D. Iwata, T. Uchimoto, T. Takagi, and M. Moroi, "Probabilistic analysis of electromagnetic acoustic resonance signals for the detection of pipe wall thinning," *Nondestructive Testing and Evaluation*, vol. 36, pp. 1-16, 2021.

[6] K. Tschöke, I. Mueller, V. Memmolo, M. Moix, J. Moll, Y. Lugovtsova, M. Golub, R. Sridaran, and L. Schubert, "Feasibility of model-assisted probability of detection principles for structural

health monitoring systems based on guided waves for fiber-reinforced composites," *IEEE Transactions on Ultrasonics, Ferroelectrics, and Frequency Control*, vol. 68, no. 10, pp. 3156-3173, 2021.

[7] A. Rosell, "Efficient finite element modelling of eddy current probability of detection with transmitter–receiver sensors," *NDT&E International*, vol. 75, pp. 48-56, 2015.

[8] P. Baskaran, D. J. Pasadas, A. Ribeiro, and H. Ramos, "Probability of detection modelling in eddy current NDE of flaws integrating multiple correlated variables," *NDT&E International*, vol. 123, pp. 1-8, 2021.

[9] R. Miorelli, C. Reboud, T. Theodoulidis, J. Martinos, N. Poulakis, and D. Lesselier, "Coupled approach VIM–BEM for efficient modeling of ECT signal due to narrow cracks and volumetric flaws in planar layered media," *NDT&E International*, vol. 62, pp. 178-183, 2014.

[10] K. Pipis, A. Skarlatos, T. Theodoulidis, and D. Lesselier, "ECT-signal calculation of cracks near fastener holes using an integral equation formalism with dedicated Green's kernel," *IEEE Transactions on Magnetics*, vol. 52. no. 4, pp. 1-8, 2015.

[11] J. Song, C. C. Lu, and W. C. Chew, "Multilevel fast multipole algorithm for electromagnetic scattering by large complex objects," *IEEE Transactions on Antennas and Propagation*, vol. 45, no. 10, pp. 1488-1493, 1997.

[12] Y. Bao, Z. Liu, J. Bowler, and J. Song, "Multilevel adaptive cross approximation for efficient modeling of 3D arbitrary shaped eddy current NDE problems," *NDT&E International*, vol. 104, pp. 1-9, 2019.

[13] W. Chai and D. Jiao, "An $?^2$-matrix-based integral-equation solver of reduced complexity and controlled accuracy for solving electrodynamic problems," *IEEE Transactions on Antennas and Propagation*, vol. 51, no. 10, pp. 3147-3159, 2009.

[14] Y. Bao, T. Wan, Z. Liu, J. Bowler, and J. Song, "Integral equation fast solver with truncated and degenerated kernel for computing flaw signals in eddy current non-destructive testing," *NDT&E International*, vol. 124, pp. 1-13, 2021.

[15] S. Bilicz, "Sparse grid surrogate models for electromagnetic problems with many parameters," *IEEE Transactions on Magnetics*, vol. 52, no. 3, pp. 1-4, 2015.

[16] L. Gratiet, B. Iooss, G. Blatman, T. Browne, S. Cordeiro, and B. Goursaud, "Model assisted probability of detection curves: New statistical tools and progressive methodology," *Journal of Nondestructive Evaluation*, vol. 36, no. 1, pp. 1-12, 2017.

[17] G. Blatman and B. Sudret, "Adaptive sparse polynomial chaos expansion based on least angle regression," *Journal of Computational Physics*, vol. 230, no. 6, pp. 2345-2367, 2011.

[18] X. Du and L. Leifsson, "Efficient uncertainty propagation for MAPOD via polynomial chaos-based Kriging," *Engineering Computations*, vol. 37, no. 1, pp. 73-92, 2020.

[19] Y. Bao, "Modeling of eddy current NDT simulations by Kriging surrogate model," *Research in Nondestructive Evaluation*, vol. 34, pp. 1-15, Sep. 2023.

[20] Y. Bao, Z. Liu, J. Bowler, and J. Song, "Nested kernel degeneration-based boundary element method solver for rapid computation of eddy current signals," *NDT&E International*, vol. 128, pp. 1-9, 2022.

[21] S. M. Stigler, "The epic story of maximum likelihood," *Statistical Science*, vol. 22, pp. 592-620, 2007.

[22] S. K. Burke, "A benchmark problem for computation of ΔZ in eddy-current nondestructive evaluation (NDE)," *Journal of Nondestructive Evaluation*, vol. 7, pp. 35-41, 1988.

Yang Bao was born in Nanjing, Jiangsu, China. He received the B.S. and M.S. degrees from Nanjing University of Posts and Telecommunications in 2011 and 2014, respectively, and the Ph.D. degree in Electrical Engineering from Iowa State University in 2019. Since 2019, he has been an Assistant Professor at Nanjing University of Posts and Telecommunications. His research interests focus on modeling and simulations of eddy current nondestructive evaluation.

Jiahao Qiu was born in Huai'an, Jiangsu, China. He received the B.S. degrees from Yancheng Institute of Technology in 2021. He is currently working toward the master's degree in College of Electronic and Optical Engineering with Nanjing University of Posts and Telecommunications. His current research interests are computational electromagnetics and machine learning.

Praveen Gurrala received the B.Tech. degree from Indian Institute of Technology Madras in 2014, and the Ph.D. degree from Iowa State University in 2020, both in Electrical Engineering. He is currently a Signal Integrity Engineer at Micron Technology, Inc. His research interests include computational modeling of ultrasonic and eddy current NDE inspections, fast-multipole boundary element methods, EMI/EMC modeling and measurements, and capacitance tomography.

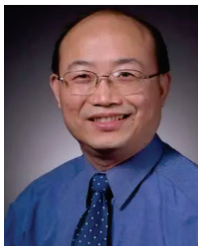

Jiming Song received the Ph.D. degree in Electrical Engineering from Michigan State University in 1993. From 1993 to 2000, he worked as a Postdoctoral Research Associate, a Research Scientist and Visiting Assistant Professor at the University of Illinois at Urbana-Champaign. From 1996 to 2000, he worked part-time as a Research Scientist at SAIC-DEMACO. Dr. Song was the principal author of the Fast Illinois Solver Code (FISC). He was a Principal Staff Engineer/Scientist at Semiconductor Products Sector of Motorola in Tempe, Arizona, before he joined Department of Electrical and Computer Engineering at Iowa State University as an Assistant Professor in 2002.

Dr. Song currently is a Professor at Iowa State University's Department of Electrical and Computer Engineering. His research has dealt with modeling and simulations of electromagnetic, acoustic and elastic wave propagation, scattering, and non-destructive evaluation, electromagnetic wave propagation in metamaterials and periodic structures and applications, interconnects on lossy silicon and radio frequency components, antenna radiation and electromagnetic wave scattering using fast algorithms, and transient electromagnetic fields. He received the NSF Career Award in 2006 and is an IEEE Fellow and ACES Fellow.